Studies of Reentrance in Pyrochlore Magnets and Machine Learning of Quenched Gauge Symmetries

by

Darren Pereira

A thesis
presented to the University of Waterloo
in fulfillment of the
thesis requirement for the degree of
Master of Science
in
Physics

Waterloo, Ontario, Canada, 2020

Author's Declaration

This thesis consists of material all of which I authored or co-authored: see Statement of Contributions included in the thesis. This is a true copy of the thesis, including any required final revisions, as accepted by my examiners.

I understand that my thesis may be made electronically available to the public.

Statement of Contributions

This thesis presents two unrelated research projects. The first half of the thesis is dedicated to the study of reentrance in the rare-earth pyrochlore magnet $Er_2Sn_2O_7$; the second half of the thesis is dedicated to exploring if machine learning can detect gauge symmetries, specifically in Mattis spin glass models. Both projects are the results of collaborations with the researchers mentioned below.

In the study of reentrance in the rare-earth pyrochlore magnet $Er_2Sn_2O_7$, single crystals were synthesized by Prof. Joseph W. Kolis of Clemson University and Dr. Liurukara D. Sanjeewa of Oak Ridge National Laboratory. The experimental studies of the crystals were conducted by Danielle Yahne under the supervision of Prof. Kate Ross, both of Colorado State University. This includes heat capacity measurements of all crystals using two different methods and under three different magnetic field directions, as well as elastic neutron scattering experiments. On the theoretical side of the project, classical Monte Carlo simulations were performed by Dr. Ludovic Jaubert of the University of Bordeaux. Prof. Matthew Enjalran of Southern Connecticut State University wrote the original variational mean-field theory code for the Heisenberg model on the pyrochlore lattice, with the option to include dipolar interactions computed via the Ewald summation. Under the supervision of Prof. Michel Gingras, the author modified this code to include generic (symmetry-allowed) nearest-neighbor interactions on the pyrochlore lattice and wrote an Ewald summation program for anisotropic magnetic moments, as detailed in Chapters 2 and 3. The author derived and programmed the spin-wave calculations detailed in Chapters 3 and 4. All calculations, simulations, and figures in Chapter 4 are the work of the author, with the exception of the classical Monte Carlo simulations, Figure 4.10, and the experimental data. The author also put forward the hypotheses in Chapter 4 explaining reentrance. This work will be presented in a forthcoming publication, in which all of the above researchers are listed as co-authors. Danielle Yahne, Prof. Kate Ross, Dr. Ludovic Jaubert, Prof. Matthew Enjalran, and Prof. Michel Gingras all contributed to the writing and editing of the manuscript.

In the study of machine learning of gauge symmetries, the author collaborated with Daniel Lozano-Gómez of the University of Waterloo, both under the supervision of Prof. Michel Gingras. The calculations and simulations were performed independently by both the author and Daniel Lozano-Gómez, in order to verify the work of each. This work is detailed in the manuscript "Unsupervised Machine Learning of Quenched Gauge Symmetries: A Proof-of-Concept Demonstration" (arXiv:2003.00039), in which all of the above researchers are co-authors. All co-authors contributed to the writing and editing of the manuscript. In this thesis, all figures (except Figure 7.1) and almost all datasets have

been generated solely by the author and are not the same as the ones used in the above manuscript.[1] The only dataset that is shared with the manuscript is for the Mattis XY gauge glass model. However, all figures in this thesis that are related to this dataset were generated by the author.

[1] As discussed further in Part II of the thesis, the datasets are generated from classical Monte Carlo simulations of the so-called Mattis Ising spin glass and Mattis XY gauge glass models. Our machine learning method is then applied to these datasets. Hence, even if the datasets used in this thesis differ from those of the manuscript, the conclusions remain unchanged because the datasets are generated and provided to the machine learning method in the same manner.

Abstract

In this thesis, we present two explorations: (1) understanding the mechanism causing reentrant behavior in the rare-earth pyrochlore magnet $Er_2Sn_2O_7$, and (2) determining if unsupervised machine learning is capable of uncovering quenched gauge symmetries.

Recent heat capacity measurements have been performed on newly-available single crystal samples of $Er_2Sn_2O_7$ under an applied magnetic field $\boldsymbol{H}$. For the [100], [110], and [111] field directions, the resulting (H, T) phase diagrams all exhibit reentrant lobes: as a function of H for certain fixed values of T, the system transitions from disordered to ordered and back to disordered. We demonstrate that, broadly speaking, multiphase competition is the origin of this reentrant behavior. In particular, two types of multiphase competition operate in $Er_2Sn_2O_7$: (1) competition that is induced by the applied field $\boldsymbol{H}$ between ordered states of different symmetry, and (2) competition present from the zero-field ground state of $Er_2Sn_2O_7$. Using a combination of classical Monte Carlo simulations, mean-field theory, and classical spin-wave expansions, we show that both types of multiphase competition produce soft spin-wave modes not present in the zero-field ground state. These increase thermal fluctuations and entropically stabilize the *ordered* phase, thereby producing reentrance. It is argued that dipolar interactions do not change this microscopic mechanism. Implications for other materials are discussed.

A major application of machine learning techniques to condensed matter physics has focused on learning thermodynamic quantities such as order parameters and phase transitions. However, since the simulated models follow physical laws that are mathematical in nature, one may ask if machine learning can provide information about the model itself. We explore this question with the Mattis Ising spin glass (MISG) and Mattis XY gauge glass (MXYGG) models, which can be mapped onto the ferromagnetic Ising and XY models under a gauge transformation. Using the well-established unsupervised Principal Component Analysis (PCA) method, we answer the above question affirmatively. PCA classifies the phases of the MISG and MXYGG models in the same manner as the regular Ising and XY models, indicating it has detected their gauge symmetries. Moreover, PCA provides a quantitative estimate of the gauge transformation that establishes this mapping, despite being provided no information about it. This demonstrates that unsupervised machine learning can provide insights into simulated models themselves. The implications of this idea are discussed.

Acknowledgements

"Beautiful is what we see. More beautiful is what we know. Most beautiful by far is what we don't." (Blessed Nicolas Steno)

The work presented in this thesis would not have been successful nor enjoyable without the presence of a number of people. First and foremost, I would like to thank my supervisor, Professor Michel Gingras. I always appreciated your effort to place me on interesting and important projects, as well as for providing patience, guidance, knowledge, and enthusiasm throughout the research process. By both word and example, you have taught me what it means to be a theoretical physicist. I am sure that if I take just a spark of the fiery passion that you carry for physics research, I will be well on my way.

I am immensely grateful to all of the officemates and staff I had the pleasure of working with. In a special way, I have to thank Alex Hickey, for being a reliable source of comic relief; Aritro Mukherjee, for stimulating religious discussions and deepening my faith in God; Cyrus Cerkauskus, for making early office mornings less lonely; Daniel Lozano-Gómez, for unintentionally becoming my uncompensated personal trainer; Kai Chung, for inspiring me to develop a broad yet mathematically precise understanding of physics; Naman Gupta, for conversations (on life, love, meaning, and the names of things) that only brothers can share; and Wen Jin, for patiently enduring my numerous silly questions. I would also like to thank Addison D. S. Richards, Bo Liu, Daniel Wong, James Chow, Jennifer Reid, Manisha Thakurathi, Rantong Gong, Steven Esau, and Subhankar Khatua for their camaraderie and support throughout my Master's, and the friendly teaching and administrative staff of the department that contributed daily joys.

I am additionally indebted to a number of academic mentors and collaborators. Thank you to Professors Roger Melko and Rob Hill for being members of my committee, encouraging me in my successes while continually challenging me to become a better researcher. Thank you also to Professor Anton Burkov for teaching me a variety of fascinating topics, and Professor David Hawthorn for serving on my defense committee. And, of course, thank you to Professor Kate Ross, Danielle Yahne, Dr. Ludovic Jaubert, and Professor Matthew Enjalran for your collaborations.

These acknowledgements would not be complete without mentioning St. Michael Catholic Church and the St. John Paul II Student Centre, which provided me with many lifelong friends and even more happy memories. I am especially grateful to my Exodus 90 brothers – Ed Gutierrez, Kevin Abraham, Kevin Widjaja, Mark Zasowski, R.J. Barbaran, Steven Ammerlaan, and Tak Shibayama. I hope I made your quarantines a little more entertaining. Thank you as well to Team St. Joseph, the Youngins, and my many other

friends from Toronto; even from a distance, your support pushed me forward and helped me persevere when times were rough.

Last, but certainly not least, thank you to my family. I always looked forward to the "weekend vacations" where I was able to spend time with you all, recharge and recuperate, and return to Waterloo with plentiful food in tow. Thank you for your unconditional love and support, and for always listening to any little (or big) ups and downs I had to share. Thank you for teaching me to work hard, to work hard on the right things, and to work hard for the right reasons. None of this would have been possible without you, so this accomplishment is as much mine as it is yours. I hope it makes you proud.

Totus tuus ego sum, et omnia mea tua sunt.
Non nisi Te, Domine.

Table of Contents

List of Figures

List of Tables

List of Abbreviations

FCC	Face-Centered Cubic
PC	Palmer-Chalker
FEPC	Field-Evolved Palmer-Chalker
FP-PM	Field-Polarized Paramagnet
PCA	Principal Component Analysis
MISG	Mattis Ising Spin Glass
MXYGG	Mattis XY Gauge Glass

PART I –
"There and Back Again": Studies of Reentrance in Pyrochlore Magnets

Chapter 1

Introduction

1.1 Magnetism and Magnetic Frustration

The study of magnetism constitutes a major sector of the field of condensed matter physics. The phenomenon of magnetism is tangibly available now as it was centuries before, even though some of the theories that undergird it (such as quantum mechanics and relativity) have only been developed relatively recently [1]. As such, magnetism may be said to hold a special place in the field of condensed matter physics: it is simultaneously amenable to acute experimental tests and theoretical analysis. The study of magnetism is therefore an excellent place to understand how well our theories of physics describe the real world, as well as to uncover new and exotic behavior.

One way in which exotic behavior commonly arises in magnetism is through frustration. Frustration refers to a system's inability to simultaneously satisfy all of its energetic preferences. For example, consider a triangular plaquette of Ising spins and antiferromagnetic nearest-neighbor interactions, as shown in Figure 1.1. If a spin on one site is aligned along the $\hat{z}$ direction, the antiferromagnetic interaction would prefer its nearest neighbor to align along the $-\hat{z}$ direction. However, the third site is a neighbor to both these sites. Regardless of which way the spin on this third site is aligned, one of the bonds will not minimize the energy of its antiferromagnetic coupling. The system is said to be frustrated; as a result of this competition between the interactions and preferred alignments, the system may attempt to arrange itself in some compromised way, or lower energy scales (e.g. from perturbatively-small interactions) may become important in determining the ultimate ordering of the system. In this way, frustrated magnets are a common home for unconventional phases or behavior.

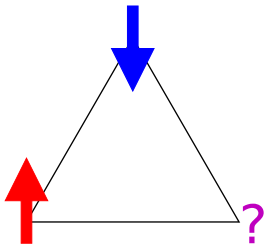

Figure 1.1: An example of geometric frustration for antiferromagnetic interactions on a triangular plaquette. If two sites are oriented antiparallel to satisfy the antiferromagnetic interaction, the orientation on the third site is not clear.

The above example demonstrates *geometric* frustration. In such cases, frustration is inherent to the lattice itself. If one considers a bipartite lattice such as the honeycomb lattice, nearest-neighbor antiferromagnetic interactions are not frustrated. It is a simple matter of arranging the spins on alternating sublattices to align along the $\hat{z}$ or $-\hat{z}$ directions. However, even in a bipartite lattice, frustration of another type is possible – namely, *exchange* frustration [2]. This may occur when the interactions within the Hamiltonian itself compete with one another and have incompatible energetic preferences. One example is the Kitaev honeycomb model [2, 3], in which each of the three types of bonds on the honeycomb lattice have an Ising-like interaction, but with respect to different axes. The anisotropic interactions that give rise to exchange frustration usually have their microscopic origins in spin-orbit coupling. This couples the orbital and spin angular momenta of the electrons in an ion, thereby allowing real-space anisotropies (from the lattice, surrounding ions, and so on) to influence the magnetic moments.

1.2 The Rare-Earth Pyrochlore Oxides

We see that frustration can arise from geometry or anisotropic exchange. A fitting family of materials to study the exotic effects of frustration is therefore the rare-earth pyrochlore oxides. The rare-earth pyrochlore oxides consist of a chemical formula $A_2B_2O_7$, where A^{3+} is a rare-earth ion and B^{4+} is a transition metal ion. The pyrochlore lattice structure consists of interpenetrating networks of corner-sharing tetrahedra; both the A-site and B-site ions form their own such network [2, 4]. For our purposes, we consider materials in which only the A-site is magnetic. Then, apart from the topic of crystal electric fields that surround the A-site ions (as discussed in Chapter 2), the A-site network of tetrahedra is

the only one we need to consider. This A-site network is displayed in Figures 1.2 and 1.3. Note that there are four sites per tetrahedron, and one upwards-facing ("up") tetrahedron for every lattice point of the face-centered cubic (FCC) lattice, as shown in Figure 1.2. However, the space between tetrahedra can also be connected to form downwards-facing ("down") tetrahedra, as shown in Figure 1.3, though this does not contribute any new sites to the conventional cubic cell. More details about the pyrochlore lattice are provided in Appendix A.

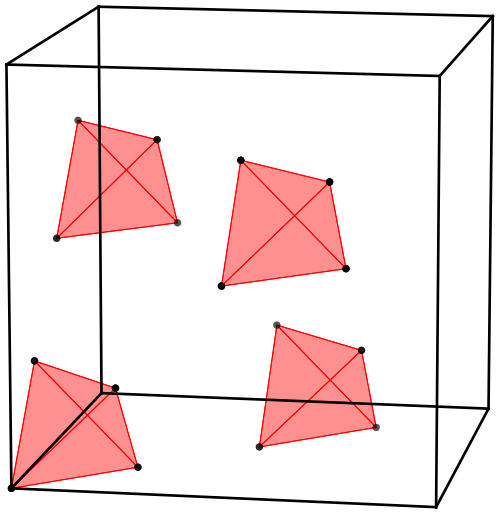

Figure 1.2: The pyrochlore lattice, displaying only the tetrahedra associated with magnetic A sites. Sites are indicated by black circles; the tetrahedra they form are shown in red. Note that there is a tetrahedron associated with each lattice point of the FCC lattice that falls within this conventional cubic cell. Only those sites, tetrahedra, and bonds that fall within this conventional cubic cell are shown. This gives 16 sites per conventional cubic cell.

There are two reasons why the rare-earth pyrochlore oxides are advantageous for studying frustrated magnetism. Firstly, each tetrahedron of A-sites is formed by four triangular faces; the elemental triangular motif of geometric frustration is therefore present. Secondly, as the rare-earth atoms have a large atomic number Z, they are usually subject to a strong

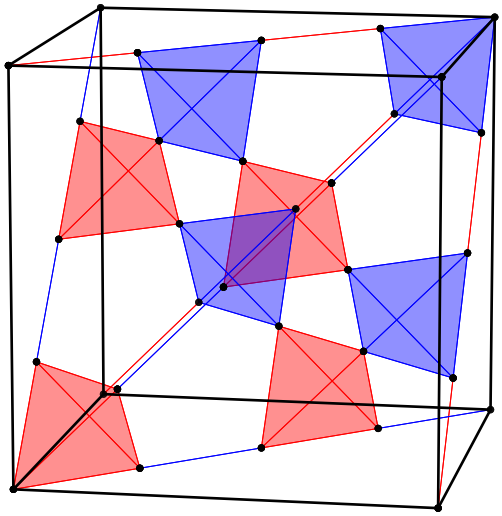

Figure 1.3: The pyrochlore lattice, displaying only the tetrahedra associated with magnetic A sites. Sites are indicated by black circles; up (down) tetrahedra are shown in red (blue). Note that the down tetrahedra are formed by connecting sites between different up tetrahedra, and hence do not exist as distinct tetrahedra of their own. Shown here are only those sites, tetrahedra, and bonds that fall within this conventional cubic cell or on its shared faces with adjacent cells.

spin-orbit coupling. This is likely to give rise to highly anisotropic interactions, paving the way for exchange frustration. Hence, the rare-earth pyrochlore oxides are a playground for both types of frustration and may therefore host novel effects and phases. Historically, this has been demonstrated well by the rare-earth titanates (where $B^{4+} = Ti^{4+}$).

1.3 Brief Overview of the Rare-Earth Titanates

Of all the magnetic pyrochlore oxide materials, the subset of rare-earth titanates is arguably the most studied. In the past few decades, experimental and theoretical analysis has

been conducted on $Ho_2Ti_2O_7$, $Dy_2Ti_2O_7$, $Gd_2Ti_2O_7$, $Er_2Ti_2O_7$, and $Yb_2Ti_2O_7$, among others [2, 4, 5]. The variation of the A-site ion leads to a subsequent diversity in physical phenomena.

The study of rare-earth titanates was initialized by $Ho_2Ti_2O_7$ [6–9] and $Dy_2Ti_2O_7$ [8–10]. As suggested in the previous section, both Ho^{3+} and Dy^{3+} are subject to strong spin-orbit coupling. Hence, the good quantum number with which to describe these two ions in free space is the *total* angular momentum $\boldsymbol{J} = \boldsymbol{L} + \boldsymbol{S}$. Specifically, $J = 8$ ($J = \frac{15}{2}$) for Ho^{3+} (Dy^{3+}), leading to a degeneracy of $2J+1 = 17$ ($2J+1 = 16$) levels. As discussed further in Chapter 2, the crystal electric fields within the lattice lift this degeneracy. This leads to a ground state doublet in both materials that is well-separated from the higher-lying states by a large energy gap [9]. As such, both materials are well described by a pseudospin $S = \frac{1}{2}$ model.[1] As well, these doublets are mostly comprised of the $J^z = J$ states and hence possess large magnetic moments, which behave classically to a good approximation [11]. Moreover, the crystal electric fields create a local Ising anisotropy: the moments prefer to lie along their "local" Ising axes (i.e. the axes pointing in/out of a tetrahedron and towards its centre). Paradoxically, it is discovered that both of these materials have net ferromagnetic interactions, yet both materials do not exhibit long-range magnetic order at low temperatures [8]! Instead, both materials enter a classical spin ice state, in which each tetrahedron has two moments that point in and two moments that point out. Since there are a variety of choices that accomplish this, the classical spin ice state has a residual entropy at zero temperature. In fact, this is equivalent to the residual entropy of water ice, where a similar disordered arrangement (termed the "ice rules") is found in two protons lying near or far from an oxygen atom [8, 9, 12]. Theoretically, it is the combination of local Ising anisotropy and the geometry of the pyrochlore lattice that renders the ferromagnetic interactions effectively antiferromagnetic[2], leading to this exotic magnetic phase.[3]

Another important titanate pyrochlore is $Gd_2Ti_2O_7$. Since Gd^{3+} has $L = 0 \implies$

[1] Physically, the two states that make up the pseudospin $S = \frac{1}{2}$ doublet are a linear combination of the original $|J, J^z\rangle$ states of the rare-earth ion.

[2] To illustrate this with a simple picture, consider a ferromagnetic interaction between between two moments, which takes the form $-J_{\text{ex}}\boldsymbol{J}_i \cdot \boldsymbol{J}_j$ for $J_{\text{ex}} > 0$. If these moments have an Ising anisotropy with respect to their local $\hat{z}$ axes, they can effectively be written as $\boldsymbol{J}_i = \langle J \rangle \sigma_i^z \hat{z}_i$ using an Ising variable $\sigma_i^z = \pm 1$. The exchange interaction then becomes $-J_{\text{ex}} \langle J \rangle^2 \sigma_i^z \sigma_j^z (\hat{z}_i \cdot \hat{z}_j)$. In the case of the pyrochlore lattice, $\hat{z}_i \cdot \hat{z}_j = -\frac{1}{3}$, yielding $\frac{J_{\text{ex}}}{3} \langle J \rangle^2 \sigma_i^z \sigma_j^z$. The change in sign of the interaction represents the change from ferromagnetic interactions to effectively antiferromagnetic interactions.

[3] Note that the strong spin-orbit coupling of $4f$ atoms implies that other interactions may be generated beyond the Ising interactions assumed here [11]. However, Rau and Gingras [11] argue that these interactions are negligible for the cases of $Ho_2Ti_2O_7$ and $Dy_2Ti_2O_7$.

$J = S = \frac{7}{2}$, $Gd_2Ti_2O_7$ may naively[4] be thought of as a Heisenberg spin model on the pyrochlore lattice [4]. Experimentally, it was determined that $Gd_2Ti_2O_7$ has antiferromagnetic interactions [15, 16]. Theoretically, the antiferromagnetic Heisenberg model on the pyrochlore lattice should form a classical spin liquid, with short-range spin correlations but no long-range order [17]. This made the study of the magnetic properties of $Gd_2Ti_2O_7$ especially exciting. It was later determined that $Gd_2Ti_2O_7$ does magnetically order at low temperatures [15]. Theoretically, the large moments of Gd^{3+} make the long-range dipolar interaction non-negligible [15], and one may expect the $\boldsymbol{q} = 0$ coplanar antiferromagnet Palmer-Chalker (PC) phase to be stabilized [18]. However, $Gd_2Ti_2O_7$ instead orders (via two transitions) into a partially-disordered magnetic phase, where $\frac{3}{4}$ of the Gd^{3+} moments order and the remaining $\frac{1}{4}$ do not [4, 19, 20]. Hence, although $Gd_2Ti_2O_7$ enters an ordered phase, the long-range order is unconventional nonetheless. This ordering is even more exotic in light of the behavior of the isostructural pyrochlore $Gd_2Sn_2O_7$. $Gd_2Sn_2O_7$ again realizes an antiferromagnetic Heisenberg model with long-range dipolar interactions [4, 21], but $Gd_2Sn_2O_7$ orders into the theoretically-expected PC phase via a single phase transition [22, 23].

A third example of a well-studied rare-earth titanate is $Er_2Ti_2O_7$. Unlike $Ho_2Ti_2O_7$, $Dy_2Ti_2O_7$, and $Gd_2Ti_2O_7$, $Er_2Ti_2O_7$ possesses a local XY anisotropy, where the moments mostly lie in the planes perpendicular to the local Ising axes [5].[5] At the mean-field level, $Er_2Ti_2O_7$ orders into the so-called Γ_5 phase [24]. This is a $\boldsymbol{q} = 0$ antiferromagnetic phase in which all four spins on a tetrahedron lie in their local xy-planes, making the same angle from their local x-axes, as discussed further in Chapter 2 and Appendix A. This phase thus possesses a $U(1)$ degeneracy, but this is not protected by the symmetry of the Hamiltonian. Hence, when quantum or thermal fluctuations are incorporated, this accidental degeneracy may be broken [25–28] in what is termed order-by-disorder [29, 30]. This may result in two subsets of the overall Γ_5 phase, a non-coplanar ψ_2 phase or a coplanar ψ_3 phase, which are also discussed in Chapter 2. Experimentally, $Er_2Ti_2O_7$ is found to order in the ψ_2 phase [25, 31], making it perhaps one of the most compelling realizations of an order-by-disorder mechanism[6] at work in an actual material [5].

A final rare-earth titanate that we discuss is $Yb_2Ti_2O_7$. Like $Er_2Ti_2O_7$, $Yb_2Ti_2O_7$ also possesses an XY anisotropy [5, 33], but it orders in a splayed ferromagnet phase that shares

[4] Note that a single-ion anisotropy of the Gd^{3+} moments has been determined experimentally [13, 14]. This is expected from the mixing of $L \neq 0$ states due to strong spin-orbit coupling [13].

[5] A picture showing what these local Ising and XY anisotropies look like on a tetrahedron is given in Figure 2.2.

[6] An alternative proposal for the selection of ψ_2 has been put forward on the basis of virtual crystal field fluctuations [32].

similarities with the spin ice state of $Ho_2Ti_2O_7$ and $Dy_2Ti_2O_7$ [8, 33]. $Yb_2Ti_2O_7$ exhibits a number of strange features, such as multiple reentrant phenomena under applied magnetic fields [34–36], a continuum of inelastic scattering within its ordered phase [37], a broad heat capacity anomaly in the paramagnetic phase [5, 38], and an extreme sensitivity to disorder [5, 39–41], to name a few. Some of these features may be the result of $Yb_2Ti_2O_7$'s close proximity to the antiferromagnetic ψ_3 phase [24, 42], which might produce strong multiphase competition. In addition, $Yb_2Ti_2O_7$'s XY anisotropy and the small J^z values that comprise its ground state doublet[7] may also enhance the role of quantum fluctuations in the material [5]. Strong quantum fluctuations could be another microscopic ingredient for $Yb_2Ti_2O_7$'s exotic phenomena, and it has already been put forward as the reason for its reentrant phase diagram under a magnetic field [34, 35, 43].

All in all, the variation of the rare-earth ion in the pyrochlore titanates gives rise to a panoply of effects – magnetic phases with residual entropy, no long-range order, or partial disorder; order-by-disorder in a real material; multiphase competition; reentrance; and more. It should be noted that a common thread has made the exploration of rare-earth titanates so effective, namely, the availability of large single crystals. With large single crystals, inelastic neutron scattering (on an ordered ground state or field-polarized magnetic state) can be fitted with theoretical spin-wave calculations to give accurate estimates of the microscopic interactions between magnetic moments in the material. Such a determination is highly important for a precise theoretical modelling and for constructing an accurate theory with predictive power. Moreover, when compared with polycrystalline or powder samples, single crystals allow for experiments and analysis that would otherwise be more complicated or less refined.[8] For example, polarized neutron scattering performed on single crystals of $Er_2Ti_2O_7$ helped determine its ψ_2 (instead of ψ_3) ground state [31]; single crystals of $Yb_2Ti_2O_7$ were also needed to uncover its sensitivity to disorder [39]. As noted earlier, the subfield of magnetism is special because it is amenable to both theoretical and experimental studies. Not surprisingly, then, pyrochlore magnetism has advanced due to the coupled efforts of crystal synthesis, high-quality experiments, and rigorous theoretical analysis.

[7] We are here referring to the small J^z values in the $|J, J^z\rangle$ states that compose the pseudospin $S = \frac{1}{2}$ doublet.

[8] The complication of using powder or polycrystalline samples comes from their mixture of differently-oriented parts of the material. In a single crystal, the entire sample is oriented in the same way, allowing one to define global directions. This permits the study of the sample under an applied magnetic field along specific global directions, for example.

1.4 An Introduction to the Stannate Pyrochlores and $Er_2Sn_2O_7$

Recently, a new so-called hydrothermal crystal growth method was developed to synthesize rare-earth pyrochlore *stannates* (i.e. $B^{4+} = Sn^{4+}$) [44]. The stannate series is the only one which can stably form the pyrochlore structure described above (i.e. the *cubic* pyrochlore structure [4]) for *all* choices of the rare-earth ion A^{3+}, due to the ionic radii of the A^{3+} and B^{4+} ions [44].[9] Although pyrochlore stannate single crystals had been grown before [46], it was only accomplished for a subset of the full lanthanide series. On the other hand, this new hydrothermal growth method allows the synthesis of $A_2Sn_2O_7$ for *any* choice of A^{3+} in the lanthanide series! As well, previous attempts at single crystal synthesis required very high temperatures, which led to defects in the oxygen sites as well as disorder between the rare-earth and tin (Sn) ions; this new hydrothermal growth method circumvents these issues by performing the synthesis in an aqueous solution rather than a furnace, reducing the temperature required [44]. The range and diversity of unconventional phenomena that occurred for the pyrochlore titanates has already been noted in the previous section, as well as the important role that single crystals played in those studies. This new hydrothermal growth method opens the door for many new and exciting discoveries to be uncovered through an exploration of the pyrochlore stannates. It even goes beyond what is provided by the titanates, in that it affords access to the *full* lanthanide family.

A suitable starting point for such an exploration might be $Er_2Sn_2O_7$. There is reason to believe that exotic physics may be at play in $Er_2Sn_2O_7$. A first point is that $Er_2Sn_2O_7$ possesses an XY anisotropy similar to $Er_2Ti_2O_7$ and $Yb_2Ti_2O_7$, as well as a pseudospin $S = \frac{1}{2}$ doublet[10] that has a major contribution from its $J^z = \frac{1}{2}$ state [5, 47]. This may imply that strong quantum effects could influence the physics of $Er_2Sn_2O_7$ [24]. A second point is that estimated exchange parameters for $Er_2Sn_2O_7$ [48, 49] place it in close proximity to the Γ_5 (ψ_2) phase. This is reminiscient of $Yb_2Ti_2O_7$'s proximity to the ψ_3 phase. As such, the role of multiphase competition may also be important for $Er_2Sn_2O_7$ and it may again give rise to interesting phenomena. A final point is that experiments on $Er_2Sn_2O_7$

[9] In particular, a rough estimate of whether this pyrochlore structure can be stably formed is given by the ionic radii r_A and r_B. If $\frac{r_A}{r_B}$ is between 1.46 and 1.80, the proposed compound may form a cubic pyrochlore structure at atmospheric pressure [45].

[10] Recall from Section 1.3 that the crystal electric fields split the $2J+1$ degenerate levels of the free rare-earth ion into doublets (for J being a half-integer). In $Er_2Sn_2O_7$, the resulting energy gap between the ground state doublet and the first excited doublet is about 5 meV [47], which is much greater than the energy scales considered in this thesis. Hence, we can effectively treat $Er_2Sn_2O_7$ using a pseudospin $S = \frac{1}{2}$ to model its ground state doublet. Again, this effective $S = \frac{1}{2}$ doublet is a linear combination of $|J, J^z\rangle$ states of the Er^{3+} ion. These points are further discussed in Chapter 2.

[49] established that it orders at $T_c \approx 108$ mK into the PC ground state. The PC state is mentioned in Section 1.3 in relation to studies of $Gd_2Ti_2O_7$ and $Gd_2Sn_2O_7$. Hence, a rich phase diagram under an applied magnetic field might also be expected for $Er_2Sn_2O_7$, as is found for $Gd_2Ti_2O_7$ [19, 50]. This phase diagram might prove especially rich due to the influence of quantum effects and multiphase competition, as mentioned in the first and second points above. For example, studies of the proximate Kitaev material α-$RuCl_3$ under an applied magnetic field suggest that it may transition into a quantum spin liquid phase [51], even though α-$RuCl_3$ transitions into a long-range ordered magnetic phase in zero field [52]. $Er_2Sn_2O_7$'s close proximity to a phase boundary suggests it may be near a region of quantum disorder [24], so studying it in the presence of an applied field may prove quite worthwhile.

1.5 Motivation and Outline

Motivated by the above considerations, single crystals of $Er_2Sn_2O_7$ were synthesized and studied under an applied magnetic field. Three directions of the applied magnetic field $\boldsymbol{H}$ were studied, namely, the [100], [111], and [110] conventional cubic directions, as shown in Figure 1.4. In all three directions, the heat capacity was measured in two ways: (1) using "short" heat pulses that slightly raise the temperature, and (2) using "long" heat pulses that greatly raise the temperature [53]. In the latter approach, the heat capacity can be determined from how the sample cools over time [53]. For example, Figure 1.5a shows the heat capacity measurements for both methods in zero field. As well, Figure 1.5b shows the heat capacity as a function of H[11] along the [110] direction. From these heat capacity measurements, phase transitions can be found and allow a (H, T) phase diagram to be mapped out. The resulting phase diagrams for each field direction is shown in Figure 1.6.

The feature that is noticeable immediately in all three field directions is the reentrant lobe(s) that each phase boundary possesses. Reentrance is when a system enters a new phase and then returns to its original phase as an external parameter is continuously tuned [54–60]. In these phase diagrams, as temperature is fixed at certain values and the magnetic field is increased, the system transitions from a disordered phase to an ordered phase and then back to a disordered phase. This occurs in all three field directions, and even multiple times for the [110] field direction. It should be noted that this reentrant behavior is found

[11] When we refer to the applied magnetic field in general, we call it $\boldsymbol{H}$. However, when the direction of the applied magnetic field is specified or implied, we simply use H to indicate the *magnitude* of the applied field along that direction.

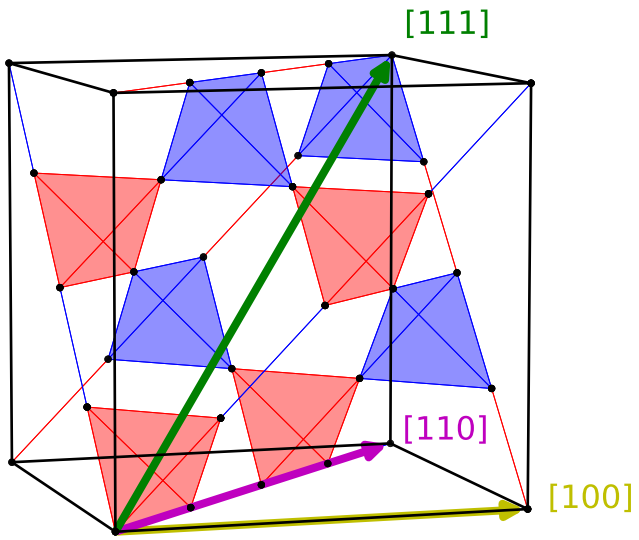

Figure 1.4: The [100] (yellow), [110] (purple), and [111] (green) high-symmetry directions within the pyrochlore lattice, as depicted within a conventional cubic cell.

for multiple crystals of different shapes, so it presumably does not originate from the demagnetization effect[12].

Given that reentrance is the most striking and common feature between all three phase diagrams, the objective of Part I of this thesis was to understand the mechanism of reentrance from a theoretical perspective, aiming to give a robust physical explanation for its microscopic origins. In doing so, important ingredients at work in the physics of $Er_2Sn_2O_7$ might be uncovered and may guide further investigations into this material and others. As discussed further in Chapter 4, *classical* Monte Carlo simulations of $Er_2Sn_2O_7$ roughly

[12]The demagnetization effect refers to the field that the magnetization of a material produces within itself, which acts against the magnetization at any given point in the sample [61]. The relation between the demagnetization field and the sample's magnetization depends on the sample's shape [61]. Hence, finding reentrant behavior in samples of different shapes indicates that the behavior does not come from the demagnetization effect.

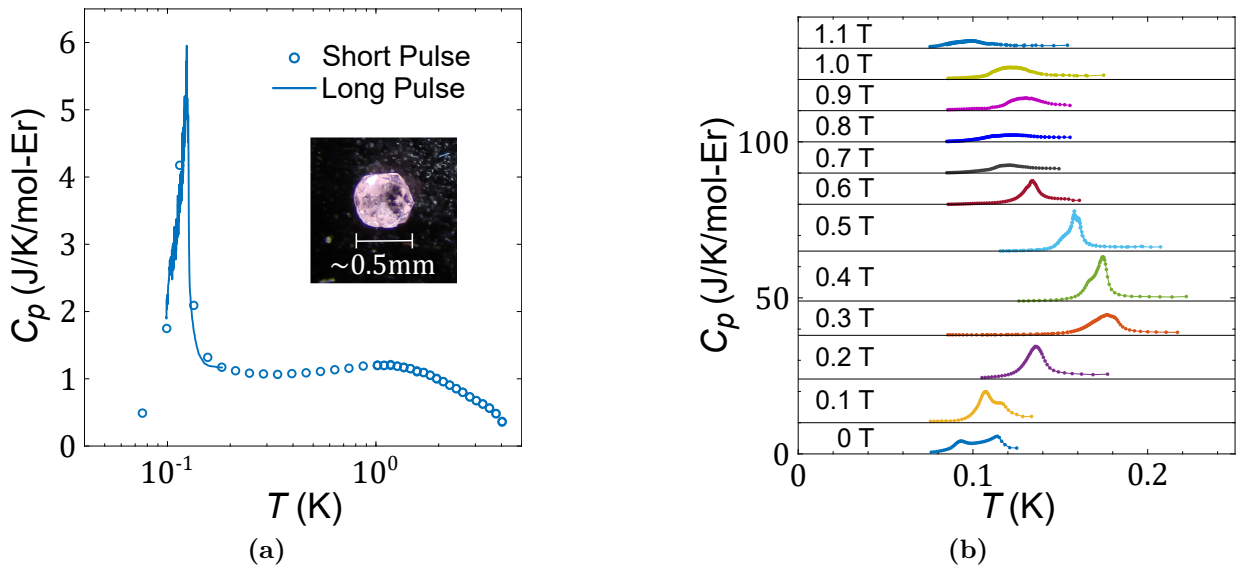

Figure 1.5: Heat capacity results for a single crystal of $Er_2Sn_2O_7$ in (a) zero field, and (b) an applied field along the [110] direction. In (a), the inset shows a single crystal of $Er_2Sn_2O_7$; in (b), curves are offset for clarity, and a broad heat capacity is visible in the lowest fields. [Figures provided by Danielle Yahne.]

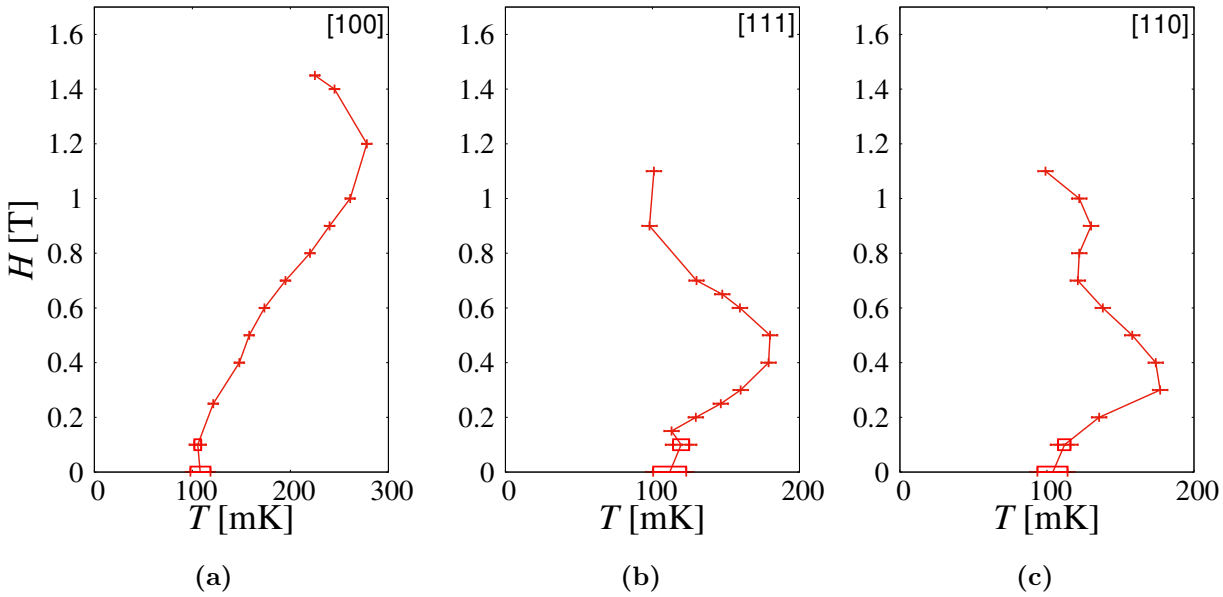

Figure 1.6: Phase boundaries for single crystals of $Er_2Sn_2O_7$, studied under applied fields along the (a) [100], (b) [111], and (c) [110] directions. Red rectangles indicate areas where broad heat capacity signatures are found. Note that the H-axis is shared between all three plots. [Data provided by Danielle Yahne and Kate Ross; figures generated by Ludovic Jaubert.]

reproduce which values of H reentrance occurs at, as well as the increase in T_c at each of these reentrant lobes. This allows us to study reentrance using the simplified model used in classical Monte Carlo simulations, as opposed to considering the full complexity of the real material. This also allows us to tackle the question of reentrance using classical methods and considerations of thermal fluctuations, since quantum fluctuations are not present in classical Monte Carlo simulations. Although this prevents us from determining how quantum effects might contribute to the occurrence of reentrance – an idea returned to in Chapter 5 – it provides a reasonable and controlled starting point for understanding reentrance.

The outline of Part I is as follows. In Chapter 2, we discuss the theoretical model that is pertinent to $Er_2Sn_2O_7$. This includes a consideration of its single-ion physics, nearest-neighbor interactions between magnetic moments, and long-range dipolar interactions. In Chapter 3, we discuss the multiple analytical and numerical methods used to study the model. In particular, we consider mean-field theory and classical spin-wave expansions. Mean-field theory ignores the effect of fluctuations and hence provides a picture of the un-

derlying phases; classical spin-wave expansions allow us to incorporate thermal fluctuations (to lowest order) beyond this mean-field treatment. These two methods together allow us to decompose and reconstruct the main ingredients of classical Monte Carlo simulations. Chapter 4 details the results of this analysis. In particular, it explains the microscopic mechanism behind reentrance for each of the applied field directions. Lastly, Chapter 5 summarizes the work, explains its implications for reentrance in other materials (magnetic or not), and discusses aspects of $Er_2Sn_2O_7$ that still require study.

Chapter 2

Models

2.1 Microscopic Details of the Effective $S = \frac{1}{2}$ Model

The materials we are considering are of the chemical formula $R_2M_2O_7$, where R^{3+} is a rare-earth ion and M^{4+} is a transition metal ion. We focus on the case of relevance to us, where R^{3+} is a Kramers ion[1] and M^{4+} is non-magnetic. As an isolated ion, the R^{3+} rare-earth ion has a large atomic number Z and is therefore expected to experience a strong atomic spin-orbit coupling. As such, the free-space description of such atoms is not in terms of the spin (angular momentum) $\boldsymbol{S}$, but rather the total angular momentum $\boldsymbol{J} = \boldsymbol{L} + \boldsymbol{S}$.[2] The proper filling of electron shells and resulting total angular momentum may be determined using Hund's rules [1].

It is with this good quantum number that we must understand what happens in a solid (i.e. the pyrochlore lattice). Within a solid, there are crystal electric fields that act upon the rare-earth ion. These crystal electric fields can influence the orbital angular momentum $\boldsymbol{L}$ and hence the total angular momentum $\boldsymbol{J}$. As a result, the original $2J + 1$ degeneracy present in free space is now lifted by the crystal electric fields. The splitting scheme can be described by exploiting the symmetries of the lattice and the surrounding atoms via their irreducible representations [1]; alternatively, a microscopic approximation to the splitting can also be described using the Stevens operator formalism [2]. However, a qualitative picture for Kramers ions is immediately available: due to time reversal symmetry, the

[1] Kramers ions are those with a half-integer angular momentum. According to Kramers' theorem [62], the energy levels of such ions are at least doubly degenerate due to time reversal symmetry.

[2] For reference, the electronic configuration of Er is [Xe] $4f^{12}\ 6s^2$. As well, Er^{3+} has $L = 6$, $S = \frac{3}{2}$, and $J = \frac{15}{2}$ [63].

original $2J+1$ degeneracy for half-integer J is split into a collection of doublets, which are superpositions of the original $|J, J^z\rangle$ eigenstates in free space.

The splitting scheme (that is, the $|J, J^z\rangle$ composition of each doublet and the energy separation between doublets) depends on the material in question and its microscopic details. Inelastic neutron scattering is an experimental method that can determine the splitting scheme in a real material [5, 47]; for many of the rare-earth pyrochlore oxides, and in particular $Er_2Sn_2O_7$, the lowest doublet is well-separated in energy from the higher-lying doublets. For exchange parameters that are on the order of 1 K and when studying these materials at similarly low temperatures, this large energy gap between the lowest doublet and the first excited doublet allows one to effectively describe the spin system by only considering its lowest doublet. Hence, the full complexity of the original physical moments is reduced to a pseudospin $S = \frac{1}{2}$ model. Generally, we may express the resulting pseudospin $S = \frac{1}{2}$ states as

$$\left|S^z = \frac{1}{2}\right\rangle = \sum_{J^z=-J}^{J} a_{J^z} \left|J, J^z\right\rangle, \tag{2.1}$$

where a_{J^z} are coefficients that give weight to the linear combination of $|J, J^z\rangle$ states.[3] Note that $\left|S^z = -\frac{1}{2}\right\rangle$ may be obtained by time reversal symmetry.

There is another consideration which needs to be made when going from free ions to ions in a solid influenced by crystal electric fields – namely, the anisotropy of the physical magnetic moments. In free space, the physical moments are isotropic; there is no preferred $\hat{z}$ direction, as all directions are the same. This may no longer be the case in a solid. In the pyrochlore lattice, each rare-earth ion is surrounded by a cage of oxygen (O^{2-}) ions [2, 4]. Specifically, for a given rare-earth ionic site on a tetrahedron, there are two oxygen ions that straddle it axially (i.e. along the local [111] direction), as shown in Figure 2.1 [2, 4]. Since these apical oxygen ions are closer to the rare-earth ion than the other surrounding oxygen ions, their crystal electric fields have a stronger influence on the anisotropy of the physical magnetic moments $\boldsymbol{J}$. Qualitatively[4], on symmetry grounds, one may therefore expect two special types of anisotropy to occur: (1) anisotropy along the local [111] direction (i.e. local $\hat{z}_i$ or Ising anisotropy), or (2) anisotropy in the plane perpendicular to the local [111] direction (i.e. local XY anisotropy). These two types of anisotropies are depicted in

[3] These coefficients can be determined (indirectly) from inelastic neutron scattering. For example, one may use inelastic neutron scattering to determine the Hamiltonian describing the crystal electric fields and then diagonalize the Hamiltonian to find the resulting eigenstates, as done by Gaudet *et al.* [47].

[4] In reality, the origin of the single-ion anisotropy is more complicated than what is presented here. However, we only aim to provide a qualitative and intuitive description of how this anisotropy arises.

Figure 2.2. This is precisely what is seen in experimental studies of the real materials and in microscopic mathematical analysis of them.

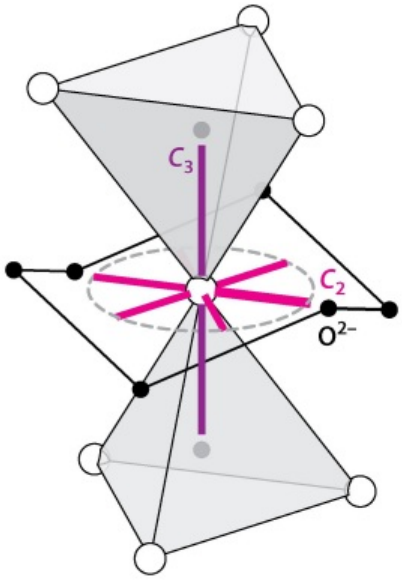

Figure 2.1: Local environment of oxygen (O^{2-}) ions surrounding the A-sites of the pyrochlore lattice (open white circles). Black filled circles represent O^{2-} ions that form a puckered ring around the A-site; grey filled circles denote O^{2-} ions that axially straddle the A-site along its local [111] direction (denoted as the C_3 rotation axis in the figure). Reprinted figure with permission from Rau and Gingras, Annu. Rev. Condens. Matter Phys. **10**, 357 (2019). Permission conveyed through Copyright Clearance Center, Inc.

When projecting from the physical magnetic moments $\boldsymbol{J}$ to the pseudospin $S = \frac{1}{2}$ model as in Eq. (2.1), one must therefore also consider how this anisotropy manifests itself in the effective pseudospin model. In particular, this is important when considering the system's response to an applied magnetic field $\boldsymbol{H}$. In terms of the physical moments $\boldsymbol{J}$, this is quantified by the Zeeman interaction,

$$\mathcal{H}_z = -g_J \mu_B \boldsymbol{J} \cdot \boldsymbol{H}. \tag{2.2}$$

Here, μ_B is the Bohr magneton (i.e. the magnitude of the magnetic moment of an electron's spin angular momentum) and g_J is the Landé g-factor (i.e. a proportionality constant that allows one to write the Zeeman interaction in terms of $\boldsymbol{J}$ rather than $\boldsymbol{L} + 2\boldsymbol{S}$) [63]. The magnetic moment of the system can then be taken to be $\boldsymbol{\mu} = \mu_B g_J \boldsymbol{J}$. When projecting into the effective pseudospin $S = \frac{1}{2}$ model, one can use the eigenstates in Eq. (2.1). For

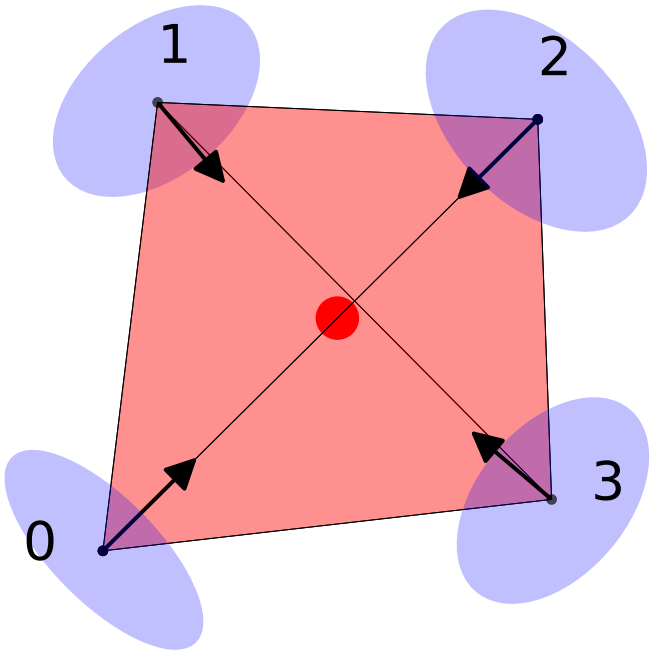

Figure 2.2: Local Ising and XY anisotropies on a single tetrahedron of the pyrochlore lattice. Black arrows represent local Ising anisotropy, with each arrow pointing to the center of the tetrahedron (depicted by a red circle). Blue circles represent local XY anisotropy, perpendicular to the local Ising axis on each sublattice.

example, consider projecting $g_J J^z$ into the pseudospin $S = \frac{1}{2}$ doublet using the projection operator $\left|S^z = \frac{1}{2}\right\rangle \left\langle S^z = \frac{1}{2}\right|$. This would yield

$$\begin{aligned} &\left|S^z = \frac{1}{2}\right\rangle \left\langle S^z = \frac{1}{2}\right| g_J J^z \left|S^z = \frac{1}{2}\right\rangle \left\langle S^z = \frac{1}{2}\right| \\ &= \left(\sum_{J^z=-J}^{J} g_J a_{J^z}^2 J^z\right) \left|S^z = \frac{1}{2}\right\rangle \left\langle S^z = \frac{1}{2}\right|. \end{aligned} \tag{2.3}$$

On the other hand, our above discussion of anisotropies indicated that a local $\hat{z}_i$ anisotropy may be generated by the crystal electric fields. Defining g_z to quantify this anisotropy in

the local frame, we analogously have (for the pseudospin $S = \frac{1}{2}$ model)

$$\begin{aligned}&\left|S^z = \frac{1}{2}\right\rangle \left\langle S^z = \frac{1}{2}\right| g_z S^z \left|S^z = \frac{1}{2}\right\rangle \left\langle S^z = \frac{1}{2}\right| \\ &= \frac{1}{2} g_z \left|S^z = \frac{1}{2}\right\rangle \left\langle S^z = \frac{1}{2}\right|. \end{aligned} \tag{2.4}$$

Comparing Eqs. (2.3) and (2.4), we arrive at the definition

$$g_z = 2g_J \left\langle S^z = \frac{1}{2}\right| J^z \left|S^z = \frac{1}{2}\right\rangle = 2g_J \sum_{J^z=-J}^{J} a_{J^z}^2 J^z. \tag{2.5}$$

One may similarly define g_{xy}, which quantifies the local XY anisotropy within the pseudospin $S = \frac{1}{2}$ model. Altogether, in the local frame of reference of a given site, we can define[5] a g-tensor to codify the response of our effective $S = \frac{1}{2}$ spin to the magnetic field $\boldsymbol{H}$. For g_{xy} and g_z defined as above, this tensor takes the diagonal form [2, 33, 48, 65]

$$\overleftrightarrow{\boldsymbol{g}} = \begin{pmatrix} g_{xy} & & \\ & g_{xy} & \\ & & g_z \end{pmatrix}, \tag{2.6}$$

and the resulting Zeeman interaction in the pseudospin $S = \frac{1}{2}$ model takes the form

$$\mathcal{H}_z = -\mu_B g^{\mu\nu} S^\mu H^\nu, \tag{2.7}$$

where summation over Cartesian components (μ and ν) is implied.

In this thesis, we will be working in a *global* frame of reference. It is therefore of interest to express the local-frame g-tensor in the global frame. As an example, consider the 0^{th} sublattice (as defined in Table A.2), in which the local z–axis is $\frac{1}{\sqrt{3}}(1,1,1)$ in the global frame. We would like to determine the matrix that rotates $\frac{1}{\sqrt{3}}(1,1,1)$ onto the global z–axis, $(0,0,1)$. To do this, one can employ the Rodrigues rotation formula [66]. Let $\boldsymbol{k}$ be the unit vector denoting the axis of rotation and let the angle of rotation (according to the right hand rule) be θ. The corresponding rotation matrix is [66]

$$\overleftrightarrow{\boldsymbol{R}} = \mathbb{I} + [\sin(\theta)]\ \overleftrightarrow{\boldsymbol{K}} + [1 - \cos(\theta)]\ \overleftrightarrow{\boldsymbol{K}}^2, \tag{2.8}$$

[5] This discussion has demonstrated how to calculate the g-tensor using eigenstates that are determined from inelastic neutron scattering. Note, however, that g_z and g_{xy} can also be measured directly using electron paramagnetic resonance [64], for example.

where

$$\overset{\leftrightarrow}{\boldsymbol{K}} = \begin{pmatrix} 0 & -k_z & k_y \\ k_z & 0 & -k_x \\ -k_y & k_x & 0 \end{pmatrix}. \tag{2.9}$$

To rotate $\boldsymbol{z}_{\text{loc}} = \frac{1}{\sqrt{3}}(1,1,1)$ into $\boldsymbol{z}_{\text{global}} = (0,0,1)$, the corresponding axis of rotation is $\boldsymbol{k} = \frac{\boldsymbol{z}_{\text{global}} \times \boldsymbol{z}_{\text{loc}}}{|\boldsymbol{z}_{\text{global}} \times \boldsymbol{z}_{\text{loc}}|} = \frac{1}{\sqrt{2}}(-1,1,0)$. This yields

$$\overset{\leftrightarrow}{\boldsymbol{K}} = -\frac{1}{\sqrt{2}} \begin{pmatrix} 0 & 0 & -1 \\ 0 & 0 & -1 \\ 1 & 1 & 0 \end{pmatrix}, \tag{2.10}$$

$$\overset{\leftrightarrow}{\boldsymbol{K}}^2 = -\frac{1}{2} \begin{pmatrix} 1 & 1 & 0 \\ 1 & 1 & 0 \\ 0 & 0 & 2 \end{pmatrix}. \tag{2.11}$$

The angle of rotation can be found with $\cos(\theta) = \boldsymbol{z}_{\text{loc}} \cdot \boldsymbol{z}_{\text{global}} = \frac{1}{\sqrt{3}} \implies \sin(\theta) = \sqrt{\frac{2}{3}}$. Calculating the rotation matrix via Eq. (2.8) and rotating Eq. (2.6) into the global frame yields:

$$\overset{\leftrightarrow}{\boldsymbol{g}}_0 = \begin{pmatrix} g_1 & g_2 & g_2 \\ g_2 & g_1 & g_2 \\ g_2 & g_2 & g_1 \end{pmatrix} \tag{2.12}$$

for

$$g_1 = \frac{2}{3} g_{xy} + \frac{1}{3} g_z, \tag{2.13}$$

$$g_2 = -\frac{1}{3} g_{xy} + \frac{1}{3} g_z. \tag{2.14}$$

A similar approach yields the g-tensors on the other sublattices, as reported in the literature [24]:

$$\overset{\leftrightarrow}{\boldsymbol{g}}_1 = \begin{pmatrix} g_1 & -g_2 & -g_2 \\ -g_2 & g_1 & g_2 \\ -g_2 & g_2 & g_1 \end{pmatrix}, \overset{\leftrightarrow}{\boldsymbol{g}}_2 = \begin{pmatrix} g_1 & -g_2 & g_2 \\ -g_2 & g_1 & -g_2 \\ g_2 & -g_2 & g_1 \end{pmatrix}, \overset{\leftrightarrow}{\boldsymbol{g}}_3 = \begin{pmatrix} g_1 & g_2 & -g_2 \\ g_2 & g_1 & -g_2 \\ -g_2 & -g_2 & g_1 \end{pmatrix}. \tag{2.15}$$

Lastly, note that when $g_{xy} \gg g_z$, as is the case for $Er_2Sn_2O_7$, these global-frame g-tensors can be approximately written as:

$$\overset{\leftrightarrow}{\boldsymbol{g}}_0 = \frac{g_{xy}}{3} \begin{pmatrix} 2 & -1 & -1 \\ -1 & 2 & -1 \\ -1 & -1 & 2 \end{pmatrix}, \overset{\leftrightarrow}{\boldsymbol{g}}_1 = \frac{g_{xy}}{3} \begin{pmatrix} 2 & 1 & 1 \\ 1 & 2 & -1 \\ 1 & -1 & 2 \end{pmatrix}, \tag{2.16}$$

$$\overleftrightarrow{\boldsymbol{g}}_2 = \frac{g_{xy}}{3}\begin{pmatrix} 2 & 1 & -1 \\ 1 & 2 & 1 \\ -1 & 1 & 2 \end{pmatrix}, \quad \overleftrightarrow{\boldsymbol{g}}_3 = \frac{g_{xy}}{3}\begin{pmatrix} 2 & -1 & 1 \\ -1 & 2 & 1 \\ 1 & 1 & 2 \end{pmatrix}. \tag{2.17}$$

2.2 Nearest-Neighbor Exchange

We now move forward from single-ion physics to interactions between ions. For a system of interacting magnetic moments, one type of interaction consists of bilinear couplings between nearest-neighbor pseudospins, of the form

$$\mathcal{H}_{\text{ex}} = \frac{1}{2}\sum_{a,b}\sum_{i,j}\sum_{\mu,\nu} J^{\mu\nu}_{ia,jb} S^{\mu}_{ia} S^{\nu}_{jb}, \tag{2.18}$$

where i and j are sublattice indices, a and b are tetrahedron indices, and μ and ν are spin component indices in the global frame. Note that the spins have length $|\boldsymbol{S}_{ia}| = \frac{1}{2}$. The factor of $\frac{1}{2}$ in Eq. (2.18) accounts for doubly counting nearest-neighbor pairs, and we assume that we are only summing over nearest-neighbors. This type of interaction is called exchange interactions; microscopically, they have their origin in the virtual hopping of electrons between ions due to electronic orbital overlap [1].

For a given bond on a tetrahedron, $J^{\mu\nu}_{ia,jb}$ is specified by nine parameters:

$$\overleftrightarrow{\boldsymbol{J}}_{ia,jb} = \begin{pmatrix} J_{11} & J_{12} & J_{13} \\ J_{21} & J_{22} & J_{23} \\ J_{31} & J_{32} & J_{33} \end{pmatrix}. \tag{2.19}$$

Translational symmetry of the lattice implies that the interaction matrix between sublattices i and j should be the same for any choice of a and b.[6]. Hence, one can use the symmetries of each bond to reduce the number of parameters involved, as has been done in Ref. [67]. For the 01 bond, the resulting interaction matrix is

$$\overleftrightarrow{\boldsymbol{J}}_{01} = \begin{pmatrix} J_2 & J_4 & J_4 \\ -J_4 & J_1 & J_3 \\ -J_4 & J_3 & J_1 \end{pmatrix}, \tag{2.20}$$

where J_1 is an XY-like interaction, J_2 is an Ising-like interaction, J_3 is a symmetric off-diagonal exchange, and J_4 is a Dzyaloshinsky-Moriya interaction [24]. Similar to the case

[6]This is to say that $\overleftrightarrow{\boldsymbol{J}}_{ia,jb} = \overleftrightarrow{\boldsymbol{J}}_{ia',jb'}$, not that $\overleftrightarrow{\boldsymbol{J}}_{ia,jb} = \overleftrightarrow{\boldsymbol{J}}_{jb,ia}$. The *order* of the sublattices still matters. Explicitly, $(\boldsymbol{S}^T_{jb}\, \overleftrightarrow{\boldsymbol{J}}_{ia,jb}\, \boldsymbol{S}_{ia})^T = \boldsymbol{S}^T_{ia}\, \overleftrightarrow{\boldsymbol{J}}^T_{ia,jb}\, \boldsymbol{S}_{jb} \equiv \boldsymbol{S}^T_{ia}\, \overleftrightarrow{\boldsymbol{J}}_{jb,ia}\, \boldsymbol{S}_{jb}$, so $\overleftrightarrow{\boldsymbol{J}}^T_{ia,jb} = \overleftrightarrow{\boldsymbol{J}}_{jb,ia}$.

of rotating the local g-tensor to get its global reference frame form, one can then use the rotational symmetries *between* bonds to relate the 01 bond's interaction matrix to that of other bonds. For example, the 01 bond is mapped onto the 02 bond by a $\frac{2\pi}{3}$ rotation around the global (i.e. conventional cubic) [111] axis, which maps $\hat{x} \to \hat{y}$, $\hat{y} \to \hat{z}$, and $\hat{z} \to \hat{x}$. The corresponding rotation matrix is thus

$$\overleftrightarrow{\boldsymbol{R}} = \begin{pmatrix} 0 & 1 & 0 \\ 0 & 0 & 1 \\ 1 & 0 & 0 \end{pmatrix}. \tag{2.21}$$

Applying this rotational change of basis to Eq. (2.20) yields

$$\overleftrightarrow{\boldsymbol{J}}_{02} = \begin{pmatrix} J_1 & -J_4 & J_3 \\ J_4 & J_2 & J_4 \\ J_3 & -J_4 & J_1 \end{pmatrix}. \tag{2.22}$$

One can similarly apply the other operations that relate the 01 bond to the remaining bonds on a tetrahedron, in order to generate the other interaction matrices [24, 33]. The remaining matrices are:

$$\overleftrightarrow{\boldsymbol{J}}_{03} = \begin{pmatrix} J_1 & J_3 & -J_4 \\ J_3 & J_1 & -J_4 \\ J_4 & J_4 & J_2 \end{pmatrix}, \quad \overleftrightarrow{\boldsymbol{J}}_{12} = \begin{pmatrix} J_1 & -J_3 & J_4 \\ -J_3 & J_1 & -J_4 \\ -J_4 & J_4 & J_2 \end{pmatrix}, \tag{2.23}$$

$$\overleftrightarrow{\boldsymbol{J}}_{13} = \begin{pmatrix} J_1 & J_4 & -J_3 \\ -J_4 & J_2 & J_4 \\ -J_3 & -J_4 & J_1 \end{pmatrix}, \quad \overleftrightarrow{\boldsymbol{J}}_{23} = \begin{pmatrix} J_2 & -J_4 & J_4 \\ J_4 & J_1 & -J_3 \\ -J_4 & -J_3 & J_1 \end{pmatrix}. \tag{2.24}$$

In conclusion, we see that the symmetries of the lattice give us much insight into both the g-tensor of the ions as well as their exchange interactions – even before or without considering the actual microscopic physics.

The g-tensor and exchange parameters for $Er_2Sn_2O_7$ have been measured experimentally using powder and polycrystalline samples [48, 49]. Keeping within the error bars of these measurements, the parameters used to model $Er_2Sn_2O_7$ in this thesis are:

$$\begin{aligned} &J_1 = 0.079 \text{ meV}, && J_2 = 0.066 \text{ meV}, && J_3 = -0.111 \text{ meV}, \ J_4 = 0.032 \text{ meV}, \\ &g_J = 1.2, && g_{xy} = 7.52, && g_z = 0.054, \end{aligned}$$

keeping in mind that $|\boldsymbol{S}_{ia}| = \frac{1}{2}$. As shown in Figure 4.1b of Chapter 4, the exchange parameters are chosen to match the critical temperature at $H = 0.4$ T in a [111] field.

2.3 Phases of the Nearest-Neighbor Exchange Model

For the nearest-neighbor exchange Hamiltonian described in the previous section, it has been proven [24] that the classical ground state is a $\boldsymbol{q} = 0$ order. This means that the ground state configuration on a *single* tetrahedron is tiled across the entire lattice by translational symmetry, while preserving the same orientation of the average (static) moment on a given sublattice as the full pyrochlore lattice is tiled. We therefore only need to focus on the ground state ordering that occurs on a single tetrahedron. One may again exploit the symmetries of the system to determine the order parameters for each possible ground state phase, as well as the exchange parameters that will lead to these phases [24, 67]. The full ground state phase diagram for $J_4 = 0$ is shown in Figure 2.3.

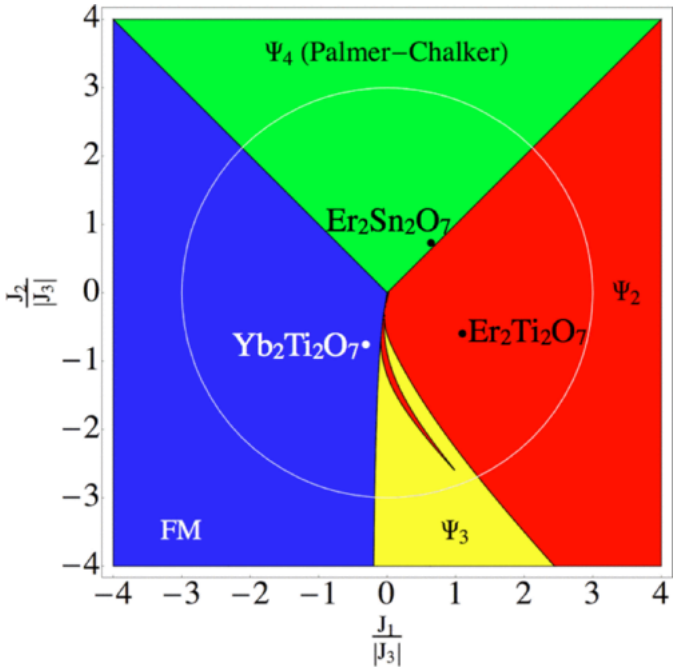

Figure 2.3: Classical ground state phase diagram of the nearest-neighbor Hamiltonian Eq. (2.18), with $J_3 < 0$ and $J_4 = 0$. The phases are described in the main text. Reprinted figure with permission from Yan *et al.*, Phys. Rev. B **95**, 094422 (2017). Copyright 2020 by the American Physical Society.

For the purpose of explaining reentrance in $Er_2Sn_2O_7$, there are two types of ordering that are most important. The first is the so-called PC phase [18]. The PC configurations are coplanar antiferromagnetic configurations: for a given xy-, xz-, or yz-plane, the spins

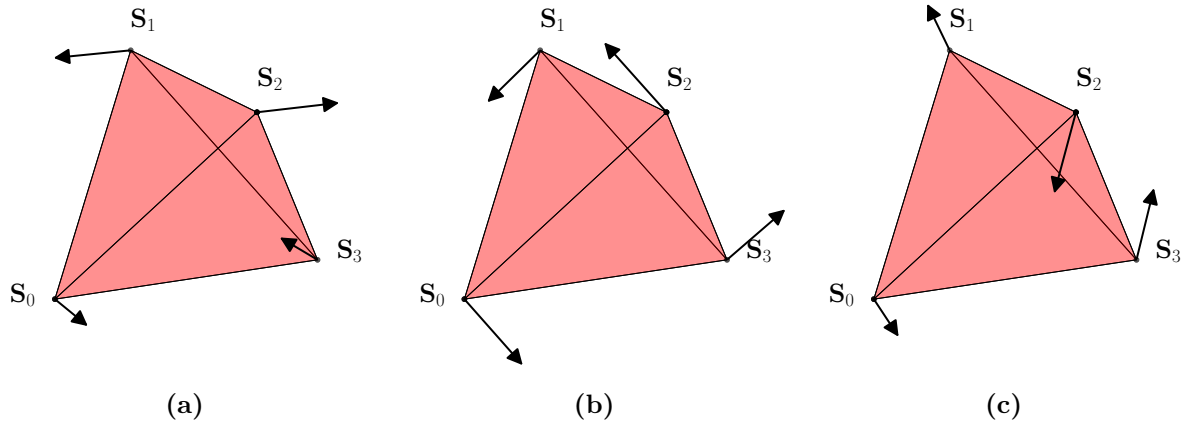

(a) **(b)** **(c)**

Figure 2.4: Example of the PC configurations (namely, (a) $\langle xy \rangle$, (b) $\langle xz \rangle$, and (c) $\langle yz \rangle$) on a single tetrahedron. Note that the remaining three PC configurations ($\langle \overline{xy} \rangle$, $\langle \overline{xz} \rangle$, and $\langle \overline{yz} \rangle$) can be obtained from reversing the spins of those shown here.

possess a chirality within the plane as viewed from the plane's normal. Since there are three planes and time reversal symmetry, there are six PC configurations. The six PC phases can be denoted by the plane in which they lie (e.g. $\langle xy \rangle$ for the configuration which lies in the xy-plane); an overbar denotes the time-reversal-symmetric configuration (e.g. $\langle \overline{xy} \rangle$). The $\langle xy \rangle$, $\langle xz \rangle$, and $\langle yz \rangle$ configurations are shown in Figures 2.4a, 2.4b, and 2.4c, respectively.

The other important type of order is the Γ_5 phase. This is also an antiferromagnetic phase in which all spins lie within their *local* xy-planes and make the same angle from their local x-axes. As such, this phase can be parameterized by a single angle θ_E[7] and has a $U(1)$ ground state degeneracy. The generic spin configurations are of the form [24]:

$$\boldsymbol{S}_0 = \sqrt{\frac{1}{6}} \left(\cos(\theta_E), \cos\left(\theta_E + \frac{2\pi}{3}\right), \cos\left(\theta_E - \frac{2\pi}{3}\right) \right), \tag{2.25}$$

$$\boldsymbol{S}_1 = \sqrt{\frac{1}{6}} \left(\cos(\theta_E), -\cos\left(\theta_E + \frac{2\pi}{3}\right), -\cos\left(\theta_E - \frac{2\pi}{3}\right) \right), \tag{2.26}$$

$$\boldsymbol{S}_2 = \sqrt{\frac{1}{6}} \left(-\cos(\theta_E), \cos\left(\theta_E + \frac{2\pi}{3}\right), -\cos\left(\theta_E - \frac{2\pi}{3}\right) \right), \tag{2.27}$$

[7]The subscript E comes from the fact that the Γ_5 phase is associated with the so-called E irreducible representation when decomposing the tetrahedral point group T_d of the pyrochlore lattice [24].

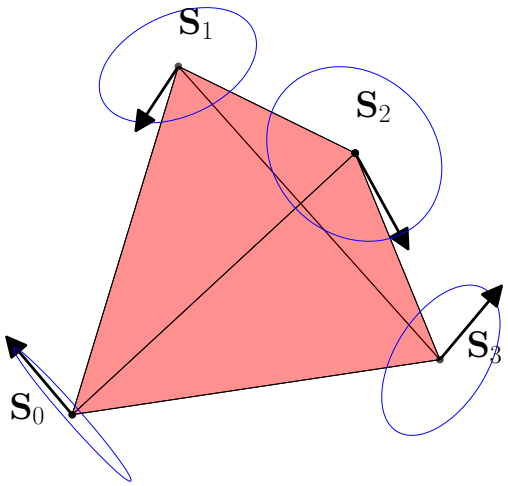

Figure 2.5: Example of a Γ_5 configuration on a single tetrahedron. Blue circles represent the local xy plane at each sublattice. All spins make the same angle θ_E from their local x-axis. Here, $\theta_E = \frac{3\pi}{4}$.

$$\boldsymbol{S}_3 = \sqrt{\frac{1}{6}}\left(-\cos(\theta_E), -\cos\left(\theta_E + \frac{2\pi}{3}\right), \cos\left(\theta_E - \frac{2\pi}{3}\right)\right). \tag{2.28}$$

An example of a generic Γ_5 configuration is displayed in Figure 2.5.

Now, the exchange Hamiltonian Eq. (2.18) does not in general possess a $U(1)$ symmetry. This is therefore an *accidental* classical degeneracy of the system which is not protected by actual symmetries of the model. Hence, the inclusion of fluctuations (thermal or quantum) may select a *subset* of this $U(1)$ manifold of states in which to order; this process has been termed order-by-disorder [25–30, 32]. With the inclusion of fluctuations, two possible subphases may arise from this $U(1)$ manifold. The first is the ψ_2 phase; this is a non-coplanar antiferromagnet for which $\theta_E = \frac{n\pi}{3}, n = 0, 1, \ldots, 5$. The second is the ψ_3 phase; this a coplanar antiferromagnet for which $\theta_E = \frac{(2n+1)\pi}{6}, n = 0, 1, \ldots, 5$. It is important to note that an estimate of $Er_2Sn_2O_7$'s exchange parameters [48, 49] places it in proximity to the ψ_2 phase. Example configurations of the ψ_3 and ψ_2 phases are shown in Figure 2.6 (Figures 2.6a and 2.6b, respectively). Lastly, note that the order parameter for the Γ_5

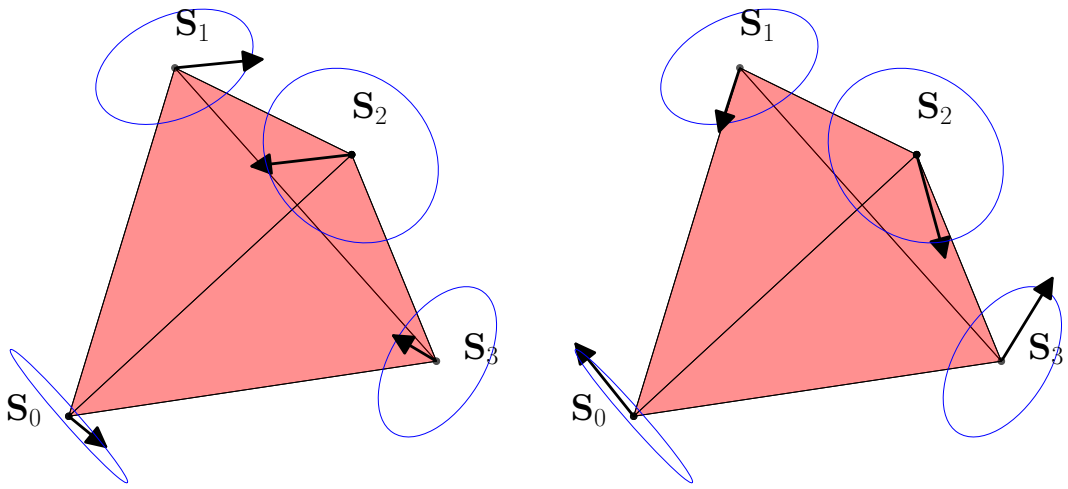

(a) **(b)**

Figure 2.6: Example of a (a) ψ_3 and (b) ψ_2 configuration on a single tetrahedron. Blue circles represent the local xy-plane at each sublattice, each normal to the local [111] cubic axis. All spins make the same angle θ_E from their local x-axis, which must be $\theta_E = \frac{(2n+1)\pi}{6}$ ($\theta_E = \frac{n\pi}{3}$) for the ψ_3 (ψ_2) state. Here, $\theta_E = \frac{\pi}{6}$ in (a) and $\theta_E = \frac{2\pi}{3}$ in (b).

phase is a two-component vector [24]:

$$\boldsymbol{m}_E = \begin{pmatrix} \frac{1}{2\sqrt{6}}(-2S_0^x + S_0^y + S_0^z - 2S_1^x - S_1^y - S_1^z + 2S_2^x + S_2^y - S_2^z + 2S_3^x - S_3^y + S_3^z) \\ \frac{1}{2\sqrt{2}}(-S_0^y + S_0^z + S_1^y - S_1^z - S_2^y - S_2^z + S_3^y + S_3^z) \end{pmatrix} \tag{2.29}$$

This two-component order parameter is parameterized by the same angle θ_E as in Eqs. (2.25) to (2.28). In particular, $\boldsymbol{m}_E = (m_E^x, m_E^y) = (\cos(\theta_E), \sin(\theta_E))$ [24]. Hence, for a given configuration $(\boldsymbol{S}_0, \boldsymbol{S}_1, \boldsymbol{S}_2, \boldsymbol{S}_3)$ on a single tetrahedron, the angle θ_E can be determined by first calculating Eq. (2.29) and then calculating $\theta_E = \arctan\left(\frac{m_E^y}{m_E^x}\right)$.

A final phase that one may consider is the splayed ferromagnet phase. When the applied field in our system is strong enough, the spins are polarized and the system enters a ferromagnetic phase, as is expected for sufficiently strong fields. However, we find in Chapter 4 that this eventual field polarization does not contribute to explaining reentrance, and we therefore do not discuss this phase further.

2.4 Long-Range Dipolar Interactions

So far, we have only considered one type of interaction between moments – namely, nearest-neighbor exchange interactions. Such an approach may be justified by an understanding of f orbitals. The $4f$ orbitals for rare-earth ions are not extended very far [68, 69] and hence orbital overlap is small. The upshot of this is that next-nearest exchange interactions are expected to be small, so restricting the model to only nearest-neighbor interactions seems reasonable.[8]

On the other hand, depending on the electron filling and crystal field effects, rare-earth ions may possess very large magnetic moments. The long-range dipolar interaction, which may be ignored in systems with smaller moments, may play an important role in the rare-earth pyrochlores. These dipolar interactions occur between all moments in the lattice, and even if their energy scale may be smaller than exchange, they may still play an important role in a frustrated magnet. Moreover, the arguments used to prove a classical $\boldsymbol{q} = 0$ ground state order in Yan *et al.* [24] no longer apply when long-range dipolar interactions are included. Altogether, it is not clear how the inclusion of this interaction will modify the physics of $Er_2Sn_2O_7$, nor what role it may play in explaining reentrance. It will therefore be important to include it.

The long-range dipolar interaction between the physical moments of the system takes the form

$$\mathcal{H}_{\text{dip}} = \frac{\mu_0}{4\pi}\frac{(g_J\mu_B)^2}{r_{\text{nn}}^3}\frac{1}{2}\sum_{k,l}\sum_{i,j}\frac{\boldsymbol{J}_{ia}\cdot\boldsymbol{J}_{jb}}{(r_{ia,jb}/r_{\text{nn}})^3} - 3\frac{(\boldsymbol{J}_{ia}\cdot\boldsymbol{r}_{ia,jb})(\boldsymbol{J}_{jb}\cdot\boldsymbol{r}_{ia,jb})}{(r_{ia,jb}/r_{\text{nn}})^3}, \tag{2.30}$$

where r_{nn} is the nearest-neighbor distance on the pyrochlore lattice and $\boldsymbol{r}_{ia,jb}$ is the displacement vector from site (i,a) to site (j,b). As before, one may use the g-tensor to project these interactions from physical angular momenta $\boldsymbol{J}_{ia}$ onto our pseudospin $S = \frac{1}{2}$ representation. This is done in Section 3.2, where the Ewald summation method for simulating the long-range dipolar interaction is discussed.

[8] It should be noted that the localized nature of the $4f$ orbitals also leads to small energy scales for the exchange interactions. For $Er_2Sn_2O_7$, they are on the order of 1 K [48, 49], so low temperatures are required to study the physics of the ordered phase. This should be contrasted with, for example, d orbital systems. There, the orbitals are much further extended, giving greater overlap and larger exchange interactions. For example, the exchange interactions for the Ni^{2+}–based pyrochlore $NaCaNi_2F_7$ is on the order of 30 K [70]!

Chapter 3

Methods

3.1 Variational Mean-Field Theory (VMFT) for Classical Spins

As a first approximation to understanding the physical behavior of the pyrochlore spin system, one may employ mean-field theory. This ignores the effect of (thermal and quantum) fluctuations on the system, thereby providing a picture of the underlying phases upon which fluctuations act. To accomplish this in a variational mean-field theory (VMFT) scheme, the density matrix of the entire spin system is assumed to be the product of single-spin density matrices, which are themselves treated as variational parameters to minimize the free energy, as will is discussed in detail below. The following derivation of variational mean-field theory follows Refs. [71–73].

Consider a classical spin system on the pyrochlore lattice, where the spin on each site is represented by a normalized three-component vector.[1] Generically, the exchange Hamiltonian can be written as

$$\mathcal{H}_0 = \frac{1}{2}\sum_{a,b}\sum_{i,j}\sum_{\mu,\nu} J^{\mu\nu}_{ia,jb} S^{\mu}_{ia} S^{\nu}_{jb}, \tag{3.1}$$

[1] The spins in this classical method are represented by normalized vectors, but the model described in Chapter 2 considers spins of length $\frac{1}{2}$, in keeping with the effective (pseudo)spin–$\frac{1}{2}$ nature of the quantum model. Hence, to go from parameters introduced for a spin–$\frac{1}{2}$ model (as in Chapter 2) to those for classical normalized spin vectors (as in this section), a factor of $\frac{1}{2}$ is introduced for every dependence on $\boldsymbol{S}_{ia}$. The exchange parameters are therefore divided by four, and the g-tensor components by two, when numerically implementing classical VMFT.

where a and b denote the chosen tetrahedra, i and j denote the sublattices chosen within those tetrahedra, and μ and ν denote the components of the spin vectors. Note that, in this form, $J^{\mu\nu}_{ia,jb}$ quantifies completely general bilinear interactions. This allows the VMFT scheme to incorporate the nearest-neighbor exchange couplings as well as long-range dipolar interactions at the same time, without requiring any modification to the following derivation. Note that, under an applied magnetic field, the full Hamiltonian is

$$\mathcal{H} = \frac{1}{2}\sum_{a,b}\sum_{i,j}\sum_{\mu,\nu} J^{\mu\nu}_{ia,jb} S^{\mu}_{ia} S^{\nu}_{jb} - \sum_{i,a} \boldsymbol{h}_{ia} \cdot \boldsymbol{S}_{ia}, \tag{3.2}$$

where

$$h^{\mu}_{ia} = \mu_{\mathrm{B}} g^{\mu\nu}_{ia} H^{\nu} \tag{3.3}$$

is the scaled magnetic field for a given applied magnetic field $\boldsymbol{H}$, with μ and ν again denoting Cartesian components. $g^{\mu\nu}_{ia}$ is the g-tensor of the ion at the given sublattice in the global frame, as discussed in Chapter 2. Note that, for the rare-earth pyrochlore systems considered here, the g-tensor depends only on the sublattice index i, not the tetrahedron index a [24].

In terms of density matrices, the free energy of the system [71–73] is given by

$$F_{\rho} = \mathrm{Tr}\left\{\rho\mathcal{H}\right\} + T\mathrm{Tr}\left\{\rho\ln\rho\right\}, \tag{3.4}$$

where ρ is the many-body density matrix and the trace sums over all possible spin configurations.[2] The VMFT approximation assumes $\rho(\{\boldsymbol{S}_{ia}\}) = \prod_{i,a}\rho_{ia}(\boldsymbol{S}_{ia})$, where ρ_{ia} is the density matrix for a *single* spin on tetrahedron a and sublattice i. Within VMFT, the single-site density matrices are treated as variational parameters, subject to the constraints of normalization ($\mathrm{Tr}\{\rho_{ia}\} = 1$) and the local order parameter (or sublattice magnetization) definition ($\mathrm{Tr}\{\rho_{ia}\boldsymbol{S}_{ia}\} = \boldsymbol{m}_{ia}$). These constraints can be respectively enforced by using Lagrange multipliers; we use the Lagrange multipliers $\{\xi_{ia}\}$ to enforce $\mathrm{Tr}\{\rho_{ia}\} = 1$ and use the Lagrange multipliers $\{\boldsymbol{A}_{ia}\}$ to enforce $\mathrm{Tr}\{\rho_{ia}\boldsymbol{S}_{ia}\} = \boldsymbol{m}_{ia}$. Subject to the constraints and the VMFT approximation, the free energy becomes:

$$F(\{\rho_{ia}\},\{\xi_{ia}\},\{\boldsymbol{A}_{ia}\}) = \mathrm{Tr}\left\{\rho\mathcal{H}\right\} + T\mathrm{Tr}\left\{\rho\ln\rho\right\} - T\mathrm{Tr}\left\{\sum_{i,a}\xi_{ia}(\rho_{ia}-1)\right\} \tag{3.5}$$

$$- T\mathrm{Tr}\left\{\sum_{i,a}(\rho_{ia}\boldsymbol{S}_{ia} - \boldsymbol{m}_{ia})\cdot\boldsymbol{A}_{ia}\right\}. \tag{3.6}$$

[2] $\mathrm{Tr}\{\rho\mathcal{H}\}$ represents a thermal averaging over the energy of the spin configurations. As well, in units where $k_{\mathrm{B}} = 1$, $-\mathrm{Tr}\left\{\rho\ln\rho\right\}$ is the von Neumann formulation of the entropy of a system. Hence, this expression for the free energy is equivalent to $F = U - TS$.

F must now be minimized with respect to the single-site density matrices, that is, $\frac{\partial F}{\partial \rho_{ia}} = 0$. To do this, the following properties of traces are used:

- $\mathrm{Tr}\{A+B\} = \mathrm{Tr}\{A\} + \mathrm{Tr}\{B\}$. This simplifies the sums over i, j, a, b, μ, and ν by separating the trace over sums into sums over traces.
- $\mathrm{Tr}\{A \otimes B\} = \mathrm{Tr}\{A\}\mathrm{Tr}\{B\}$, which simplfies traces over products of density matrices from different sites. Products of density matrices on different sites take the form $\rho_{ia} \otimes \rho_{jb}$ since each site is treated independently.
- $\mathrm{Tr}\{\rho_{ia}\} = 1$, which simplifies sums over sites we do not need to consider.
- Suppose $g(x)$ is a polynomial function or has a series expansion in terms of polynomials. Then, $\overleftrightarrow{\boldsymbol{g}}\ (\overleftrightarrow{\boldsymbol{X}})$ can be also be expanded as a series (namely, in powers of the matrix $\overleftrightarrow{\boldsymbol{X}}$) and is a matrix itself. In this case, the derivative of the trace of this resulting matrix, $\mathrm{Tr}\left\{\overleftrightarrow{\boldsymbol{g}}\ (\overleftrightarrow{\boldsymbol{X}})\right\}$, with respect to $\overleftrightarrow{\boldsymbol{X}}$, is given by $\frac{\partial \mathrm{Tr}\left\{\overleftrightarrow{\boldsymbol{g}}(\overleftrightarrow{\mathbf{X}})\right\}}{\partial \overleftrightarrow{\mathbf{X}}} = \overleftrightarrow{\boldsymbol{g}}'\ (\overleftrightarrow{\mathbf{X}})$. That is, one composes the function $g'(x)$ with the argument $\overleftrightarrow{\boldsymbol{X}}$. This simplifies derivatives of functions of a matrix.

As an example, we have:

$$\mathrm{Tr}\left\{\rho\mathcal{H}\right\} = \mathrm{Tr}\left\{\rho\left(\frac{1}{2}\sum_{a,b}\sum_{i,j}\sum_{\mu,\nu} J^{\mu\nu}_{ia,jb} S^{\mu}_{ia} S^{\nu}_{jb} - \sum_{i,a} \boldsymbol{h}_{ia}\cdot\boldsymbol{S}_{ia}\right)\right\} \tag{3.7}$$

$$= \frac{1}{2}\sum_{a,b}\sum_{i,j}\sum_{\mu,\nu} J^{\mu\nu}_{ia,jb}\mathrm{Tr}\left\{\rho S^{\mu}_{ia} S^{\nu}_{jb}\right\} - \sum_{i,a}\boldsymbol{h}_{ia}\cdot\mathrm{Tr}\left\{\rho\boldsymbol{S}_{ia}\right\} \tag{3.8}$$

$$= \frac{1}{2}\sum_{a,b}\sum_{i,j}\sum_{\mu,\nu} J^{\mu\nu}_{ia,jb}\mathrm{Tr}\left\{\rho_{ia}S^{\mu}_{ia}\rho_{jb}S^{\nu}_{jb}\prod_{\substack{k\neq i,j\\ c\neq a,b}}\rho_{kc}\right\} - \sum_{i,a}\boldsymbol{h}_{ia}\cdot\mathrm{Tr}\left\{\rho_{ia}\boldsymbol{S}_{ia}\prod_{\substack{k\neq i\\ c\neq a}}\rho_{kc}\right\} \tag{3.9}$$

$$= \frac{1}{2}\sum_{a,b}\sum_{i,j}\sum_{\mu,\nu} J^{\mu\nu}_{ia,jb}\mathrm{Tr}\left\{\rho_{ia}S^{\mu}_{ia}\right\}\mathrm{Tr}\left\{\rho_{jb}S^{\nu}_{jb}\right\}\prod_{\substack{k\neq i,j\\ c\neq a,b}}\mathrm{Tr}\left\{\rho_{kc}\right\} -$$

$$\sum_{i,a}\boldsymbol{h}_{ia}\cdot\mathrm{Tr}\left\{\rho_{ia}\boldsymbol{S}_{ia}\right\}\prod_{\substack{k\neq i\\ c\neq a}}\mathrm{Tr}\left\{\rho_{kc}\right\} \tag{3.10}$$

$$= \frac{1}{2}\sum_{a,b}\sum_{i,j}\sum_{\mu,\nu} J^{\mu\nu}_{ia,jb} m^{\mu}_{ia} m^{\nu}_{jb} - \sum_{i,a} \boldsymbol{h}_{ia}\cdot\boldsymbol{m}_{ia}. \tag{3.11}$$

Note that this final result does not depend on ρ_{ia}, so taking the derivative of this term in the free energy with respect to ρ_{ia} just gives 0.

Altogether, using the above properties to simplify the derivatives of our traces, we have:

$$\frac{\partial}{\partial\rho_{ia}}\mathrm{Tr}\left\{\rho\mathcal{H}\right\} = \frac{\partial}{\partial\rho_{ia}}\left[\frac{1}{2}\sum_{a,b}\sum_{i,j}\sum_{\mu\nu} J^{\mu\nu}_{ia,jb} m^{\mu}_{ia} m^{\nu}_{jb} - \sum_{i,a}\boldsymbol{h}_{ia}\cdot\boldsymbol{m}_{ia}\right] = 0 \tag{3.12}$$

$$\frac{\partial}{\partial\rho_{ia}}\mathrm{Tr}\left\{\rho\ln\rho\right\} = \frac{\partial}{\partial\rho_{ia}}\mathrm{Tr}\left\{\rho_{ia}\ln(\rho_{ia})\right\} = \ln(\rho_{ia})+1 \tag{3.13}$$

$$\frac{\partial}{\partial\rho_{ia}}\mathrm{Tr}\left\{\sum_{j,b}\xi_{jb}\rho_{jb}\right\} = \xi_{ia} \tag{3.14}$$

$$\frac{\partial}{\partial\rho_{ia}}\mathrm{Tr}\left\{\sum_{j,b}\rho_{jb}\boldsymbol{S}_{jb}\cdot\boldsymbol{A}_{jb}\right\} = \boldsymbol{A}_{ia}\cdot\boldsymbol{S}_{ia}. \tag{3.15}$$

Summing these terms (by taking the derivative of Eq. (3.6)) and equating to 0 to satisfy $\frac{\partial F}{\partial\rho_{ia}} = 0$[3], we have

$$0 = T\left(\ln(\rho_{ia})+1\right) - T\xi_{ia} - T\boldsymbol{A}_{ia}\cdot\boldsymbol{S}_{ia} \tag{3.16}$$

$$\implies \ln(\rho_{ia}) = \xi_{ia} - 1 + \boldsymbol{A}_{ia}\cdot\boldsymbol{S}_{ia} \tag{3.17}$$

$$\implies \rho_{ia} = e^{\xi_{ia}-1}e^{\boldsymbol{A}_{ia}\cdot\boldsymbol{S}_{ia}}. \tag{3.18}$$

The factor $e^{\xi_{ia}-1}$ does not depend on the spin configuration $\boldsymbol{S}_{ia}$ and is thus just a constant. We can therefore write the single-site density matrices as

$$\rho_{ia} = \frac{1}{Z_{ia}}e^{\boldsymbol{A}_{ia}\cdot\boldsymbol{S}_{ia}}, \tag{3.19}$$

where we identify the leading constant with the inverse of the partition function, introduced to enforce the normalization of ρ_{ia}. Since the spins $\boldsymbol{S}_{ia}$ are treated as normalized classical vectors, the partition function Z_{ia} is found by integrating over all possible spin

[3]Note that those terms in Eq. (3.6) which do not depend on ρ_{ia} are eliminated when we take the derivative with respect to ρ_{ia}.

configurations in spherical coordinates. Performing this integration (with $|\boldsymbol{S}_{ia}| = 1$ and the z–axis aligned along $\boldsymbol{A}_{ia}$), we have

$$\begin{aligned} Z_{ia} &= \mathrm{Tr}\{e^{\boldsymbol{A}_{ia}\cdot\boldsymbol{S}_{ia}}\} && (3.20)\\ &= \int_0^{2\pi}\int_0^{\pi} \sin(\theta) e^{|\boldsymbol{A}_{ia}||\boldsymbol{S}_{ia}|\cos(\theta)} d\theta d\phi && (3.21)\\ &= 2\pi \int_0^{\pi} \sin(\theta) e^{|\boldsymbol{A}_{ia}|\cos(\theta)} d\theta && (3.22)\\ &= \frac{2\pi}{|\boldsymbol{A}_{ia}|}\int_{-|\boldsymbol{A}_{ia}|}^{|\boldsymbol{A}_{ia}|} e^u du && (3.23)\\ &= \frac{4\pi}{A_{ia}}\sinh(A_{ia}). && (3.24) \end{aligned}$$

Therefore, we find the partition function to be

$$Z_{ia} = \frac{4\pi}{A_{ia}}\sinh(A_{ia}). \tag{3.25}$$

Equipped with these relations, the traces in Eq. (3.6) can be evaluated. The free energy simplifies to:

$$F = \frac{1}{2}\sum_{a,b}\sum_{i,j}\sum_{\mu,\nu} J^{\mu\nu}_{ia,jb} m^{\mu}_{ia} m^{\nu}_{jb} - \sum_{i,a} \boldsymbol{h}_{ia}\cdot\boldsymbol{m}_{ia} + \sum_{i,a}(\boldsymbol{B}_{ia}\cdot\boldsymbol{m}_{ia} - \frac{1}{\beta}\ln(Z_{ia})). \tag{3.26}$$

Here, $\boldsymbol{B}_{ia} \equiv \frac{\boldsymbol{A}_{ia}}{\beta}$ can be interpreted as a local "magnetic field". Explicitly, by minimizing the free energy with respect to the order parameter $\boldsymbol{m}_{ia}$, $\frac{\partial F}{\partial m^{\mu}_{ia}} = 0$, we have

$$B^{\mu}_{ia} = -\sum_{j,b,\nu} J^{\mu\nu}_{ia,jb} m^{\nu}_{jb} + h^{\mu}_{ia}. \tag{3.27}$$

Using this expression for B^{μ}_{ia}, the free energy averaged over all N sites of the lattice is

$$f = \frac{F}{N} = \frac{X(m)}{N} - \frac{1}{N\beta}\sum_{i,a}\ln(Z_{ia}), \tag{3.28}$$

where

$$X(m) = -\frac{1}{2}\sum_{a,b}\sum_{i,j}\sum_{\mu,\nu} J^{\mu\nu}_{ia,jb} m^{\mu}_{ia} m^{\nu}_{jb}. \tag{3.29}$$

Lastly, using the identity $\frac{\partial f}{\partial \boldsymbol{B}_{ia}} = -\boldsymbol{m}_{ia}$ for the sublattice magnetization (i.e. the thermodynamic relation for relating a magnetization with an applied field), we have

$$\boldsymbol{m}_{ia} = \frac{\boldsymbol{B}_{ia}}{|\boldsymbol{B}_{ia}|}\left[\coth\left(\beta|\boldsymbol{B}_{ia}|\right) - \frac{1}{\beta|\boldsymbol{B}_{ia}|}\right]. \tag{3.30}$$

Eqs. (3.27) and (3.30) are the major results of VMFT, as they allow one to determine the sublattice magnetization configuration[4] $\{\boldsymbol{m}_{ia}\}$ that minimizes the mean-field free energy. They also allow this mean-field free energy of the system to be calculated using Eq. (3.28). Up until now, this has been an exact analytical derivation of VMFT. We now turn to explaining how VMFT is implemented numerically in practice.

Generally, the complication in solving for the sublattice magnetization configuration $\{\boldsymbol{m}_{ia}\}$ at arbitrary T and $\boldsymbol{H}$ is that, according to Eq. (3.30), it requires the calculation of the local fields – which depend on the sublattice magnetization configuration in Eq. (3.27)! This coupled set of equations can be solved self-consistently: given an initial sublattice magnetization configuration $\{\boldsymbol{m}_{ia}\}$, one can calculate the local field at every site (mediated by the exchange couplings and the Zeeman effect) using Eq. (3.27). The local field can then be used to recalculate the sublattice magnetization configuration according to Eq. (3.30). In this way, these two equations can be self-consistently and iteratively solved in order to determine the sublattice magnetization configuration that minimizes the free energy within a mean-field approximation. Numerically, for a pyrochlore lattice of size L (i.e. L^3 conventional cubic unit cells, for a total of $N = 16L^3$ spins and with periodic boundary conditions), the self-consistent procedure is as follows[5]:

(1) Begin with $T = 0$ and some fixed magnitude and direction of the applied field $\boldsymbol{H}$. On every site (i, a) of the lattice, initialize a sublattice magnetization vector $\boldsymbol{m}_{ia}$ of unit length.[6] To study $Er_2Sn_2O_7$, the initial sublattice magnetization configuration is chosen to be one of the six PC ground states discussed in Chapter 2.

(2) Calculate the local field $\boldsymbol{B}_{ia}$ that results from this sublattice magnetization configuration using Eq. (3.27). Note that, at $T = 0$, Eq. (3.30) dictates that $\boldsymbol{m}_{ia}$ should be

[4] In anticipation of the results of Chapter 4, and similar to the $\boldsymbol{q} = 0$ ordering mentioned in Chapter 2, we refer to this as a sublattice magnetization configuration because the tetrahedron "summing index" a turns out to be spurious. A $\boldsymbol{q} = 0$ order is always found within VMFT in this thesis.

[5] Note that we take $L = 2$, giving $N = 128$.

[6] According to Eq. (3.30), when $T = 0$, the sublattice magnetizations are all normalized.

aligned with $\boldsymbol{B}_{ia}$. However, to smoothly evolve the system[7], $\boldsymbol{m}_{ia}$ is moved by some percentage η in the direction of $\boldsymbol{B}_{ia}$ with every iteration. That is, after calculating $\boldsymbol{B}_{ia}$, we take $\boldsymbol{m}_{ia} \to (1-\eta)\boldsymbol{m}_{ia} + \eta\boldsymbol{B}_{ia}$.[8] We have chosen $\eta = 5\%$ as a compromise between computation time and an accurate, smooth evolution of the sublattice magnetizations.

(3) Continue iteratively updating $\{\boldsymbol{m}_{ia}\}$ according to (2) until either (a) some maximum number of iterations is attained, or (b) $\{\boldsymbol{m}_{ia}\}$ has reached the desired level of convergence. For (a), we take 10^6 iterations as the maximum, though this is rarely attained. For (b), we decompose the sublattice magnetization vectors $\{\boldsymbol{m}_{ia}\}$ in Cartesian components into their corresponding sets of angles $\{\theta_{ia}\}$ and $\{\phi_{ia}\}$ in spherical coordinates. Convergence refers to when *all* of these angles $\{\theta_{ia}\}$ and $\{\phi_{ia}\}$ have not changed by more than some value ϵ after an iteration. We have taken $\epsilon = 10^{-8}$.

(4) Once convergence (or the maximum number of iterations) is attained, any relevant quantity of the system can be calculated (e.g. the free energy). Note that, in this thesis, the resulting sublattice magnetization configurations for all the studied directions and magnitudes of $\boldsymbol{H}$ are found to be $\boldsymbol{q} = 0$ orders.

(5) Once the process detailed in (1) through (4) have been performed for $T = 0$ and the desired range of values for the applied magnetic field, the finite-temperature sublattice magnetization configuration can be calculated. For a given value of T and a given direction and magnitude of $\boldsymbol{H}$, tile the lattice with the spin configuration corresponding to $T = 0$ (for the same magnitude and direction of $\boldsymbol{H}$).

(6) Repeat the same procedure (namely, (2) through (4)) as in the $T = 0$ case, with the modification that the full expression in Eq. (3.30) (namely, now for finite T) is used. If the initial sublattice magnetization is called $\boldsymbol{m}_{ia}$ and the new sublattice magnetization (i.e. the one calculated from Eq. (3.30)) is called $\boldsymbol{m}'_{ia}$, we again smoothly evolve the sublattice magnetizations using some parameter η (i.e. $\boldsymbol{m}_{ia} \to (1-\eta)\boldsymbol{m}_{ia} + \eta\boldsymbol{m}'_{ia}$ after an iteration[9]). We again choose $\eta = 5\%$. The maximum number of iterations is again chosen as 10^6. Convergence is attained when the angular

[7] This is because of the coupled nature of Eqs. (3.27) and (3.30). Since updating the sublattice magnetization configuration results in a change in the local fields, we do not want to change the sublattice magnetizations too abruptly. Otherwise, the sublattice magnetizations will not reliably converge towards their minimum free energy configurations.

[8] Note that these configurations are then normalized, since at $T = 0$, the sublattice magnetizations are expected to be of unit length from Eq. (3.30).

[9] In the case of finite temperature, these sublattice magnetizations are *not* normalized.

variables $\{\phi_{ia}\}$ and $\{\theta_{ia}\}$ for every sublattice magnetization vector do not change by more than some value ϵ in a single iteration. Here, we take $\epsilon = 10^{-10}$.

(7) Once convergence (or the maximum number of iterations) is attained, any relevant quantity of the system can be calculated again. We again find $\boldsymbol{q} = 0$ order for all values of T and $\boldsymbol{H}$ studied in this thesis.

Note that this entire numerical procedure must be repeated six times, once for every starting PC ground state. In this way, the evolution of each PC ground state in the presence of a global applied field $\boldsymbol{H}$ (and for any given temperature) can be tracked separately. As discussed in Chapter 4, the mechanism behind reentrance can be partially explained using this classical VMFT for (classical, normalized) spin vectors. However, for completeness, we also provide a short derivation of a *quantum* VMFT in Appendix B, where the spins are instead treated as $S = \frac{1}{2}$ *operators*.

3.2 Ewald Summation

Consider the long-range dipolar interaction between physical moments of our system $\boldsymbol{J}_{ia}$:

$$\mathcal{H}_{\text{dip}} = \frac{\mu_0}{4\pi}\frac{(g_J\mu_{\text{B}})^2}{r_{\text{nn}}^3}\frac{1}{2}\sum_{a,b}\sum_{i,j}\frac{\boldsymbol{J}_{ia}\cdot\boldsymbol{J}_{jb}}{(r_{ia,jb}/r_{\text{nn}})^3} - 3\frac{(\boldsymbol{J}_{ia}\cdot\boldsymbol{r}_{ia,jb})(\boldsymbol{J}_{jb}\cdot\boldsymbol{r}_{ia,jb})}{(r_{ia,jb}/r_{\text{nn}})^3}. \tag{3.31}$$

The factor of $\frac{1}{2}$ accounts for double counting. As described in Chapter 2, the physical moments of the system can be projected onto a pseudospin–$\frac{1}{2}$ basis, where the anisotropy of the physical moments are incorporated into a g–tensor. For the g–tensor $\overleftrightarrow{\boldsymbol{g}}_{ia}$ on a given site, this gives [28, 48]:

$$\mathcal{H}_{\text{dip}} = \frac{\mu_0}{4\pi}\frac{(g_J\mu_{\text{B}})^2}{r_{\text{nn}}^3}\frac{1}{2}\sum_{a,b}\sum_{i,j}\frac{J_{ia}^{\mu}J_{jb}^{\nu}\delta^{\mu\nu}}{(r_{ia,jb}/r_{\text{nn}})^3} - 3\frac{(J_{ia}^{\mu}r_{ia,jb}^{\mu})(J_{jb}^{\nu}r_{ia,jb}^{\nu})}{(r_{ia,jb}/r_{\text{nn}})^3} \tag{3.32}$$

$$= \frac{\mu_0}{4\pi}\frac{(\mu_{\text{B}})^2}{r_{\text{nn}}^3}\frac{1}{2}\sum_{a,b}\sum_{i,j}\frac{g_{ia}^{\mu\alpha}S_{ia}^{\alpha}g_{jb}^{\nu\beta}S_{jb}^{\beta}\delta^{\mu\nu}}{(r_{ia,jb}/r_{\text{nn}})^3} - 3\frac{(g_{ia}^{\mu\alpha}S_{ia}^{\alpha}r_{ia,jb}^{\mu})(g_{jb}^{\nu\beta}S_{jb}^{\beta}r_{ia,jb}^{\nu})}{(r_{ia,jb}/r_{\text{nn}})^3} \tag{3.33}$$

$$= \frac{\mu_0}{4\pi}\frac{(\mu_{\text{B}})^2}{r_{\text{nn}}^3}\frac{1}{2}\sum_{a,b}\sum_{i,j}S_{ia}^{\alpha}S_{jb}^{\beta}\left[\frac{g_{ia}^{\mu\alpha}g_{jb}^{\nu\beta}\delta^{\mu\nu}}{(r_{ia,jb}/r_{\text{nn}})^3} - 3\frac{(g_{ia}^{\mu\alpha}r_{ia,jb}^{\mu})(g_{jb}^{\nu\beta}r_{ia,jb}^{\nu})}{(r_{ia,jb}/r_{\text{nn}})^3}\right] \tag{3.34}$$

$$= \frac{\mu_0}{4\pi}\frac{(\mu_{\text{B}})^2}{r_{\text{nn}}^3}\frac{1}{2}\sum_{a,b}\sum_{i,j}S_{ia}^{\mu}S_{jb}^{\nu}\left[\frac{g_{ia}^{\mu\alpha}g_{jb}^{\nu\beta}\delta^{\alpha\beta}}{(r_{ia,jb}/r_{\text{nn}})^3} - 3\frac{(g_{ia}^{\mu\alpha}r_{ia,jb}^{\alpha})(g_{jb}^{\nu\beta}r_{ia,jb}^{\beta})}{(r_{ia,jb}/r_{\text{nn}})^3}\right], \tag{3.35}$$

where repeated Greek indices are summed over and the final step is a relabelling of Greek indices.[10] If we define $D_{\rm dd} \equiv D r_{\rm nn}^3$ for $D \equiv \frac{\mu_0}{4\pi}\frac{(g_J\mu_{\rm B})^2}{r_{\rm nn}^3}$, and if we sum over the Greek indices of $\delta^{\alpha\beta}$, we can reexpress the above as[11]

$$\mathcal{H}_{\rm dip} = \frac{D_{\rm dd}}{2g_J^2}\sum_{a,b}\sum_{i,j} S_{ia}^{\mu} S_{jb}^{\nu}\left[\frac{\boldsymbol{n}_{ia}^{\mu}\cdot\boldsymbol{n}_{jb}^{\nu}}{r_{ia,jb}^3} - 3\frac{(\boldsymbol{n}_{ia}^{\mu}\cdot\boldsymbol{r}_{ia,jb})(\boldsymbol{n}_{jb}^{\nu}\cdot\boldsymbol{r}_{ia,jb})}{r_{ia,jb}^3}\right]. \tag{3.36}$$

In the above, we have rewritten the g-tensor using the vectors $\{\boldsymbol{n}_{ia}^{\mu}\}$. That is, each column of the g-tensor $\overset{\leftrightarrow}{\boldsymbol{g}}_{ia}$ is represented by a vector $\boldsymbol{n}_{ia}^{\mu}$, such that the α-th component of $\boldsymbol{n}_{ia}^{\mu}$ is given by $g_{ia}^{\mu\alpha}$. For example, the first column of $\overset{\leftrightarrow}{\boldsymbol{g}}_{ia}$ is $\boldsymbol{n}_{ia}^{x}$.[12] The reason for this comes from the definition $g_J\boldsymbol{J}_{ia} = \overset{\leftrightarrow}{\boldsymbol{g}}_{ia}\,\boldsymbol{S}_{ia}$. Expanding the right-hand side gives $\boldsymbol{n}_{ia}^{x}S_{ia}^{x} + \boldsymbol{n}_{ia}^{y}S_{ia}^{y} + \boldsymbol{n}_{ia}^{z}S_{ia}^{z}$. Physically, then, the vectors $\{\boldsymbol{n}_{ia}^{\mu}\}$ represent how the physical moment $\boldsymbol{J}_{ia}$ lies within the global frame of reference that has been defined for the pseudospins $\boldsymbol{S}_{ia}$. This allows us to map the long-range dipolar interactions between the *physical moments* onto our effective *pseudospin* description. For example, for isotropic spins with $g_{ia}^{\mu\nu} = 2\delta^{\mu\nu}$, $\boldsymbol{n}_{ia}^{\mu}$ would reduce to a Cartesian vector. For example, if $g_{ia}^{\mu\nu} = 2\delta^{\mu\nu}$, then $\boldsymbol{n}_{ia}^{x} = (2,0,0)$. In such an isotropic case, the physical moments and the pseudospins lie in the same way. Note that if the g–tensor of a given sublattice is the same on any tetrahedron, the tetrahedron index a is spurious. We can then write $\boldsymbol{n}_{ia}^{\mu} = \boldsymbol{n}_{i}^{\mu}$. Moreover, if every sublattice has the same g–tensor, this can be further simplified to $\boldsymbol{n}_{i}^{\mu} = \boldsymbol{n}^{\mu}$.

When written in this way, the long-range dipolar interaction has the spin configuration (namely, S_{ia}^{μ} and S_{jb}^{ν}) separated from the long-range summation over spatial information (namely, the expression in square brackets in Eq. (3.36)). For a given spin configuration, the difficulty with calculating the dipolar interaction is in computing the sum of

$$D_{ia,jb}^{\mu\nu} = \left[\frac{\boldsymbol{n}_{ia}^{\mu}\cdot\boldsymbol{n}_{jb}^{\nu}}{r_{ia,jb}^3} - 3\frac{(\boldsymbol{n}_{ia}^{\mu}\cdot\boldsymbol{r}_{ia,jb})(\boldsymbol{n}_{jb}^{\nu}\cdot\boldsymbol{r}_{ia,jb})}{r_{ia,jb}^3}\right]. \tag{3.37}$$

This is a conditionally convergent summation [72, 74]. However, it can be evaluated by use of the Ewald summation method, which separates the summation into a real space sum and a reciprocal space sum [72, 74]. A full mathematical derivation of the Ewald

[10] The symmetry of the g–tensor under a swapping of the Greek indices has also been used – that is, $g_{ia}^{\mu\nu} = g_{ia}^{\nu\mu}$.

[11] In this thesis, we take $D = 0.022$ K for $Er_2Sn_2O_7$, as estimated by experiments [49].

[12] Note that the vectors $\{\boldsymbol{n}_{ia}^{\mu}\}$ are *not* normalized unit vectors, since they are just the columns of the g–tensor. These columns depend on g_{xy} and g_z, which also encapuslate information about the physical size of the moment $\boldsymbol{J}_{ia}$, and hence should not be normalized.

summation for spins with an isotropic g–tensor on every sublattice (i.e. the $\boldsymbol{n}_{ia}^{\mu} = \boldsymbol{n}^{\mu}$ case mentioned above) is detailed in Ref. [72]. However, our local moments have an anisotropy to them, quantified by the anisotropic g–tensor or, equivalently, by the (site-dependent) local quantization axes $\boldsymbol{n}_{ia}^{\mu}$. As noted in Ref. [72], the derivation contained therein generalizes directly from isotropic quantization axes $\boldsymbol{n}^{\mu}$ to anisotropic quantization axes $\boldsymbol{n}_{ia}^{\mu}$. We therefore quote the final result from Ref. [72], with the substitution $\boldsymbol{n}^{\mu} \to \boldsymbol{n}_{ia}^{\mu}$:

$$\begin{aligned} D_{ia,jb}^{\mu\nu} = &- \frac{4\alpha^3}{3\sqrt{\pi}}(\boldsymbol{n}_{ia}^{\mu} \cdot \boldsymbol{n}_{jb}^{\nu}) \\ &+ \frac{4\pi}{V} \sum_{\boldsymbol{G}} K^{\mu\nu}(\boldsymbol{G}) e^{-|\boldsymbol{G}|^2/4\alpha^2} e^{-i\boldsymbol{G}\cdot\boldsymbol{r}_{(ij)}} \\ &+ \sum_{i} [A_1^{\mu\nu}(\boldsymbol{r}_{ia,jb}) - A_2^{\mu\nu}(\boldsymbol{r}_{ia,jb})], \end{aligned} \tag{3.38}$$

where

$$K^{\mu\nu}(\boldsymbol{G}) = \frac{(\boldsymbol{n}_{ia}^{\mu} \cdot \boldsymbol{G})(\boldsymbol{n}_{jb}^{\nu} \cdot \boldsymbol{G})}{|\boldsymbol{G}|^2} \tag{3.39}$$

$$A_1^{\mu\nu}(\boldsymbol{r}_{ia,jb}) = (\boldsymbol{n}_{ia}^{\mu} \cdot \boldsymbol{n}_{jb}^{\nu}) \left[\frac{2\alpha}{\sqrt{\pi}} \frac{e^{-\alpha^2|\boldsymbol{r}_{ia,jb}|^2}}{|\boldsymbol{r}_{ia,jb}|^2} + \frac{\operatorname{erfc}(\alpha|\boldsymbol{r}_{ia,jb}|)}{|\boldsymbol{r}_{ia,jb}|^3} \right] \tag{3.40}$$

$$A_2^{\mu\nu}(\boldsymbol{r}_{ia,jb}) = (\boldsymbol{n}_{ia}^{\mu} \cdot \boldsymbol{r}_{ia,jb})(\boldsymbol{n}_{jb}^{\nu} \cdot \boldsymbol{r}_{ia,jb}) \times \tag{3.41}$$

$$\left[\left(\frac{4\alpha^3}{\sqrt{\pi}|\boldsymbol{r}_{ia,jb}|^2} + \frac{6\alpha}{\sqrt{\pi}|\boldsymbol{r}_{ia,jb}|^4} \right) e^{-\alpha^2|\boldsymbol{r}_{ia,jb}|^2} + 3\frac{\operatorname{erfc}(\alpha|\boldsymbol{r}_{ia,jb}|)}{|\boldsymbol{r}_{ia,jb}|^5} \right]. \tag{3.42}$$

In the above, α is a parameter that tunes how much weight to give to the real versus reciprocal lattice sums of the Ewald summation; $\sum_i$ represents a (real space) sum over all position vectors $\boldsymbol{r}_{ia,jb} \neq \boldsymbol{0}$; V is the volume of the system; $\boldsymbol{G} = \frac{2\pi}{L}(n_x, n_y, n_z)$ is a reciprocal lattice vector of the system[13] for integers $\{n_x, n_y, n_z\}$; $\sum_{\boldsymbol{G}}$ represents a (reciprocal space) sum over $\{\boldsymbol{G}\}$; and $\boldsymbol{r}_{(ij)}$ is the vector between sublattices i and j.[14]

Mathematically, the Ewald summation amounts to performing the real and reciprocal space summations (that is, $\sum_i$ and $\sum_{\boldsymbol{G}}$, respectively) in Eq. (3.38). Numerically, the procedure is as follows:

[13] Note that our numerical implementation of VMFT uses conventional cubic cells. Hence, we use the reciprocal lattice vectors of the simple cubic lattice.

[14] Note that $K^{\mu\nu}(\boldsymbol{G})$ is not well-defined at $\boldsymbol{G} = \boldsymbol{0}$. This term is related to the macroscopic field of the dipoles and hence depends on the overall shape of the system of dipoles [72]. However, as mentioned in Section 1.5, reentrance occurs for crystals of various shapes and therefore does not originate from any shape-dependent effects. So, we do not include this $\boldsymbol{G} = \boldsymbol{0}$ term in the summation over reciprocal lattice vectors.

1. Take the original physical reference system of $16L^3$ spins and replicate it by tiling it by the primitive lattice vectors. This effectively enlarges the system so that we have more positions to sum over for the long-range dipolar interactions. We tile the original system by $n_1\boldsymbol{a}_1+n_2\boldsymbol{a}_2+n_3\boldsymbol{a}_3$, where $n_i \in [-5,5]\ \forall i$ and $\{\boldsymbol{a}_i\}$ are the primitive lattice vectors of the simple cubic lattice (as we are using a conventional cubic unit cell). For this enlarged system size, we also have the corresponding reciprocal lattice vectors $\boldsymbol{G}$ as defined above.

2. Next, iterate over all possible pairs in the *original* lattice and calculate $D^{\mu\nu}_{ia,jb}$ using Eq. (3.38).[15] For a given pair of sites (i,a) and (j,b) in our original lattice, we therefore have an associated 3×3 matrix $D^{\mu\nu}$, which can be saved in a data file.

3. For any given pair of sites (i,a) and (j,b), one may then associate an index that refers to which saved matrix $D^{\mu\nu}$ to use for the long-range dipolar interaction between S^{μ}_{ia} and S^{ν}_{jb}. The contribution that dipolar interactions make to the energy can then be computed as $\mathcal{H}_{\text{dip}} = \frac{D_{\text{dd}}}{2g_J^2}\sum_{a,b}\sum_{i,j} D^{\mu\nu}_{ia,jb}S^{\mu}_{ia}S^{\nu}_{jb}$. Effectively, the Ewald summation has separated the sum over long distances that is required for the dipolar interactions from the actual dipoles S^{μ}_{ia}. That is, the former (i.e. the sum over long distances) is completely contained in $D^{\mu\nu}$ and does not require any information about the latter (i.e. the dipoles S^{μ}_{ia}) in order to be computed. Once computed, these matrices $D^{\mu\nu}$ can therefore be used to determine the dipolar interactions for any arrangement of dipoles $\{\boldsymbol{S}_{ia}\}$.

It should be noted that the exchange parameters of the system are obtained by fitting experimental data to a nearest-neighbor model. Hence, the nearest-neighbor contribution of the dipolar interactions are implicitly included in the anisotropic exchange parameters $\{J_1, J_2, J_3, J_4\}$, and we must make sure that our real space sum above does not count them again. As well, it is also important to check that α is properly selected to give a convergent sum. To verify this, one may calculate what the total energy (as a function of α) of a system may be for interacting dipoles all polarized along some given direction. When the total energy converges for some range of α, it is indicative that those values of

[15] Since we are iterating over all pairs (i,a) and (j,b) in the *original* lattice, the vectors $\boldsymbol{r}_{ia,jb}$ are restricted to the original lattice. However, we want to use the larger replicated lattice to get a better approximation of a large real space sum. We can do this by explicitly including the replicas of this pair. As the real space contribution in Eq. (3.38) only depends on the displacement between the pairs (i,a) and (j,b), the replicated positions can easily be included by adding the vector $n_1\boldsymbol{a}_1+n_2\boldsymbol{a}_2+n_3\boldsymbol{a}_3$ to the displacement vector $\boldsymbol{r}_{ia,jb}$. This then simulates a larger replicated lattice, even if $\boldsymbol{r}_{ia,jb}$ is corresponds to a vector in the original lattice. $\sum_i$ can then be thought of as summing over all $\boldsymbol{r}_{ia,jb}$ *and* their replicas $\boldsymbol{r}_{ia,jb}+n_1\boldsymbol{a}_1+n_2\boldsymbol{a}_2+n_3\boldsymbol{a}_3$.

α obtain a properly converging sum for the dipolar interactions. We have therefore chosen $\alpha = \frac{\sqrt{\pi}}{L}$, which (as shown in Figure 3.1) has a convergent total energy for polarized spins .

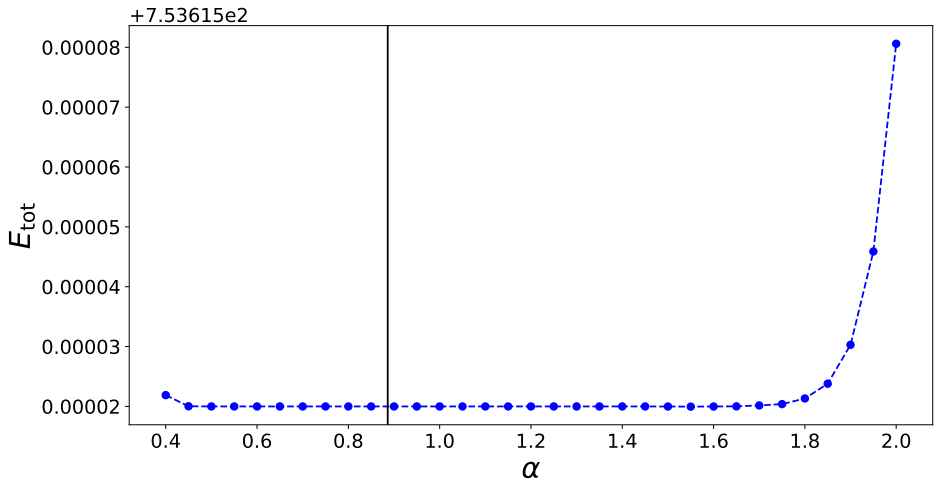

Figure 3.1: Dipolar interaction energy calculated via the Ewald summation for a range of values of α. The energy is calculated using Eqs. (3.36) and (3.38) for $g_J = D_{\text{dd}} = 1$ and for a system of size $L = 2$ with all spins polarized along the global $\hat{z}$ direction. The black vertical line marks $\alpha = \frac{\sqrt{\pi}}{L}$.

3.3 Classical Spin-Waves

Suppose that we have found the classical $T = 0$ ground state of our Hamiltonian, Eq. (3.2), using the above VMFT approach.[16] The low-temperature excitations out of this ground state can then be calculated with a standard classical spin-wave expansion [24]. This will expose the types of modes of the ground state spin configuration that may be excited via thermal fluctuations, as well as provide a qualitative estimate of how easily such modes can be excited.[17]

[16] For this section, we ignore the long-range dipolar interactions and restrict ourselves to just the nearest-neighbor exchange couplings. The justification for doing so is provided in Chapter 4.

[17] Recall the discussion from Section 1.5, which is motivated by the results shown in Chapter 4: we are trying to reproduce the essential ingredients from classical Monte Carlo simulations, which capture reentrance. Hence, we use a *classical* spin-wave expansion, as opposed to a *quantum* spin-wave expansion, to understand thermal fluctuations at lowest order.

In the absence of dipolar interactions, the zero-field ground state spin configuration of Eq. (3.2) is known to be $\boldsymbol{q} = 0$ – that is, the spin configuration on a single tetrahedron is the same for all tetrahedra. A classical spin-wave expansion for such a spin ordering (in the absence of an applied field) is detailed in Ref. [24]. Within VMFT, $\boldsymbol{q} = 0$ ordering is also found for all values of the applied magnetic field $\boldsymbol{H}$. We therefore extend the derivation found in Yan *et al.* [24] to finite fields.

The Hamiltonian is taken to be

$$\mathcal{H} = \frac{1}{2}\sum_{a}\sum_{\langle ij\rangle} J_{ij}^{\mu\nu} S_{ia}^{\mu} S_{ja}^{\nu} - \mu_{\mathrm{B}} \sum_{a}\sum_{i} g_{i}^{\mu\nu} S_{ia}^{\mu} H^{\nu}, \tag{3.43}$$

where $J_{ij}^{\mu\nu}$ is now restricted to only nearest-neighbors, and the tetrahedra indices are suppressed on $J_{ij}^{\mu\nu}$ because of the assumption of $\boldsymbol{q} = 0$ ordering. Note that the g–tensor is also the same on every tetrahedron, so the tetrahedron index has been dropped on g_i as well. However, since the tetrahedra are located at FCC points on the lattice, they have been kept on the spin variables for clarity when performing Fourier transforms. As such, a labels the tetrahedron and i labels the sublattices within this tetrahedron, and the $\boldsymbol{q} = 0$ ordering assumption allows us to sum over each tetrahedron.

Starting with the classically-ordered ground state spin configuration on a single tetrahedron at $T = 0$, define the local coordinate system at each sublattice i using mutually orthogonal vectors $\{\hat{\boldsymbol{u}}_i, \hat{\boldsymbol{v}}_i, \hat{\boldsymbol{w}}_i\}$. This coordinate system is defined such that the classical spin vector on sublattice i is of length S and points along $\hat{\boldsymbol{w}}_i$. The other two local unit vectors are defined arbitrarily, so long as mutual orthogonality is satisfied. Within this local coordinate system, the ground state spin configuration takes the form $\boldsymbol{S}_{ia} = S\hat{\boldsymbol{w}}_i = \begin{pmatrix} 0 \\ 0 \\ S \end{pmatrix}$ for any sublattice i. This ordering represents the minimum energy configuration; any excitation away from this minimum energy configuration will then arise from perturbing the spin vector $\boldsymbol{S}_{ia}$ along the directions $\hat{\boldsymbol{u}}_i$ and $\hat{\boldsymbol{v}}_i$ while maintaining the normalization S. Mathematically, this can be expressed as

$$\boldsymbol{S}_{ia} = \begin{pmatrix} \sqrt{S}\delta u_{ia} \\ \sqrt{S}\delta v_{ia} \\ \sqrt{S^2 - S\delta u_{ia}^2 - S\delta v_{ia}^2} \end{pmatrix} \approx \begin{pmatrix} \sqrt{S}\delta u_{ia} \\ \sqrt{S}\delta v_{ia} \\ S - \frac{1}{2}\delta u_{ia}^2 - \frac{1}{2}\delta v_{ia}^2 \end{pmatrix}. \tag{3.44}$$

By substituting this perturbed spin vector into the original Hamiltonian and expanding to quadratic order[18] in the fluctuations, the lowest-energy excitations away from the ground

[18]Keeping only quadratic order fluctuations allows the resulting partition function to be integrated exactly.

state can be determined. This process is equivalent to finding the Hessian of the original Hamiltonian, or taking a harmonic/quadratic approximation to the energy minima in which the system sits.

Expanding the Hamiltonian to quadratic order in the fluctuations yields

$$\begin{aligned}\mathcal{H} = &\frac{1}{2}\sum_a\sum_{ij} S^2(\hat{\boldsymbol{w}}_i\cdot\overleftrightarrow{\boldsymbol{J}}_{ij}\cdot\hat{\boldsymbol{w}}_j) - \mu_{\mathrm{B}}S\sum_a\sum_i(\hat{\boldsymbol{w}}_i\cdot\overleftrightarrow{\boldsymbol{g}}_i\cdot\boldsymbol{H}) + \frac{S}{2}\sum_a\sum_{ij}\delta u_{ia}\delta u_{ja}(\hat{\boldsymbol{u}}_i\cdot\overleftrightarrow{\boldsymbol{J}}_{ij}\cdot\hat{\boldsymbol{u}}_j)\\
&+\delta u_{ia}\delta v_{ja}(\hat{\boldsymbol{u}}_i\cdot\overleftrightarrow{\boldsymbol{J}}_{ij}\cdot\hat{\boldsymbol{v}}_j) + \delta v_{ia}\delta u_{ja}(\hat{\boldsymbol{v}}_i\cdot\overleftrightarrow{\boldsymbol{J}}_{ij}\cdot\hat{\boldsymbol{u}}_j) + \delta v_{ia}\delta v_{ja}(\hat{\boldsymbol{v}}_i\cdot\overleftrightarrow{\boldsymbol{J}}_{ij}\cdot\hat{\boldsymbol{v}}_j)\\
&-\frac{1}{2}(\delta u_{ia}^2+\delta v_{ia}^2+\delta u_{ja}^2+\delta v_{ja}^2)(\hat{\boldsymbol{w}}_i\cdot\overleftrightarrow{\boldsymbol{J}}_{ij}\cdot\hat{\boldsymbol{w}}_j) + \frac{1}{2}\mu_{\mathrm{B}}\sum_a\sum_{ij}(\delta u_{ia}^2+\delta v_{ia}^2)(\hat{\boldsymbol{w}}_i\cdot\overleftrightarrow{\boldsymbol{g}}_i\cdot\boldsymbol{H}).\end{aligned} \tag{3.45}$$

The first two terms just represent the ground state energy, ε_0. The rest of the expression encapsulates how fluctuations away from the ground state affect the Hamiltonian when they are mediated by exchange couplings and the Zeeman interaction.

We can now perform a Fourier transform over the wavevectors corresponding to the FCC lattice points, since the pyrochlore lattice has spatial periodicity under the translation vectors of the FCC lattice. For example, $\delta u_{ia} = \frac{1}{\sqrt{N_t}}\sum_{\boldsymbol{q}} e^{-i\boldsymbol{q}\cdot\boldsymbol{r}_{ia}}\delta u_i(\boldsymbol{q})$ for $N_t = \frac{N}{4}$ tetrahedra in a pyrochlore system with N spins. Note that, with this notation, $\boldsymbol{r}_{ia} = \boldsymbol{R}_a + \boldsymbol{r}_i$, where $\boldsymbol{R}_a$ is the vector from the origin to the tetrahedron a and $\boldsymbol{r}_i$ is the vector to the sublattice i within the tetrahedron a. In this way, we can view $\sum_a$ as $\sum_{\boldsymbol{R}_a}$ and $\sum_{ij}$ as $\sum_{\boldsymbol{r}_i,\boldsymbol{r}_j}$. Plugging in the Fourier transform of the fluctuations and evaluating the sum over tetrahedra will produce δ functions over the wavevectors, effectively replacing our sum over FCC points in real space with a sum over reciprocal lattice vectors of the real-space FCC lattice. Altogether, the Fourier transform results in:

$$\begin{aligned}\mathcal{H} = \varepsilon_0 + &\frac{S}{2}\sum_{ij}\sum_{\boldsymbol{q}}\Big\{e^{i\boldsymbol{q}\cdot\boldsymbol{r}_{ij}}[\delta u_i(\boldsymbol{q})\delta u_j(-\boldsymbol{q})(\hat{\boldsymbol{u}}_i\cdot\overleftrightarrow{\boldsymbol{J}}_{ij}\cdot\hat{\boldsymbol{u}}_j)\\
&+\delta u_i(\boldsymbol{q})\delta v_j(-\boldsymbol{q})(\hat{\boldsymbol{u}}_i\cdot\overleftrightarrow{\boldsymbol{J}}_{ij}\cdot\hat{\boldsymbol{v}}_j) + \delta v_i(\boldsymbol{q})\delta u_j(-\boldsymbol{q})(\hat{\boldsymbol{v}}_i\cdot\overleftrightarrow{\boldsymbol{J}}_{ij}\cdot\hat{\boldsymbol{u}}_j) + \delta v_i(\boldsymbol{q})\delta v_j(-\boldsymbol{q})(\hat{\boldsymbol{v}}_i\cdot\overleftrightarrow{\boldsymbol{J}}_{ij}\cdot\hat{\boldsymbol{v}}_j)]\\
&-\frac{1}{2}(\delta u_i(\boldsymbol{q})\delta u_i(-\boldsymbol{q}) + \delta v_i(\boldsymbol{q})\delta v_i(-\boldsymbol{q}) + \delta u_j(\boldsymbol{q})\delta u_j(-\boldsymbol{q}) + \delta v_j(\boldsymbol{q})\delta v_j(-\boldsymbol{q}))(\hat{\boldsymbol{w}}_i\cdot\overleftrightarrow{\boldsymbol{J}}_{ij}\cdot\hat{\boldsymbol{w}}_j)\Big\}\\
&+\frac{1}{2}\mu_{\mathrm{B}}\sum_i\sum_{\boldsymbol{q}}\Big[\delta u_i(\boldsymbol{q})\delta u_i(-\boldsymbol{q}) + \delta v_i(\boldsymbol{q})\delta v_i(-\boldsymbol{q}))(\hat{\boldsymbol{w}}_i\cdot\overleftrightarrow{\boldsymbol{g}}_i\cdot\boldsymbol{H})\Big].\end{aligned} \tag{3.46}$$

By relabelling indices, this can be simplified into

$$\begin{aligned}\mathcal{H} = \varepsilon_0 + \frac{S}{2}\sum_{ij}\sum_{\boldsymbol{q}}\Big\{ & e^{i\boldsymbol{q}\cdot\boldsymbol{r}_{ij}}[\delta u_i(\boldsymbol{q})\delta u_j(-\boldsymbol{q})(\hat{\boldsymbol{u}}_i\cdot\overleftrightarrow{\boldsymbol{J}}_{ij}\cdot\hat{\boldsymbol{u}}_j) \\ & + \delta u_i(\boldsymbol{q})\delta v_j(-\boldsymbol{q})(\hat{\boldsymbol{u}}_i\cdot\overleftrightarrow{\boldsymbol{J}}_{ij}\cdot\hat{\boldsymbol{v}}_j) + \delta v_i(\boldsymbol{q})\delta u_j(-\boldsymbol{q})(\hat{\boldsymbol{v}}_i\cdot\overleftrightarrow{\boldsymbol{J}}_{ij}\cdot\hat{\boldsymbol{u}}_j) + \delta v_i(\boldsymbol{q})\delta v_j(-\boldsymbol{q})(\hat{\boldsymbol{v}}_i\cdot\overleftrightarrow{\boldsymbol{J}}_{ij}\cdot\hat{\boldsymbol{v}}_j)] \\ & - \delta_{ij}(\delta u_i(\boldsymbol{q})\delta u_j(-\boldsymbol{q}) + \delta v_i(\boldsymbol{q})\delta v_j(-\boldsymbol{q}))(\sum_l \hat{\boldsymbol{w}}_l\cdot\overleftrightarrow{\boldsymbol{J}}_{lj}\cdot\hat{\boldsymbol{w}}_j)\Big\} \\ & + \frac{1}{2}\mu_{\mathrm{B}}\sum_{ij}\sum_{\boldsymbol{q}}\delta_{ij}\left[\delta u_i(\boldsymbol{q})\delta u_i(-\boldsymbol{q}) + \delta v_i(\boldsymbol{q})\delta v_i(-\boldsymbol{q}))(\hat{\boldsymbol{w}}_i\cdot\overleftrightarrow{\boldsymbol{g}}_i\cdot\boldsymbol{H})\right].\end{aligned} \tag{3.47}$$

Now, define $\boldsymbol{u}(\boldsymbol{q}) \equiv (\delta u_1(\boldsymbol{q}), \delta u_2(\boldsymbol{q}), \delta u_3(\boldsymbol{q}), \delta u_4(\boldsymbol{q}), \delta v_1(\boldsymbol{q}), \delta v_2(\boldsymbol{q}), \delta v_3(\boldsymbol{q}), \delta v_4(\boldsymbol{q}))$. This vector encapsulates the eight[19] possible fluctuations that may be excited at a given wavector $\boldsymbol{q}$. With this vector, the fluctuation contribution to the Hamiltonian (ignoring the ground state energy ε_0) is

$$\mathcal{H}_{\mathrm{CSW}} = \frac{1}{2}\sum_{\boldsymbol{q}}\boldsymbol{u}(-\boldsymbol{q})\cdot(\overleftrightarrow{\boldsymbol{M}}(\boldsymbol{q}) + \overleftrightarrow{\boldsymbol{N}}(\boldsymbol{q}))\cdot\boldsymbol{u}(\boldsymbol{q}). \tag{3.48}$$

The matrices $\overleftrightarrow{\boldsymbol{M}}(\boldsymbol{q})$ and $\overleftrightarrow{\boldsymbol{N}}(\boldsymbol{q})$ can be written in block matrix form, composed of four separate 4×4 blocks. They are:

$$\overleftrightarrow{\boldsymbol{M}}(\boldsymbol{q}) = 2S\begin{pmatrix}\overleftrightarrow{\boldsymbol{M}}^{11}(\boldsymbol{q}) & \overleftrightarrow{\boldsymbol{M}}^{12}(\boldsymbol{q}) \\ \overleftrightarrow{\boldsymbol{M}}^{21}(\boldsymbol{q}) & \overleftrightarrow{\boldsymbol{M}}^{22}(\boldsymbol{q})\end{pmatrix} \tag{3.49}$$

$$M_{ij}^{11}(\boldsymbol{q}) = \cos(\boldsymbol{q}\cdot\boldsymbol{r}_{ij})(\hat{\boldsymbol{u}}_i\cdot\overleftrightarrow{\boldsymbol{J}}_{ij}\cdot\hat{\boldsymbol{u}}_j - \delta_{ij}\sum_l\hat{\boldsymbol{w}}_l\cdot\overleftrightarrow{\boldsymbol{J}}_{lj}\cdot\hat{\boldsymbol{w}}_j) \tag{3.50}$$

$$M_{ij}^{12}(\boldsymbol{q}) = \cos(\boldsymbol{q}\cdot\boldsymbol{r}_{ij})(\hat{\boldsymbol{u}}_i\cdot\overleftrightarrow{\boldsymbol{J}}_{ij}\cdot\hat{\boldsymbol{v}}_j) \tag{3.51}$$

$$M_{ij}^{21}(\boldsymbol{q}) = \cos(\boldsymbol{q}\cdot\boldsymbol{r}_{ij})(\hat{\boldsymbol{v}}_i\cdot\overleftrightarrow{\boldsymbol{J}}_{ij}\cdot\hat{\boldsymbol{u}}_j) \tag{3.52}$$

$$M_{ij}^{22}(\boldsymbol{q}) = \cos(\boldsymbol{q}\cdot\boldsymbol{r}_{ij})(\hat{\boldsymbol{v}}_i\cdot\overleftrightarrow{\boldsymbol{J}}_{ij}\cdot\hat{\boldsymbol{v}}_j - \delta_{ij}\sum_l\hat{\boldsymbol{w}}_l\cdot\overleftrightarrow{\boldsymbol{J}}_{lj}\cdot\hat{\boldsymbol{w}}_j) \tag{3.53}$$

[19] There are eight possible fluctuations because each spin is allowed to fluctuate in two directions orthogonal to their ordering direction $\hat{\boldsymbol{w}}_i$, and there are four sublattices ($i = 0, 1, 2, 3$).

$$\overset{\leftrightarrow}{\boldsymbol{N}}(\boldsymbol{q}) = \mu_{\mathrm{B}} \begin{pmatrix} \overset{\leftrightarrow}{\boldsymbol{N}}^{11}(\boldsymbol{q}) & 0 \\ 0 & \overset{\leftrightarrow}{\boldsymbol{N}}^{22}(\boldsymbol{q}) \end{pmatrix} \tag{3.54}$$

$$N_{ij}^{11}(\boldsymbol{q}) = N_{ij}^{22}(\boldsymbol{q}) = \delta_{ij}\hat{\boldsymbol{w}}_i \cdot \overset{\leftrightarrow}{\boldsymbol{g}}_i \cdot \boldsymbol{H}. \tag{3.55}$$

Diagonalizing the classical spin-wave Hamiltonian, Eq. (3.48), yields the classical spin-wave dispersions $\kappa_\nu(\boldsymbol{q})$ as a function of the wavevector $\boldsymbol{q}$. These dispersions quantify how easy it is to thermally excite a mode with wavevector $\boldsymbol{q}$. Since the classical spin-wave Hamiltonian is quadratic, the partition function and free energy corrections from the classical spin-waves can be calculated exactly. Assuming the above diagonalization has been performed to find the normal modes $\phi_i(\boldsymbol{q})$ and dispersions $\kappa_\nu(\boldsymbol{q})$, the partition function and free energy are given by

$$Z = \int \left[\prod_{\boldsymbol{q}} \prod_{i=1}^{8} d\phi_\nu(\boldsymbol{q})\right] e^{-\frac{1}{T}(\varepsilon_0 + \frac{1}{2}\sum_{\boldsymbol{q}} \sum_{\nu=1}^{8} \kappa_\nu(\boldsymbol{q})\phi_\nu(\boldsymbol{q})\phi_\nu(-\boldsymbol{q}))} \tag{3.56}$$

$$= e^{-\frac{\varepsilon_0}{T}} \prod_{\boldsymbol{q}} \prod_{\nu=1}^{8} \sqrt{\frac{2\pi T}{\kappa_\nu(\boldsymbol{q})}} \tag{3.57}$$

$$\implies F = \varepsilon_0 - \frac{T}{2} \sum_{\boldsymbol{q}} \sum_{\nu=1}^{8} \ln\left(\frac{2\pi T}{\kappa_\nu(\boldsymbol{q})}\right) \tag{3.58}$$

$$F = \varepsilon_0 + \frac{T}{2} \sum_{\boldsymbol{q}} \sum_{\nu=1}^{8} \ln(\kappa_\nu(\boldsymbol{q})) - NT\ln(2\pi T). \tag{3.59}$$

If there are $N_q = N_t = \frac{N}{4}$ wavevectors in the sum, then the free energy per spin is:

$$f = \frac{\varepsilon_0}{N} + \frac{T}{8N_q} \sum_{\boldsymbol{q}} \sum_{\nu=1}^{8} \ln(\kappa_\nu(\boldsymbol{q})) - T\ln(2\pi T). \tag{3.60}$$

The entropy contribution (per spin) that arises from the thermal fluctuations of these classical spin-wave modes can be defined as:

$$s = -\frac{1}{8N_q} \sum_{\boldsymbol{q}} \sum_{\nu=1}^{8} \ln(\kappa_\nu(\boldsymbol{q})). \tag{3.61}$$

With a focus on the PC spin configurations, note that the above calculation can be performed for any value (and direction) of the applied magnetic field $\boldsymbol{H}$ and for any of the

six PC ground states (or their corresponding ground states in a field), just as was the case with VMFT. As will be discussed in Chapter 4, reentrance can be understood on the basis of classical spin-waves. However, for completeness, we present a derivation for *quantum* spin-waves in Appendix B.

Chapter 4

Results

4.1 Classical Monte Carlo Results

As an attempt to understand the reentrant behavior of $Er_2Sn_2O_7$'s phase diagram including flucutations, classical Monte Carlo simulations were performed by Dr. Ludovic Jaubert.[1] Classical Monte Carlo simulations capture the effect of thermal fluctuations in the spin system, but not of quantum fluctuations. The resulting phase diagram for each of the three field directions is shown in Figure 4.1, which also displays the experimentally-determined phase boundary. Immediately, it can be noticed that the classical Monte Carlo simulations are capable of qualitatively reproducing both which values of H reentrance occurs at, as well as the resulting increase in T_c at these reentrant lobes. There are three important conclusions to be drawn from this:

1. Since the reentrant lobes are present in the classical Monte Carlo simulations, we can turn our focus towards understanding the simulations rather than directly understanding the experiments. This has the benefit of reducing the complexity to be considered (i.e. in a real material, as compared to numerical simulations) without, hopefully, compromising too much our general understanding of the underlying phenomena.

2. Since classical Monte Carlo simulations incorporate the effect of thermal fluctuations but not of quantum fluctuations, the mechanism behind reentrance can be majorly

[1] These simulations use a system size of $L = 6$ or 8 (with $N = 16L^3$ spins). The spins are updated using a combination of heatbath moves [75], parallel tempering [24], and overrelaxation [24]. 10^6 or 10^7 Monte Carlo steps are used.

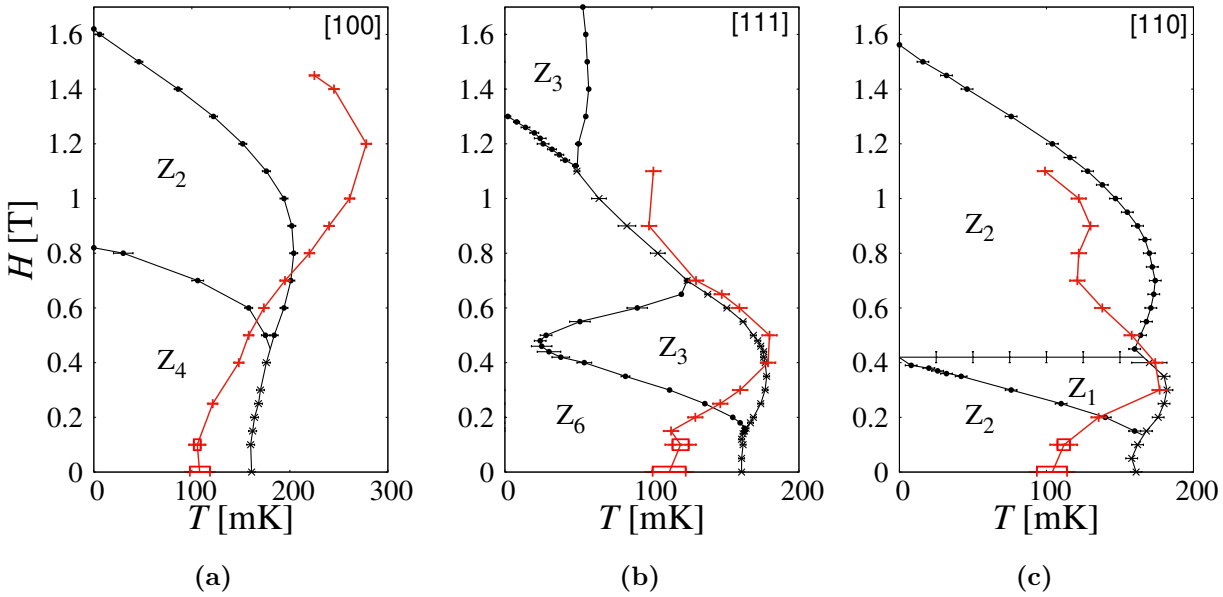

Figure 4.1: Classical Monte Carlo phase boundaries (black) for $Er_2Sn_2O_7$ under a (a) [100], (b) [111], and (c) [110] field, as compared with experimental data (red). Black crosses (circles) represent first-order (second-order) phase transitions. Red rectangles indicate areas where a broad heat capacity is found. $\mathbb{Z}_n$ represents the degeneracy of the phase, as explained in the main text. Note that the H-axis is shared between all three plots. [Figures provided by Ludovic Jaubert.]

understood from classical or thermal arguments. As such, we relegate quantum methods to Appendix B and focus our attention on classical methods in the main text, leaving a discussion of possible quantum effects for Chapter 5.

3. The classical Monte Carlo simulations performed here do not include long-range dipolar interactions, although these are important for stabilizing the Palmer-Chalker phase in antiferromagnetic pyrochlore systems [18] and could be important in a real material.[2] Hence, it would be of interest to understand how dipolar interactions could influence the occurrence of reentrance in $Er_2Sn_2O_7$. Since it is not immediately clear how dipolar interactions will change the simulation results, we can attempt to understand the reentrance in the absence of dipolar interactions first and then return to investigate the influence of them second. As such, we apply our classical methods

[2] As mentioned in Section 3.2, fitting experimental results to a nearest-neighbor exchange model automatically incorporates the dipolar interaction, but only up to nearest neighbors and no further.

without the inclusion of dipolar interactions and relegate a discussion of their effects to the end of this chapter.

4.2 Preliminary Considerations

We analyze the reentrance for the [100], [111], and [110] field directions, in that order. As seen in Section 4.3, the [100] case is the simplest to understand and introduces the major mechanism behind reentrance – namely, the apparition of soft modes due to phase transitions within the ordered PC state (referred to as branch collapse or branch merger transitions). The [111] and [110] cases mostly build upon this mechanism, with slight modifications for each.

Recall that the PC states are coplanar antiferromagnetically-ordered configurations, in which the four spins on a tetrahedron lie within the same plane in a global reference frame. This produces six PC states, since there are three planes and two possible directions for the spins to order in under time reversal symmetry. We have denoted these as $\langle xy\rangle, \langle xz\rangle$, and $\langle yz\rangle$, with their time-reversal-symmetric partners $\langle \overline{xy}\rangle, \langle \overline{xz}\rangle$, and $\langle \overline{yz}\rangle$, respectively. Under the application of a magnetic field $\boldsymbol{H}$, the spins begin to cant out of their original PC configurations. If one starts with a given PC configuration at zero field, one can study the evolution of this PC state as the field is turned on. These field-evolved Palmer-Chalker (FEPC) states will be denoted with a subscript h (e.g. $\langle xy\rangle_h$). In this way, by treating each FEPC state individually with our VMFT and classical spin-wave methods, we can trace the evolution and behavior of each FEPC independently.

The FEPC states also have different symmetries with respect to the applied magnetic field. If there is no applied field, we expect all six PC states to have the same free energy but distinct spin configurations; we refer to this as a $\mathbb{Z}_6$ degeneracy. On the other hand, if the applied field is sufficiently strong, all of the six FEPC states will become polarized into the same configuration. Hence, all six FEPC states will have the same free energy and the *same* spin configuration; we refer to this as a $\mathbb{Z}_1$ degeneracy. Now suppose (for example) there is a small applied field along the [100] direction. According to symmetry, this field direction will split the six FEPC states into two groups: $\{\langle xy\rangle_h, \langle \overline{xy}\rangle_h \langle xz\rangle_h, \langle \overline{xz}\rangle_h\}$, and $\{\langle yz\rangle_h, \langle \overline{yz}\rangle_h\}$. The first group contains all the PC configurations for which $\boldsymbol{H}$ lies in the same plane as the spins; the second group contains all PC configurations for which $\boldsymbol{H}$ is perpendicular to the plane of the spins. We know that we have a $\mathbb{Z}_6$ degeneracy at zero field and a $\mathbb{Z}_1$ degeneracy at strong fields. But, since the FEPC states are separated by symmetry into different groups, it is plausible to expect that the system will not directly transition from a $\mathbb{Z}_6$ phase to a $\mathbb{Z}_1$ phase as the magnitude of the field increases. Rather,

the applied field may cause additional transitions between these groups before polarizing all groups into the same maximally-polarized configuration. We may therefore expect multiple phase transitions as the magnitude of the applied field is increased. In fact, these branch merger transitions are precisely what is seen in Figure 4.3, for example.

With this understanding, we proceed with VMFT as follows:

1. For a given field direction, the VMFT procedure outlined in Chapter 3 is performed for each of the six FEPC states.
2. For given values of the applied field $\boldsymbol{H}$ and temperature T, the free energies of all six FEPC states are compared.
3. Of those FEPC states which minimize the free energy, the spin configurations are compared. If there are n resulting FEPC states which minimize the free energy but have distinct spin configurations, that phase is labelled with a $\mathbb{Z}_n$ degeneracy. Branch collapse/merger transitions occur between phases of different discrete symmetry.

4.3 Results for the [100] Field Direction

Consider an applied field along the [100] direction. The resulting VMFT phase diagram is shown in Figure 4.2a. Note that all six FEPC states are found to minimize the free energy at any point on the (H, T) phase diagram. At small values of the applied field H, there is a $\mathbb{Z}_6$ ordered phase with six distinct spin configurations that each minimize the free energy. As the magnitude of the field is increased, there is a transition to a $\mathbb{Z}_2$ ordered phase. Lastly, strong fields produce a field-polarized paramagnet (FP-PM), denoted by a $\mathbb{Z}_1$ degeneracy since all FEPC states are then in the same spin configuration here. A diagram representing how these FEPC states change as a function of H at $T = 0$ is shown in Figure 4.3.

It is striking to note that the location of the $T = 0$ phase transition within the ordered phase, at $H = 0.82$ T, corresponds well with the location of the reentrant lobe found in classical Monte Carlo simulations (as seen in Figure 4.2b). As such, we investigate classical spin-waves at this point. In Figure 4.4, we show the classical spin-wave dispersions for each of the six FEPC states at $H = 0$ T (Figure 4.4a) and $H = 0.82$ T (Figure 4.4b). The shaded grey region denotes energy scales that lie below the zero-field transition temperature found within classical Monte Carlo simulations, $T_c(H = 0 \text{ T}) \equiv T_{c0} \approx 160$ mK. At $H = 0$ T, the minimum of the classical spin-wave dispersions is much greater than the scale set by T_{c0}.

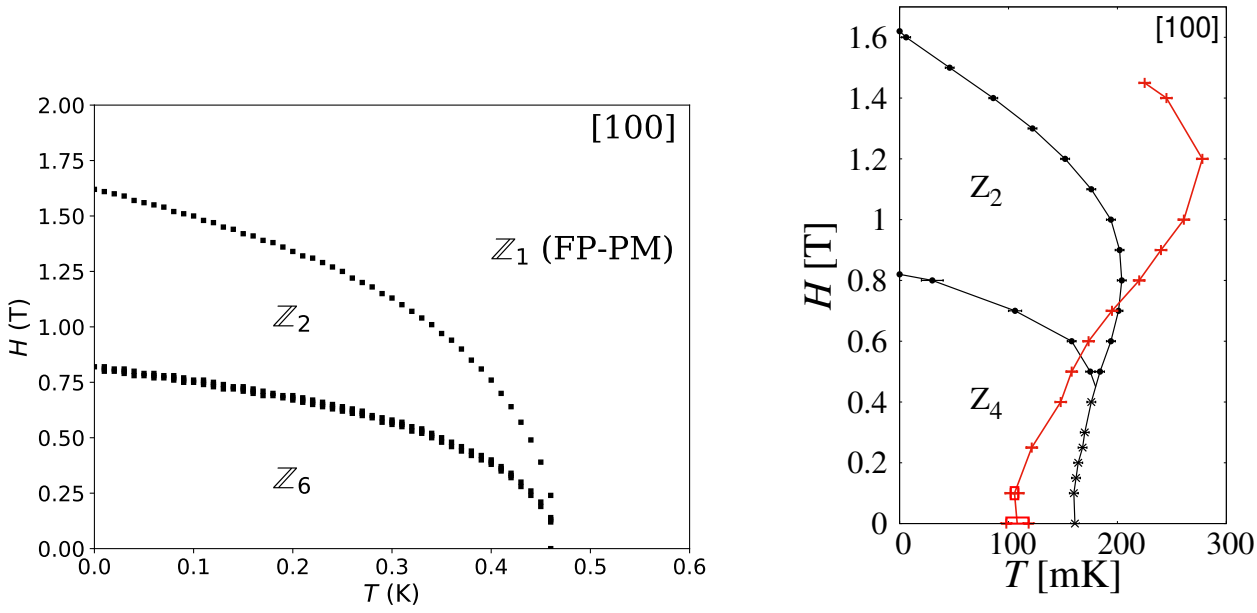

Figure 4.2: (a) Variational mean-field theory phase diagram for an applied field H along the [100] direction. $\mathbb{Z}_n$ represents the discrete degeneracy of that phase, with black squares indicating phase transitions. FP-PM stands for field-polarized paramagnet. (b) Classical Monte Carlo phase diagram for an applied field H along the [100] direction, reproduced from Figure 4.1a for comparison.

This changes as the field is increased[3], until the phase transition at $H = 0.82$ T occurs. By this point, the minimum of the classical spin-wave dispersion is much *lower* than the scale set by T_{c0}. In fact, since the minimum of the dispersion is zero, we can consider these to be soft mode fluctuations within the system.

The classical spin-wave dispersions roughly quantify the ease of exciting thermal fluctuations within (and increasing the entropy of) the system. To see this, consider Eq. (3.58). Comparing this to the usual expression for the free energy, $F = U - TS$ (for internal energy U and entropy S), we see that the classical spin-wave contribution to the entropy roughly scales as $S \sim \ln\left(\frac{T}{\kappa_\nu(\boldsymbol{q})}\right)$, for a given ν and $\boldsymbol{q}$. The natural temperature scale T to consider is $T = T_{c0} \approx 160$ mK, since reentrance usually involves thermal fluctuations increasing

[3]More detail about how the dispersions change as H is increased is given in Appendix C.

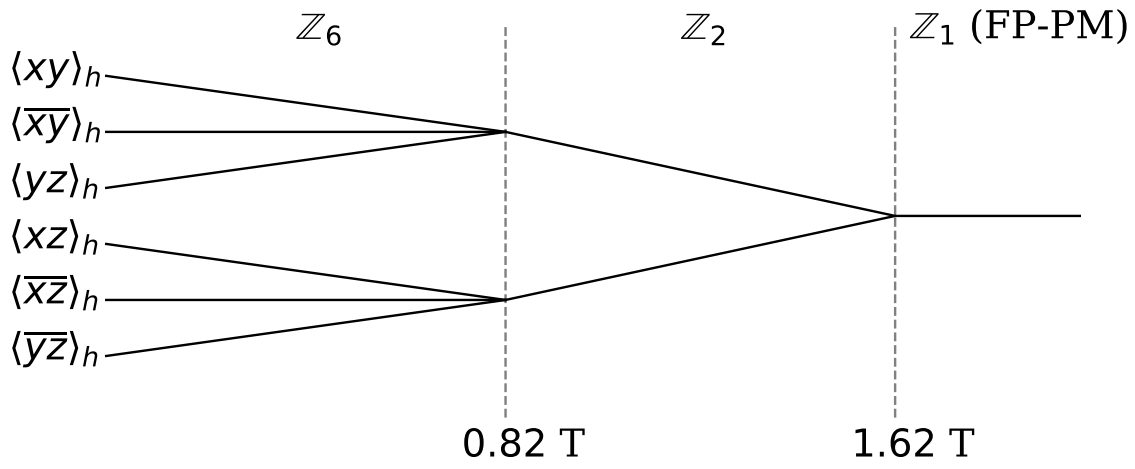

Figure 4.3: Zero-temperature diagram of the branch collapse of FEPC states in a [100] field. Notation for the FEPC states is defined in the main text. $\mathbb{Z}_n$ represents the degeneracy of FEPC states at that field value. Vertical dashed lines represent transitions between phases of different discrete degeneracy at the listed critical field values. FP-PM stands for field-polarized paramagnet.

$T_c(H)$ beyond T_{c0}. When $\kappa_\nu(\boldsymbol{q}) < T_{c0}$ (e.g. at $H = 0.82$ T), $S \sim \ln\left(\frac{T}{\kappa_\nu(\boldsymbol{q})}\right)$ implies that there is an increased entropy contribution from the classical spin-waves relative to when $\kappa_\nu(\boldsymbol{q}) > T_{c0}$ (e.g. at $H = 0$ T). Hence, comparing the $H = 0$ T dispersions in Figure 4.4a with the $H = 0.82$ T dispersions in Figure 4.4b allows us to conclude that it is much easier to excite thermal fluctuations within the system at $H = 0.82$ T than at $H = 0$ T. This means that there are stronger thermal fluctuations at $H = 0.82$ T, which increase the entropy of the system and thus decrease its free energy. Therefore, the apparition of these soft mode fluctuations entropically stabilize the *ordered* phase and increase $T_c(H = 0.82\text{ T})$ relative to T_{c0}. We thus argue that these soft modes are the main drivers of the reentrance observed in the Monte Carlo simulations.[4] The origin of these soft modes lies in the multiphase competition that results when the $\mathbb{Z}_6$ phase is brought into competition with the

[4]Not shown here are the classical spin-wave dispersions as the field approaches $H = 0.82$ T from below. As this happens, the minimum of the dispersion gradually decreases and dips below T_{c0}, reaching its minimum at $H = 0.82$ T when reentrance is at its apex. Thus, the overall lobe shape of the reentrance in the phase diagram of Figure 4.2b originates from this gradual decrease in the dispersion minimum. This is discussed in more detail in Appendix C.

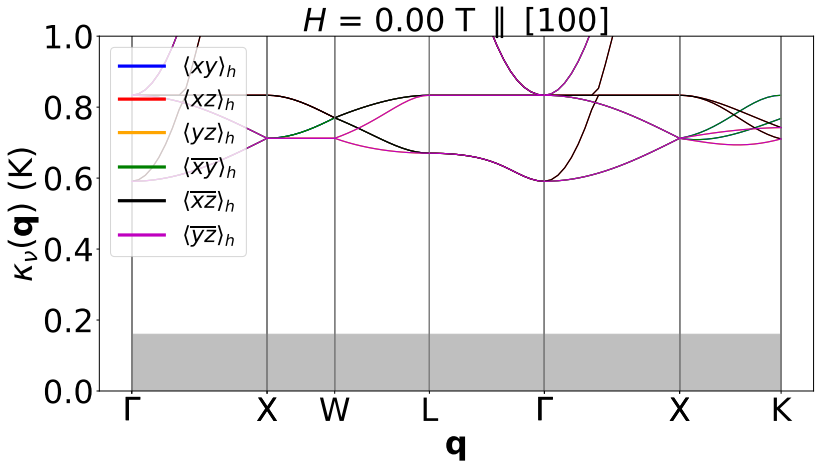

(a)

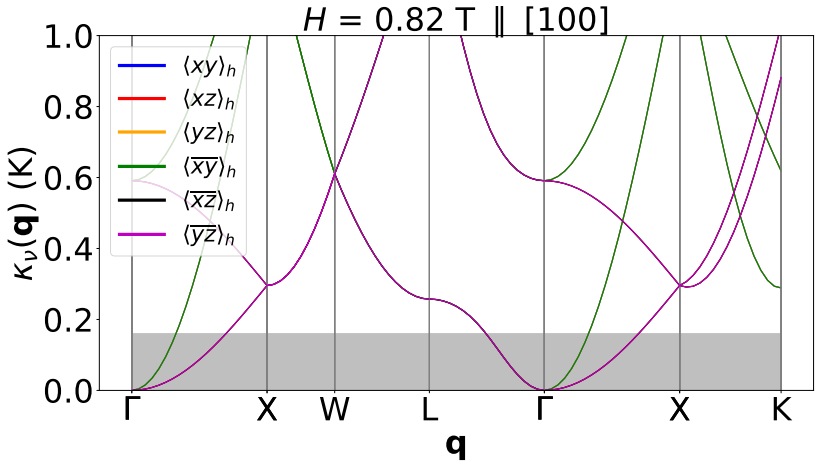

(b)

Figure 4.4: Classical spin-wave expansion at (a) $H = 0$ T (for comparison) and (b) $H = 0.82$ T, in the [100] direction. Wavevectors are taken from the FCC reciprocal lattice. The grey shaded region represents energy scales below $T_{c0} \approx 160$ mK. Note that dispersions may overlap due to degeneracies at high-symmetry points or from mergers of FEPC states induced by the field (e.g. $\langle xy \rangle_h$ and $\langle \overline{xy} \rangle_h$ for $H \geq 0.82$ T).

$\mathbb{Z}_2$ phase as the field is increased.[5] Generally, this tells us that as the dispersions $\kappa_\nu(\boldsymbol{q})$

[5]One may generally consider these stronger fluctuations to be coming from proximity to a phase transition. More specifically, the spins will fluctuate more strongly here since they are on the edge of two

(and their minima) decrease with increasing H, we can expect stronger thermal fluctuations in our system and an increased entropy of the ordered phase. This is an important recurring theme for explaining reentrance in Sections 4.4 and 4.5 (as well as in Appendix C), although the reason for $\kappa_\nu(\boldsymbol{q})$ decreasing may differ.

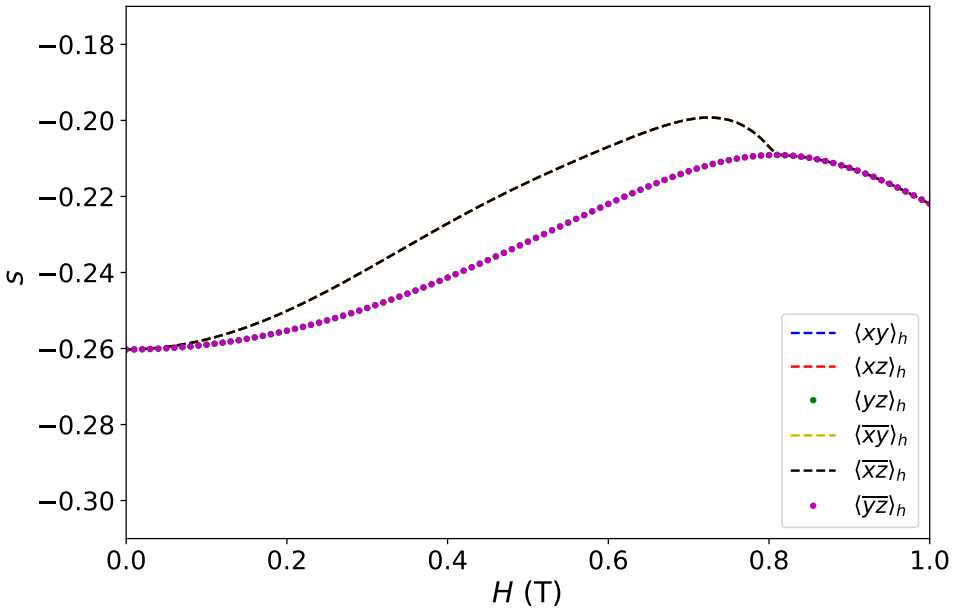

Figure 4.5: Entropy correction s (per spin, from Eq. (3.61)) to the mean-field free energy due to thermal fluctuations from classical spin-waves, for H applied along the [100] direction. Note that the curves for $\{\langle xy\rangle_h, \langle xz\rangle_h, \langle \overline{xy}\rangle_h, \langle \overline{xz}\rangle_h\}$ all overlap with each other, and the curves for $\{\langle yz\rangle_h, \langle \overline{yz}\rangle_h\}$ overlap as well. However, these two groups are plotted with different markers to show that there is no overlap *between* the two groups for $H < 0.82$ T, as expected by symmetry under a [100] field.

Furthermore, one can calculate the thermal fluctuation corrections to the mean-field free energy, which does not incorporate themal fluctuations. This is especially of interest for the low-field ordered phase. VMFT finds a $\mathbb{Z}_6$ degeneracy here, but a $\mathbb{Z}_6$ degeneracy is not protected by symmetry. In fact, a [100] field splits the six FEPC states into two groups: $\{\langle xy\rangle_h, \langle xz\rangle_h, \langle \overline{xy}\rangle_h, \langle \overline{xz}\rangle_h\}$ (in which the applied field lies in the same plane as the original PC states) and $\{\langle yz\rangle_h, \langle \overline{yz}\rangle_h\}$ (in which the applied field lies perpendicular to the plane

preferred spin orderings.

of the original PC states). Since this degeneracy is not protected by symmetry, thermal fluctuations are expected to produce an order-by-thermal-disorder effect and entropically favor one of the two groups. To determine this selection, Eq. (3.61) can be used to calculate the entropy of the six FEPC states. Calculating s from Eq. (3.61) for each of the six FEPC states individually and for a range of H values in the [100] direction produces Figure 4.5.[6] Note that the group of FEPC states $\{\langle xy\rangle_h, \langle xz\rangle_h, \langle \overline{xy}\rangle_h, \langle \overline{xz}\rangle_h\}$ are depicted with different markers than $\{\langle yz\rangle_h, \langle \overline{yz}\rangle_h\}$ to verify that the two groups have different entropic corrections for $H < 0.82$ T, as expected from symmetry. Moreover, the group of FEPC states that has the higher entropy is $\{\langle xy\rangle_h, \langle xz\rangle_h, \langle \overline{xy}\rangle_h, \langle \overline{xz}\rangle_h\}$, so thermal fluctuations entropically select this subset of the original six FEPC states. Hence, when thermal fluctuation corrections are added to VMFT, the $\mathbb{Z}_6$ degeneracy of the VMFT phase diagram should give way to a $\mathbb{Z}_4$ degeneracy.

Let us return to the classical Monte Carlo results in a [100] field, namely Figure 4.2b. As found in VMFT, there are two ordered phases with different discrete degeneracies. As well, at low fields, thermal fluctuations indeed select a $\mathbb{Z}_4$ subset of ordered FEPC states out of the original $\mathbb{Z}_6$ mean-field FEPC states. The $T = 0$ transition at $H = 0.82$ T corresponds well with the maximum of reentrance. Therefore, one can roughly conclude that building upon the VMFT results with thermal fluctuations from classical spin-waves produces reentrance, as exhibited by classical Monte Carlo simulations. This suggests that the reentrant mechanism operates as follows: strong thermal fluctuations arise in the form of soft modes in the classical spin-waves, originating from the transition between two ordered PC phases of different discrete symmetry. These strong thermal fluctuations entropically stabilize the *ordered* phase, giving an entropic advantage of the ordered phase over the disordered phase. This leads to an *increase* in T_c as H increases through certain ranges of values, producing reentrance.

4.4 Results for the [111] Field Direction

Now consider an applied field along the [111] direction. The resulting VMFT phase diagram is shown in Figure 4.6a. As for the [100] field direction, all six FEPC states are found to minimize the free energy at any given point in the (H, T) phase diagram. Comparing Figure 4.6a with the classical Monte Carlo results in Figure 4.6b, we see that classical

[6] Note that there are negative values of s in Figure 4.5 due to the definition of the entropy correction s in Eq. (3.61). However, what matters is the *relative* entropy between the FEPC states shown in Figure 4.5. If one calculated the full entropy S from Eq. (3.58) rather than just taking the contribution from classical spin-waves, the resulting S would be positive.

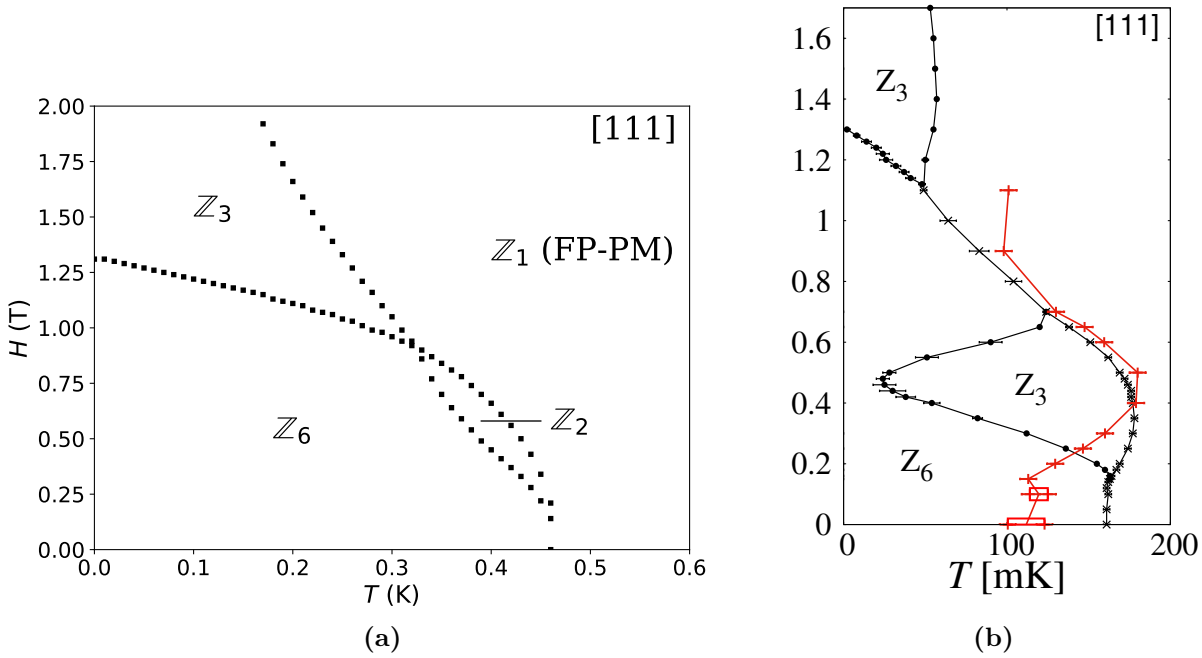

Figure 4.6: (a) Variational mean-field theory phase diagram for an applied field H along the [111] direction. $\mathbb{Z}_n$ represents the discrete degeneracy of that phase, with black squares indicating phase transitions. FP-PM stands for field-polarized paramagnet. (b) Classical Monte Carlo phase diagram for an applied field H along the [111] direction, reproduced from Figure 4.1b for comparison.

Monte Carlo simulations show a slight reentrant lobe near $H = 1.31$ T, which corresponds with the $T = 0$ transition found within VMFT at $H = 1.31$ T.[7] Figure 4.7 shows how all FEPC states evolve and merge at $T = 0$ as a function of H, and Figure 4.8 shows that soft modes emerge at this $T = 0$ transition. This is analogous to the situation for $H \parallel [100]$. However, both the experimental and classical Monte Carlo phase diagrams exhibit a *lower reentrant* lobe around $H = 0.4$ T, for which there is *no* corresponding $T = 0$ phase transition in the VMFT phase diagram. Hence, the suggestion of a branch merger transition giving soft modes (as put forward for the [100] field direction) does not apply here. An alternative suggestion must be given to understand this occurrence of reentrance.

[7] Unfortunately, it was not possible to probe the heat capacity at such high fields experimentally. In principle, however, a second reentrant lobe at higher fields might be expected.

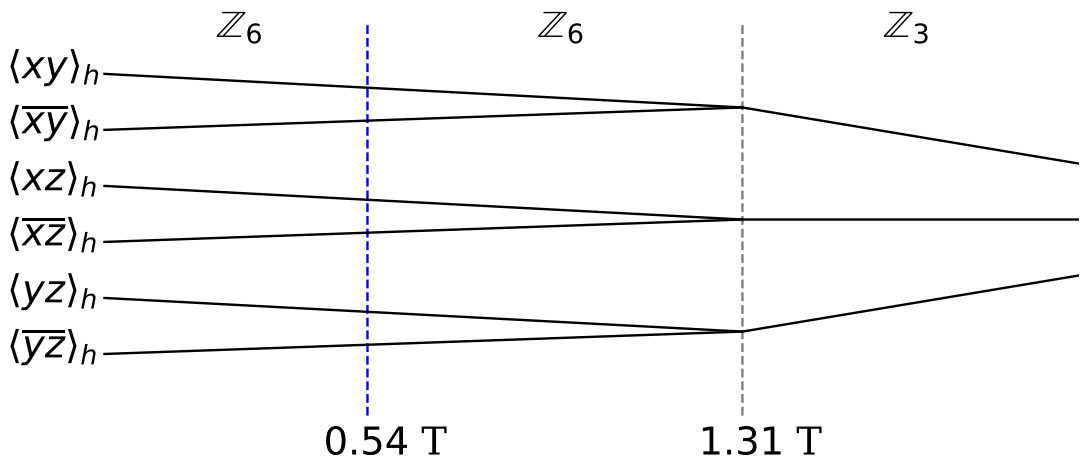

Figure 4.7: Zero-temperature diagram of the branch collapse of FEPC states in a [111] field. The notation for the FEPC states is defined in the main text. $\mathbb{Z}_n$ represents the degeneracy of FEPC states at that field value. The grey vertical dashed line represents a transition between phases of different discrete degeneracy at the listed critical field value. The blue vertical dashed line represents the field-induced selection of the (subdominant) ψ_2 order parameter.

Let us return to the classical Monte Carlo results shown in Figure 4.6b, specifically focusing on the $\mathbb{Z}_3$ ordered phase around $H \approx 0.5$ T that is associated with the lower reentrant lobe. This is still a PC phase, but there is a finite but subdominant Γ_5 order parameter that also exists. The reason for this is the canting of the spins out of their PC configurations as the applied field H is varied. When $H = 0$, the spin configurations are in pure PC configurations, and the order parameters for all other possible $\boldsymbol{q} = 0$ orders [24] are zero. As H increases, the spins canting away from the pure PC configurations implies that other order parameters become finite. If these order parameters are smaller than that of the PC phase, however, these orders can be considered "subdominant". It seems likely that the finite Γ_5 order parameter found in classical Monte Carlo simulations arises due to $Er_2Sn_2O_7$'s proximity to this phase, as mentioned in Chapter 2. Specifically for a field along the [111] direction, the lower reentrant lobe possesses a subdominant ψ_2 order. The classical spin-wave dispersions are calculated and shown in Figure 4.9 for $H = 0.54$ T, which lies in this lower reentrant region and therefore acts as a proxy for how the classical spin-waves behave here. Figure 4.9 demonstrates that $\kappa_\nu(\boldsymbol{q}) < T_{c0}$ for a range of $\boldsymbol{q}$. Therefore, although there is no $T = 0$ branch collapse transition that gives rise to

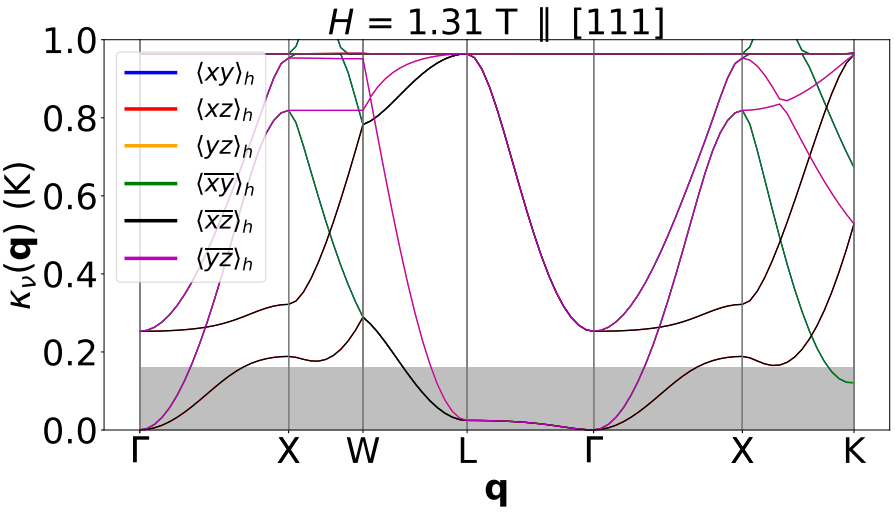

Figure 4.8: Classical spin-wave expansion for each of the FEPC states at $H = 1.31$ T in the [111] direction. Wavevectors are taken from the FCC reciprocal lattice. The grey shaded region represents energy scales below $T_{c0} \approx 160$ mK. Note that dispersions may overlap due to degeneracies at high-symmetry points or from mergers of FEPC states induced by the field (e.g. $\langle xy \rangle_h$ and $\langle \overline{xy} \rangle_h$ for $H \geq 1.31$ T).

these lowered dispersions as in the [100] case, we can still attribute the stronger thermal fluctuations and increased T_c to the fact that the dispersions $\kappa_\nu(\boldsymbol{q})$ have decreased below T_{c0}. This follows from the argument given in Section 4.3 (and slightly expanded on in Appendix C) relating the behavior of the dispersion relations to the increase or decrease of entropy and thermal fluctuations.

The origin of these decreased dispersions $\kappa_\nu(\boldsymbol{q})$ remains to be determined, though they are clearly connected with the ψ_2 phase (as it is a subdominant ψ_2 order parameter that is found where reentrance occurs). As discussed in Chapters 1 and 2, the selection of ψ_2 or ψ_3 ordering within the Γ_5 phase is usually argued to occur based on thermal or quantum order-by-disorder. However, it has been demonstrated on symmetry grounds that an applied magnetic field H may also create an energetic preference for one or the other [76]. For XY pyrochlore antiferromagnets at $T = 0$, it was shown that an applied field $\boldsymbol{H} \parallel [001]$ contributes

$$E^{[001]} \propto H^2 \cos(2\theta_E) \tag{4.1}$$

to the energy minimization condition of θ_E. This differentiates between ψ_2 selection ($\theta_E = \frac{n\pi}{3}, n = 0, 1, \ldots, 5$, shown in Figure 2.6b) and ψ_3 selection ($\theta_E = \frac{(2n+1)\pi}{6}, n = 0, 1, \ldots, 5$,

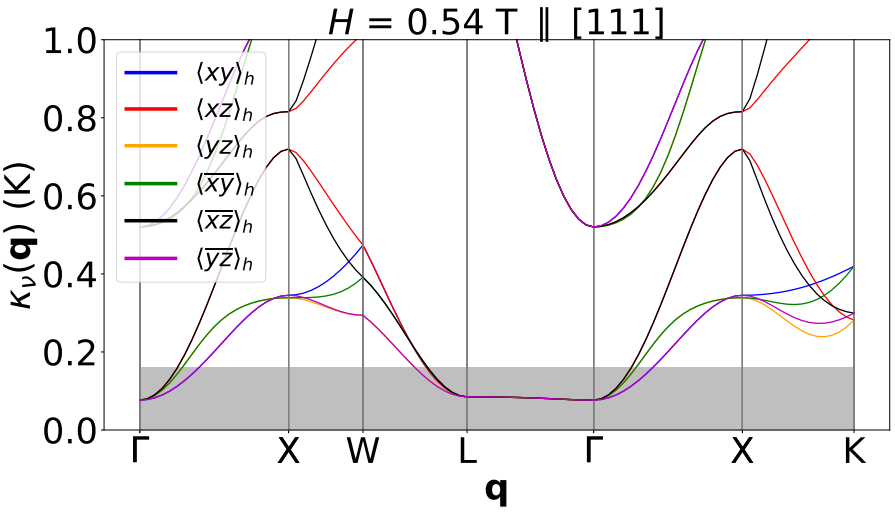

Figure 4.9: Classical spin-wave expansion for each of the FEPC states at $H = 0.54$ T in the [111] direction. Wavevectors are taken from the FCC reciprocal lattice. The grey shaded region represents energy scales below $T_{c0} \approx 160$ mK. Note that dispersions may overlap due to degeneracies at high-symmetry points or from mergers of FEPC states induced by the field (e.g. $\langle xy \rangle_h$ and $\langle \overline{xy} \rangle_h$ for $H \geq 1.31$ T).

shown in Figure 2.6a), as discussed in Chapter 2.[8] On the other hand, an applied field $\boldsymbol{H} \parallel [110]$ contributes

$$E^{[110]} \propto H^2 \cos(2\theta_E) \tag{4.2}$$

as well. The proportionality constants depend on the exchange parameters of the system. However, if $E \sim H^2 \cos(2\theta_E)$, then turning on a field will give an energetic preference for $\theta_E = \frac{\pi}{2}, \frac{3\pi}{2}$, which corresponds to ψ_3 selection minimizing the energy. On the other hand, if $E \sim -H^2 \cos(2\theta_E)$, then turning on a field will give an energetic preference for $\theta_E = 0, \pi$, which corresponds to ψ_2 selection minimizing the energy. In either case, the selection is unilateral: either ψ_2 *or* ψ_3 is energetically preferred.

The [111] field direction constitutes a special case. On symmetry grounds, two contributions to the energy (which we call $E_1^{[111]}$ and $E_2^{[111]}$) are found:

$$E_1^{[111]} \propto H^2 \cos(6\theta_E), \tag{4.3}$$

[8] Note that thermal or quantum order-by-disorder also operate to select between ψ_2 and ψ_3, contributing terms that enter as $\cos(6\theta_E)$. However, as we focus on classical spins, we do not consider the effect of quantum fluctuations on this selection. And, as we focus on $T = 0$ or on VMFT results, we neglect the effect of thermal fluctuations as well.

$$E_2^{[111]} \propto H^3 \cos(3\theta_E). \tag{4.4}$$

For a field along the [111] direction, the selection may no longer be unilateral. For small values of H, the first of the above two terms dominates, selecting ψ_2 or ψ_3 depending on the proportionality constant (negative or positive constant, respectively). For large values of H, the second term dominates and may again select ψ_2 or ψ_3 depending on the proportionality constant (negative or positive constant, respectively). For intermediate values of H, there may be a competition for selection. This explains the change in ψ_2 or ψ_3 selection shown in Figure 4.10 and discussed in the next paragraph.

This selection effect does not rely on thermal fluctuations or even temperature, but originates purely from the application of an applied field $\boldsymbol{H}$. Hence, it should be visible in both VMFT (which has an applied field $\boldsymbol{H}$ but no thermal fluctuations) and at $T = 0$. Guided by this insight, θ_E is calculated for each of the FEPC states as a function of $H \parallel [111]$ and at $T = 0$. This is done by using Eq. (2.29) to calculate $\boldsymbol{m}_E = (\cos(\theta_E), \sin(\theta_E))$ for a FEPC configuration $(\boldsymbol{S}_0, \boldsymbol{S}_1, \boldsymbol{S}_2, \boldsymbol{S}_3)$ on a single tetrahedron, implying that $\theta_E = \arctan\left(\frac{m_E^y}{m_E^x}\right)$. Figure 4.10 displays the resulting angle θ_E for each of the six FEPC states as a function of the applied field H. At low (high) values of H, the values of θ_E correspond to ψ_3 (ψ_2) states. At around $H = 0.54$ T, there is a strong selection of an angle corresponding to ψ_2 for *all* FEPC states.[9] This is precisely where the classical spin-wave dispersions decrease below T_{c0}.[10]

Altogether, then, we may conclude the following: an applied field along the [111] direction influences the selection of ψ_2 or ψ_3 ordering within the Γ_5 phase, even if such ordering is subdominant to PC ordering. At intermediate fields, a strong ψ_2 selection occurs. Given $Er_2Sn_2O_7$'s proximity to the ψ_2 phase boundary, this is associated with strong thermal fluctuations arising from the PC/ψ_2 multiphase competition. The classical spin-wave dispersions also witness to this fact by decreasing below T_{c0} as the field-induced ψ_2 selection occurs. As argued in Section 4.3, having $\kappa_\nu(\boldsymbol{q}) < T_{c0}$ results in thermal fluctuations increasing the entropy within the ordered phase. Hence, just as in the [100] case, these strong thermal fluctuations entropically stabilize the ordered phase and cause reentrance. However, the difference from the [100] case comes from the origin of these strong thermal fluctuations. It is not two PC phases of different degeneracy that are brought into competition by the field; in a [111] field, it is PC/ψ_2 competition that the applied field

[9] This is another reason why we plot the classical spin-wave dispersions for $H = 0.54$ T in Figure 4.9.

[10] Note that $\kappa_\nu(\boldsymbol{q}) < T_{c0}$ for a range of values of H and not just at $H = 0.54$ T. As explained in Appendix C, this is why reentrance occurs across a range of H values. However, the point we make here is the *reason* for $\kappa_\nu(\boldsymbol{q}) < T_{c0}$ at all – namely, proximity to the field-induced selection of ψ_2 at $H = 0.54$ T, similar to proximity to a branch collapse transition as in Section 4.3 and Appendix C.

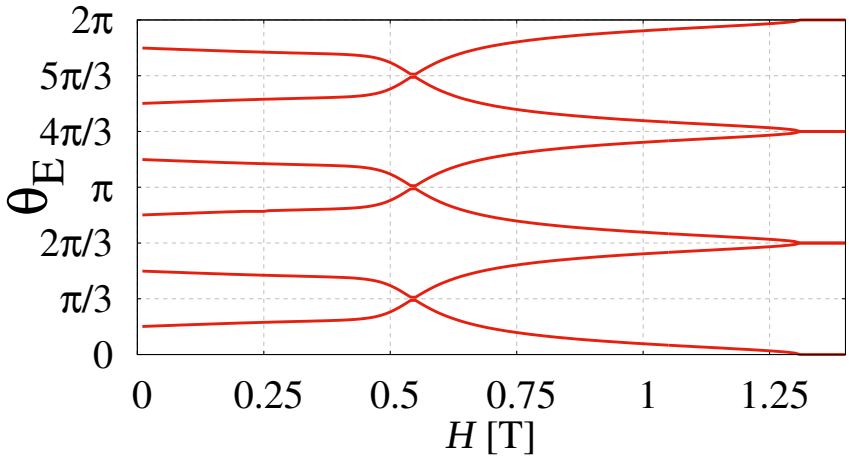

Figure 4.10: θ_E angle determining ψ_2 ($\theta_E = \frac{n\pi}{3}, n = 0, 1, \ldots, 5$) or ψ_3 ($\theta_E = \frac{(2n+1)\pi}{6}, n = 0, 1, \ldots, 5$) selection, as a function of H along the [111] direction and for each of the six FEPC states. Each red curve represents θ_E (as a function of H) for a different FEPC state. θ_E is calculated as explained in the main text. Note the selection of θ_E at $H = 0.54$ T for all six FEPC states corresponds to ψ_2. [Figure provided by Ludovic Jaubert.]

introduces.

4.5 Results for the [110] Field Direction

Next, consider an applied field along the [110] direction. Unlike the [100] and [111] field directions, the six FEPC states *do not* all minimize the free energy at any given point in the (H, T) phase diagram. This makes the [110] field direction the most complex case out of the three field directions. Care must be taken to determine the discrete degeneracy of each phase in this case; we must first determine which of the FEPC states minimize the free energy, and then count which *of these* have distinct spin configurations. Doing this produces the VMFT phase diagram in Figure 4.11a, and the $T = 0$ diagram of FEPC mergers shown in Figure 4.12. Since we are building classical spin-waves on top of the $T = 0$ ground state configurations, we focus on Figure 4.12. This shows us the branch collapse transitions, which we have seen (in the [100] and [111] cases) can be linked with the occurrence of reentrance. Figure 4.12 also shows us which FEPC states minimize the

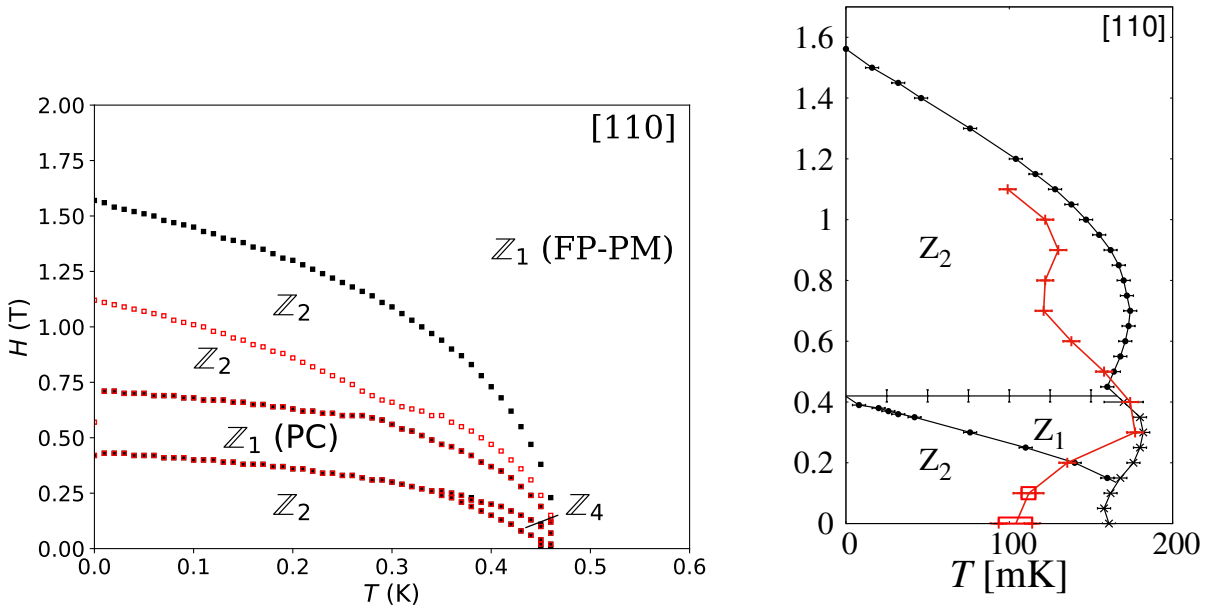

Figure 4.11: (a) Variational mean-field theory phase diagram for an applied field H along the [110] direction. $\mathbb{Z}_n$ represents the discrete degeneracy of that phase, with black squares indicating phase transitions. Open red squares represent a change in which FEPC states minimize the free energy. FP-PM stands for field-polarized paramagnet; PC stands for Palmer-Chalker. Note that the finite-temperature phases differ from the zero-temperature phases shown in Figure 4.12 due to entropic effects, as explained in Appendix D. (b) Classical Monte Carlo phase diagram for an applied field H along the [110] direction, reproduced from Figure 4.1c for comparison.

energy, which will be important in interpreting the classical spin-wave results.[11]

Let us turn to the classical Monte Carlo results, namely Figure 4.11b. There are three features that need to be understood, namely, the two reentrant lobes as well as the sudden dip in T_c that occurs between them. An initial understanding of all three features is given by again having recourse to classical spin-wave dispersions. These dispersions are shown in Figures 4.13 and 4.14 for three different values of the applied field: $H = 0.41$ T (Figure

[11]Note also that, in Figure 4.11a, the phases that occur along $T = 0$ differ from those that occur at finite temperature, even $T = 0^+$. The reason for this is discussed in Appendix D. However, as mentioned in the main text, we focus on the branch collapse transitions that occur at $T = 0$, since it is with the $T = 0$ spin configurations that we calculate the classical spin-wave dispersions.

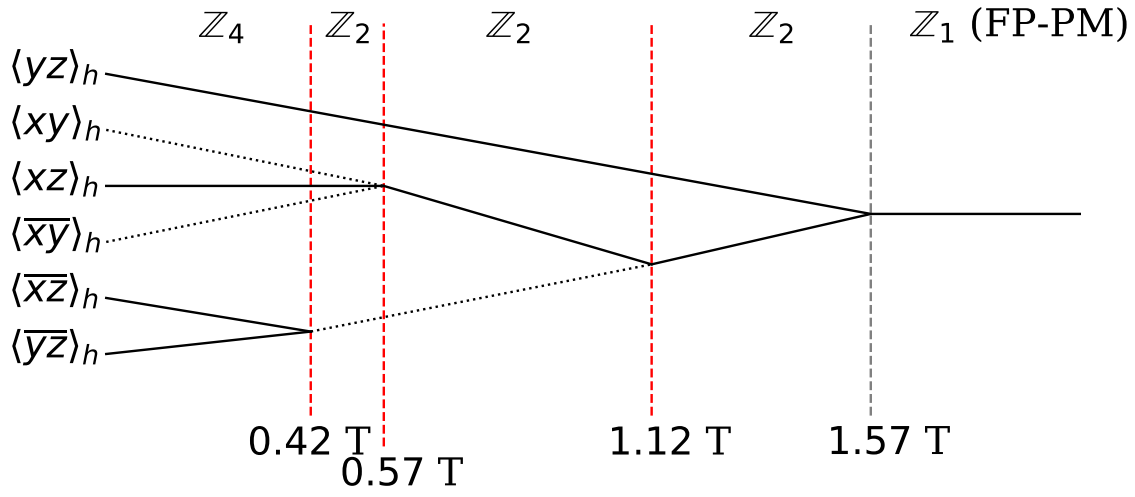

Figure 4.12: Zero-temperature diagram of the branch collapse of FEPC states in a [110] field. Notation for the FEPC states is defined in the main text. $\mathbb{Z}_n$ represents the degeneracy of FEPC states at that field value, which counts only the FEPC states that minimize the energy (solid branches) and not those which do not (dotted branches). The grey vertical dashed line represents a transition between phases of different discrete degeneracy at the listed critical field value. The red vertical dashed lines represent a change in which FEPC states minimize the energy. Note that these changes always occur where certain FEPC branches merge.

4.13a), $H = 0.42$ T (Figure 4.13b), and $H = 0.75$ T (Figure 4.14). We examine each of these in turn.

At $H = 0.41$ T in Figure 4.13a, we again have dispersions satisfying $\kappa_\nu(\boldsymbol{q}) < T_{c0}$. Following the same arguments as in Section 4.3 and Appendix C, this implies the presence of strong thermal fluctuations that are associated with the first (lower) reentrant lobe. Looking at the $T = 0$ transitions in Figure 4.12, the reason why the classical spin-wave dispersions have decreased below T_{c0} is again the proximity to a FEPC branch collapse transition (at $H = 0.42$ T).[12] As in the [100] case discussed in Section 4.3 and Appendix C, proximity to such a transition increases the fluctuations in the system, given that there are multiple competing preferences for spin ordering near this transition. However, as the field

[12] As discussed further in Appendix C, the onset of reentrance begins even below the branch collapse transition, since proximity to the transition already leads to an increase in thermal fluctuations. Hence, even though $H = 0.41$ T is a field value below the critical field $H_c = 0.42$ T for a branch collapse transition, reentrant behavior may still be found at $H = 0.41$ T.

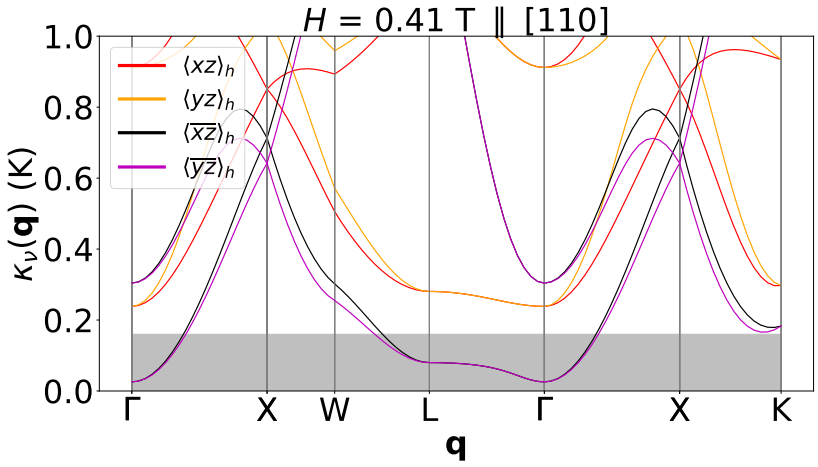

(a)

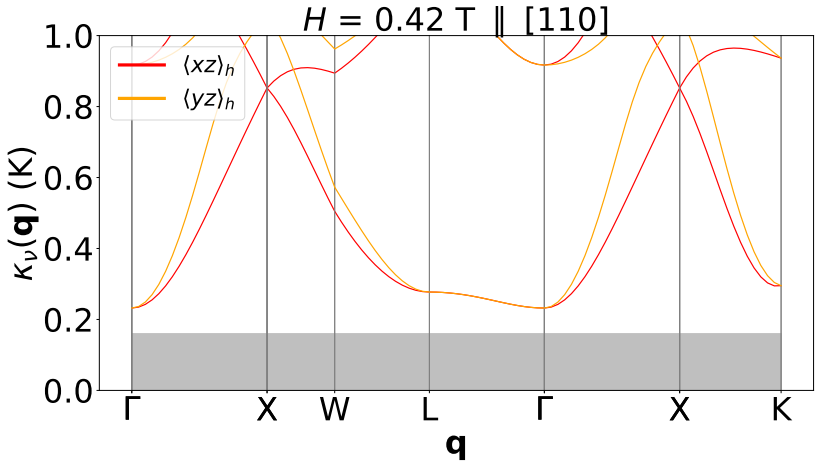

(b)

Figure 4.13: Classical spin-wave expansion at (a) $H = 0.41$ T and (b) $H = 0.42$ T, in the [110] direction. Only those field-evolved Palmer-Chalker states which minimize the energy are considered. Wavevectors are taken from the FCC reciprocal lattice. The grey shaded region represents energy scales below $T_{c0} \approx 160$ mK. Note that dispersions may overlap due to degeneracies at high-symmetry points or from mergers of FEPC states induced by the field (e.g. $\langle xy \rangle_h$, $\langle xz \rangle_h$, and $\langle \overline{xy} \rangle_h$ for $H \geq 0.57$ T).

is increased further to $H = 0.42$ T, the FEPC states that are contributing these strong thermal fluctuations (namely, $\langle \overline{xz} \rangle_h$ and $\langle \overline{yz} \rangle_h$) are no longer energetically preferred states, as shown in Figure 4.12. That is, these FEPC states no longer minimize the energy, and

the system will not find itself in these FEPC states anymore. Since the system will not be found in such states, their contribution to the classical spin-wave dispersions and thermal fluctuations should no longer be considered.[13] The resulting classical spin-wave dispersions are shown in Figure 4.13b, where the classical spin-wave dispersions of only the energy-minimizing FEPC states are shown. The dispersions corresponding to the $\langle\overline{xz}\rangle_h$ and $\langle\overline{yz}\rangle_h$ states are therefore no longer included. The entropy that their dispersions provided at $H < 0.41$ T is no longer present, which causes the sudden dip in T_c that occurs right above the first reentrant lobe.

Lastly, we again see classical spin-wave dispersions satisfying $\kappa_\nu(\boldsymbol{q}) < T_{c0}$ appearing around $H = 0.75$ T (Figure 4.14), corresponding to the second (upper) reentrant lobe. Looking at the $T = 0$ transitions in Figure 4.12, we see that there are two FEPC branch collapse transitions proximate to $H = 0.75$ T – one which occurs below 0.75 T (at $H \approx 0.52$ T) and one which occurs above 0.75 T (at $H \approx 1.12$ T). As argued in Appendix C, proximity to these phase transitions again cause the classical spin-wave dispersions to drop below T_{c0}. This increases thermal fluctuations and gives rise to reentrance. Hence, all three features of the classical Monte Carlo phase diagram can be understood from analyzing the behavior of the classical spin-wave dispersions. These again originate from FEPC branch collapse transitions. However, the situation for the [110] field direction is more complicated than that of the [100] field direction because of the changing energy degeneracy of the FEPC states.

4.6 Influence of Long-Range Dipolar Interactions

Finally, we consider the influence of long-range dipolar interactions on the above phase diagrams and arguments for reentrance. Since these interactions are long-ranged, it is not immediately obvious what influence they may have on the phases or phase diagram. Throughout this chapter and until this section, we applied the VMFT scheme of Section 3.1 to the nearest-neighbor exchange model defined in Section 2.2. However, the VMFT scheme of Section 3.1 is derived for arbitrary interactions $J^{\mu\nu}_{ia,jb}$ (specifically in Eq. (3.2)), not necessarily restricted to nearest neighbors. Hence, including long-range dipolar interactions into VMFT means including both the nearest-neighbor exchange interactions from Section 2.2 *and* the long-range dipolar interactions from Section 2.4 into $J^{\mu\nu}_{ia,jb}$. As explained in Section 3.2, the long-range dipolar interactions can be calculated and included in $J^{\mu\nu}_{ia,jb}$ by using the Ewald summation method. Apart from modifying $J^{\mu\nu}_{ia,jb}$ to include the long-range

[13] Put simply, these states cannot contribute thermal fluctuations to the system, if the system is not found in these states.

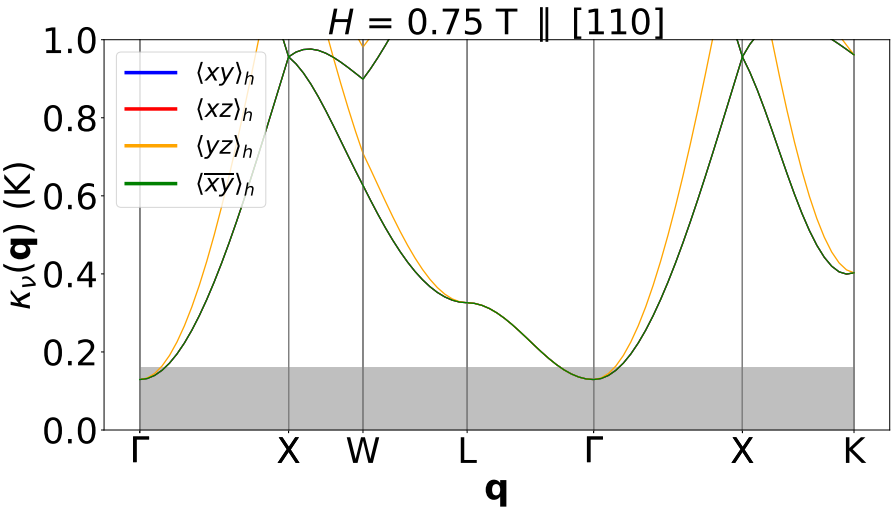

Figure 4.14: Classical spin-wave expansion at $H = 0.75$ T in the [110] direction. Only those field-evolved Palmer-Chalker states which minimize the energy are shown. Wavevectors are taken from the FCC reciprocal lattice. The grey shaded region represents energy scales below $T_{c0} \approx 160$ mK. Note that dispersions may overlap due to degeneracies at high-symmetry points or from mergers of FEPC states induced by the field (e.g. $\langle xy \rangle_h$, $\langle xz \rangle_h$, and $\langle \overline{xy} \rangle_h$ for $H \geq 0.57$ T).

dipolar interactions, there are no modifications to how VMFT is performed and how the resulting phase diagrams are produced. In particular, the self-consistent VMFT procedure outlined in Section 3.1 is the same, as are the ways of determining and labelling the $\mathbb{Z}_n$–degenerate phases outlined in Section 4.2. The resulting VMFT phase diagrams for the [100], [111], and [110] field directions are shown in Figure 4.15.

The critical temperatures and fields of the phase transitions are slightly modified by long-range dipolar interactions. However, the overall topology of the phase diagram (i.e. which phases and phase transitions exist and where they occur on the phase diagram relative to each other) remains unchanged. This suggests that the same arguments that were made for reentrance without dipolar interactions should be robust when dipolar interactions are included. Given that the critical temperatures and fields are modified, a proper accounting of the dipolar interactions would be important to achieve greater agreement with experiment.[14]

[14] As discussed further in Chapter 5, a proper accounting of quantum effects would also be important for achieving greater agreement between theory and experiment.

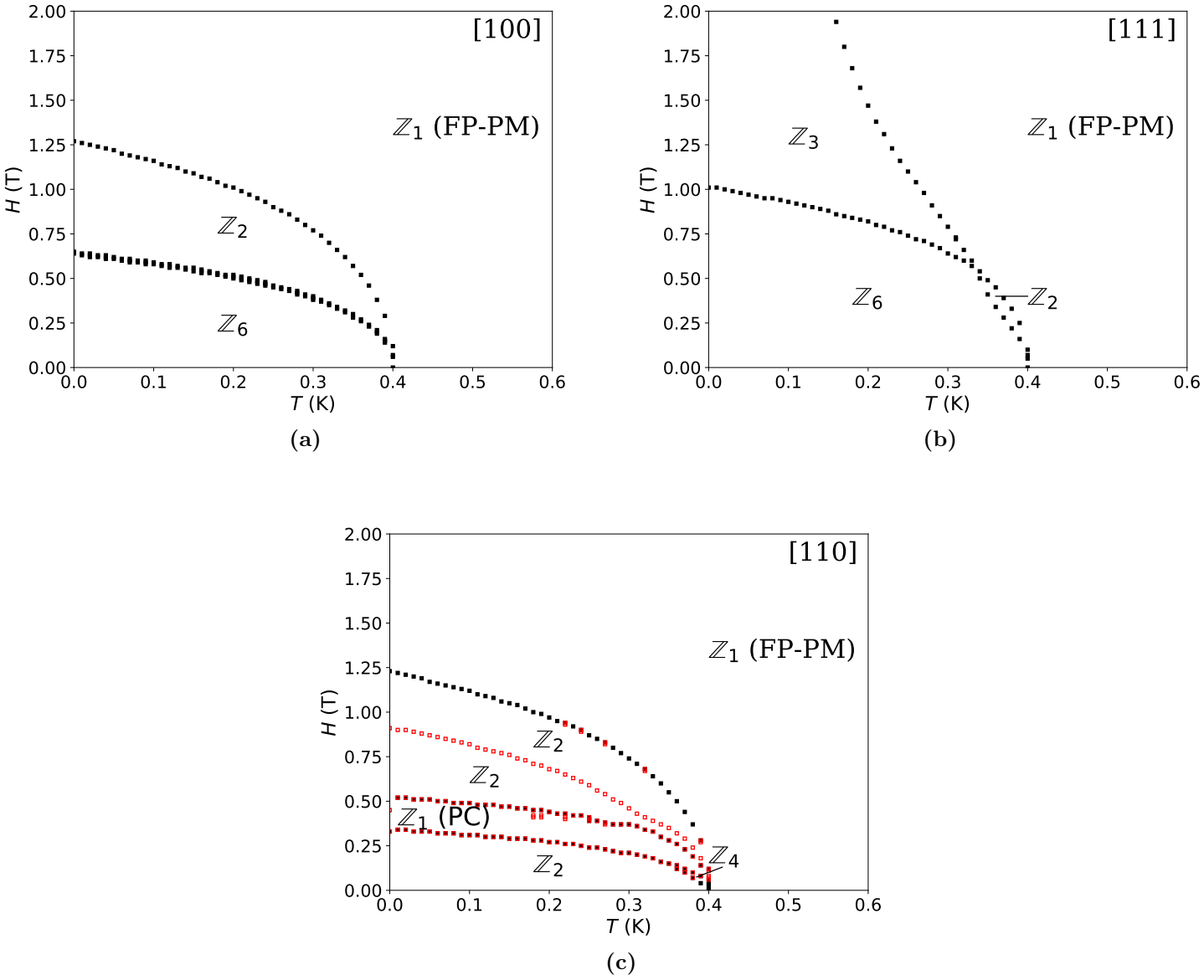

Figure 4.15: Variational mean-field theory phase diagram for an applied field H along the (a) [100], (b) [111], and (c) [110] directions, including long-range dipolar interactions. $\mathbb{Z}_n$ represents the discrete degeneracy of that phase, with black squares indicating phase transitions. Red squares represent a change in which FEPC states minimize the free energy. FP-PM stands for field-polarized paramagnet; PC stands for Palmer-Chalker.

Chapter 5

Conclusion

5.1 Summary

In this thesis, we found that single crystals of $Er_2Sn_2O_7$ display multiple reentrant phenomena under an applied magnetic field $\boldsymbol{H}$. Reentrance occurs for applied fields along the [100], [110], and [111] directions. In all three cases, this reentrant behavior is captured by classical Monte Carlo simulations. There is not precise agreement between experiments and simulations for the critical fields, critical temperatures, and locations of reentrance; however, the ability of classical Monte Carlo simulations to *qualitatively* capture the locations of the reentrant lobes motivated us to look into thermal fluctuations as the origin of reentrance. Using a combination of mean-field theory and classical spin-wave expansions, it was shown that the microscopic origin of reentrance is multiphase competition. In particular, this could happen in two ways: (1) multiphase competition induced by the applied field $\boldsymbol{H}$, as it brought two PC phases into proximity with one another, or (2) multiphase competition from $Er_2Sn_2O_7$'s proximity to the ψ_2 phase in its zero-field phase diagram. Regardless of which mechanism gives rise to multiphase competition, the result is the same: strong thermal fluctuations arise in the form of soft modes in the classical spin-waves. These strong thermal fluctuations entropically stabilize the ordered phase, giving a free-energy advantage of the ordered phase over the disordered phase. This leads to an *increase* in T_c as H increases through certain ranges of values. On the grounds of mean-field theory, it was argued that long-range dipolar interactions would not change this explanation of reentrance.

5.2 Future Work

There are a number of questions and new avenues of exploration that this work opens up, both with $Er_2Sn_2O_7$ and beyond.

Firstly, it is striking that simulations and experiments are able to reach such a level of agreement. The exchange parameters used for $Er_2Sn_2O_7$ are based on previous experiments on powder samples [48, 49], which are not expected to be as accurate as exchange parameters drawn from single crystal experiments. It is of immediate interest to use conventional methods (e.g. spin-wave fits to inelastic neutron scattering data [5, 33]) to establish more precise values of the exchange parameters. This, combined with an inclusion of long-range dipolar interactions in classical Monte Carlo simulations, may lead to much stronger and more quantitative agreement between simulations and experiment. It would also allow more precise theoretical modelling of the behavior of $Er_2Sn_2O_7$, such as the role of quantum fluctuations in the zero- or low-field states (to be discussed further below). Nevertheless, the microscopic mechanism proposed to explain reentrance in this thesis is expected to be robust against changes in the exchange parameters.

Secondly, it is interesting to contrast reentrance in $Er_2Sn_2O_7$ with reentrance in $Yb_2Ti_2O_7$. In the latter compound, reentrance was originally found experimentally under an applied field along the [111] direction [34]. The failure of classical Monte Carlo simulations to capture this reentrant behavior led to the conclusion that either long-range dipolar interactions (not included in the simulations) or quantum fluctuations are the origin of reentrance [34]. Exact diagonalization methods confirmed quantum fluctuations as the underlying mechanism [43], which is expected to be the same mechanism for the reentrance that was later found along the [110] direction [35]. At first glance, it may seem surprising that our explanation for reentrance in $Er_2Sn_2O_7$ comes from thermal fluctuations. $Er_2Sn_2O_7$ is suspected to experience strong quantum fluctuations, likely enhanced by its proximity to a zero-field phase boundary (as is also suspected for $Yb_2Ti_2O_7$) [5, 24]. This observation alone warrants an investigation into the role that quantum fluctuations play in the (H, T) phase diagram of $Er_2Sn_2O_7$; more accurate exchange parameters would greatly aid this exploration. This would also help generate a greater quantitative agreement between theory and experiment for $Er_2Sn_2O_7$'s (H, T) phase boundary. This may be especially true at zero- and low-field values, where the discrepancy between T_c from experiments and classical Monte Carlo simulations is significant and likely due to quantum fluctuations. However, there are further reasons to investigate the role of quantum fluctuations in the zero- or low-field behavior of $Er_2Sn_2O_7$. In the case of $Yb_2Ti_2O_7$, T_c begins to increase as soon as the applied field is turned on [34]. This is consistent with quantum fluctuations being the origin of reentrance, since they are suppressed as soon as the field is turned on, allowing T_c to increase

immediately. In classical Monte Carlo simulations on $Er_2Sn_2O_7$, as shown in Figure 4.1, this is clearly not the case: T_c either decreases or remains approximately the same in most regions below the reentrant lobes. However, the experimental data for $Er_2Sn_2O_7$ is less clear cut at the lowest field values. Given that the heat capacity signatures are broad, it may be possible that T_c is increasing as soon as H turns on in these experiments. This may be a signature of the suppression of strong quantum fluctuations by a field, as seen in $Yb_2Ti_2O_7$. Even though thermal fluctuations eventually overpower quantum fluctuations (as evidenced by classical Monte Carlo simulations capturing reentrance), it would be of interest to explore how quantum fluctuations are operating near criticality (i.e. the disordered-to-ordered phase transition) for small values of H.

Moving beyond $Er_2Sn_2O_7$, it is clear that our microscopic mechanism for reentrance may apply to other magnetic materials. Some of the relevant ingredients would be multiple phase transitions under an applied magnetic field and within the ordered phase, with stronger thermal flucutations at these phase transitions than are available in zero field. The simplest place to look for this is another pyrochlore magnet with a PC ground state, since some of the reentrant lobes in $Er_2Sn_2O_7$ merely result from $Er_2Sn_2O_7$'s PC ground state. In this regard, one may consider investigating $Gd_2Sn_2O_7$ under an applied magnetic field. The synthesis method discussed in Chapter 1 allows single crystals of $Gd_2Sn_2O_7$ to be grown, and it has already been mentioned that $Gd_2Sn_2O_7$ orders into the PC state. As such, one may expect to find a reentrant (H, T) phase diagram experimentally. Another case of interest is the cousin material to $Gd_2Sn_2O_7$, namely, $Gd_2Ti_2O_7$. As mentioned in Chapter 1, despite also being a pyrochlore Heisenberg antiferromagnet with non-negligible long-range dipolar interactions like $Gd_2Sn_2O_7$, $Gd_2Ti_2O_7$ instead orders into a partially-disordered phase. Yet, heat capacity measurements on $Gd_2Ti_2O_7$ [50] have already established reentrant (H, T) phase diagrams along the [111] and [110] field directions, as shown in Figure 5.1. It is striking to note that reentrance occurs whenever there is a corresponding zero-temperature transition for some critical field value H_c. Moreover, in a [112] field, there is no zero-temperature transition and no reentrant behavior. It is therefore likely that the mechanism proposed to explain reentrance in this thesis may also help explain reentrance in $Gd_2Ti_2O_7$, even if $Gd_2Ti_2O_7$ does not have a PC ground state. As well, previous studies on reentrant spin glasses [54] have indicated that partial disorder can be an important ingredient for reentrance. As mentioned in Section 1.3, $Gd_2Ti_2O_7$ orders into a partially-disordered phase. $Gd_2Ti_2O_7$ would therefore be interesting to study in order to determine the interplay between partial disorder and zero-temperature transitions as concerns reentrance. Lastly, one may look beyond pyrochlore magnets altogether. Frustrated magnets in general may have multiple phase transitions under an applied magnetic field, given the competition between exchange and Zeeman energy scales. Another place

to look may thus be triangular-lattice-based antiferromagnets. For example, recent ac susceptibility and heat capacity measurements on $Ba_2La_2MnW_2O_{12}$ [77] find a crude reentrant phase boundary with a corresponding transition at zero temperature and finite field, as shown in Figure 5.2. It is likely that strong thermal fluctuations originating from the zero-temperature transition are the cause of the finite-temperature reentrance.

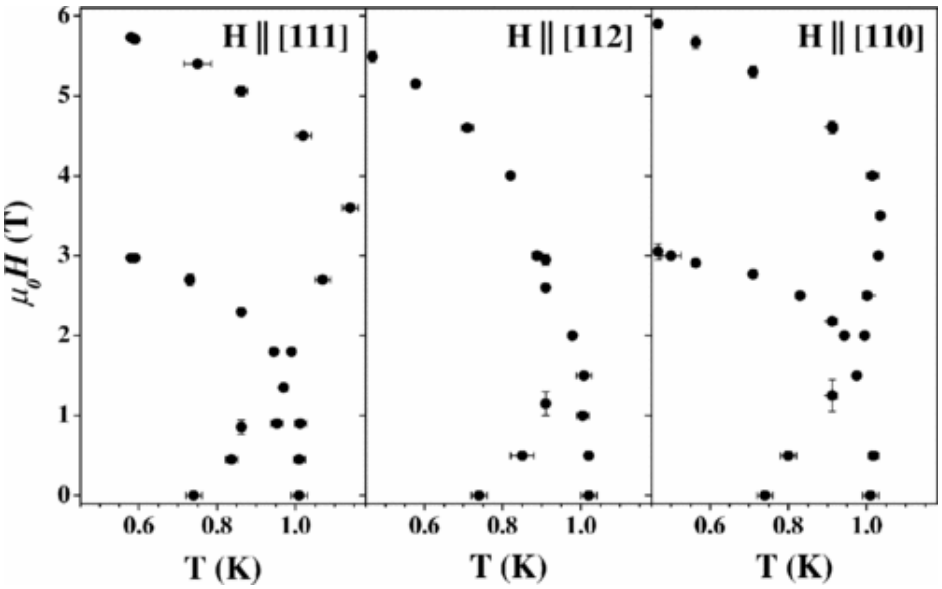

Figure 5.1: Phase diagram of $Gd_2Ti_2O_7$ under applied magnetic fields in the [111], [112], and [110] directions, as determined by specific heat measurements. Reprinted figure with permission from Petrenko *et al.*, Phys. Rev. B **70**, 012402 (2004). Copyright 2020 by the American Physical Society.

Lastly, it should be noted that reentrance is a ubiquitous phenomena that occurs beyond magnetism. There are examples of reentrance occuring in liquid mixtures [55], liquid crystals [58], superconductors [59], graphene [57], and protein systems [60]. The mechanism of reentrance for $Er_2Sn_2O_7$ may not apply to these systems. However, it is clear that our efforts to understand the microscopic origins of reentrance for $Er_2Sn_2O_7$ has given us a better understanding of the physical ingredients at play within it, as well as a broader understanding of important ingredients in the behavior of other magnetic materials. Our work therefore serves as a motivation to uncover the microscopic mechanism for reentrance in other systems, which may yield similar benefits.

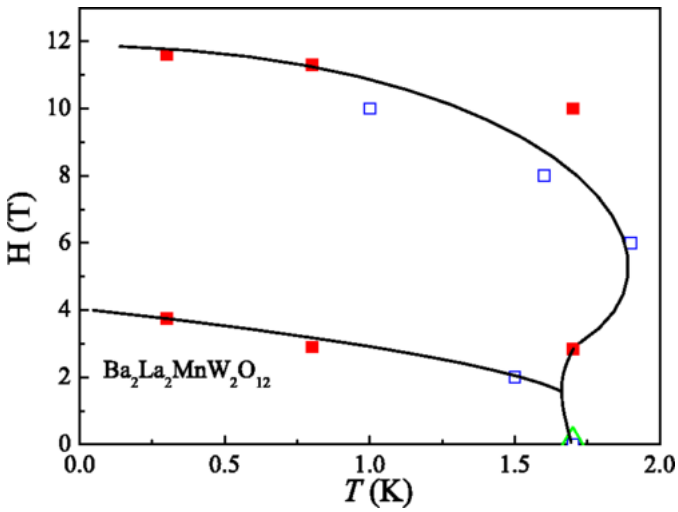

Figure 5.2: Phase diagram of $Ba_2La_2MnW_2O_{12}$, as determined by heat capacity measurements (green triangle), temperature derivatives of the ac susceptibility (red squares), and field derivatives of the ac susceptibility (blue squares). Reprinted figure with permission from Rawl *et al.*, Phys. Rev. B **95**, 174438 (2017). Copyright 2020 by the American Physical Society.

PART II –
Machine Learning of Quenched Gauge Symmetries

Chapter 6

Introduction

6.1 Machine Learning and Condensed Matter Physics

Machine learning refers to a set of techniques that are able to identify and characterize patterns in datasets, with or without information from the user. These techniques are incredibly useful in the field of physics, such as for the purpose of analyzing experimental data [78–80] or more deeply exploring connections between various areas of statistical mechanics [80–82]. In general, the intersection of machine learning and physics is promising because of the mathematical models that underlie the behavior of physical systems. This is especially true for the field of condensed matter physics, where systems with a large number of constituent particles behave according to the laws of statistical mechanics [80–82]. Although machine learning was applied to condensed matter and materials physics before [83–85], the application of machine learning to condensed matter physics rose to prominence with two seminal papers on the Ising model [86, 87]. These demonstrated the capabilities of various types of machine learning methods for identifying thermodynamic properties such as critical temperatures and order parameters. A number of machine learning techniques have been applied to a variety of systems since then. The techniques can roughly be categorized as (i) supervised (where input from the user is given to the machine to assist it in learning underlying patterns) [88–101], (ii) unsupervised (where the machine determines its own classification scheme for the data without any assistance) [99–106], and (iii) reinforcement (where the machine attempts to learn a course of action that will maximize some reward) [107, 108]. The applications of these techniques have been similarly broad, such as using reinforcement learning to generate loop moves in Monte Carlo simulations [107], detecting hidden order parameters in frustrated spin systems [90, 92],

learning topological phases and defects [91], or identifying phase transitions in many-body localized systems [89].

Despite the range of techniques available and the variety of systems studied, the major thrust of machine learning applications to condensed matter physics has remained unchanged: the identification of phases, phase transitions, and thermodynamic characteristics such as order parameters. Given that machine learning is able to learn underlying patterns from the simulated models, one may ask if it is possible to go beyond learning thermodynamic quantities. In particular, one may ask: is it possible for machine learning to provide insight into hidden or unknown properties of the *model*? Such an idea is certainly plausible; the simulated models are mathematical in nature, and machine learning seems capable of understanding mathematical patterns.[1] Such an idea may also be useful for further machine learning applications. Many such applications have benefitted from exploiting symmetries of the system, such as (for example) using translational symmetry and locality to support convolutional neural networks [86] or employing symmetry breaking to assist in order parameter identification [90, 92, 94]. If machine learning is capable of providing insight into the simulated model, then in a similar vein, this information could potentially supplement other machine learning techniques to make their learning more powerful or efficient.

6.2 Motivation and Outline

In this thesis, we explore the question posed above – namely, whether machine learning techniques can provide insight into properties of a model itself with little or no assistance. In order to explore this question, we first require appropriate models to study. Models possessing gauge symmetries are excellent candidates, as they may seem complex but are simplified by a controlled mathematical transformation. We choose to study the Mattis Ising spin glass (MISG) and Mattis XY gauge glass (MXYGG) models [111, 112]. These models possess random bond interactions in their Hamiltonians that make an analytical approach seem intractable or significantly complicated. However, under a suitable gauge transformation[2], these two models can be mapped onto the ferromagnetic Ising and XY models. In this manner, the MISG and MXYGG models are prime candidates for our proposed exploration. With these models in hand, our main question can be rephrased as: is machine learning capable of determining that the MISG and MXYGG models are simply

[1] This is suggested insofar as machine learning shares deep and rich connections with the mathematics of statistical physics [80, 81, 109, 110].

[2] This suitable gauge transformation is described in Chapter 7.

"disguised" versions of the ferromagnetic Ising and XY models – without being given any information about this hidden underlying equivalence? In other words, can machine learning determine the (quenched) gauge transformation that maps the disordered models onto their ferromagnetic counterparts?

With the appropriate models in one hand, we secondly require a suitable machine learning technique in the other. Since we would like to determine if machine learning can provide insights into our models *without* prior information, we require an unsupervised machine learning technique. As well, to determine if this technique can learn the gauge symmetries of our model, we require a technique whose classification scheme for the data can be *interpreted*. Generally, machine learning techniques possess a trade-off between interpretability (i.e. the ability to see what the technique is learning and how) and scalability (i.e. how large of a dataset is required for the technique to properly learn the salient features) [93, 101, 113]. For example, neural-network-based techniques can learn complicated patterns from large datasets, but exactly what and how they learn is difficult to expose [101, 113]. For this reason, we use the well-established Principal Component Analysis (PCA) method [87, 102, 103, 114]. PCA is a simple method that can be related to the spectral decomposition theorem of linear algebra. The matrix diagonalization of the inputted dataset can therefore be slow for very large datasets. However, PCA provides a clear interpretation for what and how it is learning from the dataset. This makes it a suitable choice for our original exploration of machine learning of quenched gauge symmetries.

The outline is as follows. In Chapter 7, we discuss the MISG and MXYGG models. We demonstrate the gauge transformation that maps them onto the ferromagnetic Ising and XY models, respectively. In Chapter 8, we explain PCA – specifically, how the method works, how the data is provided, and the quantities that PCA learns to characterize the dataset. In Chapter 9, we first review what PCA finds in the ferromagnetic Ising and XY models. We then compare this with what PCA learns from the MISG and MXYGG models, demonstrating that the gauge transformations and symmetries can indeed be learned. Lastly, Chapter 10 summarizes the work and discusses future avenues of exploration.

Chapter 7

Models

7.1 The Mattis Ising Spin Glass (MISG) Model

The Mattis Ising spin glass (MISG) model describes a disordered spin system which, under the right conditions, can actually be mapped onto the ferromagnetic Ising model via a so-called "Mattis gauge transformation" [111, 112]. Consider the Hamiltonian

$$H = -\sum_{\langle ij \rangle} J_{ij} \sigma_i^z \sigma_j^z, \tag{7.1}$$

on a square lattice, where $\{J_{ij}\}$ are quenched[1] exchange parameters that take the values $\pm J$ randomly, $\{\sigma_i^z\}$ are dynamical spin variables that can take the values ± 1, and the sum is performed over all pairs of nearest neighbors. This Hamiltonian describes a disordered system given the random selection of exchange parameters; however, suppose these exchange parameters are constrained to satisfy

$$P \equiv \prod_{\langle ij \rangle \in \square} J_{ij} > 0, \tag{7.2}$$

that is, the product of exchange parameters on any given square plaquette is positive. Under this condition, Eq. (7.1) is the MISG model; it can be mapped onto the ferromagnetic Ising model as follows. By defining on-site gauge variables $\{\epsilon_i\}$ that can take values ± 1, the

[1] By "quenched", we mean that the values of $\{J_{ij}\}$ do not change. Instead, a particular instantiation of $\{J_{ij}\}$ is initially and arbitrarily chosen (so long as it satisfies Eq. (7.2)) and *fixed* (that is, frozen in time), so that these random variables possess no dynamics.

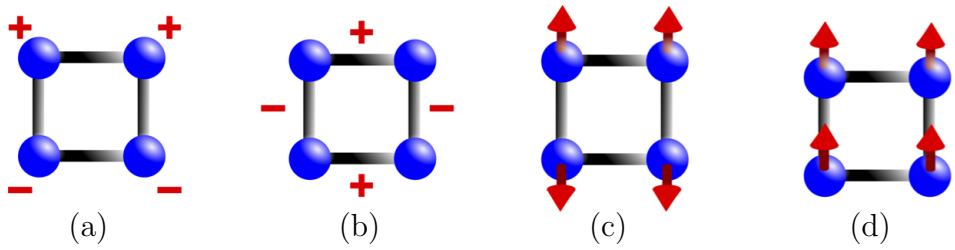

Figure 7.1: Example of the Mattis gauge transformation. (a) Choices of gauge variables $\{\epsilon_i\}$ on each site. (b) Resulting signs of $\epsilon_i\epsilon_j$ on each bond. (c) Example of a ground state configuration for σ_i^z variables, for the bond interactions given in (b). Note that the Hamiltonian is written with $-J_{ij}$. (d) Resulting spin configuration in terms of τ_i^z variables (i.e. the multiplication of (a) with (c)). [Figure provided by Daniel Lozano-Gómez.]

exchange parameters can be rewritten as $J_{ij} = \epsilon_i\epsilon_j J$. This trivially satisfies Eq. (7.2).[2,3] Then, Eq. (7.1) becomes:

$$H = -\sum_{\langle ij\rangle} J\epsilon_i\sigma_i^z\epsilon_j\sigma_j^z \equiv -\sum_{\langle ij\rangle} J\tau_i^z\tau_j^z. \tag{7.3}$$

Here, we have defined $\{\tau_i^z \equiv \epsilon_i\sigma_i^z\}$ to be new Ising variables that can take values of ± 1 on each site. In terms of the $\{\tau_i^z\}$ variables, the Hamiltonian (7.3) is revealed to be equivalent to a ferromagnetic Ising model, where the order parameter is the "τ–magnetization" $M_\tau = \frac{1}{N}\sum_i \tau_i^z$. This process of applying this gauge transformation – the "Mattis gauge transformation" – to map the MISG model to the ferromagnetic Ising model is depicted in Figure 7.1.

Although the configuration in Figure 7.1c appears disordered in the σ_i^z variables, the application of the Mattis gauge transformation reveals that it actually corresponds to the ordered ferromagnetic phase (with τ–magnetization) of the Ising model. This yields a simple interpretation of the MISG model and the Mattis gauge transformation: although the underlying order is that of an Ising ferromagnet, the $\hat{z}_i$-axis on each site differs, as quantified by the on-site gauge variable ϵ_i. The Mattis gauge transformation can thus be seen as aligning all local $\hat{z}_i$-axes along a global $\hat{z}$ direction.

[2] As well, Eq. (7.2) forces the exchange parameters on a plaquette to either be all 1, all -1, or to have two of each. By defining the on-site gauge variables $\{\epsilon_i\}$, any of these combinations of exchange parameters can be obtained. One can, for example, take all gauge variables on the plaquette to be 1, or take two to be -1, or take three (or one) to be -1.

[3] Since the definition of the on-site gauge variables trivially satisfies the plaquette constraint (7.2), one starts (in simulations of the MISG model) by defining $\{\epsilon_i\}$ rather than working backwards from $\{J_{ij}\}$.

7.2 The Mattis XY Gauge Glass (MXYGG) Model

One can apply an analogous Mattis gauge transformation on the XY model to obtain the Mattis XY gauge glass (MXYGG) model [111]. Consider the Hamiltonian

$$H = -J \sum_{\langle ij \rangle} \cos\left(\Delta\phi_{ij} - A_{ij}\right) \tag{7.4}$$

on a square lattice. Here, J is the exchange constant, $\Delta\phi_{ij} \equiv \phi_i - \phi_j$ is the difference between two angular variables ($\phi_i \in [0, 2\pi)$), and $\{A_{ij}\}$ are random phase factors associated with every bond. Suppose the random phase factors are constrained to satisfy

$$P_{XY} \equiv (\sum_{\langle ij \rangle \in \square} A_{ij}) \bmod 2\pi = 0, \tag{7.5}$$

that is, the sum of phase factors around any given square plaquette is a multiple of 2π. Under this condition, Eq. (7.4) is the MXYGG model; it can be mapped onto the ferromagnetic XY model as follows. The plaquette constraint Eq. (7.5) is trivially satisfied by defining the on-site gauge variables $\{b_i\}$ ($b_i \in [0, 2\pi)$) such that $A_{ij} = b_i - b_j$.[4] With this definition, Eq. (7.4) becomes:

$$H = -J \sum_{\langle ij \rangle} \cos\left((\phi_i - b_i) - (\phi_j - b_j)\right) \equiv -J \sum_{\langle ij \rangle} \cos\left(\Delta\theta_{ij}\right). \tag{7.6}$$

Here, we have defined $\{\theta_i \equiv \phi_i - b_i\}$ to be the new XY variables ($\theta_i \in [0, 2\pi)$), revealing that the Hamiltonian Eq. (7.6) is equivalent to a ferromagnetic XY model. Although the XY model is known to possess only quasi-long-range order with no magnetization at finite temperatures [91], one can still define a magnetization vector for finite-sized systems as $\boldsymbol{M} = \langle \sum_i (\cos(\theta_i), \sin(\theta_i)) \rangle$. For the MXYGG model, this magnetization vector is:

$$\begin{aligned} M_x &= \langle \sum_i \cos(\phi_i)\cos(b_i) + \sin(\phi_i)\sin(b_i) \rangle, \\ M_y &= \langle \sum_i \sin(\phi_i)\cos(b_i) - \cos(\phi_i)\sin(b_i) \rangle. \end{aligned} \tag{7.7}$$

Unlike the model in the thermodynamic limit, any finite-size simulation of the XY model will possess a non-zero magnetization norm $\langle |\boldsymbol{M}| \rangle$ [91].

[4] As with the MISG model, since the plaquette constraint (7.5) is trivially satisfied by this definition, one starts (in simulations of the MXYGG model) by defininining the on-site gauge variables $\{b_i\}$ first.

As with the MISG model, a simple interpretation can be made about the Mattis gauge transformation of the XY model. Each site possesses a different local $\hat{x}_i$-axis from which the angle ϕ_i is measured; these axes are quantified by the on-site gauge variables b_i, and the Mattis gauge transformation converts the MXYGG model into a ferromagnetic XY model by aligning all local $\hat{x}_i$-axes (and $\hat{y}_i$-axes) along a global $\hat{x}$ (and $\hat{y}$) direction.

Chapter 8

Methods

8.1 Principal Component Analysis (PCA)

The Principal Component Analysis (PCA) can be categorized as an unsupervised machine learning method. Qualitatively, when given a dataset, PCA determines the linear combinations of the data that best characterize the correlations within the dataset as a whole. In this way, since it reduces the complexity of the full dataset to just those most important linear combinations, PCA is also known as a dimensional reduction technique [104]. Quantitatively, the procedure is as follows. Suppose that the data is obtained from an N-site system, with a variable x_i associated with every site ($i = 1, \ldots, N$). One such configuration of the variables would be $\{x_i(T_1)\}$, although there can in general be n sets of configurations $\{x_i(T_j)\}$ ($j = 1, \ldots, n$).[1] The full dataset can then be written as a $n \times N$ matrix

$$\tilde{X}_{\text{data}} \equiv \begin{pmatrix} \{x_i(T_1)\} \\ \{x_i(T_2)\} \\ \vdots \\ \{x_i(T_n)\} \end{pmatrix} = \begin{pmatrix} x_1(T_1) & x_2(T_1) & \cdots & x_N(T_1) \\ x_1(T_2) & x_2(T_2) & \cdots & x_N(T_2) \\ \vdots & \vdots & \ddots & \vdots \\ x_1(T_n) & x_2(T_n) & \cdots & x_N(T_n) \end{pmatrix}. \tag{8.1}$$

[1] The notation of each configuration being labelled by a variable T_j is used in anticipation of our application, in which T_j will be the temperature at which the system is sampled via Monte Carlo simulations. However, in a general setting, the interpretation of the variable T_j need not be temperature. Note also that the n variables $\{T_j\}$ need not be distinct. For example, we can sample two *distinct* configurations of our system at the *same* temperature T. These two configurations are then labelled by T_1 and T_2 to distinguish them from each other, even though $T_1 = T_2 = T$.

The average of each column of $\tilde{X}_{\text{data}}$ is calculated and subtracted away in order to "center" the data. Explicitly, if $\bar{x}_i \equiv \frac{1}{n}\sum_{j=1}^{n} x_i(T_j)$, this is

$$X_{\text{data}} \equiv \begin{pmatrix} \{x_i(T_1) - \bar{x}_i\} \\ \{x_i(T_2) - \bar{x}_i\} \\ \vdots \\ \{x_i(T_n) - \bar{x}_i\} \end{pmatrix} = \begin{pmatrix} x_1(T_1) - \bar{x}_1 & x_2(T_1) - \bar{x}_2 & \cdots & x_N(T_1) - \bar{x}_N \\ x_1(T_2) - \bar{x}_1 & x_2(T_2) - \bar{x}_2 & \cdots & x_N(T_2) - \bar{x}_N \\ \vdots & \vdots & \ddots & \vdots \\ x_1(T_n) - \bar{x}_1 & x_2(T_n) - \bar{x}_2 & \cdots & x_N(T_n) - \bar{x}_N \end{pmatrix}. \tag{8.2}$$

After this, the $N \times N$ covariance matrix C can be constructed by computing the matrix product $C = X_{\text{data}}^T X_{\text{data}}$. Note that the matrix element C_{ij} is given by

$$C_{ij} = \sum_{k=1}^{n} \left(x_i(T_k) - \bar{x}_i\right)\left(x_j(T_k) - \bar{x}_j\right), \tag{8.3}$$

explicitly showing that the matrix C is measuring the covariance of the variables. In the remainder of this thesis, we assume that X_{data} has already been centered and do not explicitly write the subtraction of the average $\bar{x}_i$. Note that, in our applications, the rows of X_{data} correspond to different temperatures whereas the columns correspond to different sites.

The covariance matrix C is diagonalized in order to find the "explained variance ratios" $\{\lambda_k\}$ (i.e. the normalized eigenvalues) and the "principal components" $\{\boldsymbol{u}^{(k)}\}$ (i.e. the eigenvectors).[2] Note that this is just an application of the spectral decomposition theorem. Since C is a real, symmetric matrix, we are essentially using a decomposition into eigenvectors to write

$$C = \sum_{k=1}^{N} \lambda_k \left|\boldsymbol{u}^{(k)}\right\rangle \left\langle \boldsymbol{u}^{(k)}\right|, \tag{8.4}$$

where $\left|\boldsymbol{u}^{(k)}\right\rangle \left\langle \boldsymbol{u}^{(k)}\right|$ represents the projection onto the eigenspace spanned by the eigenvector $\boldsymbol{u}^{(k)}$. In this way, PCA attempts to approximately reconstruct the correlations in the dataset (and, indeed, the covariance matrix itself) through a weighted sum of the outer product of eigenvectors. The explained variance ratios are the weights in this sum. This means that the principal components with the highest explained variance ratios are the principal components that best explain the correlations in the dataset.

One can also define the projection $\ell^{(k)}(T_j)$ of the j^{th} configuration $\{x_i(T_j)\}$ onto the k^{th} principal component $\boldsymbol{u}^{(k)}$:

$$\ell^{(k)}(T_j) = \sum_i u_i^{(k)} x_i(T_j). \tag{8.5}$$

[2] Note that the eigenvectors can be rescaled by any factor (e.g. the system size L) for convenience.

The projections $\ell^{(k)}(T_j)$ are the linear combinations of the data that PCA uses to characterize the full dataset. $\boldsymbol{u}^{(k)}$ quantifies which linear combinations to take, whereas the explained variance ratios $\{\lambda_k\}$ quantify the relative importance of the projection $\ell^{(k)}(T_j)$. In our case where i is a site index, Eq. (8.5) implies that the components of $\boldsymbol{u}^{(k)}$ contain site-dependent information.

Lastly, note also that the principal component $\boldsymbol{u}^{(k)}$ is an eigenvector of C, which is an $N \times N$ matrix and hence does not have an explicit dependence on T_j (as seen in Eq. (8.3)). In this sense, the principal components are determined by considering how the variables $\{x_i\}$ behave across *all* T_j (again seen in Eq. (8.3)). However, we can reconstruct a good approximation of the T_j dependence of the dataset by using Eq. (8.5) for the most important principal components. Therefore, although the principal components themselves do not depend on temperature, the projections (which PCA uses to characterize the dataset) defined by Eq. (8.5) do. This dependence is "inherited" from the temperature dependence of the dataset $\{x_i(T_j)\}$. So, we can see the most important temperature-dependent features by calculating $\ell^{(k)}(T_j)$ for the most important principal components and for all T_j.

Chapter 9

Results

9.1 PCA on the Ferromagnetic Ising Model

To study the ferromagnetic Ising model with PCA, the dataset is generated via classical Monte Carlo simulations with a single spin-flip update move. A lattice size of $L = 30$ is taken, giving $N = 900$ spins. The system is sampled for 50 equally-spaced temperatures in the range $[J, 4J]$. 3×10^4 equilibration sweeps are performed at every temperature, followed by 3×10^4 measurement sweeps. Measurements are taken every 100 measurement sweeps, giving 300 measurements at every temperature [1] for a total of $n = 50 \times 300 = 1.5 \times 10^4$ configurations.[2] In reference to Eq. (8.2), the variable x_i is the Ising spin variable τ_i^z.[3] Altogether, the data matrix for this dataset is:

$$X_{\text{data}} \equiv \begin{pmatrix} \{x_i(T_1)\} \\ \{x_i(T_2)\} \\ \vdots \\ \{x_i(T_n)\} \end{pmatrix} = \begin{pmatrix} \{\tau_i^z(T_1)\} \\ \{\tau_i^z(T_2)\} \\ \vdots \\ \{\tau_i^z(T_n)\} \end{pmatrix} \tag{9.1}$$

[1] Note that 300 configurations are sampled at *each* temperature. Hence, the temperatures $T_1, T_2, \ldots, T_n$ in Eq. (8.2) are not unique.

[2] Note that every second configuration has all spins reversed. In this way, we guarantee that half the dataset (of the ordered phase) corresponds to a positive magnetization and the other half corresponds to a negative magnetization.

[3] We use τ_i^z to refer to the "pure" Ising variable (as in the rightmost side of Eq. (7.3)), since this is the variable that the MISG model should be mapped onto. We reserve σ_i^z to refer to the MISG Ising variable (as in Eq. (7.1)).

$$= \begin{pmatrix} \tau_1^z(T_1) & \tau_2^z(T_1) & \cdots & \tau_N^z(T_1) \\ \tau_1^z(T_2) & \tau_2^z(T_2) & \cdots & \tau_N^z(T_2) \\ \vdots & \vdots & \ddots & \vdots \\ \tau_1^z(T_n) & \tau_2^z(T_n) & \cdots & \tau_N^z(T_n) \end{pmatrix}. \tag{9.2}$$

PCA is then performed on this matrix.

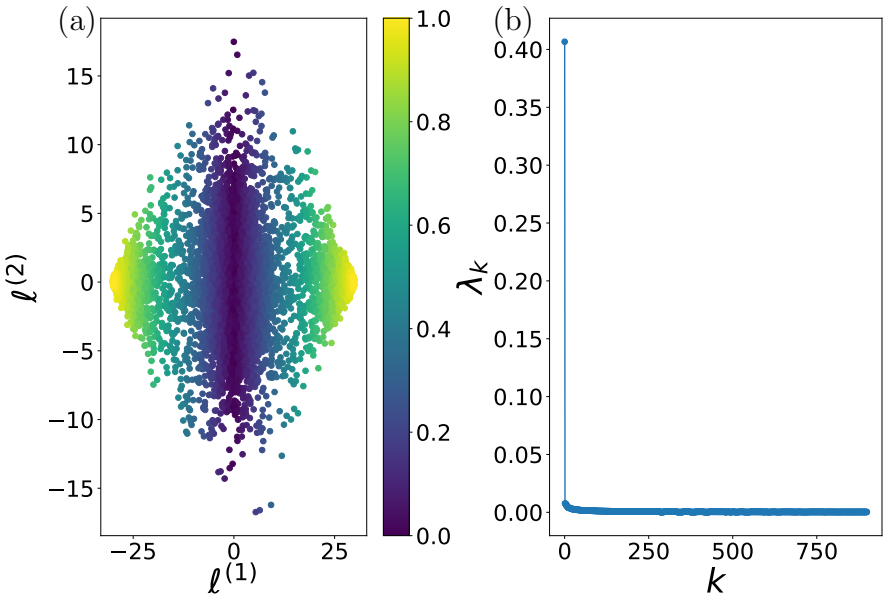

Figure 9.1: Results of PCA applied to the ferromagnetic Ising model. (a) The projections $\ell^{(1)}$ versus $\ell^{(2)}$, revealing how PCA clusters the data. Data points (which represent distinct spin configurations) are colored according to the absolute value of the magnetization associated with that spin configuration. (b) The explained variance ratios for all principal components.

Figures 9.1a visually demonstrates how PCA clusters the data, plotting the projections $\ell^{(1)}$ and $\ell^{(2)}$ against each other for all T_j. In particular, every point in this plot represents a single spin configuration at a temperature T_j. Each point therefore corresponds to one of the n configurations and is colored according to absolute value of the magnetization of that spin configuration.[4] PCA categorizes the full dataset by separating it into three

[4]We color the data points according to the magnetization as a proxy of the temperature T_j. High (low) temperatures correspond to low (high) magnetizations and blue (yellow) points. The reason for using the magnetization rather than the temperature is that there is a much smaller range of allowed values of the magnetization, hence showing the color differences more clearly. It also allows for a simple interpretation, given later in this section.

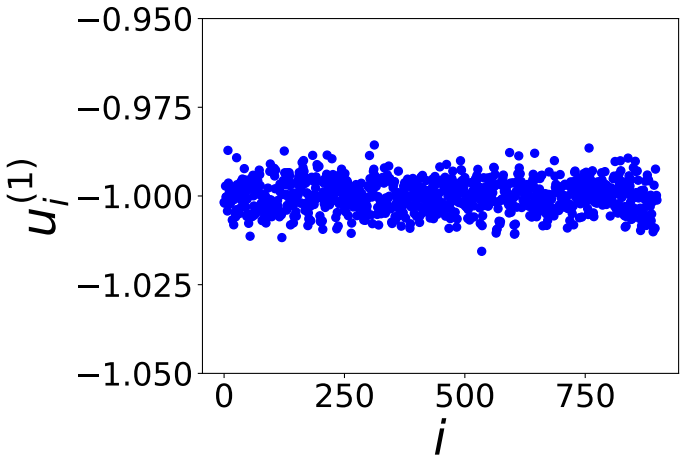

Figure 9.2: Components of $\boldsymbol{u}^{(1)}$, scaled by the system size L, for PCA applied to the ferromagnetic Ising model. No data for $\boldsymbol{u}^{(1)}$ outside the range $-1.05 < u_i^{(1)} < -0.95$ is obtained.

major "clusters", with one cluster (corresponding to high temperatures) in the middle and two clusters (corresponding to low temperatures) placed symmetrically on either side. This clustering occurs predominantly along the $\ell^{(1)}$ direction, in the sense that there is no significant variation in color (i.e. magnetization or temperature) along the $\ell^{(2)}$ direction. Hence, Figures 9.1a indicates that PCA characterizes the dataset mostly through the projection $\ell^{(1)}$.

This is further confirmed by Figure 9.1b. This displays the explained variance ratios and hence indicates which principal components and projections are most important. The first explained variance ratio is significantly larger than the rest; this implies that the first principal component is sufficient to characterize the majority of the dataset, whereas the further principal components contribute negligibly to this characterization. This explains why Figure 9.1a shows the most significant temperature-dependent separation of data along $\ell^{(1)}$, but not along $\ell^{(2)}$: the latter projection is not as capable at quantifying correlations in the dataset as the former.

Figure 9.2 displays the vector components of this first principal component $\boldsymbol{u}^{(1)}$. After scaling this eigenvector by the system size L, it is clear that each component of the

eigenvector is approximately[5] equal to -1.[6] In reference to Eq. (8.5), this implies that

$$\ell^{(1)}(T_j) = \sum_i u_i^{(1)} \tau_i^z(T_j) = \sum_i (-1)\tau_i^z(T_j) \propto \sum_i \tau_i^z(T_j). \tag{9.3}$$

However, this is just the expression for the magnetization M_τ of the system! Altogether, PCA is able to sufficiently characterize the full dataset by categorizing each configuration according to the τ-magnetization of that configuration. This is quantitatively verified in Figure 9.3, where the Ising magnetization is calculated from the classical Monte Carlo simulation and compared to $\ell^{(1)}(T_j)$.[7]

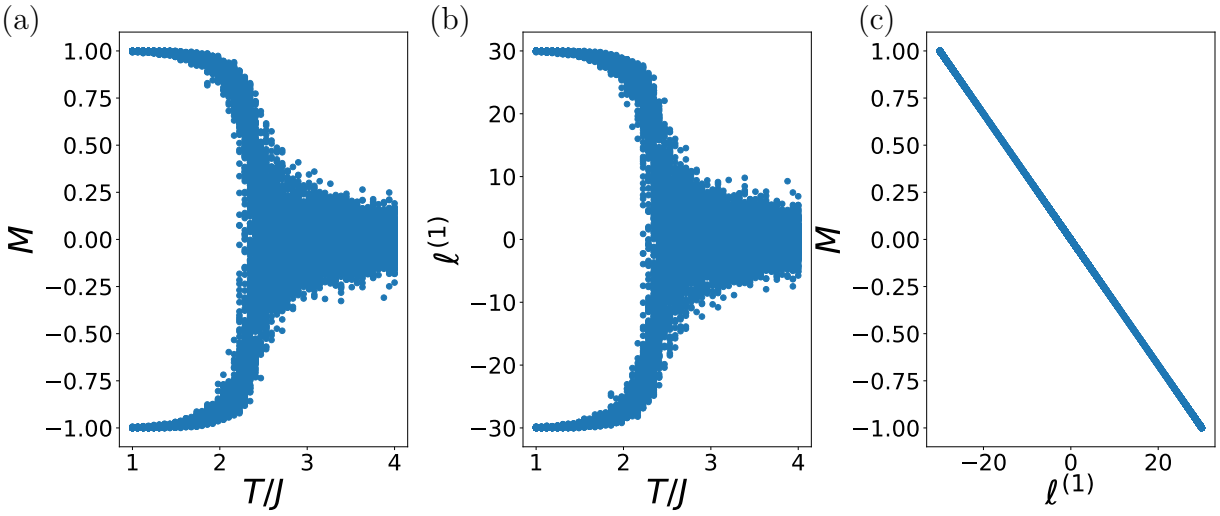

Figure 9.3: Results of PCA applied to the ferromagnetic Ising model. (a) Magnetization of the Ising model computed from Monte Carlo simulations as a function of temperature T/J. (b) Projection $\ell^{(1)}$ learned by PCA as a function of temperature T/J. (c) Magnetization from Monte Carlo simulations versus the learned projection $\ell^{(1)}$.

We now return to Figure 9.1a. In light of the above analysis, an interpretation is easily provided. The three clusters (central high-temperature cluster and peripheral low-temperature clusters) correspond to the three possible τ-magnetizations that can be found: approximately no τ-magnetization in the paramagnetic phase, or a τ-magnetization of ± 1

[5] Figure 9.2 shows the spread of the data away from $u_i^{(1)} \sim -1$, due to numerical errors of the PCA method. However, the fluctuations are minimal, so each $u_i^{(1)}$ is approximately -1.

[6] Note that the components being equal to -1, and not 1, is not a concern: there is a global $\mathbb{Z}_2$ symmetry in the model, so PCA is expected to learn one or the other.

[7] Recall that every second configuration out of all n configurations has spins reversed, in order to obtain ordered phases with both positive and negative magnetizations.

in the two possible ferromagnetic phases. The two symmetrically-placed low-temperature clusters can therefore be considered as a reflection of the $\mathbb{Z}_2$ symmetry relating the two possible ferromagnetic ground states of the Ising model.

The characterization of the full dataset into three clusters can also be understood with a simple toy model. Consider a two-spin system (τ_1^z, τ_2^z), where the paramagnetic phase has the configuration $(1, -1)$ (or vice-versa) and the ferromagnetic phase has the configuration $(1, 1)$ (or $(-1, -1)$). The set of all possible configurations can be plotted in the $\tau_1^z - \tau_2^z$ plane, as well as the first principal component $\boldsymbol{u}^{(1)} = (1, 1)$; this is shown in Figure 9.4. When all possible configurations are projected onto the first principal component, the result is three clusters along the axis defined by the principal component, displayed in Figure 9.5. All high-temperature paramagnetic configurations are projected onto the centre of the axis, whereas the low-temperature ferromagnetic configurations are projected onto the symmetric ends. For the full system of N spins, the interpretation is analogous: all possible spin configurations in the N-dimensional phase space are projected onto the first principal component, corresponding to the calculation of the system's τ-magnetization. This projects all high-temperature configurations onto a single paramagnetic cluster, while projecting all low-temperature configurations onto two possible ferromagnetic clusters.

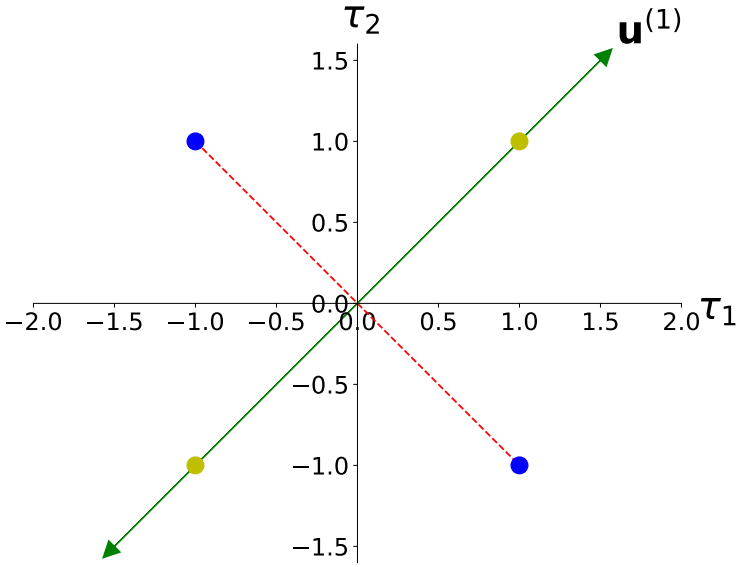

Figure 9.4: Toy model characterization of PCA applied to the ferromagnetic Ising model. Yellow (blue) circles represent ferromagnetic (antiferromagnetic) configurations of the Ising variables (τ_1, τ_2). The green vector represents the principal component $\boldsymbol{u}^{(1)}$. The red dotted line represents the projection onto this principal component.

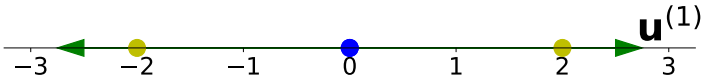

Figure 9.5: Toy model characterization of how PCA classifies the phases of the ferromagnetic Ising model. Yellow (blue) circles represent ferromagnetic (antiferromagnetic) configurations of the Ising variables (τ_1, τ_2). The green vector represents the principal component $\boldsymbol{u}^{(1)}$. Note that PCA clusters the ferromagnetic configurations into two peripheral circles (related by a $\mathbb{Z}_2$ symmetry) and the antiferromagnetic configurations into a central circle.

9.2 PCA on the Ferromagnetic XY Model

To study the ferromagnetic XY model with PCA, the dataset is generated via classical Monte Carlo simulations with a single spin-flip update move.[8] A lattice size of $L = 30$ is taken, giving 900 spins. Since these are planar spins, they can each be quantified by a singular angular variable θ_i[9] and decomposed into their x and y components, $\cos(\theta_i)$ and $\sin(\theta_i)$ respectively. The system is sampled for 50 equally-spaced temperatures in the range $[0.2J, 1.8J]$. 5×10^4 equilibration sweeps are performed at every temperature, followed by 5×10^4 measurement sweeps. Measurements are taken every 100 measurement sweeps, giving 500 measurements at every temperature for a total of $n = 50 \times 500 = 2.5 \times 10^4$ configurations.[10] The data matrix for this dataset can take three forms, depending on if the x component, y component, or both components of the spins are provided. When only one component is provided, $N = 900$ and the data matrices take the form:

$$X_{\text{half}-x} \equiv \begin{pmatrix} \{\cos(\theta_i(T_1))\} \\ \{\cos(\theta_i(T_2))\} \\ \vdots \\ \{\cos(\theta_i(T_n))\} \end{pmatrix}, \quad X_{\text{half}-y} \equiv \begin{pmatrix} \{\sin(\theta_i(T_1))\} \\ \{\sin(\theta_i(T_2))\} \\ \vdots \\ \{\sin(\theta_i(T_n))\} \end{pmatrix}. \tag{9.4}$$

When both components are provided, $N = 1800$ and the data matrix takes the form:

$$X_{\text{full}} \equiv \begin{pmatrix} \{\cos(\theta_i(T_1))\} & \{\sin(\theta_i(T_1))\} \\ \{\cos(\theta_i(T_2))\} & \{\sin(\theta_i(T_2))\} \\ \vdots & \vdots \\ \{\cos(\theta_i(T_n))\} & \{\sin(\theta_i(T_n))\} \end{pmatrix}. \tag{9.5}$$

Note that the first $\frac{N}{2} = 900$ columns contain the x components, while the following $\frac{N}{2} = 900$ columns contain the y components. To reflect this, the k^{th} projection can be written as

$$\ell^{(k)} \equiv \sum_i \left(u_i^{(kc)} \cos(\theta_i) + u_i^{(ks)} \sin(\theta_i) \right), \tag{9.6}$$

[8] For the ferromagnetic Ising model, a single spin-flip update move literally proposes moves where a spin is flipped. For the XY model, however, each planar spin is quantified by the angle it makes with the global x-axis. The proposed move used here is to perturb this angle by a random value from the range $[-\frac{\pi}{10}, \frac{\pi}{10}]$. Although this scheme could be modified by, for example, changing this range to maintain a stable acceptance rate of the proposed moves, this fixed range suffices to reproduce classical Monte Carlo simulation data of the XY model from the literature [91].

[9] We use the angular variable θ_i to refer to the "pure" XY model, since this is the angular variable to which the MXYGG model is mapped. We reserve the angular variable ϕ_i for the MXYGG model.

[10] Recall (as discussed in Chapter 8) that the temperatures T_j in Eq. (8.2) are not unique, since 500 distinct configurations are sampled at *each* of the 50 temperatures.

where the k^{th} principal component $\boldsymbol{u}^{(k)}$ has been separated into two halves. The first (last) $\frac{N}{2} = 900$ components of $\boldsymbol{u}^{(k)}$ are denoted as $u_i^{(kc)}$ ($u_i^{(ks)}$), with the additional c (s) superscript indicating that these coefficients multiply the cosine (sine) columns of Eq. (9.5).

First, consider PCA applied to the full dataset, Eq. (9.5). Figure 9.6b displays the explained variance ratios. Unlike the ferromagnetic Ising model, there are two explained variance ratios that are significant for the XY model. This indicates that the first two principal components are both needed to sufficiently characterize the dataset.[11] This also suggests that PCA will not cluster the data substantially along one projection $\ell^{(k)}$ instead of the other, as is the case for $\ell^{(1)}$ in the ferromagnetic Ising model.

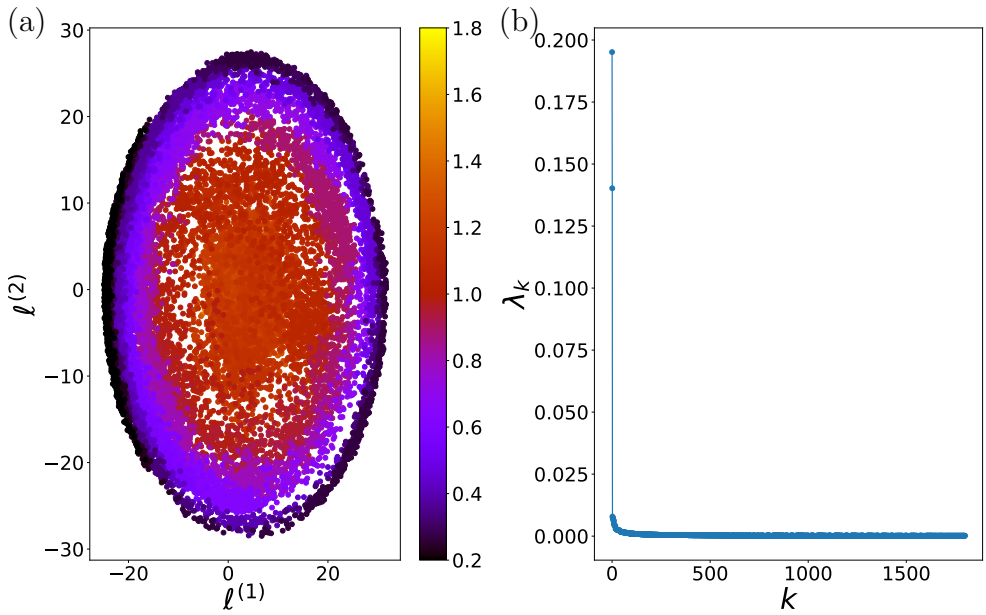

Figure 9.6: Results of PCA applied to the ferromagnetic XY model. (a) The projections $\ell^{(1)}$ versus $\ell^{(2)}$, revealing how PCA clusters the data. Temperatures are indicated in the colorbar. (b) The explained variance ratios for all principal components.

Figure 9.6a displays the clustering that PCA produces for the ferromagnetic XY model. Two important features may immediately be recognized. Firstly, in contrast to the two symmetric clusters of the ferromagnetic Ising model, the clusters that PCA forms for the

[11] Due to its $U(1)$ symmetry, the XY model should in principle have the first two explained variance ratios as being closer in value than what is shown in Figure 9.6b. It is likely that this discrepancy could be resolved by taking longer equilibration times in the classical Monte Carlo simulations.

XY model take the shape of concentric circles.[12] This implies an underlying $U(1)$ symmetry in the data[13], just as the symmetric clusters in the ferromagnetic Ising model were reflections of the $\mathbb{Z}_2$ symmetry of its ferromagnetic ground state. Secondly, the concentric circular clusters are separated according to temperature, with high-temperature circles at the centre and low-temperature circles at the perimeter. The central circles correspond to values of $\ell^{(1)}$ and $\ell^{(2)}$ close to zero, whereas the outer circles correspond to non-zero values of $\ell^{(1)}$ or $\ell^{(2)}$ (or both). Taken together, these two features suggest that PCA may be characterizing the data using the x and y components of the finite-size-induced magnetization of the XY model. To verify this quantitatively, Figure 9.7 plots $\sqrt{(\ell^{(1)})^2 + (\ell^{(2)})^2}$ for each of the n configurations, which indeed resembles the magnetization [91].

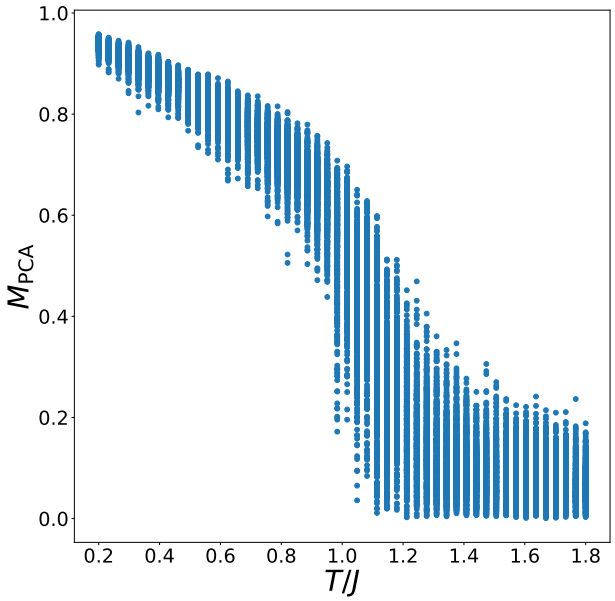

Figure 9.7: $M_{\mathrm{PCA}} = \sqrt{(\ell^{(1)})^2 + (\ell^{(2)})^2}$ as determined from PCA applied to the ferromagnetic XY model. Note that each data point corresponds to M_{PCA} calculated for one of the n configurations. Since 500 configurations are taken at every temperature, there are multiple (i.e 500) data points for any fixed value of temperature.

The vector components of the principal components are plotted in Figure 9.8. In light of Eq. (7.7) (with $b_i = 0\ \forall i$ giving the ferromagnetic XY model) and Eq. (9.6),

[12] The aspect ratio of Figure 9.6a makes these concentric circles appear elliptical; the different scales along the x– and y–axes should be noted.

[13] Rather, it implies an underlying $U(1)$ symmetry in the projections $\ell^{(1)}$ and $\ell^{(2)}$ that PCA is using to characterize the data.

one might expect that the vector components should simply be $\{u_i^{(1c)}\} = \{u_i^{(2s)}\} = 1$ and $\{u_i^{(1s)}\} = \{u_i^{(2c)}\} = 0$; this would add up all $\cos(\theta_i)$ ($\sin(\theta_i)$) terms to produce the magnetization vector in the x (y) direction. This is clearly not the case! However, this should not be surprising. The ferromagnetic XY model contains an underlying $U(1)$ symmetry, so there is no reason for PCA to compute the magnetization with respect to the global x- and y-axes defined in the classical Monte Carlo simulations. These axes may be rotated by any arbitrary angle α, and PCA may learn the magnetization with respect to *these* axes. Under such a global rotation, the corresponding x and y magnetizations would be modified as:

$$\begin{aligned} M_x = &\sum_i \cos(\theta_i + \alpha) = \sum_i \cos(\theta_i)\cos(\alpha) - \sin(\theta_i)\sin(\alpha), \\ M_y = &\sum_i \sin(\theta_i + \alpha) = \sum_i \sin(\theta_i)\cos(\alpha) + \cos(\theta_i)\sin(\alpha). \end{aligned} \tag{9.7}$$

Comparing Eq. (9.7) with Eq. (9.6) implies that the components of $\boldsymbol{u}^{(1)}$ and $\boldsymbol{u}^{(2)}$ contain the global rotation angle α. By pairing up the corresponding coefficients $u_i^{(1c)}$ and $u_i^{(1s)}$ for the same site i and taking the arctangent, this global rotation angle α may be computed. For example, looking at the expression for M_y in Eq. (9.7) and comparing with Eq. (9.6) (for $k = 1$) shows that

$$\alpha_i = \arctan\left(\frac{u_i^{(1c)}}{u_i^{(1s)}}\right) \tag{9.8}$$

is the approximation of α associated with the site i. A histogram for the distribution of α values extracted in this manner is shown in Figure 9.9. The peak in the histogram suggests a global rotation with $\alpha \approx 0.54$ rad; subtracting this angle off of the data $\{\theta_i\}$ and repeating PCA produces the principal components in Figure 9.10. Now, as expected, the coefficients take values of $\{u_i^{(1c)}\} = \{u_i^{(2s)}\} = 0$ and $\{u_i^{(1s)}\} = \{u_i^{(2c)}\} = 1$. This verifies that, not only does PCA learn the magnetization and use it to characterize the dataset, it also implicitly contains the global $U(1)$ symmetry in its principal components.[14]

Now, consider PCA applied to the half datasets in Eq. (9.4). The resulting explained variance ratios and clusters are displayed in Figures 9.11 and 9.12. In this case, there is only one significant explained variance ratio, leaving only one important principal component.

[14] One may expect the global rotation angle α to change every time PCA is applied to the dataset, since the XY model is symmetric under arbitrary rotations. However, as the temperature is lowered in classical Monte Carlo simulations, it is likely that the system begins to make only small moves about its spin configuration. This may lead to a preferred magnetization direction, and that may be why α will not change when PCA is reapplied. However, if given a new dataset, α can be expected to be different.

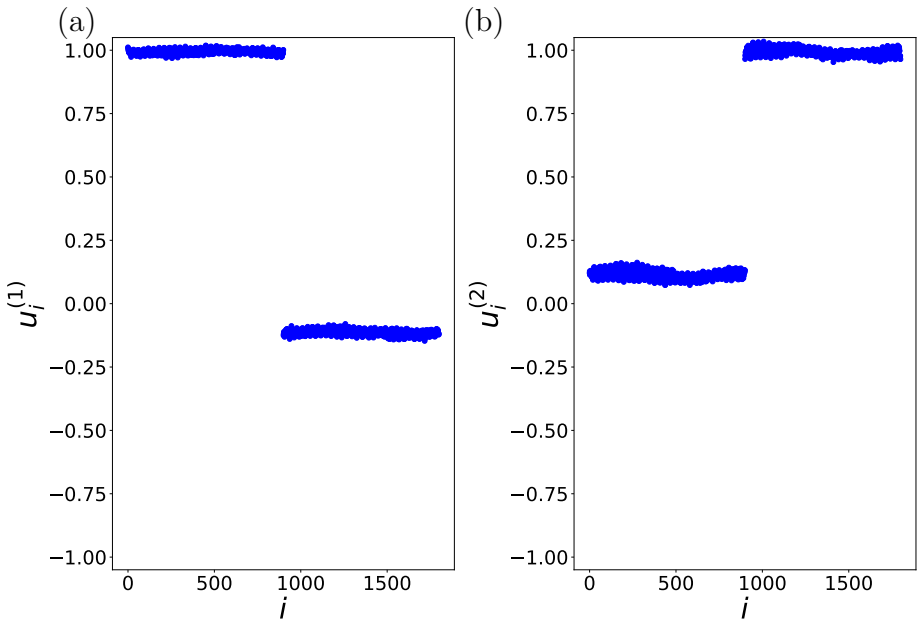

Figure 9.8: i^{th} components of (a) $\boldsymbol{u}^{(1)}$ and (b) $\boldsymbol{u}^{(2)}$ for the ferromagnetic XY model, *before* applying a global rotation α. Note that the values are not simply 0s and 1s. Recall that the first (last) 900 components of $\boldsymbol{u}^{(1)}$ and $\boldsymbol{u}^{(2)}$ correspond to the coefficients of the cosine (sine) terms in Eq. (9.6).

This behavior, as well as the resulting clusters, are reminiscient of the ferromagnetic Ising case. However, there is no clear separation of clusters as there is in the Ising case, since the spin variables are now allowed to vary continuously rather than take values of ± 1. Nevertheless, this Ising-like behaviour may be interpreted as decomposing the magnetization vector that PCA learns into its two separate components.

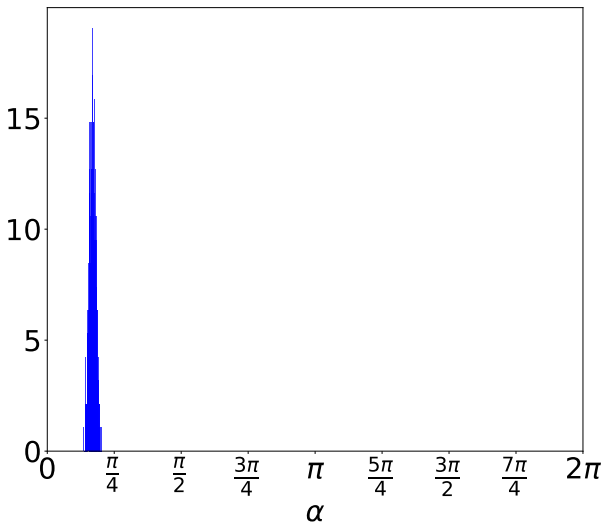

Figure 9.9: Histogram of the extracted $U(1)$ rotation angle α, as determined from PCA applied to the ferromagnetic XY model.

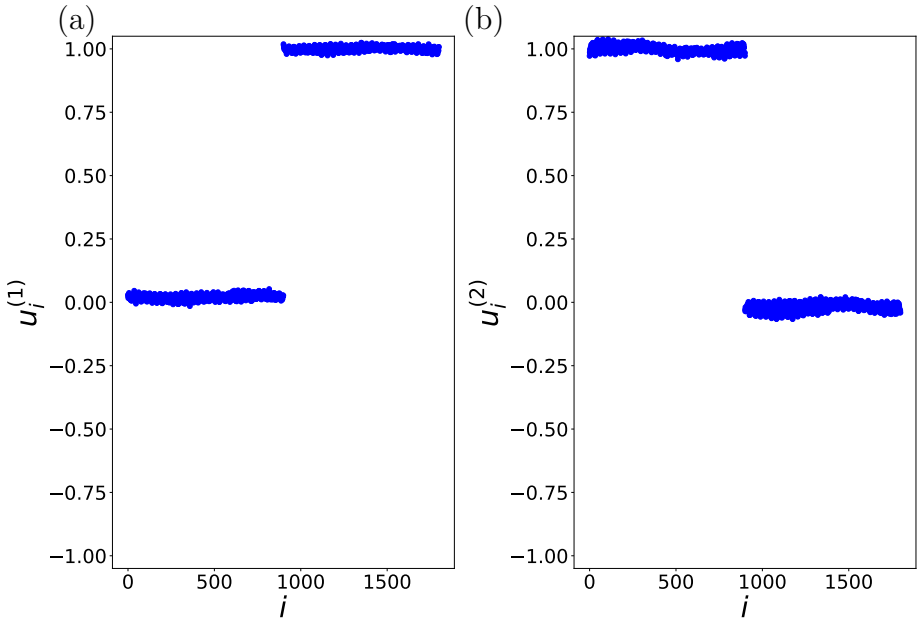

Figure 9.10: i^{th} components of (a) $\boldsymbol{u}^{(1)}$ and (b) $\boldsymbol{u}^{(2)}$ for the ferromagnetic XY model, *after* applying a global rotation α. Note that the values are approximately 0s and 1s, in contrast with Figure 9.8. Recall that the first (last) 900 components of $\boldsymbol{u}^{(1)}$ and $\boldsymbol{u}^{(2)}$ correspond to the coefficients of the cosine (sine) terms in Eq. (9.6).

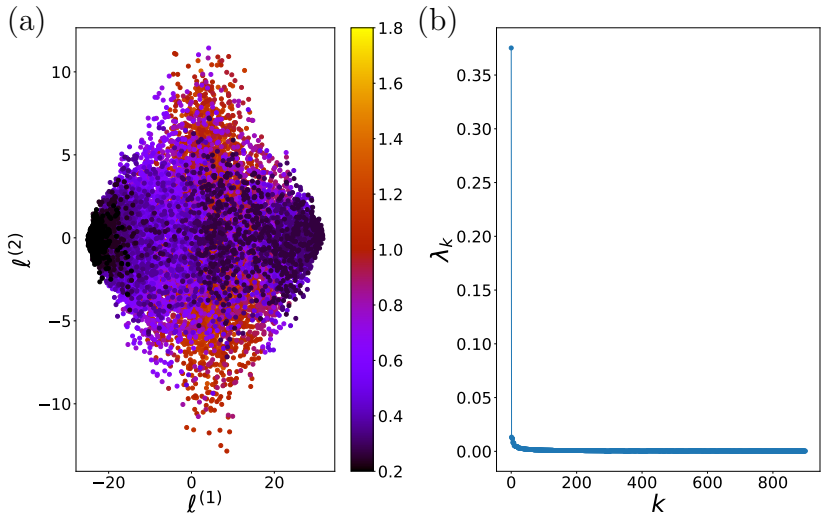

Figure 9.11: Results of PCA applied to the x-component data of the ferromagnetic XY model. (a) The projections $\ell^{(1)}$ versus $\ell^{(2)}$, revealing how PCA clusters the data. (b) The explained variance ratios for all principal components.

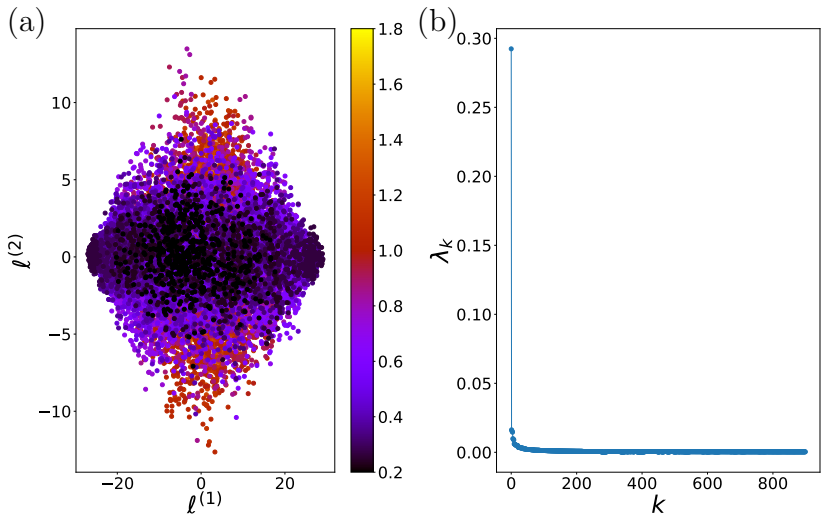

Figure 9.12: Results of PCA applied to the y-component data of the ferromagnetic XY model. (a) The projections $\ell^{(1)}$ versus $\ell^{(2)}$, revealing how PCA clusters the data. (b) The explained variance ratios for all principal components.

9.3 PCA on the MISG Model

Having studied the ferromagnetic Ising model with PCA, we now turn to the MISG model. To study the MISG model with PCA, the dataset is generated via classical Monte Carlo simulations with a single spin-flip update move. A lattice size of $L = 30$ is taken, giving $N = 900$ spins. For a given site i, the gauge variable ϵ_i is chosen to be 1 or -1 with a 50% probability. The system is sampled for 50 equally-spaced temperatures in the range $[J, 4J]$. 3×10^4 equilibration sweeps are performed at every temperature, followed by 3×10^4 measurement sweeps. Measurements are taken every 100 measurement sweeps, giving 300 measurements at every temperature for a total of $n = 50 \times 300 = 1.5 \times 10^4$ configurations. In reference to Eq. (8.2), the variable x_i is the spin variable σ_i^z; note that PCA is not given any information about ϵ_i nor $\tau_i^z = \epsilon_i\sigma_i^z$. Altogether, the data matrix for this dataset is:

$$X_{\text{data}} \equiv \begin{pmatrix} \{x_i(T_1)\} \\ \{x_i(T_2)\} \\ \vdots \\ \{x_i(T_n)\} \end{pmatrix} = \begin{pmatrix} \{\sigma_i^z(T_1)\} \\ \{\sigma_i^z(T_2)\} \\ \vdots \\ \{\sigma_i^z(T_n)\} \end{pmatrix}. \tag{9.9}$$

PCA is performed on this matrix in order to assess whether PCA can "discover" the gauge variables $\{\epsilon_i\}$ without any prior knowledge.

The explained variance ratios are shown in Figure 9.13b. As with the ferromagnetic Ising model, there is only one significant principal component. This is suggestive that PCA *is* able to detect the underlying Ising model. Further qualitative evidence for this implication is provided in the clustering of the dataset, shown in Figure 9.13a. Clearly, PCA clusters the data in exactly the same way as with the ferromagnetic Ising model.

To verify these findings quantitatively, the projection $\ell^{(1)}$ is plotted in Figure 9.14 and compared with the corresponding τ-magnetization. When plotted against one another, it is evident that PCA learns the τ-magnetization exactly. PCA also uses the τ-magnetization to categorize the data of the MISG model into the paramagnetic and ferromagnetic phases of the underlying Ising model! What is most remarkable about this categorization is its implication that PCA has somehow identified the gauge variables $\{\epsilon_i\}$. PCA was only provided with $\{\sigma_i^z(T_j)\}$; however, from this, it was able to categorize the data using the quantity $M_\tau = \frac{1}{N}\sum_i \tau_i^z = \frac{1}{N}\sum_i \epsilon_i\sigma_i^z$. In light of Eq. (8.5), this implies that the components of $\boldsymbol{u}^{(1)}$ directly contain the gauge variables $\{\epsilon_i\}$ – that is, $u_i^{(1)}$ should correspond to what PCA has learned to be ϵ_i.

As confirmation of this implication, histograms of the known and learned gauge variables $\{\epsilon_i\}$ and bond interactions $\{J_{ij}\}$ are shown in Figure 9.15. Recall that $J_{ij} = \epsilon_i\epsilon_j J$.

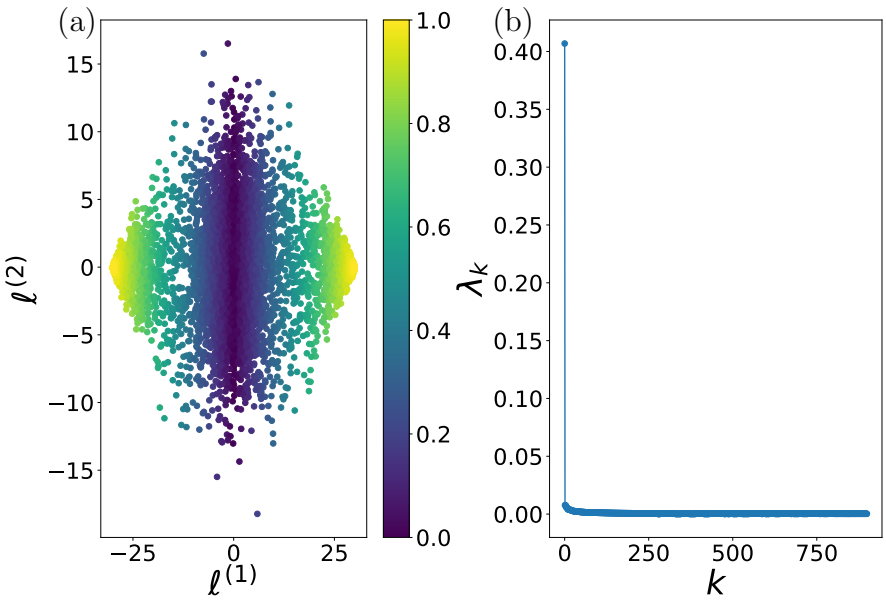

Figure 9.13: Results of PCA applied to the MISG model. (a) The projections $\ell^{(1)}$ versus $\ell^{(2)}$, revealing how PCA clusters the data. Data points (which represent distinct spin configurations) are colored according to the absolute value of the τ–magnetization associated with that spin configuration. (b) The explained variance ratios for all principal components.

So, taking $J = 1$, we can compute estimates of J_{ij} from PCA by using PCA's learned values of $\{\epsilon_i\}$. The histograms comparing what was entered into the Monte Carlo simulations and what is learned by PCA (i.e. the components of $\boldsymbol{u}^{(1)}$, with the i^{th} component representing the learned ϵ_i) are essentially identical. Of course, there is some spread in the histograms associated with PCA's learned values, as seen in Figure 9.15. Due to slight numerical errors in the process of using PCA, the learned values of $\{J_{ij}\}$ and $\{\epsilon_i\}$ are expected to slightly differ from pure ± 1 values. However, the learned values are centered on ± 1 and with very minimal spread, which is why we consider this result to be essentially identical (within numerical errors) to the original $\{J_{ij}\}$ and $\{\epsilon_i\}$ values. All three of these checks demonstrate that PCA is able to determine the Mattis gauge transformation that maps the MISG model onto the ferromagnetic Ising model, even without any prior knowledge of such a gauge transformation.

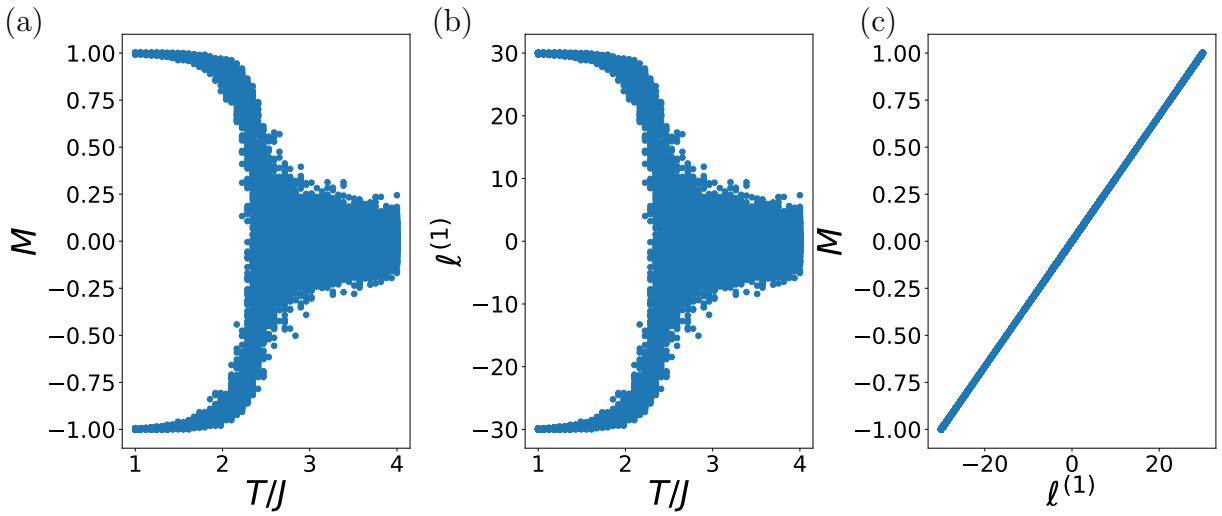

Figure 9.14: Results of PCA applied to the MISG model. (a) τ-magnetization of the Ising model computed from Monte Carlo simulations as a function of temperature T/J. (b) Projection $\ell^{(1)}$ learned by PCA as a function of temperature T/J. (c) τ-magnetization from Monte Carlo simulations versus the learned projection $\ell^{(1)}$.

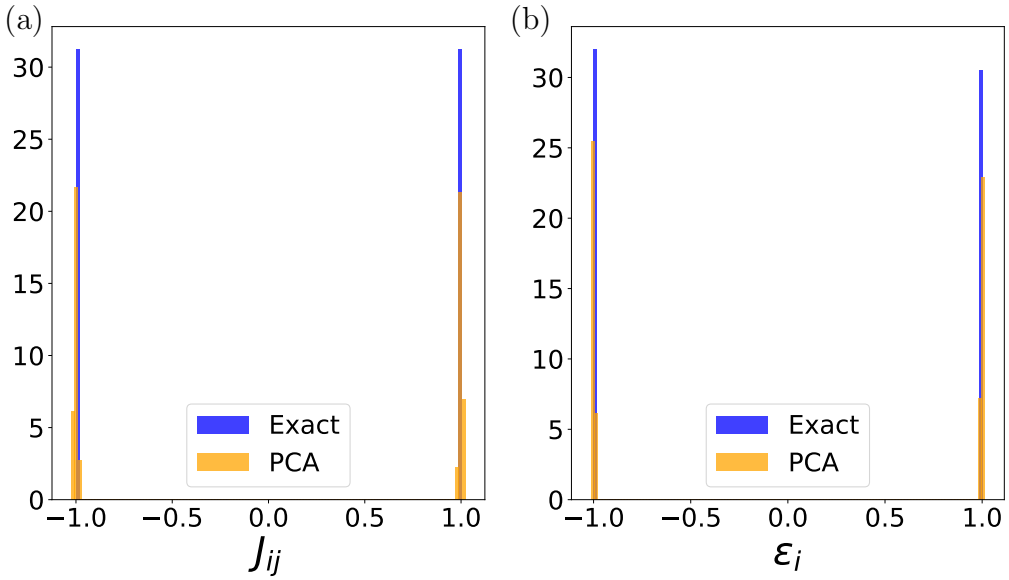

Figure 9.15: Histograms of (a) the bond interactions $\{J_{ij}\}$ and (b) the gauge variables $\{\epsilon_i\}$ of the MISG model. Exact values are those initialized in Monte Carlo simulations, shown in blue; orange values are those determined by PCA.

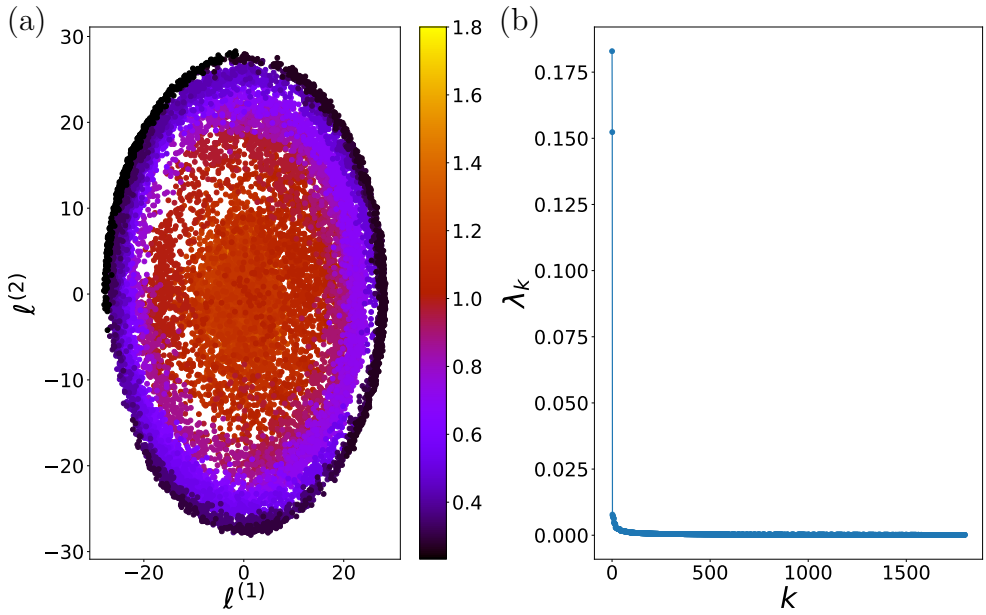

Figure 9.16: Results of PCA applied to the MXYGG model, to be compared with Figure 9.6. (a) The projections $\ell^{(1)}$ versus $\ell^{(2)}$, revealing how PCA clusters the data. (b) The explained variance ratios for all principal components.

9.4 PCA on the MXYGG Model

To study the MXYGG model with PCA, the dataset is generated via classical Monte Carlo simulations with a single spin-flip update move, as was the case with the ferromagnetic XY model in Section 9.2. A lattice size of $L = 30$ is taken, giving 900 spins described by the planar angles $\{\phi_i\}$. As in Section 9.2, these spins can be decomposed into their x and y components, $\cos(\phi_i)$ and $\sin(\phi_i)$ respectively. The system is sampled for 50 equally-spaced temperatures in the range $[0.2J, 1.8J]$. 3×10^4 equilibration sweeps are performed at every temperature, followed by 5×10^4 measurement sweeps. Measurements are taken every 100 measurement sweeps, giving 500 measurements at every temperature for a total of $n = 50 \times 500 = 2.5 \times 10^4$ configurations. Lastly, for a given site i, the gauge variable b_i is randomly chosen from a set of five values, $\{\frac{2\pi n}{5} | n = 1, \ldots, 5\}$, all with equal probabilities. As with the MISG model, the objective is to determine if PCA can learn the gauge transformation described by the gauge variables $\{b_i\}$. Hence, a discrete set of gauge variables is chosen; it is much easier to verify if PCA has learned the gauge variables if they vary discretely rather than continuously. The reason for this is discussed at the end of this section.

The data matrix for this dataset can take three forms, depending on if the x component, y component, or both components of the spins are provided, just as was the case with the ferromagnetic XY model in Section 9.2. However, in contrast to Eqs. (9.4) and (9.5), the angles $\{\phi_i\}$ are used instead of $\{\theta_i\}$. In this way, PCA has no prior knowledge of the gauge transformation: it is not provided with any information regarding $\{b_i\}$ nor $\{\theta_i\}$. PCA is then performed on the corresponding matrices from Eqs. (9.4) and (9.5), given either one or both components of the planar spins.

Figure 9.16 displays the results when PCA is performed on the full dataset. In comparison with Figure 9.6 of the ferromagnetic XY model, the results are strikingly similar: there are again two significant explained variance ratios, and PCA clusters the data into concentric circles when the first two projections $\ell^{(1)}$ and $\ell^{(2)}$ are plotted against one another (for all T_j). The interpretations that were made for the ferromagnetic XY model in Section 9.2 can thus be made again here – namely, that there is an underlying $U(1)$ symmetry in the data, that the data is being categorized according to its magnetization vector, and that the two principal components used to characterize the data correspond to two axes along which the magnetization vector is decomposed. Qualitatively, Figure 9.16 suggests that PCA has uncovered the underlying XY model and is characterizing the MXYGG model in exactly the same way.

However, Figures 9.17 and 9.18 shows the resulting clusters that PCA produces when given only one component of the planar spins. There is a marked difference relative to the ferromagnetic XY model result shown in Figure 9.6. In the ferromagnetic XY model, decomposing the dataset into its x and y components resulted in only one significant explained variance ratio, as well as clusters that could be described as Ising-like. In the MXYGG model, on the other hand, there are still two significant explained variance ratios, producing a $U(1)$-symmetric clustering *even when* only one component is provided.

There are two important implications to be drawn from this. Firstly, the difference between Figures 9.11 (9.12) and 9.17 (9.18) indicates that PCA can discriminate between data from the MXYGG model and data from the ferromagnetic XY model, even though the similarities between Figures 9.6 and 9.16 suggests that both models can be characterized in the same way. Secondly, the $U(1)$ symmetry of these clusters suggests that whatever is causing this difference between the two models possesses a $U(1)$ symmetry itself. The first of these implications qualitatively suggests that PCA has detected the presence of the gauge transformation that relates the MXYGG and XY models; this would cause a difference in the one-component analysis of the MXYGG model, but not in the two-component analysis. The second implication hints at the $U(1)$ nature of this transformation; this motivates a similar analysis as in the ferromagnetic XY model, when the global rotation angle α was determined in Section 9.2.

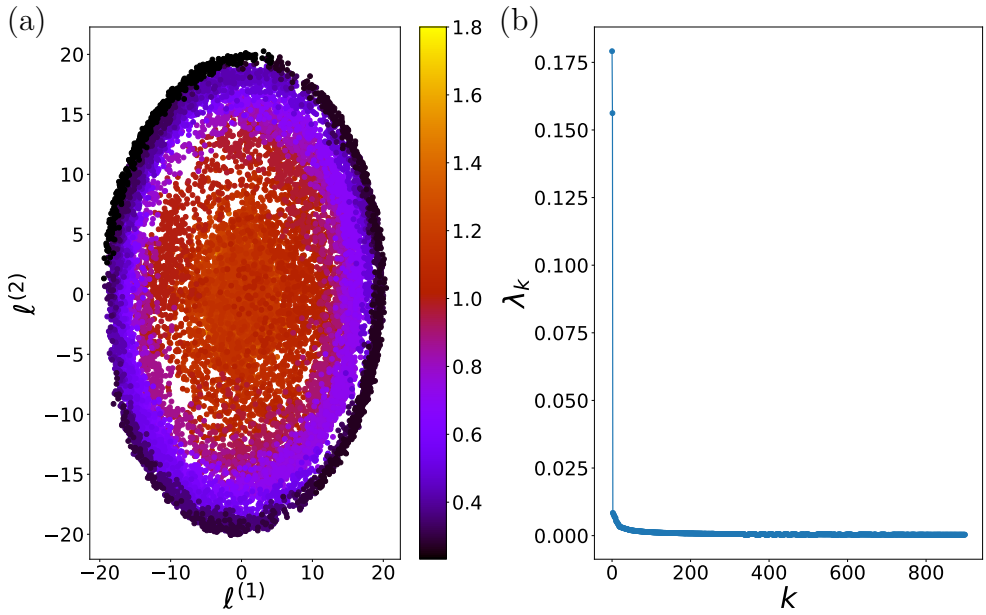

Figure 9.17: Results of PCA applied to the x-component data of the MXYGG model, to be compared with Figure 9.11. (a) The projections $\ell^{(1)}$ versus $\ell^{(2)}$, revealing how PCA clusters the data. (b) The explained variance ratios for all principal components.

Returning to the results of the full dataset, the first and second projections take the form:

$$\ell^{(1)} \equiv \sum_i \left(u_i^{(1c)} \cos(\phi_i) + u_i^{(1s)} \sin(\phi_i) \right), \tag{9.10}$$

$$\ell^{(2)} \equiv \sum_i \left(u_i^{(2c)} \cos(\phi_i) + u_i^{(2s)} \sin(\phi_i) \right). \tag{9.11}$$

In the ferromagnetic XY model in Section 9.2, this was compared to the two-component magnetization vector under a global rotation by an angle α:

$$\begin{aligned} M_x &= \sum_i \cos(\theta_i + \alpha) = \sum_i \cos(\theta_i)\cos(\alpha) - \sin(\theta_i)\sin(\alpha), \\ M_y &= \sum_i \sin(\theta_i + \alpha) = \sum_i \sin(\theta_i)\cos(\alpha) + \cos(\theta_i)\sin(\alpha). \end{aligned} \tag{9.12}$$

For the MXYGG model, a single global rotation angle α should not be expected, or else PCA would have discovered no difference between the MXYGG and ferromagnetic XY datasets. However, comparing Eqs. (9.10), (9.11), and (9.12), one can still take the arctangent of the ratio of principal component coefficients as was done for the XY model

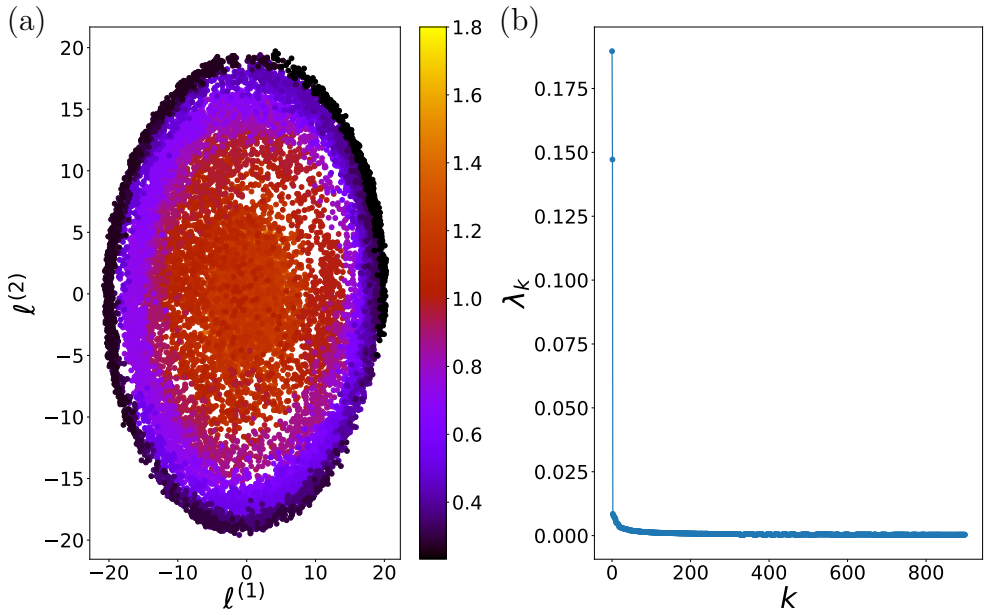

Figure 9.18: Results of PCA applied to the y-component data of the MXYGG model, to be compared with Figure 9.12. (a) The projections $\ell^{(1)}$ versus $\ell^{(2)}$, revealing how PCA clusters the data. (b) The explained variance ratios for all principal components.

in Eq. (9.8). If there are multiple possible values of α (that is, if α in the above expressions was replaced with some β_k for some index k), then the corresponding expression for the MXYGG model is:

$$\begin{aligned} M_x &= \sum_i \cos(\phi_i + \beta_k) = \sum_i \left[\cos(\phi_i)\cos(\beta_k) - \sin(\phi_i)\sin(\beta_k)\right], \\ M_y &= \sum_i \sin(\phi_i + \beta_k) = \sum_i \left[\sin(\phi_i)\cos(\beta_k) + \cos(\phi_i)\sin(\beta_k)\right]. \end{aligned} \tag{9.13}$$

In the case of the ferromagnetic XY model, the $U(1)$ symmetry only applied to the angular variable θ_i; this was the only angular variable with this degree of freedom. However, there are now two angular degrees of freedom to which a global rotation by a single angle α can be applied. As in the ferromagnetic XY model, the global rotation α may be applied to the angular variables $\{\phi_i\}$:

$$\begin{aligned} M_x &= \sum_i \cos(\phi_i + \beta_k + \alpha) = \sum_i \cos(\phi_i + \alpha)\cos(\beta_k) - \sin(\phi_i + \alpha)\sin(\beta_k), \\ M_y &= \sum_i \sin(\phi_i + \beta_k + \alpha) = \sum_i \sin(\phi_i + \alpha)\cos(\beta_k) + \cos(\phi_i + \alpha)\sin(\beta_k). \end{aligned} \tag{9.14}$$

As in the ferromagnetic XY model, this choice corresponds to the $U(1)$ symmetry of the PCA clusters when given the full dataset. On the other hand, the global rotational symmetry could be applied to the angular variables β_k:

$$\begin{aligned} M_x &= \sum_i \cos(\phi_i + \beta_k + \alpha) = \sum_i \cos(\phi_i)\cos(\beta_k + \alpha) - \sin(\phi_i)\sin(\beta_k + \alpha), \\ M_y &= \sum_i \sin(\phi_i + \beta_k + \alpha) = \sum_i \sin(\phi_i)\cos(\beta_k + \alpha) + \cos(\phi_i)\sin(\beta_k + \alpha). \end{aligned} \tag{9.15}$$

This choice was not possible in the ferromagnetic XY model. When PCA is provided with only one component of the planar spins, as in Figures 9.17 and 9.18, this "internal" $U(1)$ rotational symmetry still results in circular clusters, unlike in the ferromagnetic XY model (Figures 9.11 and 9.12).

Going further, one may extract the values of β_k in the same manner as α was extracted for the ferromagnetic XY model, namely, using Eq. (9.8) to determine β_k on each site i (instead of α_i) from the principal components.[15] Doing this produces the histogram shown in Figure 9.19. The five equally-spaced peaks demonstrate that PCA is able to find the five discrete choices of the gauge variable b_i that were chosen in the classical Monte Carlo simulation. Since the principal component coefficients are site-dependent, the gauge variable at any given site can be determined. This is also the reason why five discrete choices of gauge variables were chosen: if the gauge variables $\{b_i\}$ continuously varied, the resulting histogram would show a continuous range of learned gauge variables $\{\beta_k\}$ rather than discrete peaks. It is clearly much easier to interpret the discrete peaks as evidence of PCA learning the gauge variables than a continuously-ranging, nondescript spread of β_k values. Again, as in the MISG model, we see that PCA can determine (1) the presence of a gauge transformation, and (2) the actual gauge variables $\{b_i\}$ responsible for this gauge transformation, despite being provided no information about it.

[15] Of course, these values of β_k will also only be known up to some global rotation.

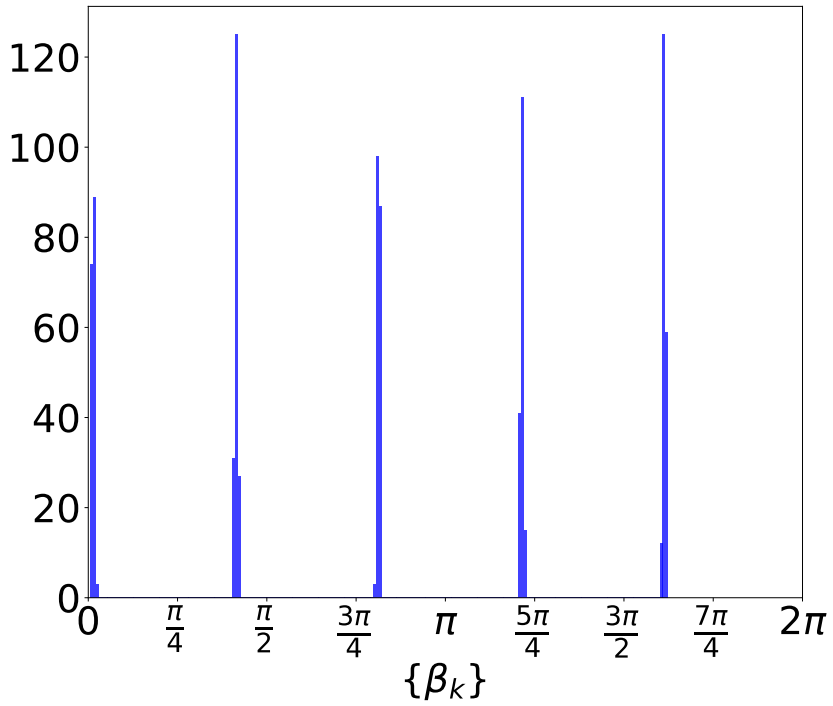

Figure 9.19: Histogram of the extracted rotation angles β_k (described in the main text), as determined from PCA applied to the MXYGG model. Note that these learned gauge variables are known up to a global rotation α and hence do not occur exactly at values of $\frac{2\pi n}{5}$.

Chapter 10

Conclusion

10.1 Summary

In Part II of this thesis, we used the Principal Component Analysis (PCA) method on the Mattis Ising spin glass (MISG) and Mattis XY gauge glass (MXYGG) models to determine if machine learning could learn quenched gauge symmetries. The answer to this question is affirmative. In the MISG model, the clusters that PCA produces to categorize the dataset are identical to those of the ferromagnetic Ising model. As well, the projection that PCA learns to characterize the dataset is seen to be identical to the magnetization of the underlying ferromagnetic Ising model. This implies that the principal components themselves contain the gauge variables necessary to transform the MISG model into the ferromagnetic Ising model, which is confirmed by a histogram comparison. The case of the MXYGG model is similar. The clusters that PCA produces to categorize the full dataset are reminiscient of those of the ferromagnetic XY model. However, a difference is detected when only one component of the spins is provided to PCA, indicative of the underlying gauge transformation. For both the MISG and MXYGG models, the gauge variables quantifying this gauge transformation were also argued to be contained within the principal components themselves, which is confirmed by extracting the learned gauge variables and producing a histogram of the results.

10.2 Future Work

In light of the work presented here, one immediate extension would be the study of other gauge-symmetric spin glass models. The MISG and MXYGG models possess $\mathbb{Z}_2$ and $U(1)$ gauge symmetries, respectively. It should therefore be possible to use a similar approach on, for example, a spin glass model with an $O(3)$ gauge symmetry [115].

More abstractly, the idea of this work – namely, the machine-learning of gauge symmetries – may be useful in other contexts. We have shown that PCA, a simple machine learning technique, is capable of learning a gauge transformation that simpifies our original mathematical model. In this way, machine learning is able to provide insights into the simulated model itself and not just thermodynamic quantities such as order parameters. It would be of interest to test this idea with other unsupervised learning methods. For example, the autoencoder is an unsupervised learning technique that uses a neural network and shares similarities with PCA [104, 105]. This may make it capable of learning non-linear or complex features of a model that a linear matrix-based method like PCA is not able to learn.

However, the trade-off for this descriptive power is the interpretability of an autoencoder, which is complicated by the use of a neural network. If, for example, an autoencoder is employed to learn gauge symmetries in a model, this relative lack of interpretability may make it difficult to determine the exact mathematical form of the gauge transformation, which is not the case for PCA. Even then, our work suggests an additionally useful idea: unsupervised machine learning may be able to *simplify* a dataset by exploiting features that it learns, such as gauge symmetries. In our case, PCA simplifies the disordered MISG and MXYGG models by mapping them onto the ferromagnetic Ising and XY models. In general, this suggests that one could use an unsupervised learning technique to efficiently categorize and label input data, and then provide the data and labels to a *supervised* technique. This benefit would apply to unsupervised techniques that are difficult to interpret as well, such as autoencoders. An application of this idea in a previous work [101] demonstrates that PCA and a neural network could together learn an $SU(2)$ gauge theory order parameter. In this way, unsupervised and supervised methods can work in tandem to more effectively classify a dataset.

Lastly, our work demonstrates that models possessing gauge symmetries may be of particular interest for future machine learning applications. Such models are amenable to analytical study by the physicist. Our work shows that the mathematical nature of these gauge symmetries also make it possible for machine learning techniques to detect them. In this way, gauge-symmetric models hold a special place at the intersection of physics and

machine learning: by applying machine learning techniques to gauge-symmetric models, it may be possible to explore what these techniques are actually learning and how.

Letters of Copyright Permission

Annual Reviews, Inc. - License Terms and Conditions

Order Date	11-Sep-2020	**Type of Use**	Republish in a thesis/dissertation
Order license ID	1062398-1		
ISSN	1947-5462	**Publisher**	Annual Reviews
		Portion	Image/photo/illustration

LICENSED CONTENT

Publication Title	Annual review of condensed matter physics	**Publication Type**	Journal
Article Title	Frustrated Quantum Rare-Earth Pyrochlores	**Start Page**	357
		End Page	386
Date	01/01/2010	**Issue**	1
Language	English	**Volume**	10
Country	United States of America	**URL**	http://www.annualreviews.org/journal/conmatphys
Rightsholder	Annual Reviews, Inc.		

REQUEST DETAILS

Portion Type	Image/photo/illustration	**Distribution**	Worldwide
Number of images / photos / illustrations	1	**Translation**	Original language of publication
Format (select all that apply)	Electronic	**Copies for the disabled?**	No
		Minor editing privileges?	No
Who will republish the content?	Academic institution	**Incidental promotional use?**	No
Duration of Use	Life of current and all future editions	**Currency**	USD
Lifetime Unit Quantity	Up to 499		
Rights Requested	Main product		

NEW WORK DETAILS

Title	Studies of Reentrance in Pyrochlore Magnets and Machine Learning of Quenched Gauge Symmetries	**Institution name**	University of Waterloo
		Expected presentation date	2020-09-17
Instructor name	Professor Michel Gingras		

ADDITIONAL DETAILS

Order reference number	N/A	**The requesting person / organization to appear on the license**	Darren Pereira

REUSE CONTENT DETAILS

Title, description or numeric reference of the portion(s)	Figure 1b	**Title of the article/chapter the portion is from**	Frustrated Quantum Rare-Earth Pyrochlores
Editor of portion(s)	Rau, Jeffrey G.; Gingras, Michel J.P.	**Author of portion(s)**	Rau, Jeffrey G.; Gingras, Michel J.P.
Volume of serial or monograph	10	**Issue, if republishing an article from a serial**	1
Page or page range of portion	357-386	**Publication date of portion**	2019-03-10

CCC Republication Terms and Conditions

1. Description of Service; Defined Terms. This Republication License enables the User to obtain licenses for republication of one or more copyrighted works as described in detail on the relevant Order Confirmation (the "Work(s)"). Copyright Clearance Center, Inc. ("CCC") grants licenses through the Service on behalf of the rightsholder identified on the Order Confirmation (the "Rightsholder"). "Republication", as used herein, generally means the inclusion of a Work, in whole or in part, in a new work or works, also as described on the Order Confirmation. "User", as used herein, means the person or entity making such republication.

2. The terms set forth in the relevant Order Confirmation, and any terms set by the Rightsholder with respect to a particular Work, govern the terms of use of Works in connection with the Service. By using the Service, the person transacting for a republication license on behalf of the User represents and warrants that he/she/it (a) has been duly authorized by the User to accept, and hereby does accept, all such terms and conditions on behalf of User, and (b) shall inform User of all such terms and conditions. In the event such person is a "freelancer" or other third party independent of User and CCC, such party shall be deemed jointly a "User" for purposes of these terms and conditions. In any event, User shall be deemed to have accepted and agreed to all such terms and conditions if User republishes the Work in any fashion.

3. Scope of License; Limitations and Obligations.

    3.1. All Works and all rights therein, including copyright rights, remain the sole and exclusive property of the Rightsholder. The license created by the exchange of an Order Confirmation (and/or any invoice) and payment by User of the full amount set forth on that document includes only those rights expressly set forth in the Order Confirmation and in these terms and conditions, and conveys no other rights in the Work(s) to User. All rights not expressly granted are hereby reserved.

    3.2. General Payment Terms: You may pay by credit card or through an account with us payable at the end of the month. If you and we agree that you may establish a standing account with CCC, then the following terms apply: Remit Payment to: Copyright Clearance Center, 29118 Network Place, Chicago, IL 60673-1291. Payments Due: Invoices are payable upon their delivery to you (or upon our notice to you that they are available to you for downloading). After 30 days, outstanding amounts will be subject to a service charge of 1-1/2% per month or, if less, the maximum rate allowed by applicable law. Unless otherwise specifically set forth in the Order Confirmation or in a separate written agreement signed by CCC, invoices are due and payable on "net 30" terms. While User may exercise the rights licensed immediately upon issuance of the Order Confirmation, the license is automatically revoked and is null and void, as if it had never been issued, if complete payment for the license is not received on a timely basis either from User directly or through a payment agent, such as a credit card company.

3.3. Unless otherwise provided in the Order Confirmation, any grant of rights to User (i) is "one-time" (including the editions and product family specified in the license), (ii) is non-exclusive and non-transferable and (iii) is subject to any and all limitations and restrictions (such as, but not limited to, limitations on duration of use or circulation) included in the Order Confirmation or invoice and/or in these terms and conditions. Upon completion of the licensed use, User shall either secure a new permission for further use of the Work(s) or immediately cease any new use of the Work(s) and shall render inaccessible (such as by deleting or by removing or severing links or other locators) any further copies of the Work (except for copies printed on paper in accordance with this license and still in User's stock at the end of such period).

3.4. In the event that the material for which a republication license is sought includes third party materials (such as photographs, illustrations, graphs, inserts and similar materials) which are identified in such material as having been used by permission, User is responsible for identifying, and seeking separate licenses (under this Service or otherwise) for, any of such third party materials; without a separate license, such third party materials may not be used.

3.5. Use of proper copyright notice for a Work is required as a condition of any license granted under the Service. Unless otherwise provided in the Order Confirmation, a proper copyright notice will read substantially as follows: "Republished with permission of [Rightsholder's name], from [Work's title, author, volume, edition number and year of copyright]; permission conveyed through Copyright Clearance Center, Inc. " Such notice must be provided in a reasonably legible font size and must be placed either immediately adjacent to the Work as used (for example, as part of a by-line or footnote but not as a separate electronic link) or in the place where substantially all other credits or notices for the new work containing the republished Work are located. Failure to include the required notice results in loss to the Rightsholder and CCC, and the User shall be liable to pay liquidated damages for each such failure equal to twice the use fee specified in the Order Confirmation, in addition to the use fee itself and any other fees and charges specified.

3.6. User may only make alterations to the Work if and as expressly set forth in the Order Confirmation. No Work may be used in any way that is defamatory, violates the rights of third parties (including such third parties' rights of copyright, privacy, publicity, or other tangible or intangible property), or is otherwise illegal, sexually explicit or obscene. In addition, User may not conjoin a Work with any other material that may result in damage to the reputation of the Rightsholder. User agrees to inform CCC if it becomes aware of any infringement of any rights in a Work and to cooperate with any reasonable request of CCC or the Rightsholder in connection therewith.

4. Indemnity. User hereby indemnifies and agrees to defend the Rightsholder and CCC, and their respective employees and directors, against all claims, liability, damages, costs and expenses, including legal fees and expenses, arising out of any use of a Work beyond the scope of the rights granted herein, or any use of a Work which has been altered in any unauthorized way by User, including claims of defamation or infringement of rights of copyright, publicity, privacy or other tangible or intangible property.

5. Limitation of Liability. UNDER NO CIRCUMSTANCES WILL CCC OR THE RIGHTSHOLDER BE LIABLE FOR ANY DIRECT, INDIRECT, CONSEQUENTIAL OR INCIDENTAL DAMAGES (INCLUDING WITHOUT LIMITATION DAMAGES FOR LOSS OF BUSINESS PROFITS OR INFORMATION, OR FOR BUSINESS INTERRUPTION) ARISING OUT OF THE USE OR INABILITY TO USE A WORK, EVEN IF ONE OF THEM HAS BEEN ADVISED OF THE POSSIBILITY OF SUCH DAMAGES. In any event, the total liability of the Rightsholder and CCC (including their respective employees and directors) shall not exceed the total amount actually paid by User for this license. User assumes full liability for the actions and omissions of its principals, employees, agents, affiliates, successors and assigns.

6. Limited Warranties. THE WORK(S) AND RIGHT(S) ARE PROVIDED "AS IS". CCC HAS THE RIGHT TO GRANT TO USER THE RIGHTS GRANTED IN THE ORDER CONFIRMATION DOCUMENT. CCC AND THE RIGHTSHOLDER DISCLAIM ALL OTHER WARRANTIES RELATING TO THE WORK(S) AND RIGHT(S), EITHER EXPRESS OR IMPLIED, INCLUDING WITHOUT LIMITATION IMPLIED WARRANTIES OF MERCHANTABILITY OR FITNESS FOR A PARTICULAR PURPOSE. ADDITIONAL RIGHTS MAY BE REQUIRED TO USE ILLUSTRATIONS, GRAPHS, PHOTOGRAPHS, ABSTRACTS, INSERTS OR OTHER PORTIONS OF THE WORK (AS OPPOSED TO THE ENTIRE WORK) IN A MANNER CONTEMPLATED BY USER;

USER UNDERSTANDS AND AGREES THAT NEITHER CCC NOR THE RIGHTSHOLDER MAY HAVE SUCH ADDITIONAL RIGHTS TO GRANT.

7. Effect of Breach. Any failure by User to pay any amount when due, or any use by User of a Work beyond the scope of the license set forth in the Order Confirmation and/or these terms and conditions, shall be a material breach of the license created by the Order Confirmation and these terms and conditions. Any breach not cured within 30 days of written notice thereof shall result in immediate termination of such license without further notice. Any unauthorized (but licensable) use of a Work that is terminated immediately upon notice thereof may be liquidated by payment of the Rightsholder's ordinary license price therefor; any unauthorized (and unlicensable) use that is not terminated immediately for any reason (including, for example, because materials containing the Work cannot reasonably be recalled) will be subject to all remedies available at law or in equity, but in no event to a payment of less than three times the Rightsholder's ordinary license price for the most closely analogous licensable use plus Rightsholder's and/or CCC's costs and expenses incurred in collecting such payment.

8. Miscellaneous.

    8.1. User acknowledges that CCC may, from time to time, make changes or additions to the Service or to these terms and conditions, and CCC reserves the right to send notice to the User by electronic mail or otherwise for the purposes of notifying User of such changes or additions; provided that any such changes or additions shall not apply to permissions already secured and paid for.

    8.2. Use of User-related information collected through the Service is governed by CCC's privacy policy, available online here:https://marketplace.copyright.com/rs-ui-web/mp/privacy-policy

    8.3. The licensing transaction described in the Order Confirmation is personal to User. Therefore, User may not assign or transfer to any other person (whether a natural person or an organization of any kind) the license created by the Order Confirmation and these terms and conditions or any rights granted hereunder; provided, however, that User may assign such license in its entirety on written notice to CCC in the event of a transfer of all or substantially all of User's rights in the new material which includes the Work(s) licensed under this Service.

    8.4. No amendment or waiver of any terms is binding unless set forth in writing and signed by the parties. The Rightsholder and CCC hereby object to any terms contained in any writing prepared by the User or its principals, employees, agents or affiliates and purporting to govern or otherwise relate to the licensing transaction described in the Order Confirmation, which terms are in any way inconsistent with any terms set forth in the Order Confirmation and/or in these terms and conditions or CCC's standard operating procedures, whether such writing is prepared prior to, simultaneously with or subsequent to the Order Confirmation, and whether such writing appears on a copy of the Order Confirmation or in a separate instrument.

    8.5. The licensing transaction described in the Order Confirmation document shall be governed by and construed under the law of the State of New York, USA, without regard to the principles thereof of conflicts of law. Any case, controversy, suit, action, or proceeding arising out of, in connection with, or related to such licensing transaction shall be brought, at CCC's sole discretion, in any federal or state court located in the County of New York, State of New York, USA, or in any federal or state court whose geographical jurisdiction covers the location of the Rightsholder set forth in the Order Confirmation. The parties expressly submit to the personal jurisdiction and venue of each such federal or state court.If you have any comments or questions about the Service or Copyright Clearance Center, please contact us at 978-750-8400 or send an e-mail to support@copyright.com.

v 1.1

American Physical Society
Reuse and Permissions License

06-Jul-2020

This license agreement between the American Physical Society ("APS") and Darren Pereira ("You") consists of your license details and the terms and conditions provided by the American Physical Society and SciPris.

Licensed Content Information

License Number:	**RNP/20/JUL/027833**
License date:	06-Jul-2020
DOI:	10.1103/PhysRevB.95.094422
Title:	Theory of multiple-phase competition in pyrochlore magnets with anisotropic exchange with application to ${\mathrm{Yb}}_{2}{\mathrm{Ti}}_{2}{\mathrm{O}}_{7},{\mathrm{Er}}_{2}{\mathrm{Ti}}_{2}{\mathrm{O}}_{7}$, and ${\mathrm{Er}}_{2}{\mathrm{Sn}}_{2}{\mathrm{O}}_{7}$
Author:	Han Yan et al.
Publication:	Physical Review B
Publisher:	American Physical Society
Cost:	USD $ 0.00

Request Details

Does your reuse require significant modifications: No

Specify intended distribution locations:	Worldwide (Online)
Reuse Category:	Reuse in a thesis/dissertation
Requestor Type:	Student
Items for Reuse:	Figures/Tables
Number of Figure/Tables:	1
Figure/Tables Details:	Classical ground-state phase diagram for a pyrochlore magnet with anisotropic exchange interactions.
Format for Reuse:	Electronic

Information about New Publication:

University/Publisher:	University of Waterloo
Title of dissertation/thesis:	Studies of Reentrance in Pyrochlore Magnets and Machine Learning of Quenched Gauge Symmetries
Author(s):	Darren Pereira
Expected completion date:	Aug. 2020

License Requestor Information

Name:	Darren Pereira
Affiliation:	Individual
Email Id:	d22perei@uwaterloo.ca
Country:	Canada

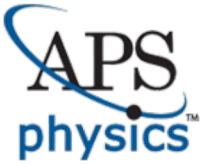

American Physical Society
Reuse and Permissions License

TERMS AND CONDITIONS

The American Physical Society (APS) is pleased to grant the Requestor of this license a non-exclusive, non-transferable permission, limited to Electronic format, provided all criteria outlined below are followed.

1. You must also obtain permission from at least one of the lead authors for each separate work, if you haven't done so already. The author's name and affiliation can be found on the first page of the published Article.

2. For electronic format permissions, Requestor agrees to provide a hyperlink from the reprinted APS material using the source material's DOI on the web page where the work appears. The hyperlink should use the standard DOI resolution URL, http://dx.doi.org/{DOI}. The hyperlink may be embedded in the copyright credit line.

3. For print format permissions, Requestor agrees to print the required copyright credit line on the first page where the material appears: "Reprinted (abstract/excerpt/figure) with permission from [(FULL REFERENCE CITATION) as follows: Author's Names, APS Journal Title, Volume Number, Page Number and Year of Publication.] Copyright (YEAR) by the American Physical Society."

4. Permission granted in this license is for a one-time use and does not include permission for any future editions, updates, databases, formats or other matters. Permission must be sought for any additional use.

5. Use of the material does not and must not imply any endorsement by APS.

6. APS does not imply, purport or intend to grant permission to reuse materials to which it does not hold copyright. It is the requestor's sole responsibility to ensure the licensed material is original to APS and does not contain the copyright of another entity, and that the copyright notice of the figure, photograph, cover or table does not indicate it was reprinted by APS with permission from another source.

7. The permission granted herein is personal to the Requestor for the use specified and is not transferable or assignable without express written permission of APS. This license may not be amended except in writing by APS.

8. You may not alter, edit or modify the material in any manner.

9. You may translate the materials only when translation rights have been granted.

10. APS is not responsible for any errors or omissions due to translation.

11. You may not use the material for promotional, sales, advertising or marketing purposes.

12. The foregoing license shall not take effect unless and until APS or its agent, Aptara, receives payment in full in accordance with Aptara Billing and Payment Terms and Conditions, which are incorporated herein by reference.

13. Should the terms of this license be violated at any time, APS or Aptara may revoke the license with no refund to you and seek relief to the fullest extent of the laws of the USA. Official written notice will be made using the contact information provided with the permission request. Failure to receive such notice will not nullify revocation of the permission.

14. APS reserves all rights not specifically granted herein.

15. This document, including the Aptara Billing and Payment Terms and Conditions, shall be the entire agreement between the parties relating to the subject matter hereof.

American Physical Society
Reuse and Permissions License

06-Jul-2020

This license agreement between the American Physical Society ("APS") and Darren Pereira ("You") consists of your license details and the terms and conditions provided by the American Physical Society and SciPris.

Licensed Content Information

License Number:	**RNP/20/JUL/027834**
License date:	06-Jul-2020
DOI:	10.1103/PhysRevB.70.012402
Title:	Magnetic phase diagram of the antiferromagnetic pyrochlore ${\text{Gd}}_{2}{\text{Ti}}_{2}{\mathrm{O}}_{7}$
Author:	O. A. Petrenko et al.
Publication:	Physical Review B
Publisher:	American Physical Society
Cost:	USD $ 0.00

Request Details

Does your reuse require significant modifications: No

Specify intended distribution locations:	Worldwide (Online)
Reuse Category:	Reuse in a thesis/dissertation
Requestor Type:	Student
Items for Reuse:	Figures/Tables
Number of Figure/Tables:	4
Figure/Tables Details:	Magnetic phase diagrams of Gd2Ti2O7 for three different orientations of an applied magnetic field.
Format for Reuse:	Electronic

Information about New Publication:

University/Publisher:	University of Waterloo
Title of dissertation/thesis:	Studies of Reentrance in Pyrochlore Magnets and Machine Learning of Quenched Gauge Symmetries
Author(s):	Darren Pereira
Expected completion date:	Aug. 2020

License Requestor Information

Name:	Darren Pereira
Affiliation:	Individual
Email Id:	d22perei@uwaterloo.ca
Country:	Canada

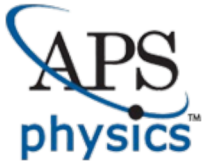

American Physical Society
Reuse and Permissions License

TERMS AND CONDITIONS

The American Physical Society (APS) is pleased to grant the Requestor of this license a non-exclusive, non-transferable permission, limited to Electronic format, provided all criteria outlined below are followed.

1. You must also obtain permission from at least one of the lead authors for each separate work, if you haven't done so already. The author's name and affiliation can be found on the first page of the published Article.

2. For electronic format permissions, Requestor agrees to provide a hyperlink from the reprinted APS material using the source material's DOI on the web page where the work appears. The hyperlink should use the standard DOI resolution URL, http://dx.doi.org/{DOI}. The hyperlink may be embedded in the copyright credit line.

3. For print format permissions, Requestor agrees to print the required copyright credit line on the first page where the material appears: "Reprinted (abstract/excerpt/figure) with permission from [(FULL REFERENCE CITATION) as follows: Author's Names, APS Journal Title, Volume Number, Page Number and Year of Publication.] Copyright (YEAR) by the American Physical Society."

4. Permission granted in this license is for a one-time use and does not include permission for any future editions, updates, databases, formats or other matters. Permission must be sought for any additional use.

5. Use of the material does not and must not imply any endorsement by APS.

6. APS does not imply, purport or intend to grant permission to reuse materials to which it does not hold copyright. It is the requestor's sole responsibility to ensure the licensed material is original to APS and does not contain the copyright of another entity, and that the copyright notice of the figure, photograph, cover or table does not indicate it was reprinted by APS with permission from another source.

7. The permission granted herein is personal to the Requestor for the use specified and is not transferable or assignable without express written permission of APS. This license may not be amended except in writing by APS.

8. You may not alter, edit or modify the material in any manner.

9. You may translate the materials only when translation rights have been granted.

10. APS is not responsible for any errors or omissions due to translation.

11. You may not use the material for promotional, sales, advertising or marketing purposes.

12. The foregoing license shall not take effect unless and until APS or its agent, Aptara, receives payment in full in accordance with Aptara Billing and Payment Terms and Conditions, which are incorporated herein by reference.

13. Should the terms of this license be violated at any time, APS or Aptara may revoke the license with no refund to you and seek relief to the fullest extent of the laws of the USA. Official written notice will be made using the contact information provided with the permission request. Failure to receive such notice will not nullify revocation of the permission.

14. APS reserves all rights not specifically granted herein.

15. This document, including the Aptara Billing and Payment Terms and Conditions, shall be the entire agreement between the parties relating to the subject matter hereof.

American Physical Society
Reuse and Permissions License

06-Jul-2020

This license agreement between the American Physical Society ("APS") and Darren Pereira ("You") consists of your license details and the terms and conditions provided by the American Physical Society and SciPris.

Licensed Content Information

License Number:	**RNP/20/JUL/027835**
License date:	06-Jul-2020
DOI:	10.1103/PhysRevB.95.174438
Title:	Magnetic properties of the triangular lattice magnets ${A}_{4}{B}^{'}{B}_{2}{\mathrm{O}}_{12}$ ($A=\mathrm{Ba}$, Sr, La; ${B}^{'}=\mathrm{Co}$, Ni, Mn; $B=\mathrm{W}$, Re)
Author:	R. Rawl et al.
Publication:	Physical Review B
Publisher:	American Physical Society
Cost:	USD $ 0.00

Request Details

Does your reuse require significant modifications: No

Specify intended distribution locations:	Worldwide (Online)
Reuse Category:	Reuse in a thesis/dissertation
Requestor Type:	Student
Items for Reuse:	Figures/Tables
Number of Figure/Tables:	9
Figure/Tables Details:	Magnetic phase diagram of Ba2La2MnW2O12.
Format for Reuse:	Electronic

Information about New Publication:

University/Publisher:	University of Waterloo
Title of dissertation/thesis:	Studies of Reentrance in Pyrochlore Magnets and Machine Learning of Quenched Gauge Symmetries
Author(s):	Darren Pereira
Expected completion date:	Aug. 2020

License Requestor Information

Name:	Darren Pereira
Affiliation:	Individual
Email Id:	d22perei@uwaterloo.ca
Country:	Canada

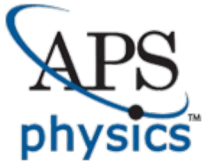

American Physical Society
Reuse and Permissions License

TERMS AND CONDITIONS

The American Physical Society (APS) is pleased to grant the Requestor of this license a non-exclusive, non-transferable permission, limited to Electronic format, provided all criteria outlined below are followed.

1. You must also obtain permission from at least one of the lead authors for each separate work, if you haven't done so already. The author's name and affiliation can be found on the first page of the published Article.

2. For electronic format permissions, Requestor agrees to provide a hyperlink from the reprinted APS material using the source material's DOI on the web page where the work appears. The hyperlink should use the standard DOI resolution URL, http://dx.doi.org/{DOI}. The hyperlink may be embedded in the copyright credit line.

3. For print format permissions, Requestor agrees to print the required copyright credit line on the first page where the material appears: "Reprinted (abstract/excerpt/figure) with permission from [(FULL REFERENCE CITATION) as follows: Author's Names, APS Journal Title, Volume Number, Page Number and Year of Publication.] Copyright (YEAR) by the American Physical Society."

4. Permission granted in this license is for a one-time use and does not include permission for any future editions, updates, databases, formats or other matters. Permission must be sought for any additional use.

5. Use of the material does not and must not imply any endorsement by APS.

6. APS does not imply, purport or intend to grant permission to reuse materials to which it does not hold copyright. It is the requestor's sole responsibility to ensure the licensed material is original to APS and does not contain the copyright of another entity, and that the copyright notice of the figure, photograph, cover or table does not indicate it was reprinted by APS with permission from another source.

7. The permission granted herein is personal to the Requestor for the use specified and is not transferable or assignable without express written permission of APS. This license may not be amended except in writing by APS.

8. You may not alter, edit or modify the material in any manner.

9. You may translate the materials only when translation rights have been granted.

10. APS is not responsible for any errors or omissions due to translation.

11. You may not use the material for promotional, sales, advertising or marketing purposes.

12. The foregoing license shall not take effect unless and until APS or its agent, Aptara, receives payment in full in accordance with Aptara Billing and Payment Terms and Conditions, which are incorporated herein by reference.

13. Should the terms of this license be violated at any time, APS or Aptara may revoke the license with no refund to you and seek relief to the fullest extent of the laws of the USA. Official written notice will be made using the contact information provided with the permission request. Failure to receive such notice will not nullify revocation of the permission.

14. APS reserves all rights not specifically granted herein.

15. This document, including the Aptara Billing and Payment Terms and Conditions, shall be the entire agreement between the parties relating to the subject matter hereof.

References

[1] P. Fazekas, *Lecture Notes on Electron Correlation and Magnetism* (World Scientific Publishing, 1999).

[2] J. G. Rau and M. J. P. Gingras, "Frustrated Quantum Rare-Earth Pyrochlores", Annu. Rev. Condens. Matter Phys. **10**, 357 (2019).

[3] A. Kitaev, "Anyons in an exactly solved model and beyond", Ann. Physics **321**, 2 (2006).

[4] J. S. Gardner, M. J. P. Gingras, and J. E. Greedan, "Magnetic pyrochlore oxides", Rev. Mod. Phys. **82**, 53 (2010).

[5] A. M. Hallas, J. Gaudet, and B. D. Gaulin, "Experimental Insights into Ground-State Selection of Quantum XY Pyrochlores", Annu. Rev. Condens. Matter Phys. **9**, 105 (2018).

[6] M. J. Harris, S. T. Bramwell, D. F. McMorrow, T. Zeiske, and K. W. Godfrey, "Geometrical Frustration in the Ferromagnetic Pyrochlore $Ho_2Ti_2O_7$", Phys. Rev. Lett. **79**, 2554 (1997).

[7] S. T. Bramwell, M. J. Harris, B. C. den Hertog, M. J. P. Gingras, J. S. Gardner, D. F. McMorrow, A. R. Wildes, A. L. Cornelius, J. D. M. Champion, R. G. Melko, and T. Fennell, "Spin Correlations in $Ho_2Ti_2O_7$: A Dipolar Spin Ice System", Phys. Rev. Lett. **87**, 047205 (2001).

[8] S. T. Bramwell and M. J. P. Gingras, "Spin Ice State in Frustrated Magnetic Pyrochlore Materials", Science **294**, 1495 (2001).

[9] M. Gingras, "Spin Ice", in *Introduction to Frustrated Magnetism*, edited by C. Lacroix, P. Mendels, and F. Mila (Springer-Verlag Berlin Heidelberg, 2011) Chap. 12.

[10] A. P. Ramirez, A. Hayashi, R. J. Cava, R. Siddharthan, and B. S. Shastry, "Zero-point entropy in 'spin ice'", Nature **399**, 333 (1999).

[11] J. G. Rau and M. J. P. Gingras, "Magnitude of quantum effects in classical spin ices", Phys. Rev. B **92**, 144417 (2015).

[12] L. Pauling, "The Structure and Entropy of Ice and of Other Crystals with Some Randomness of Atomic Arrangement", J. Am. Chem. Soc. **57**, 2680 (1935).

[13] V. N. Glazkov, M. Zhitomirsky, A. I. Smirnov, C. Marin, J.-P. Sanchez, A. Forget, D. Colson, and P. Bonville, "Single-ion anisotropy and transverse magnetization in the frustrated gadolinium pyrochlores", J. Phys. Condens. Matter **19**, 145271 (2007).

[14] V. N. Glazkov, M. E. Zhitomirsky, A. I. Smirnov, H.-A. Krug von Nidda, A. Loidl, C. Marin, and J.-P. Sanchez, "Single-ion anisotropy in the gadolinium pyrochlores studied by electron paramagnetic resonance", Phys. Rev. B **72**, 020409 (2005).

[15] N. P. Raju, M. Dion, M. J. P. Gingras, T. E. Mason, and J. E. Greedan, "Transition to long-range magnetic order in the highly frustrated insulating pyrochlore antiferromagnet $Gd_2Ti_2O_7$", Phys. Rev. B **59**, 14489 (1999).

[16] J. D. Cashion, A. H. Cooke, M. J. M. Leask, T. L. Thorp, and M. R. Wells, "Crystal growth and magnetic susceptibility of some rare-earth compounds", J. Mater. Sci. **3**, 402 (1968).

[17] R. Moessner and J. T. Chalker, "Properties of a Classical Spin Liquid: The Heisenberg Pyrochlore Antiferromagnet", Phys. Rev. Lett. **80**, 2929 (1998).

[18] S. E. Palmer and J. T. Chalker, "Order induced by dipolar interactions in a geometrically frustrated antiferromagnet", Phys. Rev. B **62**, 488 (2000).

[19] A. P. Ramirez, B. S. Shastry, A. Hayashi, J. J. Krajewski, D. A. Huse, and R. J. Cava, "Multiple Field-Induced Phase Transitions in the Geometrically Frustrated Dipolar Magnet: $Gd_2Ti_2O_7$", Phys. Rev. Lett. **89**, 067202 (2002).

[20] J. D. M. Champion, A. S. Wills, T. Fennell, S. T. Bramwell, J. S. Gardner, and M. A. Green, "Order in the Heisenberg pyrochlore: The magnetic structure of $Gd_2Ti_2O_7$", Phys. Rev. B **64**, 140407 (2001).

[21] V. Bondah-Jagalu and S. T. Bramwell, "Magnetic susceptibility study of the heavy rare-earth stannate pyrochlores", Can. J. Phys. **79**, 11 (2001).

[22] P. Bonville, J. A. Hodges, E. Bertin, J.-P. Bouchaud, P. Dalmas de Réotier, L.-P. Regnault, H. M. Rønnow, J.-P. Sanchez, S. Sosin, and A. Yaouanc, "Transitions and Spin Dynamics at Very Low Temperature in the Pyrochlores $Yb_2Ti_2O_7$ and $Gd_2Sn_2O_7$", Hyperfine Interact. **156**, 103 (2004).

[23] A. S. Wills, M. E. Zhitomirsky, B. Canals, J.-P. Sanchez, P. Bonville, P. Dalmas de Réotier, and A. Yaouanc, "Magnetic ordering in $Gd_2Sn_2O_7$: the archetypal Heisenberg pyrochlore antiferromagnet", J. Phys. Condens. Matter **18**, L37 (2006).

[24] H. Yan, O. Benton, L. Jaubert, and N. Shannon, "Theory of multiple-phase competition in pyrochlore magnets with anisotropic exchange with application to $Yb_2Ti_2O_7$, $Er_2Ti_2O_7$, and $Er_2Sn_2O_7$", Phys. Rev. B **95**, 094422 (2017).

[25] J. D. M. Champion, M. J. Harris, P. C. W. Holdsworth, A. S. Wills, G. Balakrishnan, S. T. Bramwell, E. Čižmár, T. Fennell, J. S. Gardner, J. Lago, D. F. McMorrow, M. Orendáč, A. Orendáčová, D. M. Paul, R. I. Smith, M. T. F. Telling, and A. Wildes, "$Er_2Ti_2O_7$: Evidence of quantum order by disorder in a frustrated antiferromagnet", Phys. Rev. B **68**, 020401 (2003).

[26] L. Savary, K. A. Ross, B. D. Gaulin, J. P. C. Ruff, and L. Balents, "Order by Quantum Disorder in $Er_2Ti_2O_7$", Phys. Rev. Lett. **109**, 167201 (2012).

[27] M. E. Zhitomirsky, M. V. Gvozdikova, P. C. W. Holdsworth, and R. Moessner, "Quantum Order by Disorder and Accidental Soft Mode in $Er_2Ti_2O_7$", Phys. Rev. Lett. **109**, 077204 (2012).

[28] J. Oitmaa, R. R. P. Singh, B. Javanparast, A. G. R. Day, B. V. Bagheri, and M. J. P. Gingras, "Phase transition and thermal order-by-disorder in the pyrochlore antiferromagnet $Er_2Ti_2O_7$: A high-temperature series expansion study", Phys. Rev. B **88**, 220404 (2013).

[29] J. R. Tessman, "Magnetic Anisotropy at 0K", Phys. Rev. **96**, 1192 (1954).

[30] J. Villain, R. Bidaux, J.-P. Carton, and R. Conte, "Order as an effect of disorder", J. Phys. France **41**, 1263 (1980).

[31] A. Poole, A. S. Wills, and E. Lelièvre-Berna, "Magnetic ordering in the XY pyrochlore antiferromagnet $Er_2Ti_2O_7$: a spherical neutron polarimetry study", J. Phys. Condens. Matter **19**, 452201 (2007).

[32] J. G. Rau, S. Petit, and M. J. P. Gingras, "Order by virtual crystal field fluctuations in pyrochlore XY antiferromagnets", Phys. Rev. B **93**, 184408 (2016).

[33] K. A. Ross, L. Savary, B. D. Gaulin, and L. Balents, "Quantum Excitations in Quantum Spin Ice", Phys. Rev. X **1**, 021002 (2011).

[34] A. Scheie, J. Kindervater, S. Säubert, C. Duvinage, C. Pfleiderer, H. J. Changlani, S. Zhang, L. Harriger, K. Arpino, S. M. Koohpayeh, O. Tchernyshyov, and C. Broholm, "Reentrant Phase Diagram of $Yb_2Ti_2O_7$ in a 111 Magnetic Field", Phys. Rev. Lett. **119**, 127201 (2017).

[35] S. Säubert, A. Scheie, C. Duvinage, J. Kindervater, S. Zhang, H. J. Changlani, G. Xu, S. M. Koohpayeh, O. Tchernyshyov, C. L. Broholm, and C. Pfleiderer, "Orientation dependence of the magnetic phase diagram of $Yb_2Ti_2O_7$", Phys. Rev. B **101**, 174434 (2020).

[36] W. H. Toews, J. A. Reid, J. D. Thompson, D. Prabhakaran, R. Coldea, and R. W. Hill, "Low-temperature thermal transport measurements of oxygen-annealed $Yb_2Ti_2O_7$", Phys. Rev. B **102**, 014434 (2020).

[37] J. D. Thompson, P. A. McClarty, D. Prabhakaran, I. Cabrera, T. Guidi, and R. Coldea, "Quasiparticle Breakdown and Spin Hamiltonian of the Frustrated Quantum Pyrochlore $Yb_2Ti_2O_7$ in a Magnetic Field", Phys. Rev. Lett. **119**, 057203 (2017).

[38] J. A. Hodges, P. Bonville, A. Forget, A. Yaouanc, P. Dalmas de Réotier, G. André, M. Rams, K. Królas, C. Ritter, P. C. M. Gubbens, C. T. Kaiser, P. J. C. King, and C. Baines, "First-Order Transition in the Spin Dynamics of Geometrically Frustrated $Yb_2Ti_2O_7$", Phys. Rev. Lett. **88**, 077204 (2002).

[39] A. Yaouanc, P. Dalmas de Réotier, C. Marin, and V. Glazkov, "Single-crystal versus polycrystalline samples of magnetically frustrated $Yb_2Ti_2O_7$: Specific heat results", Phys. Rev. B **84**, 172408 (2011).

[40] K. E. Arpino, B. A. Trump, A. O. Scheie, T. M. McQueen, and S. M. Koohpayeh, "Impact of stoichiometry of $Yb_2Ti_2O_7$ on its physical properties", Phys. Rev. B **95**, 094407 (2017).

[41] G. Sala, M. J. Gutmann, D. Prabhakaran, D. Pomaranski, C. Mitchelitis, J. B. Kycia, D. G. Porter, C. Castelnovo, and J. P. Goff, "Vacancy defects and monopole dynamics in oxygen-deficient pyrochlores", Nat. Mater. **13**, 488 (2014).

[42] L. D. C. Jaubert, O. Benton, J. G. Rau, J. Oitmaa, R. R. P. Singh, N. Shannon, and M. J. P. Gingras, "Are Multiphase Competition and Order by Disorder the Keys to Understanding $Yb_2Ti_2O_7$?", Phys. Rev. Lett. **115**, 267208 (2015).

[43] H. J. Changlani, "Quantum versus classical effects at zero and finite temperature in the quantum pyrochlore $Yb_2Ti_2O_7$", arXiv:1710.02234 .

[44] M. Powell, L. D. Sanjeewa, C. D. McMillen, K. A. Ross, C. L. Sarkis, and J. W. Kolis, "Hydrothermal Crystal Growth of Rare Earth Tin Cubic Pyrochlores, $RE_2Sn_2O_7$ (RE = La – Lu): Site Ordered, Low Defect Single Crystals", Cryst. Growth Des. **19**, 4920 (2019).

[45] M. A. Subramanian, G. Aravamudan, and G. V. Subba Rao, "Oxide pyrochlores – a review", Prog. Solid State Chem **15**, 55 (1983).

[46] D. Prabhakaran, S. Wang, and A. T. Boothroyd, "Crystal growth of pyrochlore rare-earth stannates", J. Cryst. Growth **468**, 335 (2017).

[47] J. Gaudet, A. M. Hallas, A. I. Kolesnikov, and B. D. Gaulin, "Effect of chemical pressure on the crystal electric field states of erbium pyrochlore magnets", Phys. Rev. B **97**, 024415 (2018).

[48] S. Guitteny, S. Petit, E. Lhotel, J. Robert, P. Bonville, A. Forget, and I. Mirebeau, "Palmer-Chalker correlations in the XY pyrochlore antiferromagnet $Er_2Sn_2O_7$", Phys. Rev. B **88**, 134408 (2013).

[49] S. Petit, E. Lhotel, F. Damay, P. Boutrouille, A. Forget, and D. Colson, "Long-Range Order in the Dipolar XY Antiferromagnet $Er_2Sn_2O_7$", Phys. Rev. Lett. **119**, 187202 (2017).

[50] O. A. Petrenko, M. R. Lees, G. Balakrishnan, and D. M. Paul, "Magnetic phase diagram of the antiferromagnetic pyrochlore $Gd_2Ti_2O_7$", Phys. Rev. B **70**, 012402 (2004).

[51] Y. Kasahara, T. Ohnishi, Y. Mizukami, O. Tanaka, S. Ma, K. Sugii, N. Kurita, H. Tanaka, J. Nasu, Y. Motome, T. Shibauchi, and Y. Matsuda, "Majorana quantization and half-integer thermal quantum Hall effect in a Kitaev spin liquid", Nature **559**, 227 (2018).

[52] J. A. Sears, M. Songvilay, K. W. Plumb, J. P. Clancy, Y. Qiu, Y. Zhao, D. Parshall, and Y.-J. Kim, "Magnetic order in $\alpha-RuCl_3$: A honeycomb-lattice quantum magnet with strong spin-orbit coupling", Phys. Rev. B **91**, 144420 (2015).

[53] A. Scheie, "LongHCPulse: Long-Pulse Heat Capacity on a Quantum Design PPMS", J. Low Temp. Phys. **193**, 60 (2018).

[54] H. T. Diep, *Magnetic Systems with Competing Interactions (Frustrated Spin Systems)* (World Scientific Publishing, 1994).

[55] C. A. Vause and J. S. Walker, "Reappearing Phases", Sci. Am. **256**, 98 (1987).

[56] M. J. P. Gingras and E. S. Sørensen, "Evidence for a genuine ferromagnetic to paramagnetic reentrant phase transition in a Potts spin-glass model", Phys. Rev. B **57**, 10264 (1998).

[57] I. V. Lebedeva and A. M. Popov, "Two Phases with Different Domain Wall Networks and a Reentrant Phase Transition in Bilayer Graphene under Strain", Phys. Rev. Lett. **124**, 116101 (2020).

[58] S. Singh, "Reentrant phase transitions in liquid crystals", Phase Transit. **72**, 183 (2000).

[59] T. H. Lin, X. Y. Shao, M. K. Wu, P. H. Hor, X. C. Jin, C. W. Chu, N. Evans, and R. Bayuzick, "Observation of a reentrant superconducting resistive transition in granular $BaPb_{0.75}Bi_{0.25}O_3$ superconductor", Phys. Rev. B **29**, 1493 (1984).

[60] C. L. Dias, T. Ala-Nissila, J. Wong-ekkabut, I. Vattulainen, M. Grant, and M. Karttunen, "The hydrophobic effect and its role in cold denaturation", Cryobiology **60**, 91 (2010).

[61] J. M. D. Coey, *Magnetism and Magnetic Materials* (Cambridge University Press, 2009).

[62] J. J. Sakurai and J. Napolitano, *Modern Quantum Mechanics*, 2nd ed. (Addison-Wesley, 2011).

[63] J. Jensen and A. R. Mackintosh, *Rare Earth Magnetism* (Clarendon Press, 1991).

[64] C. L. Sarkis, J. G. Rau, L. D. Sanjeewa, M. Powell, J. Kolis, J. Marbey, S. Hill, J. A. Rodriguez-Rivera, H. S. Nair, M. J. P. Gingras, and K. A. Ross, "Unravelling competing microscopic interactions at a phase boundary: a single crystal study of the metastable antiferromagnetic pyrochlore $Yb_2Ge_2O_7$", arXiv:1912.09448 .

[65] J. D. Thompson, P. A. McClarty, H. M. Rønnow, L. P. Regnault, A. Sorge, and M. J. P. Gingras, "Rods of Neutron Scattering Intensity in $Yb_2Ti_2O_7$: Compelling Evidence for Significant Anisotropic Exchange in a Magnetic Pyrochlore Oxide", Phys. Rev. Lett. **106**, 187202 (2011).

[66] O. Rodrigues, "Des lois géométriques qui régissent les déplacements d'un système solide dans l'espace, et de la variation des coordonnées provenant de ces déplacements considérés indépendants des causes qui peuvent les produire", J. Math. Pures Appl. **5**, 380 (1840).

[67] J. O. Benton, *Classical and quantum spin liquids on the pyrochlore lattice*, Ph.D. thesis, University of Bristol (2015).

[68] F.-Y. Li, Y.-D. Li, Y. Yu, A. Paramekanti, and G. Chen, "Kitaev materials beyond iridates: Order by quantum disorder and Weyl magnons in rare-earth double perovskites", Phys. Rev. B **95**, 085132 (2017).

[69] J. Xing, E. Feng, Y. Liu, E. Emmanouilidou, C. Hu, J. Liu, D. Graf, A. P. Ramirez, G. Chen, H. Cao, and N. Ni, "Néel-type antiferromagnetic order and magnetic field–temperature phase diagram in the spin-$\frac{1}{2}$ rare-earth honeycomb compound $YbCl_3$", Phys. Rev. B **102**, 014427 (2020).

[70] S. Zhang, H. J. Changlani, K. W. Plumb, O. Tchernyshyov, and R. Moessner, "Dynamical Structure Factor of the Three-Dimensional Quantum Spin Liquid Candidate $NaCaNi_2F_7$", Phys. Rev. Lett. **122**, 167203 (2019).

[71] J. N. Reimers, A. J. Berlinsky, and A.-C. Shi, "Mean-field approach to magnetic ordering in highly frustrated pyrochlores", Phys. Rev. B **43**, 865 (1991).

[72] M. Enjalran and M. J. P. Gingras, "Theory of paramagnetic scattering in highly frustrated magnets with long-range dipole-dipole interactions: The case of the $Tb_2Ti_2O_7$ pyrochlore antiferromagnet", Phys. Rev. B **70**, 174426 (2004).

[73] M. Enjalran, A. Del Maestro, and M. J. P. Gingras, "Mean-Field Theory of the Soft Mode Spectrum and Field-Driven Transitions in a Dipolar Heisenberg Pyrochlore Antiferromagnet Model", unpublished (2012).

[74] P. Ewald, "Evaluation of optical and electrostatic lattice potentials", Ann. Phys. (Leipzig) **64**, 253 (2018).

[75] J. A. Olive, A. P. Young, and D. Sherrington, "Computer simulation of the three-dimensional short-range Heisenberg spin glass", Phys. Rev. B **34**, 6341 (1986).

[76] V. S. Maryasin, M. E. Zhitomirsky, and R. Moessner, "Low-field behavior of an XY pyrochlore antiferromagnet: Emergent clock anisotropies", Phys. Rev. B **93**, 100406 (2016).

[77] R. Rawl, M. Lee, E. S. Choi, G. Li, K. W. Chen, R. Baumbach, C. R. dela Cruz, J. Ma, and H. D. Zhou, "Magnetic properties of the triangular lattice magnets $A_4B'B_2O_{12}$ (A = Ba, Sr, La; B' = Co, Ni, Mn; B = W, Re)", Phys. Rev. B **95**, 174438 (2017).

[78] S. Ghosh, M. Matty, R. Baumbach, E. D. Bauer, K. A. Modic, A. Shekhter, J. A. Mydosh, E.-A. Kim, and B. J. Ramshaw, "One-component order parameter in URu_2Si_2 uncovered by resonant ultrasound spectroscopy and machine learning", Sci. Adv **6**, eaaz4074 (2020).

[79] Y. Zhang, A. Mesaros, K. Fujita, S. D. Edkins, M. H. Hamidian, K. Ch'ng, H. Eisaki, S. Uchida, J. C. Séamus Davis, E. Khatami, and E.-A. Kim, "Machine learning in electronic-quantum-matter imaging experiments", Nature **570**, 484 (2019).

[80] G. Carleo, I. Cirac, K. Cranmer, L. Daudet, M. Schuld, N. Tishby, L. Vogt-Maranto, and L. Zdeborová, "Machine learning and the physical sciences", Rev. Mod. Phys. **91**, 045002 (2019).

[81] Y. Bahri, J. Kadmon, J. Pennington, S. S. Schoenholz, J. Sohl-Dickstein, and S. Ganguli, "Statistical Mechanics of Deep Learning", Annu. Rev. Condens. Matter Phys. **11**, 501 (2019).

[82] P. Mehta, M. Bukov, C.-H. Wang, A. G. R. Day, C. Richardson, C. K. Fisher, and D. J. Schwab, "A high-bias, low-variance introduction to Machine Learning for physicists", Phys. Rep. **810**, 1 (2019).

[83] L.-F. Arsenault, A. Lopez-Bezanilla, O. A. von Lilienfeld, and A. J. Millis, "Machine learning for many-body physics: The case of the Anderson impurity model", Phys. Rev. B **90**, 155136 (2014).

[84] S. V. Kalinin, B. G. Sumpter, and R. K. Archibald, "Big-deep-smart data in imaging for guiding materials design", Nat. Mater. **14**, 973 (2015).

[85] L. M. Ghiringhelli, J. Vybiral, S. V. Levchenko, C. Draxl, and M. Scheffler, "Big Data of Materials Science: Critical Role of the Descriptor", Phys. Rev. Lett. **114**, 105503 (2015).

[86] J. Carrasquilla and R. G. Melko, "Machine learning phases of matter", Nat. Phys **13**, 431 (2017).

[87] L. Wang, "Discovering phase transitions with unsupervised learning", Phys. Rev. B **94**, 195105 (2016).

[88] M. Matty, Y. Zhang, Z. Papić, and E.-A. Kim, "Multifaceted machine learning of competing orders in disordered interacting systems", Phys. Rev. B **100**, 155141 (2019).

[89] J. Venderley, V. Khemani, and E.-A. Kim, "Machine Learning Out-of-Equilibrium Phases of Matter", Phys. Rev. Lett. **120**, 257204 (2018).

[90] J. Greitemann, K. Liu, and L. Pollet, "Probing hidden spin order with interpretable machine learning", Phys. Rev. B **99**, 060404 (2019).

[91] M. J. S. Beach, A. Golubeva, and R. G. Melko, "Machine learning vortices at the Kosterlitz-Thouless transition", Phys. Rev. B **97**, 045207 (2018).

[92] J. Greitemann, K. Liu, L. D. C. Jaubert, H. Yan, N. Shannon, and L. Pollet, "Identification of emergent constraints and hidden order in frustrated magnets using tensorial kernel methods of machine learning", Phys. Rev. B **100**, 174408 (2019).

[93] P. Ponte and R. G. Melko, "Kernel methods for interpretable machine learning of order parameters", Phys. Rev. B **96**, 205146 (2017).

[94] K. Liu, J. Greitemann, and L. Pollet, "Learning multiple order parameters with interpretable machines", Phys. Rev. B **99**, 104410 (2019).

[95] H. Théveniaut and F. Alet, "Neural network setups for a precise detection of the many-body localization transition: Finite-size scaling and limitations", Phys. Rev. B **100**, 224202 (2019).

[96] A. Canabarro, S. Brito, and R. Chaves, "Machine Learning Nonlocal Correlations", Phys. Rev. Lett. **122**, 200401 (2019).

[97] X. Liang, W.-Y. Liu, P.-Z. Lin, G.-C. Guo, Y.-S. Zhang, and L. He, "Solving frustrated quantum many-particle models with convolutional neural networks", Phys. Rev. B **98**, 104426 (2018).

[98] A. Decelle, V. Martin-Mayor, and B. Seoane, "Learning a local symmetry with neural networks", Phys. Rev. E **100**, 050102 (2019).

[99] C. Casert, T. Vieijra, J. Nys, and J. Ryckebusch, "Interpretable machine learning for inferring the phase boundaries in a nonequilibrium system", Phys. Rev. E **99**, 023304 (2019).

[100] A. Canabarro, F. F. Fanchini, A. L. Malvezzi, R. Pereira, and R. Chaves, "Unveiling phase transitions with machine learning", Phys. Rev. B **100**, 045129 (2019).

[101] S. J. Wetzel and M. Scherzer, "Machine learning of explicit order parameters: From the Ising model to $SU(2)$ lattice gauge theory", Phys. Rev. B **96**, 184410 (2017).

[102] C. Wang and H. Zhai, "Machine learning of frustrated classical spin models (I): Principal component analysis", Phys. Rev. B **96**, 144432 (2017).

[103] C. Wang and H. Zhai, "Machine learning of frustrated classical spin models (II): Kernel principal component analysis", Front. Phys. **13**, 130507 (2018).

[104] W. Hu, R. R. P. Singh, and R. T. Scalettar, "Discovering phases, phase transitions, and crossovers through unsupervised machine learning: A critical examination", Phys. Rev. E **95**, 062122 (2017).

[105] S. J. Wetzel, "Unsupervised learning of phase transitions: from principal component analysis to variational autoencoders", Phys. Rev. E **96**, 022140 (2017).

[106] Y. Wu and H. Zhai, "Generalized Independent Component Analysis for Extracting Eigen-Modes of a Quantum System", arXiv:1904.05067 .

[107] K.-W. Zhao, W.-H. Kao, K.-H. Wu, and Y.-J. Kao, "Generation of ice states through deep reinforcement learning", Phys. Rev. E **99**, 062106 (2019).

[108] H. Xu, J. Li, L. Liu, Y. Wang, H. Yuan, and X. Wang, "Generalizable control for quantum parameter estimation through reinforcement learning", npj Quantum Inf. **5**, 82 (2019).

[109] P. Mehta, M. Bukov, C.-H. Wang, A. G. R. Day, C. Richardson, C. K. Fisher, and D. J. Schwab, "A high-bias, low-variance introduction to Machine Learning for physicists", Phys. Rep. **810**, 1 (2019).

[110] V. Vanchurin, "Towards a theory of machine learning", arXiv:2004.09280 .

[111] K. H. Fischer and J. A. Hertz, *Spin Glasses* (Cambridge University Press, 1991).

[112] D. Mattis, "Solvable spin systems with random interactions", Physics Letters A **56**, 421 (1976).

[113] Y. Iwasaki, R. Sawada, V. Stanev, M. Ishida, A. Kirihara, Y. Omori, H. Someya, I. Takeuchi, E. Saitoh, and S. Yorozu, "Identification of advanced spin-driven thermoelectric materials via interpretable machine learning", npj Comput. Mater. **5**, 103 (2019).

[114] K. Pearson, "On lines and planes of closest fit to systems of points in space", Philos. Mag. **2**, 559 (1901).

[115] H. Nishimori, *Statistical Physics of Spin Glasses and Information Processing: An Introduction* (Oxford University Press, 2001).

APPENDICES

Appendix A

Pyrochlore Lattice Structure

As mentioned throughout this thesis, the pyrochlore lattice with chemical formula $A_2B_2O_7$ consists of interpenetrating networks of corner-sharing tetrahedra. The A-site and B-site ions both form these networks of tetrahedra, but since we consider B^{4+} ions that are nonmagnetic, we only focus on the network created by the A^{3+} rare-earth ions, as shown in Figures 1.2 and 1.3.

The lattice of magnetic ions can be formed by associating a tetrahedron with the sites of a FCC lattice. For example, one can consider the conventional cubic cell representation of the FCC lattice, which contains four FCC lattice points. One can then "attach" a tetrahedron to each of these points, leading to 16 sites (4 FCC lattice points $\times$ four tetrahedral sublattices) per conventional cubic cell. This results in Figure 1.2. By tiling this cell using the cubic primitive lattice vectors in each direction, one can create a system of $L \times L \times L = L^3$ cubic cells, for a total of $16L^3$ magnetic sites. Note that this construction creates what we call "up" tetrahedra. The space in between up tetrahedra also share four sites and form a tetrahedron of opposite orientation, which we call "down" tetrahedra, as shown in Figure 1.3. However, since the down tetrahedra are formed by connecting sites between up tetrahedra, they do not contribute any new sites of their own and do not stand apart as distinct tetrahedra. There are therefore still only $16L^3$ sites.

The usage of up and down tetrahedra is convenient for considering nearest-neighbor interactions. Consider an arbitrary site of the pyrochlore lattice, which has six nearest neighbors. If one thinks only in terms of up tetrahedra as in Figure 1.2, then three of these neighbors exist on the same tetrahedron of the site in consideration, while three exist on different tetrahedra. On the other hand, if one thinks in terms of up *and* down tetrahedra as in Figure 1.3, then this site is a vertex connecting an up and down tetrahedra. Hence,

three neighbors come from the connected up tetrahedron, while the remaining three come from the connected down tetrahedron. This latter picture is more convenient, since nearest-neighbor interactions on differently-oriented tetrahedra are related by a matrix transpose, as discussed in Section 2.2.

$\boldsymbol{r}_1$	$\frac{a}{4}(0,0,0)$
$\boldsymbol{r}_2$	$\frac{a}{4}(1,1,0)$
$\boldsymbol{r}_3$	$\frac{a}{4}(1,0,1)$
$\boldsymbol{r}_4$	$\frac{a}{4}(0,1,1)$

Table A.1: One convention for the four sublattice positions of a given tetrahedron. Note that a is the lattice constant.

One convention for the four sites of a tetrahedron is given in Table A.1 [73] and shown in Figure A.1. The generic position vector to a site on the pyrochlore lattice is then given by $\boldsymbol{r}_{ia} = \boldsymbol{R}_a + \boldsymbol{r}_i$, where a denotes an FCC point (or a tetrahedron) at position $\boldsymbol{R}_a$ and i denotes a sublattice index at a position $\boldsymbol{r}_i$ away from the FCC point. Note that, in this convention, sublattice 1 coincides with the origin when $\boldsymbol{R}_a = \boldsymbol{0}$.

$\boldsymbol{r}_0$	$\frac{a}{8}(1,1,1)$
$\boldsymbol{r}_1$	$\frac{a}{8}(1,-1,-1)$
$\boldsymbol{r}_2$	$\frac{a}{8}(-1,1,-1)$
$\boldsymbol{r}_3$	$\frac{a}{8}(-1,-1,1)$

Table A.2: A second convention for the four sublattice positions of a given tetrahedron, used more commonly in the recent literature. Note that a is the lattice constant.

An alternative convention for labelling the sublattice positions (which is commonly used in the recent literature [24, 33]) is given in Table A.2 and shown in Figure A.2. Note that, in this convention, the origin is located at the *center* of the tetrahedron when $\boldsymbol{R}_a = \boldsymbol{0}$, as shown in Figure A.2. These two conventions can be mapped onto one another by shifting sublattice 0 of this second convention to coincide with the origin. The resulting position vectors between the two conventions can then be mapped onto one another to establish the conversion from one convention to the other. In this thesis, we use the second convention, in keeping with the recent literature. However, for ease of display, we show up tetrahedra in our figures (e.g. Figure 2.2) as opposed to the defined down tetrahedron shown in Figure A.2. Note that, in this convention, the local axes associated with each sublattice can be taken as shown in Table A.3 [24, 33].

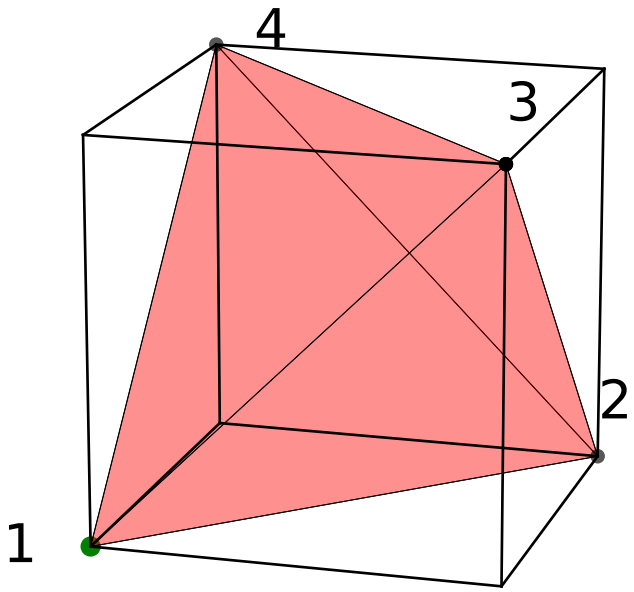

Figure A.1: One convention for the four sublattice positions of a given tetrahedron, as defined in Table A.1. The cube circumscribing the resulting tetrahedron is shown for reference. Note that the origin (green circle) coincides with sublattice 1. The tetrahedron is colored red to indicate it is an up tetrahedron.

Lastly, note that an alternative way to form the pyrochlore lattice is to use the primitive unit cell of the FCC lattice instead of the conventional cubic unit cell. The unit cell would then be tiled using the primitive lattice vectors of the FCC lattice instead of those of the simple cubic lattice. Since there is one FCC point per primitive lattice cell, this would generate $4L^3$ sites.

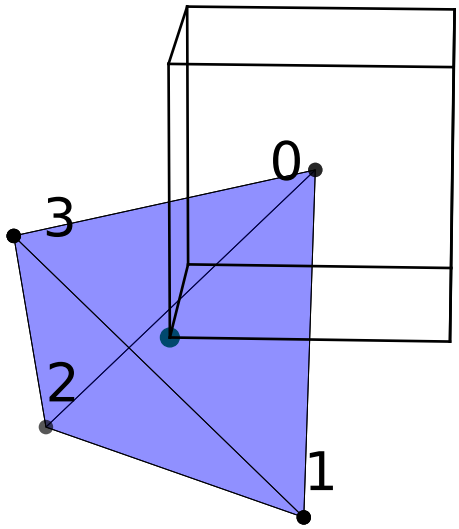

Figure A.2: Another convention for the four sublattice positions of a given tetrahedron, as defined in Table A.2. The same cube circumscribing the tetrahedron of Figure A.1 is shown for reference. Note that the origin (green circle) coincides with the center of the tetrahedron. The tetrahedron is colored blue to indicate it is a down tetrahedron.

	$\hat{\boldsymbol{x}}^{\text{local}}$	$\hat{\boldsymbol{y}}^{\text{local}}$	$\hat{\boldsymbol{z}}^{\text{local}}$
$\boldsymbol{r}_0$	$\frac{1}{\sqrt{6}}(-2,1,1)$	$\frac{1}{\sqrt{2}}(0,-1,1)$	$\frac{1}{\sqrt{3}}(1,1,1)$
$\boldsymbol{r}_1$	$\frac{1}{\sqrt{6}}(-2,-1,-1)$	$\frac{1}{\sqrt{2}}(0,1,-1)$	$\frac{1}{\sqrt{3}}(1,-1,-1)$
$\boldsymbol{r}_2$	$\frac{1}{\sqrt{6}}(2,1,-1)$	$\frac{1}{\sqrt{2}}(0,-1,-1)$	$\frac{1}{\sqrt{3}}(-1,1,-1)$
$\boldsymbol{r}_3$	$\frac{1}{\sqrt{6}}(2,-1,1)$	$\frac{1}{\sqrt{2}}(0,1,1)$	$\frac{1}{\sqrt{3}}(-1,-1,1)$

Table A.3: Convention for the local x-, y-, and z-axes at each of the four sublattice positions.

Appendix B

Methods for Quantum Spins

B.1 Variational Mean-Field Theory (VMFT) for Quantum Spins

The derivation in Chapter 3 focused on classical pseudospins described by normalized three-component vectors. However, one can easily generalize the process to quantum mechanical pseudospins with $S = \frac{1}{2}$ [33]. Start from Eq. (3.2) and assume that the spins S_{ia}^{μ} are now quantum mechanical operators. The mean-field ansatz in this case is to take $S_{ia}^{\mu} = \langle S_{ia}^{\mu} \rangle + \delta S_{ia}^{\mu}$, where $\delta S_{ia}^{\mu} = S_{ia}^{\mu} - \langle S_{ia}^{\mu} \rangle$, and to expand the Hamiltonian while ignoring contributions that are quadratic in the fluctuations δS_{ia}^{μ}. Again assuming $\boldsymbol{q} = 0$ order and no dipolar interactions, doing so gives:

$$\mathcal{H} = \frac{1}{2} \sum_{a,b} \sum_{i,j} \sum_{\mu,\nu} J_{ia,jb}^{\mu\nu} S_{ia}^{\mu} S_{jb}^{\nu} - \sum_{i,a} \boldsymbol{h}_{ia} \cdot \boldsymbol{S}_{ia} \tag{B.1}$$

$$\approx \frac{1}{2} \sum_{a,b} \sum_{i,j} \sum_{\mu,\nu} J_{ia,jb}^{\mu\nu} \left[-\langle S_{ia}^{\mu} \rangle \langle S_{jb}^{\nu} \rangle + S_{ia}^{\mu} \langle S_{jb}^{\nu} \rangle + \langle S_{ia}^{\mu} \rangle S_{jb}^{\nu} \right] - \sum_{i,a} \boldsymbol{h}_{ia} \cdot \boldsymbol{S}_{ia}. \tag{B.2}$$

Define $m_{ia}^{\mu} \equiv \langle S_{ia}^{\mu} \rangle$. Using the properties that $J_{jb,ia}^{\nu\mu} = J_{ia,jb}^{\mu\nu}$ and $g_i^{\mu\nu} = g_i^{\nu\mu}$, the mean-field Hamiltonian can be simplified into

$$\mathcal{H}_{\mathrm{MF}} = -\frac{1}{2} \sum_{a,b} \sum_{i,j} \sum_{\mu,\nu} J_{ia,jb}^{\mu\nu} m_{ia}^{\mu} m_{jb}^{\nu} - \sum_{i,a} \boldsymbol{B}_{ia} \cdot \boldsymbol{S}_{ia}, \tag{B.3}$$

where B_{ia}^{μ} is again defined by Eq. (3.27). The mean-field partition function Z_{MF} can be evaluated by tracing over the Boltzmann factor, $Z_{\mathrm{MF}} = \mathrm{Tr}\left\{ e^{-\beta \mathcal{H}_{\mathrm{MF}}} \right\}$; however, as opposed

to the classical VMFT derivation, this trace is now evaluated by expressing the Hamiltonian in terms of Pauli matrices and summing over all possible spin-$\frac{1}{2}$ kets, rather than evaluating integrals over solid angles. In particular, noting that tracing over $J^{\mu\nu}_{ia,jb} m^{\mu}_{ia} m^{\nu}_{jb}$ only produces some constant factor C, this yields:

$$Z_{\mathrm{MF}} = \mathrm{Tr}\left\{e^{-\beta \mathcal{H}_{\mathrm{MF}}}\right\} \tag{B.4}$$

$$= C\mathrm{Tr}\left\{e^{\beta \sum_{i,a} \boldsymbol{B}_{ia}\cdot \boldsymbol{S}_{ia}}\right\} \tag{B.5}$$

$$= C\prod_{i,a} \mathrm{Tr}\left\{e^{\beta B^{\mu}_{ia} S^{\mu}_{ia}}\right\}. \tag{B.6}$$

Expressing the spin operators in terms of Pauli matrices, $S^{\mu}_{ia} = \frac{1}{2}\sigma^{\mu}_{ia}$, the argument of the exponential becomes

$$B^{\mu}_{ia} S^{\mu}_{ia} = \frac{1}{2}\begin{pmatrix} B^{z}_{ia} & B^{x}_{ia} - iB^{y}_{ia} \\ B^{x}_{ia} + iB^{y}_{ia} & -B^{z}_{ia} \end{pmatrix}. \tag{B.7}$$

The trace can now be evaluated by summing over the basis of eigenvectors of Eq. (B.7), in which case the operators in the trace are simply replaced by their eigenvalues. Diagonalizing Eq. (B.7) yields eigenvalues $\lambda_{\pm} = \pm\frac{1}{2}|\boldsymbol{B}_{ia}|$. Evaluating the trace thus yields

$$Z_{\mathrm{MF}} = C\prod_{i,a}(e^{-\beta\lambda_{+}} + e^{-\beta\lambda_{-}}) = C\prod_{i,a} 2\cosh\left(\frac{1}{2}\beta|\boldsymbol{B}_{ia}|\right). \tag{B.8}$$

This can be contrasted with Eq. (3.25). The mean-field free energy can be obtained from Eq. (B.8) via $F_{\mathrm{MF}} = -T\ln(Z_{\mathrm{MF}})$. As well, the sublattice magnetizations (that is, the sublattice spin expectation values) can be obtained in the same manner as before, by calculating $\boldsymbol{m}_{ia} = \langle \boldsymbol{S}_{ia}\rangle = -\frac{\partial F_{\mathrm{MF}}}{\partial \boldsymbol{B}_{ia}}$. The resulting self-consistency equation in this case is

$$\boldsymbol{m}_{ia} = \frac{\boldsymbol{B}_{ia}}{2|\boldsymbol{B}_{ia}|}\tanh\left(\frac{1}{2}\beta|\boldsymbol{B}_{ia}|\right), \tag{B.9}$$

as opposed to Eq. (3.30).

The numerical implementation of VMFT (outlined in Section 3.1) for classical or quantum spins is identical. The ultimate difference between the two methods is the expression for the free energy and the self-consistency equation used to iteratively update the spin configuration. As well, given that the norm of the spins is unit length in the classical case but $\frac{1}{2}$ in the quantum case, the exchange parameters and g-tensor must be accordingly renormalized to make the two approaches consistent with one another.

B.2 Quantum Spin-Waves

The derivation of classical spin-waves in Chapter 3 demonstrated how thermal fluctuations may excite the system out of its ground state at finite temperatures. One may employ a similar *quantum* spin-wave expansion to determine the effect of *quantum* fluctuations on the system. The resulting dispersion quantifies the energy-wavevector relation of these quantized spin-waves, or magnons. As in the above derivation, we ignore dipolar interactions, assume a $\boldsymbol{q} = 0$ ordering wavevector for the system, and extend the derivation found in Yan *et al.* [24] to finite values of the applied magnetic field $\boldsymbol{H}$.

Suppose that we have already found the classically-ordered ground state spin configuration on a single tetrahedron at $T = 0$ for the Hamiltonian Eq. (3.48). We define again the same ordering vectors $\{\hat{\boldsymbol{u}}_i, \hat{\boldsymbol{v}}_i, \hat{\boldsymbol{w}}_i\}$ on a given sublattice i. Now, however, the fluctuations are quantified by quantizing the spin operators in our Hamiltonian using Holstein-Primakoff bosons. These will characterize the fluctuation away from (and reduction of) the ordered spin along the $\hat{\boldsymbol{w}}_i$ direction due to the propagation of magnon excitations. We define:

$$S_i^w = S - a_i^\dagger a_i, \tag{B.10}$$

$$S_i^+ = (\sqrt{2S - a_i^\dagger a_i})a_i \approx \sqrt{2S}a_i, \tag{B.11}$$

$$S_i^- = a_i^\dagger(\sqrt{2S - a_i^\dagger a_i}) \approx \sqrt{2S}a_i^\dagger. \tag{B.12}$$

As bosonic excitations and operators, a_i and $a_j^\dagger$ satisfy $[a_i, a_j^\dagger] = \delta_{ij}$; all other combinations of these operators commute. Using the standard relations between S^+, S^-, S^x, and S^y (where $u = x$ and $v = y$ in our local coordinate system), we have $S_i^u = \frac{1}{2}(S_i^+ + S_i^-)$ and $S_i^v = \frac{1}{2i}(S_i^+ - S_i^-)$. Starting from our Hamiltonian Eq. (3.43), we have:

$$\mathcal{H} = \frac{1}{2}\sum_a \sum_{ij} J_{ij}^{\mu\nu} S_{ia}^\mu S_{ja}^\nu - \mu_\mathrm{B} \sum_a \sum_i g_i^{\mu\nu} S_{ia}^\mu H^\nu \tag{B.13}$$

$$= \frac{1}{2}\sum_a \sum_{ij} \boldsymbol{S}_{ia} \cdot \overleftrightarrow{\boldsymbol{J}}_{ij} \cdot \boldsymbol{S}_{ja} - \mu_\mathrm{B} \sum_a \sum_i \boldsymbol{S}_{ia} \cdot \boldsymbol{h}_i, \tag{B.14}$$

where $h_i^\mu = g_i^{\mu\nu} H^\nu$. We can now substitute the previous relations between spin operators

and magnon operators. This yields:

$$\begin{aligned}\mathcal{H} = &\frac{1}{2}\sum_a\sum_{ij}\left[\frac{1}{2}(S^+_{ia}+S^-_{ia})\hat{u}_i+\frac{1}{2i}(S^+_{ia}-S^-_{ia})\hat{v}_i+S^w_{ia}\hat{w}_i\right]\cdot\overleftrightarrow{\boldsymbol{J}}_{ij}\cdot\\ &\left[\frac{1}{2}(S^+_{ja}+S^-_{ja})\hat{u}_j+\frac{1}{2i}(S^+_{ja}-S^-_{ja})\hat{v}_j+S^w_{ja}\hat{w}_j\right] \qquad \text{(B.15)}\\ &-\mu_{\mathrm{B}}\sum_a\sum_i\boldsymbol{h}_i\cdot\left[\frac{1}{2}(S^+_{ia}+S^-_{ia})\hat{u}_i+\frac{1}{2i}(S^+_{ia}-S^-_{ia})\hat{v}_i+S^w_{ia}\hat{w}_i\right]\\ &=\frac{1}{2}\sum_a\sum_{ij}\left[a_i\sqrt{\frac{S}{2}}(\hat{u}_i-i\hat{v}_i)+a_i^\dagger\sqrt{\frac{S}{2}}(\hat{u}_i+i\hat{v}_i)+(S-a_i^\dagger a_i)\hat{w}_i\right]\cdot\overleftrightarrow{\boldsymbol{J}}_{ij}\cdot\\ &\left[a_j\sqrt{\frac{S}{2}}(\hat{u}_j-i\hat{v}_j)+\quad a_j^\dagger\sqrt{\frac{S}{2}}(\hat{u}_j+i\hat{v}_j)+(S-a_j^\dagger a_j)\hat{w}_j\right] \qquad \text{(B.16)}\\ &-\mu_{\mathrm{B}}\sum_a\sum_i\boldsymbol{h}_i\cdot\left[a_i\sqrt{\frac{S}{2}}(\hat{u}_i-i\hat{v}_i)+a_i^\dagger\sqrt{\frac{S}{2}}(\hat{u}_i+i\hat{v}_i)+(S-a_i^\dagger a_i)\hat{w}_i\right].\end{aligned}$$

We can define the new unit vector $\hat{c}_i=\frac{1}{\sqrt{2}}(\hat{u}_i+i\hat{v}_i)$ to simplify this to

$$\begin{aligned}\mathcal{H} = &\frac{1}{2}\sum_a\sum_{ij}\left[a_i\sqrt{S}\hat{c}_i^*+a_i^\dagger\sqrt{S}\hat{c}_i+(S-a_i^\dagger a_i)\hat{w}_i\right]\cdot\overleftrightarrow{\boldsymbol{J}}_{ij}\cdot\left[a_j\sqrt{S}\hat{c}_j^*+a_j^\dagger\sqrt{S}\hat{c}_j+(S-a_j^\dagger a_j)\hat{w}_j\right]\\ &-\mu_{\mathrm{B}}\sum_a\sum_i\boldsymbol{h}_i\cdot\left[a_i\sqrt{S}\hat{c}_i^*+a_i^\dagger\sqrt{S}\hat{c}_i+(S-a_i^\dagger a_i)\hat{w}_i\right].\end{aligned} \qquad \text{(B.17)}$$

Expanding these expressions and only keeping up to quadratic order in the bosonic operators, in keeping with a linear spin-wave approximation, we have:

$$\begin{aligned}\mathcal{H} = &\frac{1}{2}\sum_a\sum_{ij}(S\hat{w}_i)\cdot\overleftrightarrow{\boldsymbol{J}}_{ij}\cdot(S\hat{w}_j)-\mu_{\mathrm{B}}\sum_a\sum_i\boldsymbol{h}_i\cdot(S\hat{w}_i)\\ &+\frac{1}{2}\sum_a\sum_{ij}S\Big[a_ia_j\hat{c}_i^*\cdot\overleftrightarrow{\boldsymbol{J}}_{ij}\cdot\hat{c}_j^*+a_ia_j^\dagger\hat{c}_i^*\cdot\overleftrightarrow{\boldsymbol{J}}_{ij}\cdot\hat{c}_j\\ &+a_i^\dagger a_j\hat{c}_i\cdot\overleftrightarrow{\boldsymbol{J}}_{ij}\cdot\hat{c}_j^*+a_i^\dagger a_j^\dagger\hat{c}_i\cdot\overleftrightarrow{\boldsymbol{J}}_{ij}\cdot\hat{c}_j-(a_i^\dagger a_i+a_j^\dagger a_j)\hat{w}_i\cdot\overleftrightarrow{\boldsymbol{J}}_{ij}\cdot\hat{w}_j\Big]\\ &+\mu_{\mathrm{B}}\sum_a\sum_i a_i^\dagger a_i\boldsymbol{h}_i\cdot\hat{w}_i.\end{aligned} \qquad \text{(B.18)}$$

The first line in the above expression is merely the ground state energy ϵ_0; the rest of the expression is the linear spin-wave Hamiltonian, $\mathcal{H}_{\text{LSW}}$, which must be diagonalized in order to find the contribution of quantum fluctuations to the energy.

We use the same definition of the Fourier transform as in Chapter 3 in order to transform the bosonic operators, using the translational symmetry of the FCC lattice. Introducing these Fourier-transformed operators and summing over all tetrahedra positions to simplify the wavevector relations with δ functions, we obtain as before:

$$\begin{aligned}\mathcal{H} = \frac{1}{2}\sum_{ij}\sum_{\boldsymbol{q}} S\Big[& e^{i\boldsymbol{q}\cdot\boldsymbol{r}_{ij}} a_i(\boldsymbol{q})a_j(-\boldsymbol{q})\hat{c}_i^*\cdot \overleftrightarrow{\boldsymbol{J}}_{ij}\cdot\hat{c}_j^* + e^{i\boldsymbol{q}\cdot\boldsymbol{r}_{ij}} a_i(\boldsymbol{q})a_j^\dagger(\boldsymbol{q})\hat{c}_i^*\cdot \overleftrightarrow{\boldsymbol{J}}_{ij}\cdot\hat{c}_j \\ & + e^{-i\boldsymbol{q}\cdot\boldsymbol{r}_{ij}} a_i^\dagger(\boldsymbol{q})a_j(\boldsymbol{q})\hat{c}_i\cdot \overleftrightarrow{\boldsymbol{J}}_{ij}\cdot\hat{c}_j^* + e^{-i\boldsymbol{q}\cdot\boldsymbol{r}_{ij}} a_i^\dagger(\boldsymbol{q})a_j^\dagger(-\boldsymbol{q})\hat{c}_i\cdot \overleftrightarrow{\boldsymbol{J}}_{ij}\cdot\hat{c}_j \\ & - (a_i^\dagger(\boldsymbol{q})a_i(\boldsymbol{q}) + a_j^\dagger(\boldsymbol{q})a_j(\boldsymbol{q}))\hat{w}_i\cdot \overleftrightarrow{\boldsymbol{J}}_{ij}\cdot\hat{w}_j\Big] \\ & + \mu_{\text{B}}\sum_a\sum_i a_i^\dagger(\boldsymbol{q})a_i(\boldsymbol{q})\boldsymbol{h}_i\cdot\hat{w}_i.\end{aligned} \tag{B.19}$$

Now, note that:

$$\sum_{ij}\left(a_i^\dagger(\boldsymbol{q})a_i(\boldsymbol{q}) + a_j^\dagger(\boldsymbol{q})a_j(\boldsymbol{q})\right)\left(\hat{w}_i\cdot \overleftrightarrow{\boldsymbol{J}}_{ij}\cdot\hat{w}_j\right) \tag{B.20}$$

$$= \sum_i a_i^\dagger(\boldsymbol{q})a_i(\boldsymbol{q})\sum_j \hat{w}_i\cdot \overleftrightarrow{\boldsymbol{J}}_{ij}\cdot\hat{w}_j + \sum_j a_j^\dagger(\boldsymbol{q})a_j(\boldsymbol{q})\sum_i \hat{w}_i\cdot \overleftrightarrow{\boldsymbol{J}}_{ij}\cdot\hat{w}_j \tag{B.21}$$

$$= \sum_i a_i^\dagger(\boldsymbol{q})a_i(\boldsymbol{q})\sum_l \hat{w}_i\cdot \overleftrightarrow{\boldsymbol{J}}_{il}\cdot\hat{w}_l + \sum_j a_j^\dagger(\boldsymbol{q})a_j(\boldsymbol{q})\sum_l \hat{w}_l\cdot \overleftrightarrow{\boldsymbol{J}}_{lj}\cdot\hat{w}_j \tag{B.22}$$

$$= \sum_{ij}\delta_{ij}a_i^\dagger(\boldsymbol{q})a_i(\boldsymbol{q})\sum_l \hat{w}_l\cdot \overleftrightarrow{\boldsymbol{J}}_{li}\cdot\hat{w}_i + \sum_{ij}\delta_{ij}a_i^\dagger(\boldsymbol{q})a_i(\boldsymbol{q})\sum_l \hat{w}_l\cdot \overleftrightarrow{\boldsymbol{J}}_{li}\cdot\hat{w}_i. \tag{B.23}$$

We can thus simplify our overall expression to:

$$\begin{aligned}\mathcal{H} = \frac{1}{2}\sum_{ij}\sum_{\boldsymbol{q}} 2S\cos\left(\boldsymbol{q}\cdot\boldsymbol{r}_{ij}\right)\Big[& a_i^\dagger(\boldsymbol{q})a_j(\boldsymbol{q})\hat{c}_i\cdot \overleftrightarrow{\boldsymbol{J}}_{ij}\cdot\hat{c}_j^* + a_i^\dagger(\boldsymbol{q})a_j^\dagger(-\boldsymbol{q})\hat{c}_i\cdot \overleftrightarrow{\boldsymbol{J}}_{ij}\cdot\hat{c}_j \\ & + a_i(-\boldsymbol{q})a_j(\boldsymbol{q})\hat{c}_i^*\cdot \overleftrightarrow{\boldsymbol{J}}_{ij}\cdot\hat{c}_j^* + a_i(-\boldsymbol{q})a_j^\dagger(-\boldsymbol{q})\hat{c}_i^*\cdot \overleftrightarrow{\boldsymbol{J}}_{ij}\cdot\hat{c}_j \\ & - \delta_{ij}a_i^\dagger(\boldsymbol{q})a_i(\boldsymbol{q})\sum_l \hat{w}_l\cdot \overleftrightarrow{\boldsymbol{J}}_{li}\cdot\hat{w}_i - \delta_{ij}a_i^\dagger(\boldsymbol{q})a_i(\boldsymbol{q})\sum_l \hat{w}_l\cdot \overleftrightarrow{\boldsymbol{J}}_{li}\cdot\hat{w}_i\Big] \\ & + \frac{1}{2}\mu_{\text{B}}\sum_a\sum_{ij}\delta_{ij}a_i^\dagger(\boldsymbol{q})a_i(\boldsymbol{q})\boldsymbol{h}_i\cdot\hat{w}_i + \delta_{ij}a_j^\dagger(-\boldsymbol{q})a_j(-\boldsymbol{q})\boldsymbol{h}_j\cdot\hat{w}_j.\end{aligned} \tag{B.24}$$

We define the vector operator $A^\dagger(\boldsymbol{q}) = \Big(a_0^\dagger(\boldsymbol{q}), a_1^\dagger(\boldsymbol{q}), a_2^\dagger(\boldsymbol{q}), a_3^\dagger(\boldsymbol{q}), a_0(-\boldsymbol{q}), a_1(-\boldsymbol{q}), a_2(-\boldsymbol{q}), a_3(-\boldsymbol{q})\Big)$, and $A(\boldsymbol{q})$ is defined by the Hermitian conjugate of this. With this definition, we can write the above expression as a matrix multiplication of the form:

$$\mathcal{H} = \frac{1}{2}\sum_{\boldsymbol{q}} A^\dagger(\boldsymbol{q})(\overleftrightarrow{\boldsymbol{X}}(\boldsymbol{q}) + \overleftrightarrow{\boldsymbol{N}}(\boldsymbol{q}))A(\boldsymbol{q}), \tag{B.25}$$

where:

$$\overleftrightarrow{\boldsymbol{X}}(\boldsymbol{q}) = 2S\begin{pmatrix} \overleftrightarrow{\boldsymbol{X}}^{11}(\boldsymbol{q}) & \overleftrightarrow{\boldsymbol{X}}^{12}(\boldsymbol{q}) \\ \overleftrightarrow{\boldsymbol{X}}^{21}(\boldsymbol{q}) & \overleftrightarrow{\boldsymbol{X}}^{22}(\boldsymbol{q}) \end{pmatrix}, \tag{B.26}$$

$$X_{ij}^{11} = \cos(\boldsymbol{q}\cdot\boldsymbol{r}_{ij})\left(\hat{c}_i\cdot\overleftrightarrow{\boldsymbol{J}}_{ij}\cdot\hat{c}_j^* - \delta_{ij}\sum_l \hat{w}_l\cdot\overleftrightarrow{\boldsymbol{J}}_{lj}\cdot\hat{w}_j\right) \tag{B.27}$$

$$X_{ij}^{12} = \cos(\boldsymbol{q}\cdot\boldsymbol{r}_{ij})\left(\hat{c}_i\cdot\overleftrightarrow{\boldsymbol{J}}_{ij}\cdot\hat{c}_j\right) \tag{B.28}$$

$$X_{ij}^{21} = \cos(\boldsymbol{q}\cdot\boldsymbol{r}_{ij})\left(\hat{c}_i^*\cdot\overleftrightarrow{\boldsymbol{J}}_{ij}\cdot\hat{c}_j^*\right) \tag{B.29}$$

$$X_{ij}^{22} = \cos(\boldsymbol{q}\cdot\boldsymbol{r}_{ij})\left(\hat{c}_i^*\cdot\overleftrightarrow{\boldsymbol{J}}_{ij}\cdot\hat{c}_j - \delta_{ij}\sum_l \hat{w}_l\cdot\overleftrightarrow{\boldsymbol{J}}_{lj}\cdot\hat{w}_j\right). \tag{B.30}$$

$N(\boldsymbol{q})$ is defined in the same way as for the classical spin-wave expansion.

We must now diagonalize this Hamiltonian for every $\boldsymbol{q}$. This amounts to taking a ($\boldsymbol{q}$-dependent) linear combination of the creation and annihilation operators for the magnons in such a way that the Hamiltonian is diagonal. However, there is the constraint that the operators must obey bosonic commutation relations. To proceed generally, we do not assume that the transformation which diagonalizes the Hamiltonian is unitary; we only assume that bosonic commutation relations are satisfied and derive the resulting consequences for the transformation. Suppose that our diagonalized bosonic operators are defined by $B^\dagger(\boldsymbol{q}) = \Big(b_0^\dagger(\boldsymbol{q}), b_1^\dagger(\boldsymbol{q}), b_2^\dagger(\boldsymbol{q}), b_3^\dagger(\boldsymbol{q}), b_0(-\boldsymbol{q}), b_1(-\boldsymbol{q}), b_2(-\boldsymbol{q}), b_3(-\boldsymbol{q})\Big)$; $B(\boldsymbol{q})$ is defined by the Hermitian conjugate. This will be a linear transformation applied to the original $A^\dagger(\boldsymbol{q})$ and $A(\boldsymbol{q})$ vector operators, so we can define:

$$B^\dagger(\boldsymbol{q}) = A^\dagger(\boldsymbol{q})\,\overleftrightarrow{\boldsymbol{U}}^\dagger(\boldsymbol{q}), \tag{B.31}$$

$$B(\boldsymbol{q}) = \overleftrightarrow{\boldsymbol{U}}(\boldsymbol{q})A(\boldsymbol{q}). \tag{B.32}$$

Here, $\overleftrightarrow{\boldsymbol{U}}\ (\boldsymbol{q})$ is the matrix that codifies the linear combination of the original Holstein-Primakoff boson operators. The diagonalized bosonic operators satisfy the proper commutation relations if we impose $\left[B_i(\boldsymbol{q}), B_j^\dagger(\boldsymbol{q'})\right] = \sigma_{ij}\delta_{\boldsymbol{qq'}}$ for the matrix $\sigma = \begin{pmatrix} \mathbb{I} & 0 \\ 0 & -\mathbb{I} \end{pmatrix}$. Here, $\mathbb{I}$ is a 4x4 identity matrix, and the lower diagonal negative sign comes from the swapping of the ordering of the creation and annihilation operators in $B^\dagger(\boldsymbol{q})$ and $B(\boldsymbol{q})$. Similarly, we would also have $\left[A_i(\boldsymbol{q}), A_j^\dagger(\boldsymbol{q'})\right] = \sigma_{ij}\delta_{\boldsymbol{qq'}}$, as these are also bosonic operators. Using the transformation matrix $\overleftrightarrow{\boldsymbol{U}}\ (\boldsymbol{q})$, we then have:

$$\sigma_{ij}\delta_{\boldsymbol{qq'}} = \left[B_i(\boldsymbol{q}), B_j^\dagger(\boldsymbol{q'})\right] \tag{B.33}$$

$$\sigma_{ij}\delta_{\boldsymbol{qq'}} = B_i(\boldsymbol{q})B_j^\dagger(\boldsymbol{q'}) - B_j^\dagger(\boldsymbol{q'})B_i(\boldsymbol{q}) \tag{B.34}$$

$$\sigma_{ij}\delta_{\boldsymbol{qq'}} = (U_{ik}(\boldsymbol{q})A_k(\boldsymbol{q}))(A_l^\dagger(\boldsymbol{q'})U_{lj}^\dagger(\boldsymbol{q'})) - (A_l^\dagger(\boldsymbol{q'})U_{lj}^\dagger(\boldsymbol{q'}))(U_{ik}(\boldsymbol{q})A_k(\boldsymbol{q})) \tag{B.35}$$

$$\sigma_{ij}\delta_{\boldsymbol{qq'}} = U_{ik}(\boldsymbol{q})\left[A_k(\boldsymbol{q}), A_l^\dagger(\boldsymbol{q'})\right]U_{lj}^\dagger \tag{B.36}$$

$$\sigma_{ij}\delta_{\boldsymbol{qq'}} = U_{ik}(\boldsymbol{q})\sigma_{kl}U_{lj}^\dagger(\boldsymbol{q'})\delta_{\boldsymbol{qq'}} \tag{B.37}$$

$$\implies \overleftrightarrow{\boldsymbol{\sigma}} = \overleftrightarrow{\boldsymbol{U}}\ (\boldsymbol{q})\ \overleftrightarrow{\boldsymbol{\sigma}}\overleftrightarrow{\boldsymbol{U}}^\dagger\ (\boldsymbol{q}) \tag{B.38}$$

$$\implies \overleftrightarrow{\boldsymbol{U}}^{-1}\ (\boldsymbol{q}) = \overleftrightarrow{\boldsymbol{\sigma}}\overleftrightarrow{\boldsymbol{U}}^\dagger\ (\boldsymbol{q})\ \overleftrightarrow{\boldsymbol{\sigma}}\,. \tag{B.39}$$

Clearly, the relation is not a unitary one. Applying the transformation $\overleftrightarrow{\boldsymbol{U}}\ (\boldsymbol{q})$ to our original bosonic operators and making use of this condition on the inverse of $\overleftrightarrow{\boldsymbol{U}}\ (\boldsymbol{q})$, we can diagonalize our spin-wave Hamiltonian:

$$\mathcal{H} = \frac{1}{2}\sum_{\boldsymbol{q}} A^\dagger(\boldsymbol{q})(\overleftrightarrow{\boldsymbol{X}}\ (\boldsymbol{q}) + \overleftrightarrow{\boldsymbol{N}}\ (\boldsymbol{q}))A(\boldsymbol{q}) \tag{B.40}$$

$$= \frac{1}{2}\sum_{\boldsymbol{q}} \left[B^\dagger(\boldsymbol{q})(\overleftrightarrow{\boldsymbol{U}}^\dagger)^{-1}(\boldsymbol{q})\right](\overleftrightarrow{\boldsymbol{X}}\ (\boldsymbol{q}) + \overleftrightarrow{\boldsymbol{N}}\ (\boldsymbol{q}))\left[\overleftrightarrow{\boldsymbol{U}}^{-1}\ (\boldsymbol{q})B(\boldsymbol{q})\right] \tag{B.41}$$

$$= \frac{1}{2}\sum_{\boldsymbol{q}} B^\dagger(\boldsymbol{q})\left[\overleftrightarrow{\boldsymbol{\sigma}}\overleftrightarrow{\boldsymbol{U}}^\dagger\ (\boldsymbol{q})\ \overleftrightarrow{\boldsymbol{\sigma}}\right](\overleftrightarrow{\boldsymbol{X}}\ (\boldsymbol{q}) + \overleftrightarrow{\boldsymbol{N}}\ (\boldsymbol{q}))\left[\overleftrightarrow{\boldsymbol{U}}^{-1}\ (\boldsymbol{q})\right]B(\boldsymbol{q}) \tag{B.42}$$

$$= \frac{1}{2}\sum_{\boldsymbol{q}} B^\dagger(\boldsymbol{q})\ \overleftrightarrow{\boldsymbol{\sigma}}\overleftrightarrow{\boldsymbol{U}}^\dagger\ (\boldsymbol{q})\left[\overleftrightarrow{\boldsymbol{\sigma}}\ (\overleftrightarrow{\boldsymbol{X}}\ (\boldsymbol{q}) + \overleftrightarrow{\boldsymbol{N}}\ (\boldsymbol{q}))\right]\overleftrightarrow{\boldsymbol{U}}^{-1}\ (\boldsymbol{q})B(\boldsymbol{q}) \tag{B.43}$$

Our transformation matrix $\overleftrightarrow{\boldsymbol{U}}\ (\boldsymbol{q})$ thus amounts to diagonalizing the matrix $\overleftrightarrow{\boldsymbol{\sigma}}\ (\overleftrightarrow{\boldsymbol{X}}\ (\boldsymbol{q}) + \overleftrightarrow{\boldsymbol{N}}\ (\boldsymbol{q}))$. Doing this numerically yields the dispersion relation of the magnon modes,

$\omega_\nu(\boldsymbol{q})$. We find:

$$\mathcal{H} = \frac{1}{2}\sum_{\boldsymbol{q}} B^\dagger(\boldsymbol{q})\sigma \begin{pmatrix} \omega_\nu(\boldsymbol{q}) & 0 \\ 0 & -\omega_\nu(\boldsymbol{q}) \end{pmatrix} B(\boldsymbol{q}) \tag{B.44}$$

$$= \frac{1}{2}\sum_{\boldsymbol{q}} B^\dagger(\boldsymbol{q}) \begin{pmatrix} \omega_\nu(\boldsymbol{q}) & 0 \\ 0 & \omega_\nu(\boldsymbol{q}) \end{pmatrix} B(\boldsymbol{q}) \tag{B.45}$$

$$= \frac{1}{2}\sum_{\boldsymbol{q}}\sum_{\nu} \omega_\nu(\boldsymbol{q}) b_\nu^\dagger(\boldsymbol{q}) b_\nu(\boldsymbol{q}) + \omega_\nu(\boldsymbol{q}) b_\nu(-\boldsymbol{q}) b_\nu^\dagger(-\boldsymbol{q}) \tag{B.46}$$

$$= \frac{1}{2}\sum_{\boldsymbol{q}}\sum_{\nu} \omega_\nu(\boldsymbol{q}) \left[b_\nu^\dagger(\boldsymbol{q}) b_\nu(\boldsymbol{q}) + \frac{1}{2} \right]. \tag{B.47}$$

This completes the diagonalization of the linear spin-wave Hamiltonian, giving us the dispersion relation of the magnon excitations. From this linear spin-wave theory, the effect of quantum fluctuations on various quantities can be calculated. For example,

$$E_{\mathrm{QSW}} = \frac{1}{2}\sum_{\boldsymbol{q}}\sum_{\nu} \omega_\nu(\boldsymbol{q}) \left[b_\nu^\dagger(\boldsymbol{q}) b_\nu(\boldsymbol{q}) + \frac{1}{2} \right] \tag{B.48}$$

represents the zero-point energy contribution of the quantum spin-wave modes to the classical ground state energy of the ordered configuration [24]. If S_i^w represents the ordered moment on sublattice i (where spins have a length S), then the reduction of the ordered moment by quantum fluctuations can be computed via [24]

$$\langle S_i^w \rangle = S - \left\langle a_i^\dagger a_i \right\rangle. \tag{B.49}$$

The thermal expectation value $\left\langle a_i^\dagger a_i \right\rangle$ can be computed by first transforming from the Holstein-Primakoff bosons to the diagonalizing bosons $b_\nu(\boldsymbol{q})$. The Bose-Einstein statistics of these latter bosons can then be used to calculate the thermal average [24]. Lastly, one can also calculate the inelastic scattering cross-section $S(\boldsymbol{q},\omega)$ that these quantum spin-waves produce in inelastic neutron scattering experiments. For a system of N spins on the pyrochlore lattice, with sublattices i and j and tetrahedra a and b, the expression for this is [24]

$$S(\boldsymbol{q},\omega) = \frac{1}{2\pi}\frac{4}{N}\sum_{\alpha\beta}\sum_{\gamma\lambda}\sum_{ij}(\delta_{\alpha\beta} - \frac{q_\alpha q_\beta}{q^2}) g_i^{\alpha\gamma} g_j^{\beta\lambda} \times$$

$$\int dt\ dt' \sum_{\boldsymbol{R}_a,\boldsymbol{R}_b} e^{i\omega(t-t')} e^{i\boldsymbol{q}\cdot(\boldsymbol{R}_b-\boldsymbol{R}_a)} \left\langle S_i^{\gamma}(\boldsymbol{R}_a,t) S_j^{\lambda}(\boldsymbol{R}_b,t') \right\rangle . \tag{B.50}$$

One can then expand the spin operators in this expression in terms of the bosons $b_\nu(\boldsymbol{q})$.

Appendix C

Further Comments on the Classical Spin-Wave Results

In this Appendix, we support some of the arguments made in Section 4.3 by providing more figures of the relevant classical spin-wave dispersions for an applied field H along the [100] direction. We then show how these arguments are general and important for the [111] and [110] cases detailed in Sections 4.4 and 4.5.

For the [100] case, in addition to Figures 4.4a and 4.4b, it is useful to view the classical spin-wave dispersions for values of H that lie below and above the critical value $H_c(T = 0) = 0.82$ T. This is shown in Figure C.1 for $H = \{0.1, 0.3, 0.5, 0.7, 0.9, 1.1\}$ T. As H increases from 0 and approaches the branch merger transition at $H = 0.82$ T, the dispersions begin to decrease across a range of $\boldsymbol{q}$ values, as seen in Figures C.1a, C.1b, C.1c, and C.1d. In particular, we see that $\kappa_\nu(\boldsymbol{q}) < T_{c0}$ for some dispersions at $H = 0.5$ T (Figure C.1c) and $H = 0.7$ T (Figure C.1d). Comparing with Figure 4.2b, we also see that this gradual decrease in the dispersions $\kappa_\nu(\boldsymbol{q})$ as H increases is accompanied by an increase in $T_c(H)$. This is expected from the entropic arguments made in Section 4.3 on the basis of classical spin-waves, where it is argued that decreasing $\kappa_\nu(\boldsymbol{q})$ leads to an increased entropy of the ordered phase. Hence, even though the branch collapse transition occurs at $H_c = 0.82$ T, the classical spin-wave dispersions decrease on *approaching* this critical value, and the onset of reentrance starts even for $H < 0.82$ T.

Alternatively, one can also view the dispersions $\kappa_\nu(\boldsymbol{q})$ for $H > 0.82$ T. These can be seen in Figures C.1e and C.1f. As H increases beyond the critical value of 0.82 T, the dispersions begin to *increase*. Comparing with Figure 4.2b, this increase in $\kappa_\nu(\boldsymbol{q})$ with increasing H is accompanied by a decrease in $T_c(H)$. This is also expected from the same

entropic arguments presented in Section 4.3: if decreasing $\kappa_\nu(\boldsymbol{q})$ leads to a greater entropy contribution from the classical spin-waves, then increasing $\kappa_\nu(\boldsymbol{q})$ should correspondingly decrease the entropy in the ordered phase. This is because lower (higher) values of $\kappa_\nu(\boldsymbol{q})$ correspond to stronger (weaker) thermal fluctuations in the system and greater (lesser) entropy of the ordered phase.

Altogether, we see that the behavior of the dispersions $\kappa_\nu(\boldsymbol{q})$ as a function of H is linked with the behavior of the reentrant lobe. As $\kappa_\nu(\boldsymbol{q})$ tends to decrease (increase), the entropy of these classical spin-waves increases (decreases), leading to a corresponding increase (decrease) in T_c. This is why the reentrant lobe in Figure 4.2b has a lobe shape. As well, it is at the branch merger transition (at $H_c = 0.82$ T in Figure 4.4b) that these dispersions reach their minimum. So, the increase or decrease of $\kappa_\nu(\boldsymbol{q})$ as a function of H is really a measure of proximity to this branch merger transition. Approaching $H_c = 0.82$ T from below leads to a decrease in $\kappa_\nu(\boldsymbol{q})$ due to proximity to the upcoming transition, even if H is not yet equal to H_c. This is why the reentrant lobe is centered on $H_c = 0.82$ T in Figure 4.2b, but exists for a range of H values, including values of $H < 0.82$ T.

Finally, note that this discussion has focused on the [100] field direction, but these arguments are analogous for the classical spin-wave dispersions in the [111] and [110] field directions. For example, in the [111] direction, there is a range of H values near $H = 0.54$ T for which $\kappa_\nu(\boldsymbol{q}) < T_{c0}$. A few examples are shown for $H = 0.40$ T (Figure C.2a), $H = 0.45$ T (Figure C.2b), $H = 0.50$ T (Figure C.2c), and $H = 0.60$ T (Figure C.2d). This is why reentrance occurs for a range of field values H, even though the ψ_2 selection by the applied field (as discussed in Section 4.4) occurs most strongly at $H = 0.54$ T. It is proximity to this selection (i.e. the gradual selection of a θ_E value that corresponds to the ψ_2 phase, as H varies) that leads to a decreased $\kappa_\nu(\boldsymbol{q})$ for a range of field values near 0.54 T, similar to proximity to a branch merger transition in the [100] case.

A similar argument can be made for the [110] field direction. For example, Figure 4.14 shows that $\kappa_\nu(\boldsymbol{q}) < T_{c0}$, and it is argued (in Section 4.5) that the reason is proximity to two branch collapse transitions (at $H = 0.52$ T and $H = 1.12$ T). Further confirmation of this is given by calculating the classical spin-wave dispersions for $H = 0.65$ T (Figure C.3a), $H = 0.70$ T (Figure C.3b), $H = 0.80$ T (Figure C.3c), and $H = 0.90$ T (Figure C.3d). In all four cases, we see there are dispersions satisfying $\kappa_\nu(\boldsymbol{q}) < T_{c0}$, which give thermal fluctuations that sustain the upper reentrant lobe in Figure 4.11b. Again, $\kappa_\nu(\boldsymbol{q}) < T_{c0}$ occurs for a range of field values H due to proximity to branch collapse transitions, just as in the [100] case.

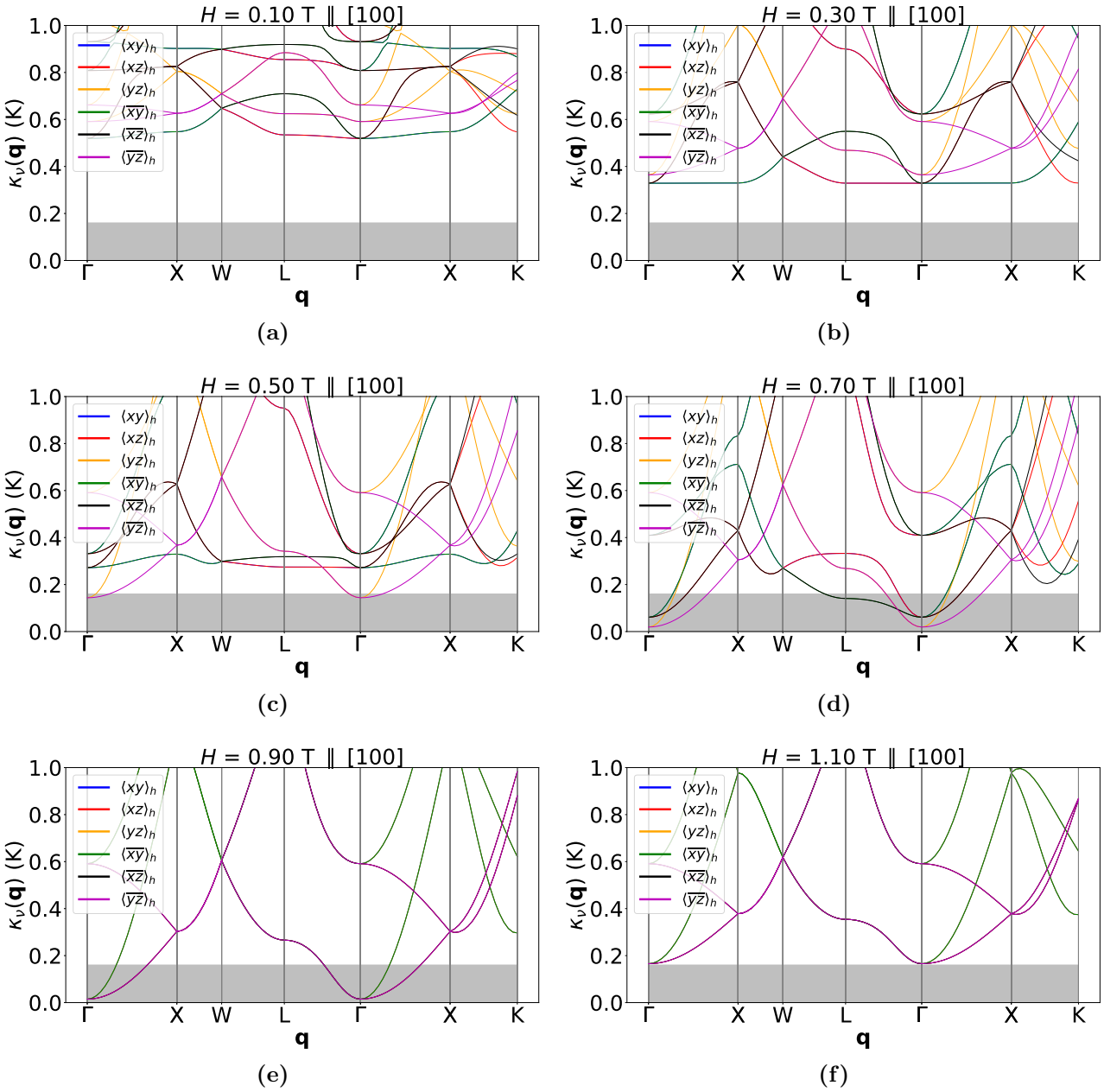

Figure C.1: Classical spin-wave expansion at (a) $H = 0.10$ T, (b) $H = 0.30$ T, (c) $H = 0.50$ T, (d) $H = 0.70$, (e) $H = 0.90$ T, and (f) $H = 1.10$ T in the [100] direction. Wavevectors are taken from the FCC reciprocal lattice. The grey shaded region represents energy scales below $T_{c0} \approx 160$ mK. Note that dispersions may overlap due to degeneracies at high-symmetry points or from mergers of FEPC states induced by the field (e.g. $\langle xy \rangle_h$ and $\langle \overline{xy} \rangle_h$ for $H \geq 0.82$ T).

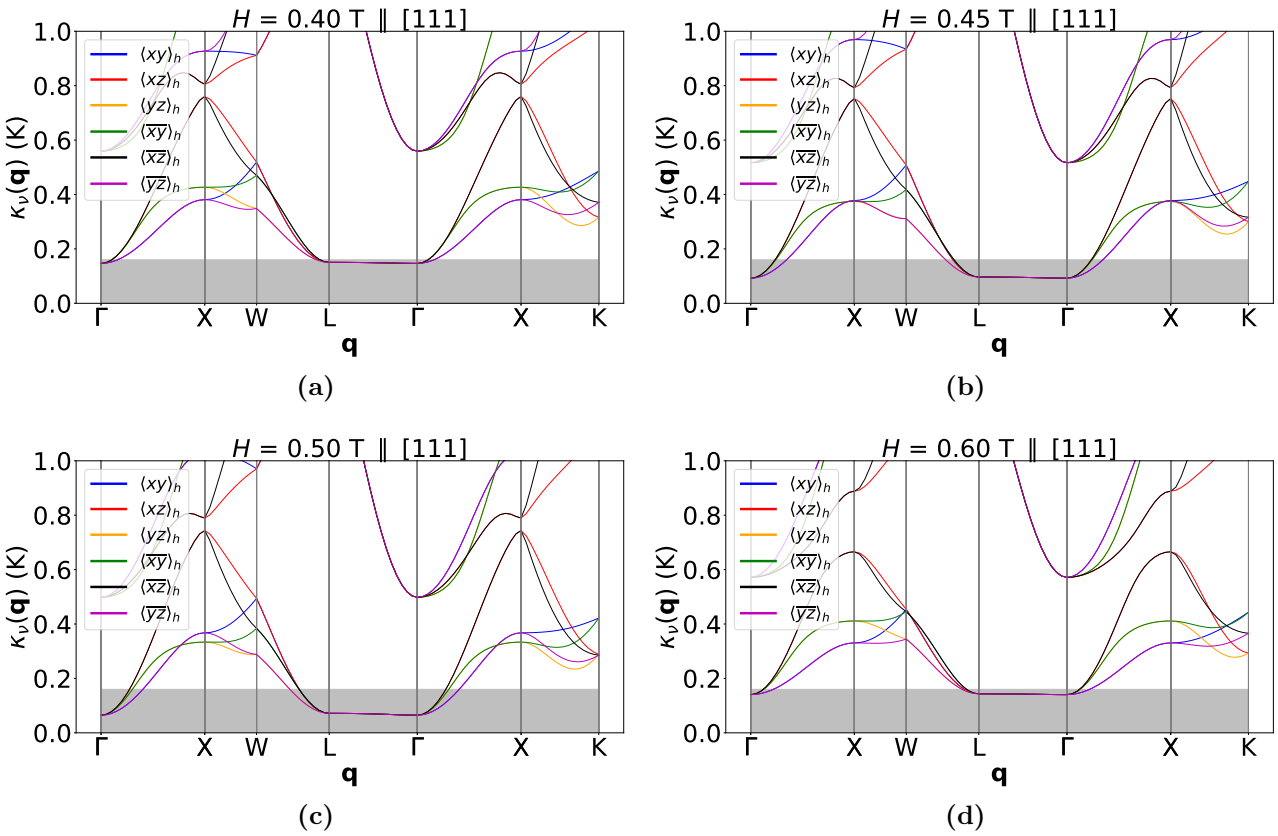

Figure C.2: Classical spin-wave expansion at (a) $H = 0.40$ T, (b) $H = 0.45$ T, (c) $H = 0.50$ T, and (d) $H = 0.60$ T in the [111] direction. Wavevectors are taken from the FCC reciprocal lattice. The grey shaded region represents energy scales below $T_{c0} \approx 160$ mK. Note that dispersions may overlap due to degeneracies at high-symmetry points or from mergers of FEPC states induced by the field (e.g. $\langle xy \rangle_h$ and $\langle \overline{xy} \rangle_h$ for $H \geq 1.31$ T).

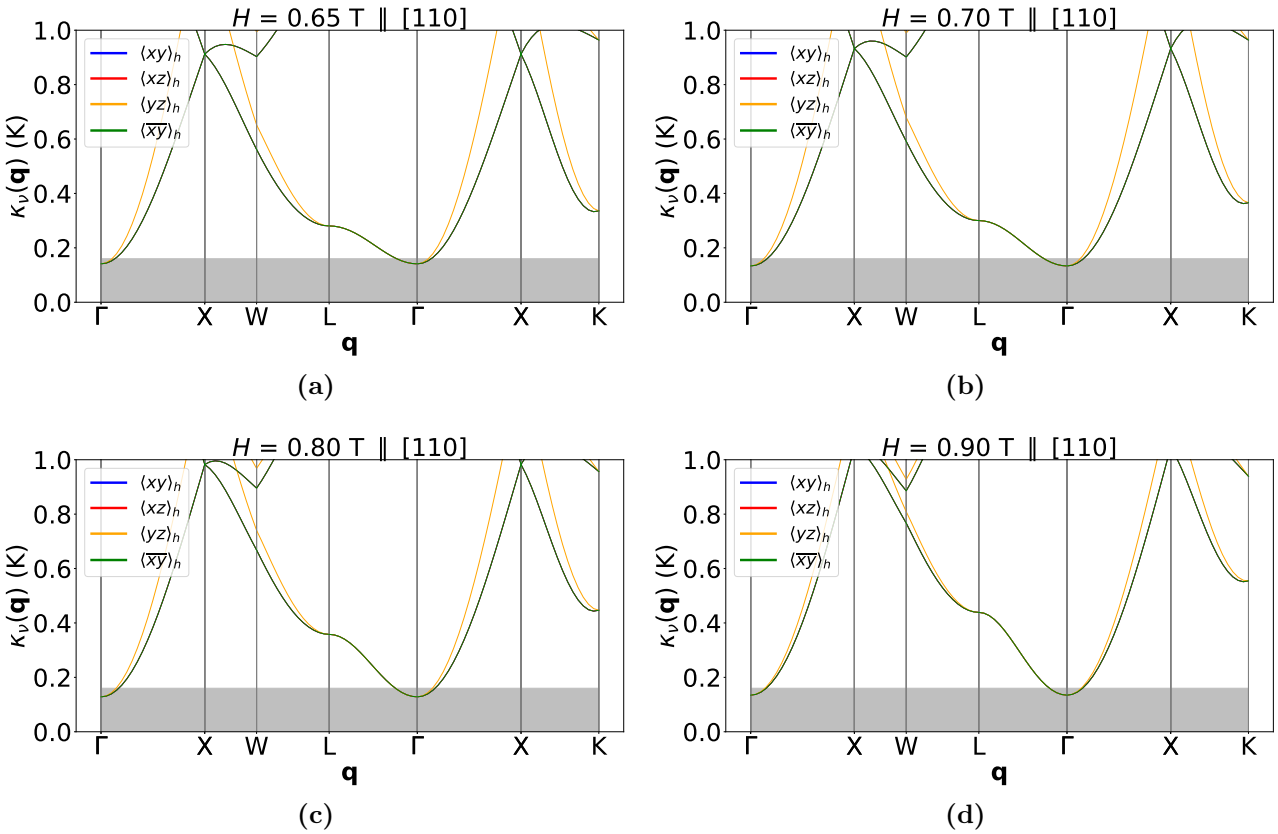

Figure C.3: Classical spin-wave expansion at (a) $H = 0.65$ T, (b) $H = 0.70$ T, (c) $H = 0.80$ T, and (d) $H = 0.90$ T in the [110] direction. Only those field-evolved Palmer-Chalker states which minimize the energy are considered. Wavevectors are taken from the FCC reciprocal lattice. The grey shaded region represents energy scales below $T_{c0} \approx 160$ mK. Note that dispersions may overlap due to degeneracies at high-symmetry points or from mergers of FEPC states induced by the field (e.g. $\langle xy \rangle_h$, $\langle xz \rangle_h$, and $\langle \overline{xy} \rangle_h$ for $H \geq 0.57$ T).

Appendix D

Further Analysis of the [110] Field Direction

In this Appendix, we further anaylze the results in the [110] field direction. In particular, we return to the difference between the $T = 0$ and $T = 0^+$ phases shown in Figure 4.11a. Note that this occurs purely within VMFT; we are not dealing with any classical spin-waves or thermal fluctuations here. Hence, it should be emphasized that this is not a thermal order-by-disorder effect. This difference between the $T = 0$ and $T = 0^+$ phases must be understood purely on the grounds of VMFT.

For field values of $H < 0.42$ T, we see that we go from a $\mathbb{Z}_4$ degeneracy at $T = 0$ to a $\mathbb{Z}_2$ degeneracy at $T = 0^+$ in Figure 4.11a. An applied field in the [110] direction separates the six FEPC states into two groups according to symmetry: $\mathcal{G}_1 = \{\langle xy\rangle_h, \langle\overline{xy}\rangle_h\}$ (for which the applied field lies in the same plane as the original PC states) and $\mathcal{G}_2 = \{\langle xz\rangle_h, \langle yz\rangle_h, \langle\overline{xz}\rangle_h, \langle\overline{yz}\rangle_h\}$ (for which the applied field does not lie in the same plane as the original PC states). At $T = 0$, the $\mathbb{Z}_4$ degeneracy corresponds to $\mathcal{G}_2$; these are the four FEPC states that the system is found in. At $T = 0^+$, the $\mathbb{Z}_2$ degeneracy corresponds to $\mathcal{G}_1$; these are the two FEPC states that the system is found in. Therefore, when temperature is increased from $T = 0$ to $T = 0^+$, the $\mathbb{Z}_4 \to \mathbb{Z}_2$ change corresponds to a change of preference from $\mathcal{G}_2$ to $\mathcal{G}_1$. This already indicates that this difference between the $T = 0$ and $T = 0^+$ phases is not from thermal order-by-disorder (which is not surprising, since this is a mean-field treatment with no fluctuations). Thermal order-by-disorder would mean that, at finite temperatures, thermal fluctuations select some *subset* of the original four states in $\mathcal{G}_2$, but the $\mathbb{Z}_2$ degeneracy at finite temperatures is not from a subset of $\mathcal{G}_2$. It is rather from a different set of FEPC states entirely.

As there is a change in the preferred FEPC states as temperature becomes finite, the origin must be related to the entropy calculated within VMFT. At $T = 0$, there is no entropy contribution to the system, and the free energy simply reduces to the energy. At $T = 0^+$, entropy has an influence on the free energy of the system. We must therefore look at the entropy calculated within VMFT to understand what changes between $T = 0$ and $T = 0^+$. Consider Eq. (3.28):

$$f = \frac{F}{N} = \frac{X(m)}{N} - \frac{1}{N\beta}\sum_{i,a} \ln(Z_{ia}). \tag{D.1}$$

At $T = 0$, the only contribution is the first term, which is the energy. Suppose $T = \epsilon$ for $\epsilon \to 0^+$. There will now be a contribution from the entropy as well, which is related to the second term. Namely, this contribution is:

$$\frac{1}{N\beta}\sum_{i,a} \ln(Z_{ia}) = \frac{\epsilon}{N}\sum_{i,a} \ln\left(\frac{4\pi}{A_{ia}}\sinh(A_{ia})\right) \tag{D.2}$$

$$= \frac{\epsilon}{N}\sum_{i,a} \ln\left(\frac{4\pi\epsilon}{|\boldsymbol{B}_{ia}|}\sinh\left(\frac{|\boldsymbol{B}_{ia}|}{\epsilon}\right)\right) \tag{D.3}$$

$$= \frac{\epsilon}{N}\sum_{i,a} \ln\left(\frac{4\pi\epsilon}{|\boldsymbol{B}_{ia}|}\right) + \ln\left(\sinh\left(\frac{|\boldsymbol{B}_{ia}|}{\epsilon}\right)\right). \tag{D.4}$$

For $\epsilon \to 0^+$, $\epsilon\ln(\epsilon) \to 0$. However, $\sinh\left(\frac{|\boldsymbol{B}_{ia}|}{\epsilon}\right) \sim e^{\frac{|\boldsymbol{B}_{ia}|}{\epsilon}}$, so $\ln\left(\sinh\left(\frac{|\boldsymbol{B}_{ia}|}{\epsilon}\right)\right) \sim \frac{|\boldsymbol{B}_{ia}|}{\epsilon}$. Altogether, we have:

$$\frac{1}{N\beta}\sum_{i,a} \ln(Z_{ia}) \approx \frac{\epsilon}{N}\sum_{i,a}\frac{|\boldsymbol{B}_{ia}|}{\epsilon} = \frac{1}{N}\sum_{i,a}|\boldsymbol{B}_{ia}|. \tag{D.5}$$

Hence, the entropic contribution to the free energy at $T = 0^+$ scales roughly as the average magnitude of the local field. We must therefore take a closer look at how the local field is different for the states in $\mathcal{G}_1$ versus $\mathcal{G}_2$.

As shown in Eq. (3.27), there are two contributions to the local field at every site: (1) the exchange contribution due to interactions with the site's nearest-neighbors, and (2) the Zeeman contribution due to the applied field. When an applied field is turned on, the Zeeman contribution comes from $h^{\mu}_{ia} = \mu_B g^{\mu\nu}_{ia} H^{\nu}$, as shown in Eq. (3.27). Returning to the g-tensors shown in Eqs. (2.12) and (2.15), there is a special coincidence that occurs for

$\boldsymbol{H} \parallel [110]$ and for the xy–planar PC states. For two of the sublattices (namely, sublattices 1 and 2 in Eq. (2.15)), the Zeeman contribution h_{ia}^{μ} on these sublattices satisfy

$$\boldsymbol{h}_1 \propto \begin{pmatrix} g_1 & -g_2 & -g_2 \\ -g_2 & g_1 & g_2 \\ -g_2 & g_2 & g_1 \end{pmatrix} \begin{pmatrix} 1 \\ 1 \\ 0 \end{pmatrix} \propto \begin{pmatrix} 1 \\ 1 \\ 0 \end{pmatrix}, \tag{D.6}$$

$$\boldsymbol{h}_2 \propto \begin{pmatrix} g_1 & -g_2 & g_2 \\ -g_2 & g_1 & -g_2 \\ g_2 & -g_2 & g_1 \end{pmatrix} \begin{pmatrix} 1 \\ 1 \\ 0 \end{pmatrix} \propto \begin{pmatrix} 1 \\ 1 \\ 0 \end{pmatrix}. \tag{D.7}$$

These Zeeman contributions $\boldsymbol{h}_1$ and $\boldsymbol{h}_2$ are exactly parallel to the spins $\boldsymbol{S_1}$ and $\boldsymbol{S}_2$ (as shown in Figure 2.4a) of the PC states $\langle xy \rangle$ and $\langle \overline{xy} \rangle$![1]

Physically, this means that for small values of H and for $\langle xy \rangle$ and $\langle \overline{xy} \rangle$, instead of *canting* out of the PC configuration in the presence of a field, the spins on sublattices 1 and 2 do not change, but remain in their same orientation. We see that this differentiates the states in $\mathcal{G}_1$ from those in $\mathcal{G}_2$: the FEPC states in $\mathcal{G}_1$ do not completely benefit from the Zeeman interaction because some of the spins do not cant in the presence of the field. On the other hand, all FEPC states in $\mathcal{G}_2$ cant in the presence of an applied magnetic field. Returning to Eq. (D.5), this causes a slight difference in the local field $\boldsymbol{B}_{ia}$ for the FEPC states in $\mathcal{G}_1$ relative to $\mathcal{G}_2$. This is therefore the origin of the entropic difference between the two groups as temperature is changed from $T = 0$ to $T = 0^+$, leading to the $\mathbb{Z}_4 \to \mathbb{Z}_2$ change in Figure 4.11a as temperature becomes finite.

[1] Note that this coincidence does not occur when the field points along the [100] or [111] directions.